# CHARACTERIZATION OF METAGENOMICALLY IDENTIFIED CHANNELRHODOPSINS

# Charakterisierung metagenomisch identifizierter Kanalrhodopsine

## DISSERTATION

zur Erlangung des akademischen Grades
*Doctor rerum naturalium*
(Dr. rer. nat.)
im Fach Biophysik

eingereicht an der
Lebenswissenschaftlichen Fakultät der Humboldt-Universität zu Berlin

von
Johannes Oppermann, M. Sc.

Präsidentin der Humboldt-Universität zu Berlin:
Prof. Dr.-Ing. Dr. Sabine Kunst

Dekan der Lebenswissenschaftlichen Fakultät:
Prof. Dr. Dr. Christian Ulrichs

Gutachter 1. Prof. Dr. Peter Hegemann

2. Prof. Dr. Franz Bartl

3. Prof. Dr. Peter Hildebrandt

Tag der mündlichen Prüfung: 10.03.2021

*'This isn't magic, is it?'*

*'I don't think so,' said Johnny. 'It's probably just very, very, very strange science.'*

*'Oh, good,' said Yo-Less. 'Er .... What's the difference?'*

- Terry Pratchett, Johnny and the Bomb

# MerMAIDs
## need strong bouncers

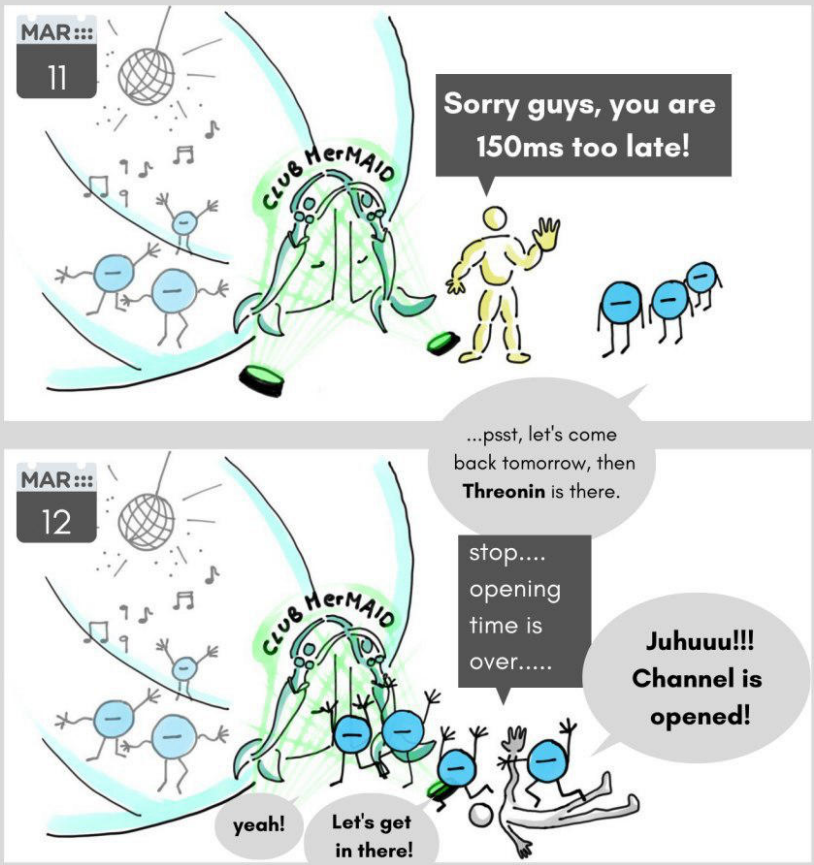


MerMAID | Cystein | Threonin | Anions

made by fine.stuhr-wulff@fu-berlin.de

# Abstract

Channelrhodopsins (ChRs) are light-gated ion channels mediating phototactic responses in motile algae and widely used as optogenetic tools to manipulate cellular activity using light. Many cation- and anion-conducting ChRs (CCRs and ACRs) have been identified from culturable chlorophyte and cryptophyte species. However, most microbial organisms cannot be cultured, resulting in an incomplete view of the diversity of ChRs. Metagenomics opens the door to gather insights on the distribution of ChRs in uncultured organisms. Here, the biophysical characterization of two groups of metagenomically identified ChRs is described.

The MerMAIDs (Metagenomically discovered marine, anion-conducting, and intensely desensitizing ChRs) represent a new ChR family with near-complete photocurrent desensitization under continuous illumination. The photocurrents can be explained by a single photocycle leading to the accumulation of a long-lived and non-conducting photointermediate. A conserved cysteine is critical for this phenomenon, as its substitution results in a strongly reduced desensitization.

The prasinophyte ChRs, harboring large carboxy-terminal extensions, were identified in marine giant viruses that acquired them from their motile and unicellular green algal hosts via lateral gene transfer. Expressed in cell culture, the viral ChRs are only functional upon the addition of trafficking sequences and carboxy-terminal truncation. The green algal and viral ChRs are anion-conducting and display non-desensitizing photocurrents when expressed in mammalian cells, though the viral representatives are less conductive and cytotoxic. Nonetheless, this group of ChRs represents the first green algal and viral ACRs.

This thesis highlights a broad distribution of ACRs among marine microbial organisms and the importance of functional metagenomics in discovering new ChRs.

# Zusammenfassung

Kanalrhodopsine (ChRs), lichtgesteuerte Ionenkanäle, vermitteln phototaktische Reaktionen in beweglichen Algen und sind als optogenetische Werkzeuge zur Manipulation der Zellaktivität mittels Lichts weit verbreitet. Viele Kationen- und Anionen-leitende ChRs (CCRs und ACRs) wurden aus kultivierbaren Chlorophyten- und Cryptophytenarten identifiziert. Die meisten mikrobiellen Organismen kann jedoch nicht kultiviert werden, was zu einem unvollständigen Bild der ChR-Vielfalt führt. Die Metagenomik öffnet die Tür für Erkenntnisse über die Verteilung von ChRs in unkultivierten Organismen. Diese Arbeit beschreibt die biophysikalische Charakterisierung von zwei Gruppen metagenomisch identifizierter ChRs.

Die MerMAIDs (*Metagenomically discovered marine, anion-conducting, and intensely desensitizing ChRs*) sind eine neue ChR-Familie und zeigen nahezu komplette Photostrom-Inaktivierung unter Dauerlicht. Die Photoströme lassen sich durch einen Photozyklus erklären, der zur Akkumulation eines langlebigen und nicht-leitenden Photointermediats führt. Ein konserviertes Cystein ist für dieses Phänomen entscheidend, da seine Substitution zu einer stark reduzierten Inaktivierung führt.

Die Prasinophyten ChRs, die große carboxyterminale Domänen aufweisen, wurden in großen, marinen Viren identifiziert, die sie von ihren beweglichen und einzelligen Grünalgen-Wirten durch lateralen Gentransfer übernommen haben. Heterolog exprimiert, sind die viralen ChRs nur nach Ergänzung von Transportsequenzen und carboxyterminaler Kürzung funktional. Die Grünalgen- und viralen ChRs sind Anionen-leitend mit nicht-inaktivierenden Photoströmen, wenn sie in Säugetierzellen exprimiert werden, obwohl die viralen Vertreter weniger leitfähig und zytotoxisch sind. Nichtsdestotrotz repräsentiert diese ChR-Gruppe die ersten Grünalgen- und Virus-ACRs.

Diese Arbeit zeigt eine breite Verteilung der ACRs unter marinen mikrobiellen Organismen und die Bedeutung der Funktionsmetagenomik bei der Entdeckung neuer ChRs.

# Contributions to the scientific community

## Parts of this work are published

**Oppermann, J.**, P. Fischer, A. Silapetere, B. Liepe, S. Rodriguez-Rozada, J. Flores-Uribe, E. Peter, A. Keidel, J. Vierock, J. Kaufmann, M. Broser, M. Luck, F. Bartl, P. Hildebrandt, J. Simon Wiegert, O. Béjà, P. Hegemann, and J. Wietek (2019). “MerMAIDs: A Family of Metagenomically Discovered Marine Anion-Conducting and Intensely Desensitizing Channelrhodopsins”. *Nature Communications* 10, 1, 3315.

Rozenberg, A.*, **J. Oppermann***, J. Wietek, R. G. Fernandez Lahore, R.-A. Sandaa, G. Bratbak, P. Hegemann, and O. Béjà (2020). "Lateral gene transfer of anion-conducting channelrhodopsins between green algae and giant viruses". *Current Biology* 30, 1-11.
*These authors contributed equally

## Parts of this work have been presented on conferences and meetings

| | |
|---|---|
| 02/2020 | Collaborative Research Center 1078 - Annual Meeting; Berlin, Germany; **J. Oppermann** and P. Hegemann; "Metagenomically identified Channelrhodopsins", *Talk*. |
| 08/2019 | Photobiology 2019; Barcelona, Spain; **J. Oppermann** *et al.*; "MerMAIDs: Novel metagenomically discovered, marine, anion-conducting and intensely desensitizing channelrhodopsins", *Poster*. |
| 02/2019 | Collaborative Research Center 1078 - Annual Meeting; Berlin, Germany; **J. Oppermann** *et al.*; "Novel Anion-Conducting Channelrhodopsins with Near-Complete Desensitization", *Poster* and *Talk*. |
| 09/2018 | 18$^{th}$ International Conference on Retinal Proteins (ICRP); Ontario, Canada; **J. Oppermann** *et al.*; "Novel Anion-Conducting Channelrhodopsins with Near-Complete Desensitization", *Poster*. |
| 03/2018 | Collaborative Research Center 1078 - Annual Meeting; Rauischholzhausen, Germany; **J. Oppermann**, J. Wietek, O. Béjà, and P. Hegemann; "Novel Anion-Conducting Channelrhodopsins with Near-Complete Desensitization", *Poster* and *Talk*. |

03/2018 Gordon Research Conference and Seminar - Photosensory Receptors & Signal Transduction; Lucca (Barga), Italy; **J. Oppermann**, J. Wietek, O. Béjà, and P. Hegemann; "Novel Anion-Conducting Channelrhodopsins with Near-Complete Desensitization", *Poster (Conference/Seminar)* and *Talk (Seminar)*.

# Acknowledgments

Bevor es mit dieser Doktorarbeit ans Eingemachte geht, möchte ich die Gelegenheit nutzen und zunächst den Leuten danken, ohne die dieses Abenteuer so nicht möglich gewesen wäre!

Besonderer Dank gilt Prof. Peter Hegemann für die Bereitstellung des Themas, Unterstützung wann immer diese nötig war und die Möglichkeit meine Arbeit auf mehreren Konferenzen und Meetings vorzustellen.

Großer Dank gilt auch meiner Familie und besonders meinen Eltern, die mich stets haben machen lassen und mich in der Wahl einer akademischen Laufbahn unterstützten und bestärkten.

Bei Prof. Oded Béjà bedanke ich mich für die bestehende Kolaboration, die im späteren Verlauf durch Dr. Andrey Rozenberg ergänzt wurde.

Des Weiteren möchte ich mich bei Jonas bedanken für Unterstützung besonders zu Beginn des Projektes sowie Tipps und Tricks für elektrophysiologische Messungen licht-gesteuerter Ionenkanäle. Auch danke ich der gesamten Arbeitsgruppe "Experimentelle Biophysik" für ein ausserordentlich angenehmes Arbeitsumfeld und problemlose Kooperationen. Für die Unterstützung bei der Aufreinigung von Membranproteinen möchte ich mich bei Matthias und Melanie bedanken und für Unterstützung bei molekular- und zellbiologischen Arbeiten im Labor bei Sandra, Tharsana und Maila. Den Elektrophysiologen danke ich für rege Diskussionen zu gesammelten Daten und möchte hierbei Berni nicht unerwähnt lassen, der im Zuge seiner Projektarbeit einen substantiellen Beitrag zum MerMAIDs-Projekt geleistet hat. Des weiteren danke ich Prof. Peter Hildebrandt und Anke Keidel für Resonanz Raman Spektroskopie, Paul für "*amazing and ingenious*" FTIR Spektroskopie, Arita für Flash Photolyse, Enno für MD Simulationen und Rodrigo für *Confocal Imaging*.

Die gute Gruppendynamik hat sich nicht nur im Labor bemerkbar gemacht, sondern auch für viel Spaß und Freude im Privaten gesorgt. Rodrigo, Enno, Sandra und Matt danke ich für unzählbare Stunden beim Bouldern, aber auch allen anderen Doktoranden möchte ich für viele schöne Abende danken, die wir zusammen bei Speis, Trank und Spiel verbracht haben.

Für das Korrekturlesen der Dissertation bedanke ich mich ganz herzlich bei Enno, Arita, Rodrigo, Johannes und Matt. Bei den Mitgliedern der Promotionskommission bedanke ich mich für die Begutachtung dieser Dissertation.

# Contents

# List of Figures

# List of Tables

# Abbreviations

| | |
|---|---|
| $\Delta E_{rev}$ | shifts of the reversal potential |
| $\lambda_e$ | excitation wavelength (in resonance Raman spectroscopic experiments) |
| $\lambda_i$ | isosbestic point |
| $\lambda_{max}$ | wavelength of maximum absorption or activity |
| $\tau_{des,\ app}$ | apparent kinetic of the transient photocurrent desensitization |
| $\tau_{des}$ | kinetics of the transient photocurrent desensitization |
| $\tau_{off,\ app}$ | apparent kinetic of the photocurrent decay |
| $\tau_{off}$ | kinetics of the return of stationary photocurrents to the baseline |
| $\tau_{rec}$ | kinetics of the transient photocurrent recovery |
| 7TM | heptahelical transmembrane domain |
| $[Cl^-]_e$ | extracellular $Cl^-$ concentration |
| $[Cl^-]_i$ | intracellular $Cl^-$ concentration |
| $pH_e$ | extracellular pH |
| $pH_i$ | intracellular pH |
| $E_{hold}$ | holding potential |
| $E_{rev}$ | reversal potential |
| ACR | anion-conducting channelrhodopsin |
| AP | action potential |
| ATP | adenosine triphosphate |
| BLUF | blue-light using flavin |
| BR | Bacteriorhodopsin |
| cAMP | cyclic adenosine monophosphate |
| CCR | cation-conducting channelrhodopsin |
| cDNA | complementary desoxyribonucleic acid |
| cGMP | cyclic guanosine monophosphate |
| ChR | Channelrhodopsin |
| CI | conical intersection |
| Ci | counterion |
| cNMP | cyclic nucleotide monophosphate |
| CRISPR/Cas | clustered regularly interspaced short palindromic repeats / CRISPR-associated protein |
| DMEM | Dulbeccos Modified Eagle Medium |
| DNA | desoxyribonucleic acid |
| DSB | dark-state bleach |
| $E_{1\text{-}5}$ | glutamate residues highly conserved in chlorophyte CCRs |
| EADS | evolution-associated difference spectra |

| | |
|---|---|
| EC | extracellular side |
| ECG | extracellular gate |
| ER | endoplasmic reticulum release signal |
| eYFP | enhanced yellow fluorescent protein |
| FAD | flavin adenosine dinucleotide |
| FC | Franck-Condon point |
| FCS | Fetal Calf Serum |
| FD | fast digest |
| FMN | flavin mononucleotide |
| FRET | Förster energy resonance transfer |
| FTIR | Fourier-transform infrared |
| GPCR | G-protein-coupled receptor |
| HEK | human embryonic kidney |
| HK | histidine kinase |
| HKR | histidine kinase rhodopsin |
| HOOP | hydrogen-out-of-plane |
| HPLC | high performance liquid chromatography |
| HR | Halorhodopsin |
| $I_{-60\,mV}$ | transient photocurrent amplitudes at a holding potential of $-60\,mV$ |
| $I_p$ | transient photocurrent amplitude |
| $I_s$ | stationary photocurrent amplitude |
| IC | intracellular side |
| ICG | intracellular gate |
| IR | infrared |
| LED | light-emitting diode |
| LJP | Liquid Junction Potential |
| LOV | light-oxygen-voltage |
| MD | molecular dynamics |
| MerMAIDs | metagenomically discovered, marine, anion-conducting and intensely desensitizing channelrhodopsins |
| MES | MerMAID-expressing species |
| N | amino terminus |
| NCBI | National Center for Biotechnology Information |
| ND | Neutral Density |
| ND7/23 | neuroblastoma-derived cell line |
| NMDG | N-methyl-D-glucamine |
| NTP | nucleotide triphosphate |
| OD | optical density |
| OPO | optical parametric oscillator |

| | |
|---|---|
| $P_{\lambda_{max}}$ | photointermediate with denoted maximum absorption wavelength |
| PBS | Phosphate buffered saline |
| PCR | polymerase chain reaction |
| PDB | protein data base |
| PDL | Poly-D-Lysine |
| PYP | photoactive yellow protein |
| RhoPDE | rhodopsin phosphodiesterase |
| RNA | ribonucleic acid |
| RP | resting membrane potential |
| RR | resonance Raman |
| RR-like | histidine-kinase response regulator-like |
| RSB | retinal Schiff base |
| $RSBH^+$ | protonated retinal Schiff base |
| $S_0$ | electronic ground state |
| $S_1$ | first electronic excited state |
| SEM | standard error of the mean |
| SR | Sensory Rhodopsin |
| SST | sea surface temperatures |
| TM1-7 | transmembrane helices 1-7 |
| TS | membrane-trafficking signal |
| UV | ultraviolet |
| UVR8 | ultraviolet-resistance locus 8 |

# 1. Introduction

Light is a form of electromagnetic radiation and can be considered as a particle (photon) when interacting with matter or as a wave when traveling through space. It is categorized depending on its wavelength ($\lambda$ in nm), i. e. the distance between the wave's successive maxima or minima. At wavelengths between 380 nm to 740 nm, it is referred to as visible light and perceived as colors from purple to red by humans. The light outside the visible spectrum and of $\lambda = <380$ nm is referred to as ultraviolet (UV) light, while the light of $\lambda = >740$ nm is called infrared (IR) light.

Archaea, bacteria, and eukarya form the three domains of life on earth. For many organisms, light is fundamental for survival. For example, light serves as a source of energy during photosynthesis or as a carrier of environmental information. Depending on the light intensity and wavelength, organisms can adjust their behavior and physiology.

To sense light, various proteins and protein complexes have evolved in all life domains, collectively called photosensory proteins or photoreceptors. The majority of these proteins incorporate chromophores, small organic and aromatic molecules, which extend their sensitivity to the visible light spectrum (Möglich *et al.*, 2010; Kottke *et al.*, 2018). These molecules are unsaturated organic compounds with alternating C−C and C=C systems and $\pi$-electrons delocalized across the polyene. In other words, the chromophores are aromatic conjugated $\pi$-electron systems. The size of this system defines the absorption wavelength: the larger the system is, the longer the absorbed wavelength (Möglich *et al.*, 2010).

This dissertation describes the characterization of metagenomically identified channelrhodopsins (ChRs) using electrophysiology and spectroscopy. ChRs are members of the versatile superfamily of microbial rhodopsins and generally found in algae. This chapter will introduce photosensory proteins and microbial rhodopsins with an emphasis on ChRs. Furthermore, a short introduction to the field of metagenomics will is included.

## 1.1. Photosensory proteins

Most photosensory proteins are structurally organized into separate sensor and effector domains (Möglich *et al.*, 2010) and share basic principles in their photoactivation mechanisms. Upon excitation by a photon, a sequential series of intermediate states can be distinctly identified via transient changes of the absorption maximum, ultimately returning to the initial dark state. Generally, these states are referred to as photointermediates, and their sequence as photocycle. The primary photochemical reaction occurs in the sub-ns range and results in a distorted chromophore sterically interfering with its binding pocket. Conformational changes in the protein backbone are preceded or accompanied by proton and electron transfer reactions (Kottke *et al.*, 2018).

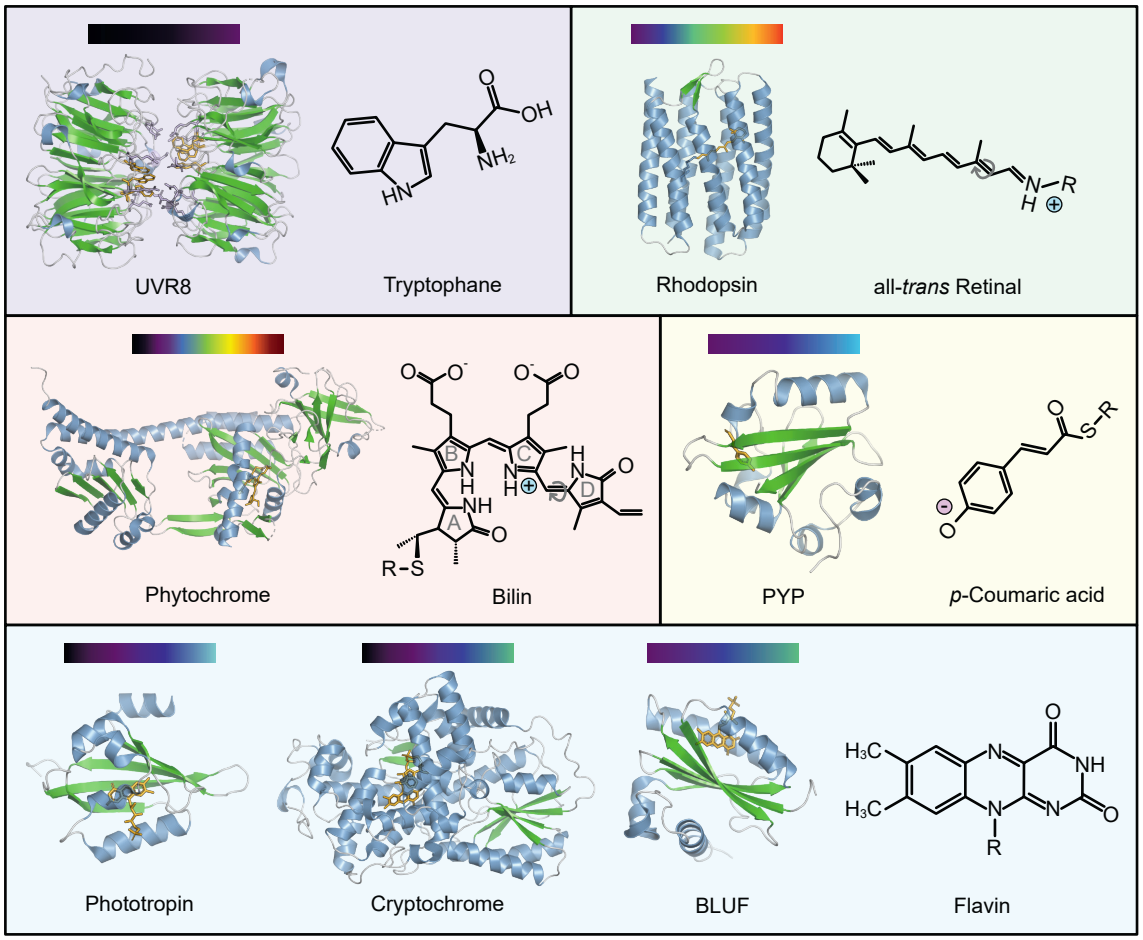


**Figure 1.: Overview of photosensory proteins.** Representative crystal structures of UVR8 (*At*UVR8; PDB: 4D9S; Christie *et al.*, 2012), rhodopsin (*Np*SRII; PDB: 1JGJ; Luecke *et al.*, 2001), phytochrome (Cph1; PDB: 2VEA; Essen *et al.*, 2008), PYP (*Hh*PYP; PDB: 1NWZ; Getzoff *et al.*, 2003), phototropin (*At*Phot2; PDB: 2Z6D; Nakasako *et al.*, 2008), cryptochrome (*At*Cry3; PDB: 2J4D; Klar *et al.*, 2007), and BLUF (*Rs*BlrB; PDB: 2BYC; A. Jung *et al.*, 2005) are shown, with the covered spectral range indicated as a colored bar above, respectively, and the chromophore chemical structure on the right. In the structures, $\alpha$-helices are colored blue, $\beta$-sheets green, and the chromophore yellow. Abbreviations: BLUF, blue-light using flavin; PYP, photoactive yellow protein; UVR8, ultraviolet-resistance locus 8.

## UV-light receptors

The plant photoreceptor Ultraviolet Resistance Locus 8 (UVR8) senses UV-light between 280 nm and 320 nm. Unlike many photosensory proteins, UVR8 does not incorporate a cofactor as a chromophore. The photosensor is organized as a symmetric homodimer, consisting mostly of $\beta$-sheets (Fig. 1, top left). The dimer is stabilized by arginine residues. These interact with tryptophan residues, which act as the chromophore.

Upon photon absorption by the tryptophan residues, the dimer is destabilized and transitions into an active monomeric state (Rizzini *et al.*, 2011; Di Wu *et al.*, 2012), ultimately triggering the expression of UV-protective metabolites like flavonols as well as morphological adaptations to prevent damage from UV-B light (B. A. Brown *et al.*, 2005; Galvão and Fankhauser, 2015; Losi *et al.*, 2018). Similarly, in LITE-1, a sensor responsible for UV-

light avoidance in *Caenorhabditis elegans*, photosensitivity is conferred by two tryptophan residues (Gong *et al.*, 2016).

### Rhodopsins

Among the best described and understood photosensory proteins are rhodopsins (Fig. 1, top right), found in eukarya, bacteria, and archaea. Microbial (type-1) and animal (type-2) rhodopsins show differences on a sequence and function level. However, they are remarkably similar in their structural organization (Ernst *et al.*, 2014). Therefore, a shared common ancestor was suggested (Yee *et al.*, 2013; Shalaeva *et al.*, 2015).

Rhodopsins are membrane-bound, which makes them unique among the photosensory proteins shown in figure 1. Type-1 and type-2 rhodopsins share a heptahelical transmembrane domain architecture (7TM; TM1-7) with the amino-terminus located extracellularly and the carboxy-terminus intracellularly. Retinal is incorporated as the chromophore and covalently bound to a highly conserved lysine in TM7 via a Schiff base. Microbial rhodopsins preferentially bind all-*trans* retinal which isomerizes to the 13-*cis* conformation upon photon absorption. On the other hand, animal rhodopsins bind 11-*cis* retinal that isomerizes to all-*trans* upon excitation by a photon (Ernst *et al.*, 2014).

In microbial rhodopsins, the chromophore reverts thermally to the dark state. Animal rhodopsins, on the other hand, are enzymatically inactivated, followed by the release of the chromophore and its recycling in neighboring cells (Kiser *et al.*, 2014). Type-2 rhodopsins are a subclass of G-protein-coupled receptors (GPCRs) and widely known for their visual function (Shichida and Matsuyama, 2009), but also exhibit non-visual functions (Terakita, 2005). The microbial rhodopsins are described in more detail in chapter 1.2.

### Phytochromes

Bilin, a linear tetrapyrrole, is incorporated as the chromophore in the amino-terminal photosensory domain of plant phytochromes (Butler *et al.*, 1959), cyanobacteriochromes (Yeh *et al.*, 1997; Hughes *et al.*, 1997), and bacteriophytochromes (Davis *et al.*, 1999). Phytochromes (Fig. 1, center left) show a broad spectral range (Anders and Essen, 2015) and transition between two thermally stable states, generally referred to as $P_r$ (inactive, red-light absorbing state) and $P_{fr}$ (active, far-red-light absorbing state; Fankhauser and Staiger, 2002), with at least one exception shown in bathybacteriophytochromes (Rockwell *et al.*, 2006).

Photon absorption induces the isomerization of the chromophore around $C_{15}$=$C_{16}$ (Rockwell *et al.*, 2006). Subsequently, in plant cells, the protein translocates to the nucleus (Sakamoto and Nagatani, 1996), controlling de-etiolation, vegetative growth, and the transition to flowering (Fankhauser and Staiger, 2002). Bacteriophytochromes and cyanobacteriochromes are coupled with histidine-kinase domains and function as light-regulated

enzymes (Yeh *et al.*, 1997; Bhoo *et al.*, 2001).

### Xanthopsins

The xanthopsins are small, blue-light-absorbing photoreceptors (Fig. 1, center right). Photoactive yellow protein (PYP; 126 amino acids) is the best-known representative, potentially involved in the photophobic behavior of *Ectothiorhodospira halophila* (Sprenger *et al.*, 1993).

The chromophore 4-hydroxycinnamic acid (*p*-coumaric acid) is covalently bound via a thioester to a conserved cysteine (Kort *et al.*, 1996b) and stabilized by hydrogen bonds to close-by residues (Anderson *et al.*, 2004). Upon photon absorption, the chromophore's *trans-cis* isomerization is observed (Kort *et al.*, 1996a). In contrast to most photosensory proteins, all photointermediates are structurally identified by serial crystallography in the range from ns to s (Ihee *et al.*, 2005).

### Phototropins

Light-oxygen-voltage (LOV) sensors, blue-light using flavin (BLUF) proteins, and cryptochromes incorporate different flavin molecules as chromophores (Fig. 1, bottom). The amino-terminal light-sensing domain of phototropins consists of two LOV sensors that bind flavin mononucleotide (FMN; Christie, 2007). Absorption of blue light leads to the formation of a thioether between the chromophore and a conserved cysteine through a triplet-excited state (Kottke *et al.*, 2003; Schleicher *et al.*, 2004; Matsuoka *et al.*, 2007). Ultimately, structural changes lead to the activation of a carboxy-terminal serine/threonine kinase and autophosphorylation of the protein (Christie *et al.*, 1998).

Plant phototropins are, as the name suggests, intricately involved in the phototropism of the hypocotyl upon blue-light absorption (Sakai *et al.*, 2001). Furthermore, they play minor roles in the opening of stomata (Kinoshita *et al.*, 2001), chloroplast movement (Sakai *et al.*, 2001), and light-regulated ion fluxes (Babourina *et al.*, 2002). In the alga *Chlamydomonas reinhardtii*, blue-light responses of the sexual life cycle (Huang and Beck, 2003) and the expression of photoprotective genes (Petroutsos *et al.*, 2016) are associated with phototropins.

### BLUFs

BLUF domains are prokaryotic blue-light sensors and bind flavin adenosine dinucleotide (FAD) as chromophore (Gomelsky and Kaplan, 1998; Gomelsky and Klug, 2002). Light absorption induces an electron transfer from a tyrosine residue to the chromophore. Subsequently, the chromophore transitions to a radical state, with only minimal conformational changes detected (Masuda *et al.*, 2004).

These domains confer blue-light sensitivity to proteins such as AppA that affects transcription of genes dependent on oxygen levels (Gomelsky and Kaplan, 1998; Masuda and Bauer, 2002; Braatsch and Klug, 2004), but were also found to be linked to cyclase- or phosphodiesterase-domains (Gomelsky and Klug, 2002).

### Cryptochromes

The first described flavin-binding photosensory proteins were the cryptochromes (Ahmad and Cashmore, 1993). While the function of their carboxy-terminal domain is unknown, the amino-terminus shows high similarities with DNA photolyases and binds Pterin or FAD as a chromophore (Fankhauser and Staiger, 2002). Similar to the BLUF domains, a radical FAD intermediate is formed upon photon absorption and acts as a signaling state.

Subsequent absorption of green light produces a non-signaling photointermediate from which FAD returns to the initial dark state independent of light (Bouly *et al.*, 2007; Möglich *et al.*, 2010). In animals, cryptochromes are involved in the circadian rhythm, either by being part of the central oscillator or its entrainment (Stanewsky *et al.*, 1998; van der Horst *et al.*, 1999). In plants, they are associated with de-etiolation and transition from vegetative to reproductive growth (Fankhauser and Staiger, 2002).

## 1.2. Microbial rhodopsins

The microbial rhodopsins are a diverse group of proteins, comprising light-activated ion pumps, ion channels, enzymes, and light sensors interacting with transducer proteins (Fig. 2A). The first identified microbial rhodopsin was the proton pump Bacteriorhodopsin (*Hs*BR), expressed in purple membrane patches of the archaea *Halobacterium salinarum*[1] (Oesterhelt and Stoeckenius, 1971; Dunn *et al.*, 1981).

In anaerobic conditions, *H. salinarum* accumulates the purple membranes. The outward-pumping activity of *Hs*BR establishes a $H^+$ gradient, used by the ATP-synthase to produce adenosine triphosphate (Oesterhelt and Stoeckenius, 1973; Matsuno-Yagi and Mukohata, 1977).

Besides *Hs*BR, three other microbial rhodopsins were identified in *H. salinarum*: the $Cl^-$ pump Halorhodopsin (*Hs*HR), and Sensory Rhodopsin I and II (*Hs*SRI and *Hs*SRII; Matsuno-Yagi and Mukohata, 1977; Bogomolni and Spudich, 1982; Schobert and Lanyi, 1982; K.-H. Jung, 2007).

Over 7000 microbial rhodopsins have been identified and described (Govorunova *et al.*, 2017a) from organisms living in a large variety of photic environments (Finkel *et al.*, 2013). Microbial rhodopsins are functionally and phylogenetically diverse, with representatives found in archaea, bacteria, and eukarya like algae and fungi (Fig. 1B). Among the microbial

[1] formerly *Halobacterium halobium*.

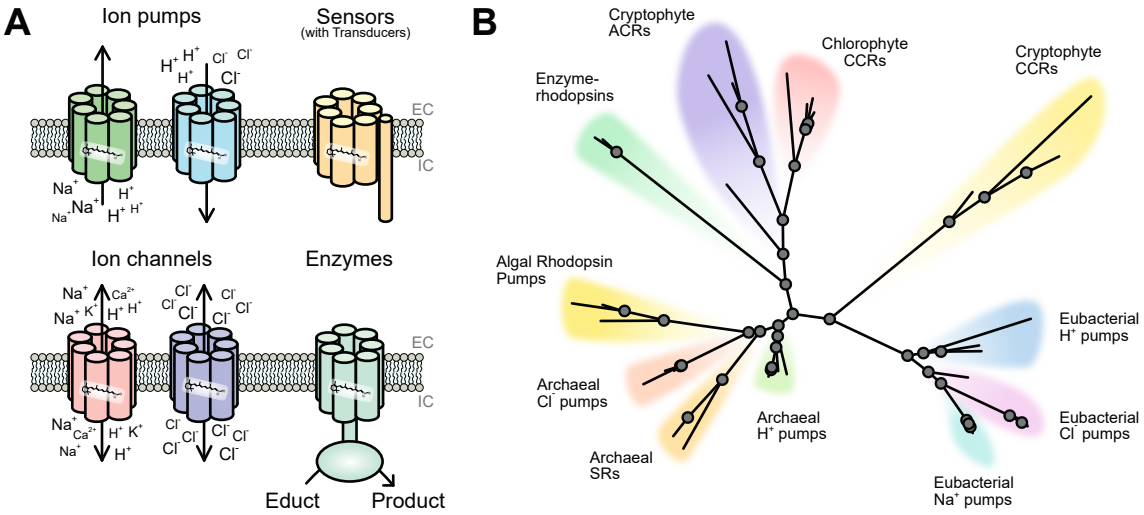


**Figure 2.: The family of microbial rhodopsins.** **A,** Overview of the functional diversity of microbial rhodopsins. Ion pumps actively transport ions against their electrochemical gradient out or into the cell; ion channels allow passive conduction of cations or anions; sensors activate secondary signaling pathways via transducer proteins; enzymes catalyze chemical reactions to form a product from an educt. Proteins are shown as cartoon with the embedded all-*trans* retinal chromophore overlayed. Arrows indicate the direction of ion translocation. The translocated ions are denoted. Note: Ion pumps only transport one type of ion (e.g. $Na^+$). **B,** Phylogeny of microbial rhodopsins. A list of the included protein sequences can be found in table S1. Abbreviations: ACRs, anion-conducting channelrhodopsins; CCRs, cation-conducting channelrhodopsins; EC, extracellular; IC, intracellular; SR, Sensory Rhodopsins.

rhodopsins, ion pumps show an extensive diversity, with ion selectivity not only for $H^+$ but also for $Na^+$ or $Cl^-$ (Pinhassi *et al.*, 2016).

In *Hs*BR, Asp85, Thr89, and Asp96 are critical residues of the proton-pumping mechanism, with Asp85 and Asp96 as the primary $H^+$ acceptor and donor, respectively (Lanyi, 2006). These residues are referred to as the DTD motif, showing high conservation within the archaeal proton-pumping rhodopsins. Interestingly, all microbial rhodopsin ion pumps can be categorized according to the residues homologous to the DTD motif (Béjà and Lanyi, 2014; Inoue *et al.*, 2015). In eubacterial proton pumps like proteorhodopsins (Béjà *et al.*, 2000) or *Gloeobacter* rhodopsin (Miranda *et al.*, 2009), the primary proton donor is less conserved. Therefore, this group is characterized instead by a DTX motif. On the other hand, in *Coccomyxa subellipsoidea* rhodopsin (*Cs*R; Vogt *et al.*, 2015) and *Acetabularia* rhodopsin (Lee *et al.*, 2011), two algal proton-pumping rhodopsins, the DTD motif is conserved. In archaeal and eubacterial $Cl^-$ pumps (Inoue *et al.*, 2014; Yoshizawa *et al.*, 2014), the proton acceptor and donor are not conserved and replaced by uncharged polar residues, changing the motif to TSA and NTQ, respectively. $Na^+$-pumping rhodopsins are, so far, exclusively identified in marine bacteria (Inoue *et al.*, 2013; Tsunoda *et al.*, 2017), showing a characteristic NDQ motif.

The second class of electrogenic microbial rhodopsins are the ChRs (Fig. 2A). Cation- and anion-conducting ChRs (CCRs and ACRs) have been identified in chlorophyte and

cryptophyte algae (Nagel *et al.*, 2002, 2003; Govorunova *et al.*, 2015, 2016b), but not in archaea or bacteria. They will be described in more detail in chapter 1.3.

Sensory microbial rhodopsins like *Hs*SRI and *Hs*SRII are non-electrogenic and have been mainly identified in archaea (Fig. 2A). They associate with transducer proteins in the cell membrane and control the positive and negative phototaxis of archaea via a signaling cascade involving CheA and CheY (Spudich, 2006). Outside of archaea, sensory rhodopsins have only been found in one cyanobacterium, *Anabaena sp.* (not included in figure 2B). Interestingly, the *Anabaena* sensory rhodopsin (ASR) uses cytosolic signal transmitters instead of membrane-bound transducer proteins (K.-H. Jung *et al.*, 2003). Pinhassi *et al.* (2016) suggest that the group of cyanobacterial sensory rhodopsins comprises more members, though experimental evidence for this hypothesis has not been presented yet.

The enzymerhodopsins (Fig. 2A) found in eukarya are similar to the archaeal sensory rhodopsins. However, instead of interacting with secondary signal-transmitting proteins, they harbor large intracellular catalytical domains connected via linker domains to the light-sensing rhodopsin domain (Mukherjee *et al.*, 2019). Histidine kinase rhodopsins (HKRs) have been found in motile unicellular algae (Luck *et al.*, 2012) and possibly involved in cell differentiation and the circadian rhythm (Mukherjee *et al.*, 2019). Rhodopsin phosphodiesterases (RhoPDEs) were found in choanoflagellates (Yoshida *et al.*, 2017; Brunet *et al.*, 2019). These enzymes, catalyzing the hydrolyzation of cNMPs to 5'NMPs, are, for example, involved in the collective contractility of choanoflagellate colonies (Brunet *et al.*, 2019). Their enzyme counterpart are rhodopsin cyclases, catalyzing the production of cNMPs from NTPs and identified in motile zoospores of fungi (Avelar *et al.*, 2014) and in algae (Tian *et al.*, 2018), associated with phototaxis and development, respectively.

### 1.2.1. Primary photochemical reaction

Microbial rhodopsins bind all-*trans* retinal covalently via a Schiff base between $C_{15}$ of the chromophore and the $\epsilon$-amino group of a conserved lysine in TM7, the retinal Schiff base (RSB). In the dark state, the RSB is protonated (RSBH+) and the positive charge is stabilized by negative charges (the counterions, Ci; Fig. 3A, bottom). In the gas phase, an absorption maximum of 610 nm was determined for the $RSBH^+$ (Rajput *et al.*, 2010; Andersen *et al.*, 2005), indicating that the opsin-shift is hypsochromic. The opsin-shift refers to the change of the absorption maximum of the retinal chromophore upon binding to the opsin (Nakanishi *et al.*, 1980), i. e. the protein backbone. It demonstrates the spectral tuning of the protein environment and its importance for the broad spectral range of microbial rhodopsins, covering the full visible spectrum (Ernst *et al.*, 2014). Photon absorption induces the isomerization of the retinal chromophore around $C_{13}$=$C_{14}$, resulting in the 13-*cis* isomer (Fig. 3A, top).

In *Hs*BR, this primary photochemical reaction occurs on a sub-ps timescale (Mathies *et al.*, 1988; Dobler *et al.*, 1988; Herbst *et al.*, 2002) and can be depicted as a potential energy

diagram along the reaction coordinate of $C_{13}$=$C_{14}$ (Fig. 3C). The isomerization of the chromophore is observable as a bathochromic shift of the absorption maximum (Sharkov *et al.*, 1985). The difference of the electronic ground state ($S_0$) energy level of the all-*trans* and 13-*cis* isomers (Fig. 3C) is approximately 40 kJ mol$^{-1}$ to 50 kJ mol$^{-1}$ (Logunov and El-Sayed, 1997), an energy barrier high enough to reduce the chance of spontaneous isomerization.

The energy barrier is overcome by absorption of a photon, elevating the conjugated $\pi$-electron system (Salem and Bruckmann, 1975) to the Franck-Condon point[2] of the first electronic excited state ($S_1$) with subsequent transition to the energy minimum of $S_1$ (I in Fig. 3C).

Changes in the bond lengths and torsion around $C_{13}$=$C_{14}$ result in the entry of the conical intersection (CI) where the electronic states' energy surfaces are closest. At this point, a transition to $S_0$ is most likely with equal probability to reach either the parent state or the primary photoproduct (Warshel, 1978; Garavelli, 2006; Schapiro *et al.*, 2011). Before the $C_{13}$=$C_{14}$ isomerization can be completed, a secondary potential minimum (J in Fig. 3C) must be overcome.

The potential energy surfaces along $C_7$=$C_8$, $C_9$=$C_{10}$, and $C_{11}$=$C_{12}$ of retinal should be similar to those of $C_{13}$=$C_{14}$ shown here (Fig. 3C; Ernst *et al.*, 2014). However, due to interactions of the protein environment with the chromophore, the energy barriers for isomerization around the other ethylenic bonds are elevated, making the isomerization around $C_{13}$=$C_{14}$ energetically more favorable (Tavan *et al.*, 1985). The protein backbone further contributes to the isomerization efficiency by minimizing steric hindrances, supporting the rearrangement of the chromophore nuclei (Gai *et al.*, 1998).

Additionally, $C_{15}$=N can isomerize between a 15-*anti* and 15-*syn* configuration (Fig. 3B). The 13-*cis*,15-*anti* configuration is unstable within the context of the protein backbone. Its back reaction to all-*trans*,15-*anti* occurs within 100 ms to 250 ms at room temperature in *Hs*BR (Váró and Lanyi, 1991). However, the 13-*cis*,15-*syn* chromophore is stable. This stability may result from a similar space occupancy as the all-*trans*,15-*anti* chromophore within the retinal-binding pocket (Harbison *et al.*, 1984). This results in a mixed isomer composition in the dark state of dark-adapted *Hs*BR with absorption maxima of 568 nm and 548 nm for all-*trans*,15-*anti* and 13-*cis*,15-*syn*, respectively (Maeda *et al.*, 1977; Harbison *et al.*, 1984; S. O. Smith *et al.*, 1984).

The maximum absorption wavelength resembles the difference between the energy levels of $S_0$ and $S_1$ ($\Delta E = h\nu = hc\lambda^{-1}$)[3]. $\Delta E$ is determined by three basic principles (Kakitani *et al.*, 1985; Hoffmann *et al.*, 2006; W. Wang *et al.*, 2014): 1) ground state stabilization; 2) excited state stabilization; 3) chromophore planarity (Fig. 3D). These principles are

[2] Franck-Condon principle: Upon an electronic transition of a molecule, the nuclear configuration of the molecule remains unaffected. Therefore, vibrational levels in the excited state that are most similar to vibrational levels of the ground state are favored (Luis *et al.*, 2003).

[3] $h$, Planck constant; $\nu$, frequency; $c$, speed of light; $\lambda$, wavelength.

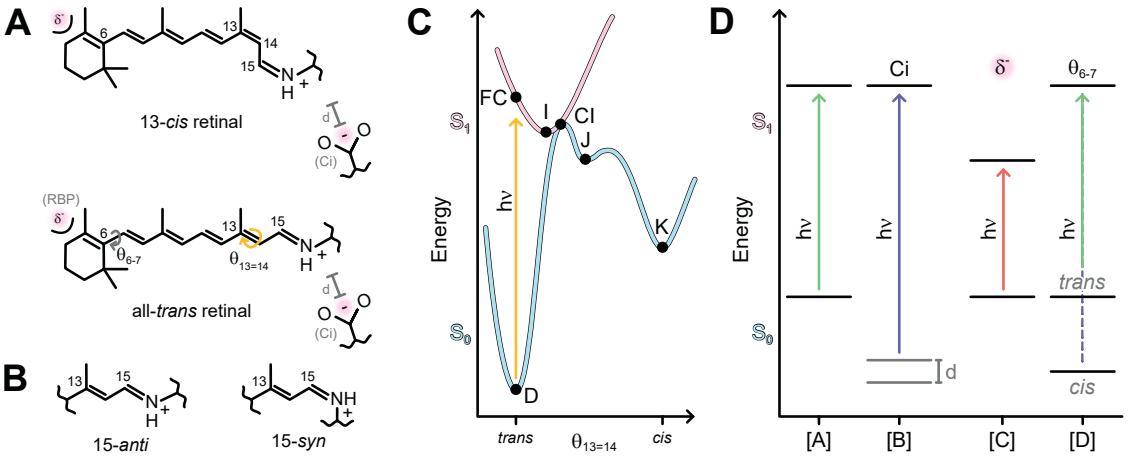


**Figure 3.: Primary photochemical reaction and determinants of the absorption wavelength.** **A,** Chemical structure of the retinal all-*trans* (bottom) and 13-*cis* isomers (top). Upon photon absorption, all-*trans* retinal isomerizes around $C_{13}$=$C_{14}$ (orange arrow) and forms the 13-*cis* isomer. Determinants of the absorption wavelength (distance (d) of counterions (Ci) to the RSB; polarity of the retinal binding pocket ($\delta^-$); torsion of $C_6$–$C_7$ ($\Theta_{6\text{-}7}$)) are indicated. **B,** Chemical structure of the protonated retinal Schiff base in the *anti* and the *syn* configuration. **C,** Potential energy diagram of the *trans-cis* isomerization around $C_{13}$=$C_{14}$, according to Nogly *et al.* (2018). Absorption of a photon elevates all-*trans* retinal from the electronic ground state ($S_0$) to the Franck-Condon point (FC) of the first electronic excited state ($S_1$) from where it relaxes back to $S_0$ through the conical intersection (CI), going through local energy minima relating to the I, J, and K photointermediates in the photocycle of *Hs*BR. **D,** Determinants of the absorption wavelength, according to Ernst *et al.* (2014). [A], Destabilization of $S_0$ and $S_1$; [B], Negatively charged counterions stabilize $S_0$ with a dependence on the distance between Ci and $RSBH^+$; [C], Stabilization of $S_1$ by polar residues close to the $\beta$-ionone ring; [D], Torsion of $C_6$–$C_7$ affects planarity of the chromophore. In the *trans* conformation, planarity is increased and $S_0$ destabilized, while the *cis* conformation distorts the planarity, shortening the $\pi$-electron system and stabilizing $S_0$.

directly affected by interactions between the chromophore and its protein environment. Stabilization, in this context, refers to a lowered energy level of the respective electronic state.

In the dark state, the $RSBH^+$ is stabilized by the counterions ([B] in Fig. 3D). The stabilization level is affected by the number of counterions and their distance to the $RSBH^+$ (Blatz *et al.*, 1972). Upon photon absorption, the $\pi$-electron distribution shifts towards the $\beta$-ionone ring of the retinal (Kobayashi *et al.*, 2001; Schenkl *et al.*, 2005). The energy level of $S_1$ is mainly affected by the polarity of the retinal-binding pocket ([C] in Fig. 3D). The charge transition is affected by aromatic residues along the polyene chain (Houjou *et al.*, 2001; Kloppmann *et al.*, 2005). The planarity of the chromophore determines the length of the conjugated $\pi$-electron system ([D] in Fig. 3D). Torsion of $C_6$–$C_7$, i. e. a 6s-*cis* configuration, affects the planarity of the chromophore, thereby shortening the conjugated $\pi$-electron system and lowering the energy level of $S_0$. Generally, microbial rhodopsins stabilize the retinal in the 6s-*trans* form (Harbison *et al.*, 1985).

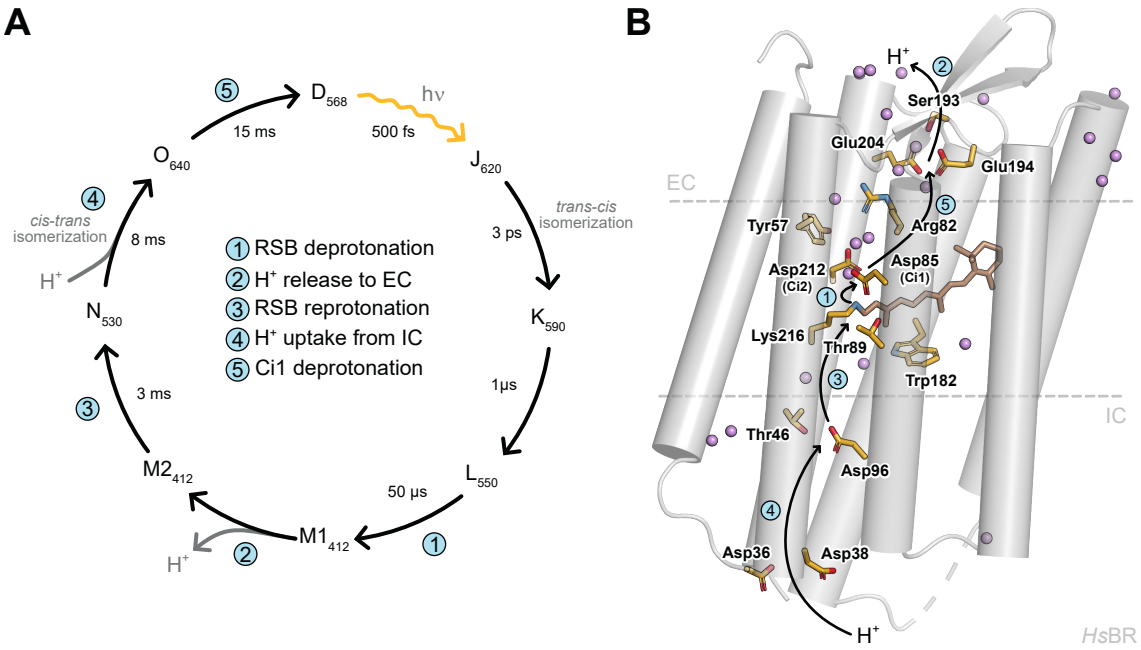


**Figure 4.: The photocycle of Bacteriorhodopsin. A**, Model of the photocycle of *Hs*BR. Photointermediates are named alphabetically from J to O with the dark state indicated as D. The maximum absorption wavelength of the different intermediates is indicated as lower case number, respectively. The sequential steps of the $H^+$ transport from the inside to the outside are indicated at the respective photointermediate transitions. The orange arrow indicates photon absorption and initiation of the photocycle. Photointermediate kinetics are given, according to Heberle *et al.* (2000). **B**, Structure of the dark state ($D_{568}$) of *Hs*BR (PDB: 1C3W; Luecke *et al.*, 1999b) with the individual steps of the vectorial $H^+$ transport indicated by arrows and circled numbers. The covalently bound retinal chromophore in the all-*trans* configuration (brown) and relevant residues (yellow) are depicted as sticks with oxygens marked red and nitrogens marked blue. Stabilized waters (purple) are shown as spheres.

### 1.2.2. The photocycle of a proton pump

The primary photochemical reaction (Ch. 1.2.1) merely covers the first two steps of the photocycle of *Hs*BR (Fig. 4A). The photocycle is a series of transient spectral intermediates that the protein transforms into upon photon absorption, ultimately returning to the initial dark state and accompanied by proton transfer reactions (Fig. 4B; A. Lewis *et al.*, 1974; Lozier *et al.*, 1975; Lozier and Niederberger, 1977). The mixed isomer composition of the dark-adapted *Hs*BR (Maeda *et al.*, 1977; Harbison *et al.*, 1984; S. O. Smith *et al.*, 1984) makes the clear identification of spectral intermediates difficult. At neutral pH, the photocycle initiated from a dark state populated by 13-*cis*,15-*syn* retinal lacks proton translocation across the membrane (Gergely *et al.*, 1994). However, upon pre-illumination, the dark state is populated exclusively by all-*trans*,15-*anti* retinal, referred to as light-adaptation (Oesterhelt and Stoeckenius, 1973; Jan, 1975; Dencher *et al.*, 1990). Here, the photocycle of *Hs*BR will be described starting from a dark state with all-*trans*,15-*anti* retinal. Classically, the photointermediates are named alphabetically from J to O (Fig. 4A). This nomenclature was adopted for other microbial rhodopsins to denote photointermediates

of similar absorption wavelength. Alternatively, intermediates are denoted by $P_{\lambda_{max}}$, where $\lambda_{max}$ refers to the maximum absorption wavelength of the photointermediate.

Absorption of light at 568 nm initiates the photocycle of light-adapted *Hs*BR (Fig. 4A). Within 200 fs, the $\pi$-electron distribution located at the $RSBH^+$ in the dark state, transitions towards the $\beta$-ionone ring of retinal (Schenkl *et al.*, 2005; Kobayashi *et al.*, 2001). The J intermediate can be detected 500 fs after excitation, with the absorption wavelength shifted bathochromic to 620 nm (Nuss *et al.*, 1985; Mathies *et al.*, 1988; Herbst *et al.*, 2002). Upon the formation of $J_{620}$, the retinal chromophore is twisted and completes the *trans-cis* isomerization around $C_{13}$=$C_{14}$ resulting in its relaxation to $K_{590}$ within 3 ps (Fig. 3A; Nuss *et al.*, 1985; Polland *et al.*, 1986; Atkinson *et al.*, 1989; Doig *et al.*, 1991; Nogly *et al.*, 2018).

A hydrogen-bonding network composed of Asp85 (Ci1), Asp212 (Ci2), and a water molecule (w402) stabilizes the positively charged $RSBH^+$ in the dark state (Marti *et al.*, 1991). Formation of $L_{550}$ within 1 µs leads to the reorientation of the $RSBH^+$ towards the cytoplasmic side, where it points into a hydrophobic pocket (Nango *et al.*, 2016). Subsequently, the hydrogen bond between w402 and the $RSBH^+$ is disrupted (Nogly *et al.*, 2018; Gai *et al.*, 1998), affecting the p$K_a$ of the RSB (Sheves *et al.*, 1986). Furthermore, during the formation of $L_{550}$, a bending of TM3 can be observed. This structural change may promote the interaction between the $RSBH^+$ and the primary proton acceptor Asp85 (Nango *et al.*, 2016). This primer for the proton transfer (L. S. Brown *et al.*, 1994) is potentially mediated by Thr89 (Lanyi, 2006).

The deprotonation of the RSB (Step 1 in Fig. 4) is detected as a large blue-shift of the absorption maximum and marks the formation of $M1_{412}$ (A. Lewis *et al.*, 1974; Aton *et al.*, 1977). The protonation of Asp85 triggers the release of a proton from the proton release complex (Step 2 in Fig. 4) during the transition from $M1_{412}$ to $M2_{412}$ (Garczarek *et al.*, 2005). This so-called excess proton is delocalized, oscillating between two hydrogen-bonded waters, Glu194 and Glu204 (Lanyi, 2006). The proton release is mediated by Arg82, which is connected to Asp85 via two waters. Upon protonation of Asp85, this network collapses and Arg82 orients towards Glu194 and Glu204 (Luecke *et al.*, 1999a, 2000; Sass *et al.*, 2000). Protonation of Asp85 further leads to the loss of hydrogen bonds to Thr89 and a water, accompanied by a p$K_a$-increase of Asp85. RSB reorientation towards the cytoplasmic side and a p$K_a$ increase of Asp85 combined prohibit RSB reprotonation from Asp85, enabling the vectorial $H^+$ transport in *Hs*BR (L. S. Brown *et al.*, 1994; Richter *et al.*, 1996; Ernst *et al.*, 2014; Nango *et al.*, 2016).

In a time frame of 3 ms, the RSB is reprotonated via Asp96, the primary proton donor, on the intracellular side (Gerwert *et al.*, 1989), forming $N_{530}$ (Step 3 in Fig. 4). However, at 11 Å, the two sites are at a prohibitive distance to initiate direct proton transfer. Nonetheless, structural changes allow the rearrangement of water molecules to form a proton wire between Asp96 and the RSB. Subsequently, a hydrogen bond between Asp96 and Thr46

breaks, lowering the p$K_a$ of Asp96 (Zscherp *et al.*, 1999; Luecke *et al.*, 2000; Schobert *et al.*, 2003) and allowing proton transition to the RSB via a Grotthus mechanism (Dellago *et al.*, 2003; Freier *et al.*, 2011).

The deprotonation of Asp96 triggers the unlocking of a cytoplasmic half-channel (T. Wang *et al.*, 2013), which allows the reprotonation of Asp96 from the cytoplasm (Step 4 in Fig. 4). Charged protein surface residues are potentially supporting the reprotonation (Checover *et al.*, 1997; Kimura *et al.*, 1997). Asp96-reprotonation coincides with the *cis-trans* isomerization of the retinal chromophore and the formation of $O_{640}$ within 8 ms (Lozier *et al.*, 1975). The substantial bathochromic shift of the O intermediate can be explained by a lack of charge compensation of the $RSBH^+$ since Asp85 is still protonated and cannot act as a counterion, as well as by a twisted conformation of the retinal chromophore (Blatz *et al.*, 1972; S. O. Smith *et al.*, 1983; Richter *et al.*, 1996). During the last step of the *Hs*BR photocycle, the proton-releasing complex is reprotonated via Asp85 (Step 5 in Fig. 4). The twisted chromophore relaxes within 15 ms. The exact nature of the Asp85-deprotonation is not understood yet, but it has been suggested that Asp212 (Ci2) is involved (Bousché *et al.*, 1992; Dioumaev *et al.*, 1999).

### 1.2.3. The photocycle of a chloride pump

The photocycle of the inward-directed $Cl^-$ pump *Hs*HR (Schobert and Lanyi, 1982) has been less thoroughly investigated than its $H^+$-pumping counterpart. Nonetheless, some striking differences and similarities were discovered.

Key residues of the photocycle in *Hs*BR, namely Asp85, Asp96, and Glu204, are neutralized in *Hs*HR (Váró, 2000). As predicted by Fourier-transform infrared (FTIR) spectroscopy (Walter and Braiman, 1994), a $Cl^-$ is found close to the $RSBH^+$ in crystal structures of the dark state, supposedly compensating the lack of stabilizing charges at the Schiff base region (Kolbe *et al.*, 2000; Kouyama *et al.*, 2010). In contrast to this finding, the absorption maximum shifts bathochromic when NaCl is added to the sample (Ogurusu *et al.*, 1981, 1982), which indicates a destabilization of the protonated RSB in the presence of $Cl^-$ (Fig. 3D).

However, the anion is not directly bound by the $RSBH^+$ (Maeda *et al.*, 1985; Shibata and Kandori, 2005), but interacts with Arg108 at the protein's extracellular side (Braiman *et al.*, 1994; Essen, 2002). The Schiff base region is more accessible in the *Hs*HR dark state, leading to a stronger chloride- and pH-dependence compared to *Hs*BR (Zimanyi and Lanyi, 1989; Ames *et al.*, 1992; Inoue *et al.*, 2014). *Hs*HR exhibits a mixture of all-*trans*,15-*anti* and 13-*cis*,15-*syn* retinal isomers in the dark state. However, its light adaptation is not complete (Lanyi, 1986). Absorption of 578 nm-light by the all-*trans*,15-*anti* chromophore induces the isomerization to its 13-*cis*,15-*anti* form (Rothschild *et al.*, 1988) and initiates a photocycle with intermediate states similar to *Hs*BR. However, in stark contrast, no formation of a strongly blue-shifted M-like photointermediate is observed

in *Hs*HR, indicating that the $RSBH^+$ remains protonated during the photocycle (Hegemann *et al.*, 1985; Oesterhelt *et al.*, 1985; Zimanyi *et al.*, 1989; Váró *et al.*, 1995).

The chromophore isomerization triggers changes of the electrostatic and hydrogen-bonding environment at the extracellular $Cl^-$-binding site that promote a loss of the connection between Arg108 and $Cl^-$ and instead strengthen interactions of $Cl^-$ with the $RSBH^+$ (Braiman *et al.*, 1994; Shibata and Kandori, 2005). These changes result in the movement of $Cl^-$ to the cytosolic binding site of the protein during the $K_{585}$-to-$L1_{530}$ transition (Váró *et al.*, 1995; Váró, 2000; Essen, 2002). Similar to *Hs*BR during the $M1_{412}$-to-$M2_{412}$ transition, the accessibility of the $RSBH^+$ changes from the extracellular to the intracellular side during the transition from $L1_{530}$ to $L2_{530}$ (Chon *et al.*, 1999; Kolbe *et al.*, 2000). With the formation of the $N_{580}$ intermediate, the $Cl^-$ is released to the intracellular medium (Váró *et al.*, 1995; Váró, 2000; Essen, 2002; Gruia *et al.*, 2005).

During the final step of the *Hs*HR-photocycle, the accessibility of the $RSBH^+$ switches back to the extracellular side, the chromophore isomerizes from 13-*cis*,15-*anti* to all-*trans*,15-*anti*, and a $Cl^-$ occupies the extracellular $Cl^-$-binding site (Ames *et al.*, 1992; Váró *et al.*, 1995; Kolbe *et al.*, 2000; Essen, 2002).

## 1.3. Channelrhodopsins

Unicellular, flagellated algae like the chlorophyte *Chlamydomonas reinhardtii* show phototactic behavior associated with a small eyespot (Fig. 5A, B; Mast, 1916). In this subcellular region, carotenoid granules accumulate, restricting the photoreceptor's light perception from one direction (Kreimer, 2009; Engel *et al.*, 2015; Williams, 2016). Upon light perception at the eyespot, the flagella beating pattern changes and with it the swimming direction (Fig. 5B; Hegemann, 1997).

The photoreceptor responsible for this behavior remained elusive, but reconstitution experiments with blind *C. reinhardtii* mutants and phototaxis action spectra recordings suggested it to be a rhodopsin (Foster and Smyth, 1980; Foster *et al.*, 1984; Hegemann *et al.*, 1991). Photocurrent recordings from cell-wall-deficient *C. reinhardtii* cells revealed fast-rising inward currents upon flash or continuous illumination, carried mainly by $Ca^{2+}$ and other divalent cations or, in their absence, by monovalent cations (Harz and Hegemann, 1991; Holland *et al.*, 1996; Nonnengässer *et al.*, 1996). When the light-induced currents exceed a threshold level, flagellar currents are triggered (Fig. 5C), directly linking the rhodopsin photoreceptor to the flagellar beating. Therefore, Harz *et al.* (1992) hypothesized that the rhodopsin and the ion channel responsible for the light-activated currents are close to each other in the plasmalemma or one protein complex.

After a decade-long search, two sequences were identified in a cDNA database of *C. reinhardtii* with homologies to microbial rhodopsins. Their role in the phototaxis of the chlorophyte alga was shown, using RNA interference (Sineshchekov *et al.*, 2002;

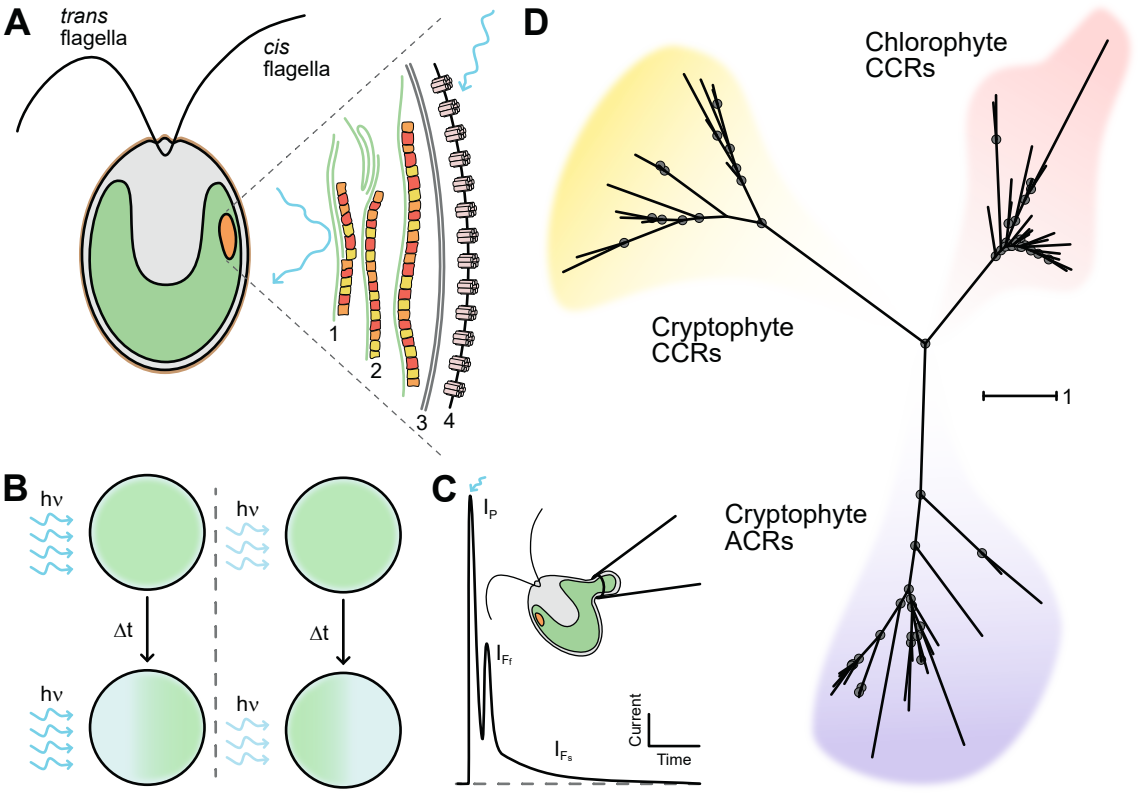


**Figure 5.: Eyespot and phototaxis in *C. reinhardtii* - The physiological role of channelrhodopsins.** **A**, Schematic of a flagellated *C. reinhardtii* cell with the cell wall (brown), the chloroplast (green), and the eyespot (orange) shown. The *cis* and *trans* flagella, close to and far from the eyespot, are indicated. The eyespot is magnified and illustrated according to Kreimer (2009) and Engel *et al.* (2015). The thylakoid membrane (1), carotenoid granule layers (2), chloroplast membrane (3), and the cell membrane with incorporated channelrhodopsin proteins (4) are shown. Incident light (blue arrows) from the front can activate the channelrhodopsins, while the carotenoid granule layers block it on the rear side. **B**, Phototaxis of *C. reinhardtii*. Illumination of a homogeneous solution of *C. reinhardtii* cells with high-intensity light (left) results in a photophobic reaction and migration of the cells away from the light, while low-intensity light (right) leads to a phototactic movement towards the light. **C**, Sketch of flash-induced photocurrents recorded from cell-wall-deficient *C. reinhardtii* with the eyespot outside the patch pipette, according to Harz *et al.* (1992). The photoreceptor current ($I_P$) rises and decays quickly and is followed by a flagellar current with a fast and a slow component ($I_{Ff}$ and $I_{Fs}$). **D**, Unrooted phylogenetic tree of the channelrhodopsin family. Cryptophyte CCRs, cryptophyte ACRs, and chlorophyte CCRs form distinct subfamilies. The average number of residue-substitutions per site is indicated by the scale bar. A list of the used protein sequences and their accession numbers can be found in table S1. Abbreviations: ACRs, anion-conducting channelrhodopsins; CCRs, cation-conducting channelrhodopsins.

Govorunova *et al.*, 2004) and, simultaneously, their function as ion channels was proven by heterologous expression in *Xenopus laeavis* oocytes and photocurrent measurements using the two-electrode voltage-clamp method (Nagel *et al.*, 2002, 2003). Accordingly, the proteins have been named Channelrhodopsin 1 and Channelrhodopsin 2 (*Cr*ChR1 and *Cr*ChR2). Channelrhodopsins are now widely appreciated for their application in the field of optogenetics (Ch. 1.4), boosting the search for new ChRs. Many ChRs have been discovered in chlorophyte and cryptophyte algae (Fig. 5D), conducting cations or

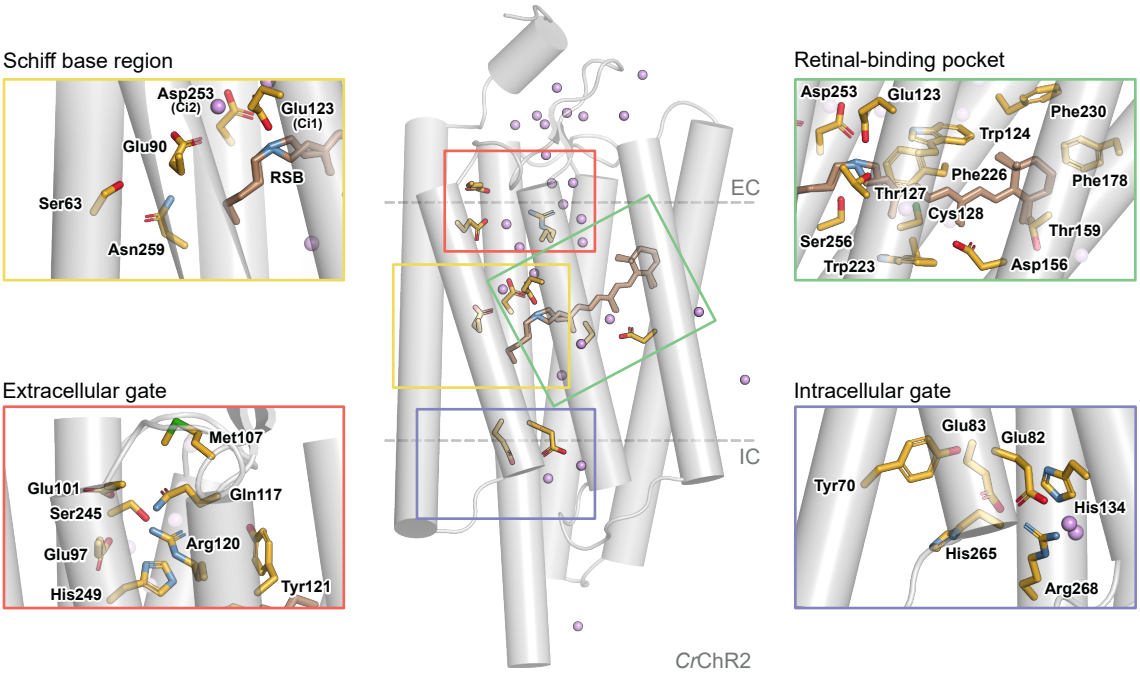


**Figure 6.: Structure of the cation-conducting channelrhodopsin *Cr*ChR2. Center**, Structure of the *Cr*ChR2 monomer (PDB: 6EID; Volkov *et al.*, 2017). The typical architecture comprising seven transmembrane helices, an extracellular amino-terminus, and an intracellular carboxy-terminus can be identified. The all-*trans*, 15-*anti* and 13-*cis*, 15-*syn* conformation of the retinal chromophore (brown), covalently bound to Lys257 via a Schiff base, are overlayed. Colored squares indicate magnified regions on the left and the right side. Stable water molecules are represented as purple spheres. **Top left**, Magnification of the Schiff base region with the central gate and the counterion complex. The central gate is comprised of Ser63, Glu90, Asp253, and Asn259. The counterions Glu123 (Ci1) and Asp253 (Ci2) are connected to the RSB via salt bridges and incorporated into a complex hydrogen-bonding network (not shown). **Top right**, The retinal-binding pocket is shown with selected residues represented as stick models in yellow. **Bottom left**, The extracellular gate with the central Arg120 connected via hydrogen bonds to all other residues comprising the extracellular gate (Met107, Gln117, Tyr121, Trp124, Ser245, and His249). **Bottom right**, The intracellular gate comprises the residues Tyr70, Glu82, Glu83, His134, His265, and Arg268. Abbreviations: EC, extracellular; IC, intracellular; RSB, retinal Schiff base.

anions (Govorunova *et al.*, 2017a). The elicited photocurrents are highly variable in terms of kinetics, amplitudes, and wavelength sensitivity (Ch. 1.3.2).

The exact roles of *Cr*ChR1 and *Cr*ChR2 in the light responses of *C. reinhardtii* have not been completely elucidated yet; however, *Cr*ChR1 has been suggested as the predominant actuator for the phototaxis (Berthold *et al.*, 2008). New gene-editing tools like the CRISPR/Cas-method makes the precise knock-out of genes possible, enabling the detailed analysis of their contributions to physiological responses and behavior (Greiner *et al.*, 2017).

### 1.3.1. Molecular structure

The protein 3D structure of *Hs*BR and other microbial rhodopsin ion pumps has been solved several times (Henderson *et al.*, 1990; Grigorieff *et al.*, 1996), reaching resolutions

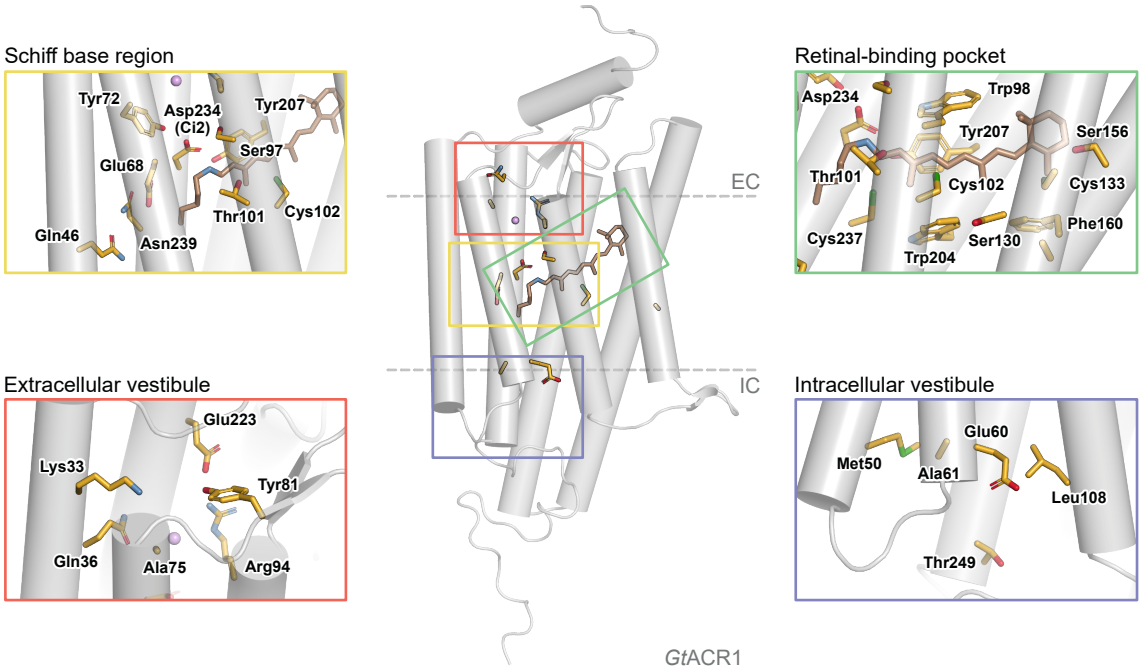


**Figure 7.: Structure of the anion-conducting channelrhodopsin *Gt*ACR1. Center**, Overview of the structure of *Gt*ACR1 (PDB: 6CSM; Kim *et al.*, 2018). The monomer shows the typical seven transmembrane helices with the amino-terminus and carboxy-terminus extra- and intracellular. The all-*trans*, 15-*anti* retinal chromophore (brown) is covalently bound to Lys238 via a Schiff base. Colored squares indicate magnified regions on the left and the right side. Stable water molecules are represented as purple spheres. **Top left**, The only constriction site in the proposed ion conduction pathway is the Schiff base region. The central gate is comprised of Gln46, Glu68, and Asn239. Only Ci2 is conserved (Asp234) and is connected to the RSB, Tyr71, and Tyr207 via hydrogen bonds. Ser97 replaces Ci1. **Top right**, The retinal-binding pocket is shown with selected residues represented as stick models in yellow. **Bottom left**, The extracellular opening of the proposed ion conduction pathway is not gated and instead shifted in *Gt*ACR1 compared to *Cr*ChR2 due to interactions between Tyr81, Arg94, and Glu223 and stronger tilted TM1 and TM2. **Bottom right**, The intracellular opening of the ion conduction pathway is not gated either. Compared to *Cr*ChR2, the majority of charged residues is neutralized. Abbreviations: EC, extracellular; IC, intracellular; RSB, retinal Schiff base.

up to 1.4 Å (Schobert *et al.*, 2002). Recently, it became possible to follow the structural evolution during the photocycle of *Hs*BR using femtosecond serial crystallography (Nogly *et al.*, 2018; Nango *et al.*, 2016).

So far, only a few structures of ChRs have been solved, all of which are in the dark state with an obstructed ion conduction pathway (Kato *et al.*, 2012; Volkov *et al.*, 2017; Kim *et al.*, 2018; Oda *et al.*, 2018; H. Li *et al.*, 2019). The first structure of a ChR was published by Kato *et al.* (2012), showing the chimeric construct C1C2, consisting of the first five transmembrane helices of *Cr*ChR1 and TM6 and TM7 of *Cr*ChR2. This chimera is distinctly different in the light-induced structural changes compared to native *Cr*ChR2, namely reduced deprotonation of a central glutamate (Inaguma *et al.*, 2015). Therefore, solving the structure of the widely used and extensively investigated *Cr*ChR2 remained a major goal. Volkov *et al.* (2017) succeeded in solving a high-resolution X-ray structure

of *Cr*ChR2, enabling a better understanding of its molecular processes. Shortly after this achievement, two groups independently succeeded in obtaining a structure of an anion-conducting ChR, ACR1 from the cryptophyte alga *Guillardia theta* (Kim *et al.*, 2018; H. Li *et al.*, 2019). The structures of *Cr*ChR2 (PDB: 6EID; Volkov *et al.*, 2017) and *Gt*ACR1 (PDB: 6CSM; Kim *et al.*, 2018) will be described and compared to point out key differences between cation- and anion-conducting ChRs.

As is typical for most rhodopsins, both *Cr*ChR2 (Fig. 6) and *Gt*ACR1 (Fig. 7) have a heptahelical transmembrane domain architecture with the retinal chromophore covalently bound via a Schiff base to a lysine residue in TM7 (Volkov *et al.*, 2017; Kim *et al.*, 2018). The TM7 $\alpha$-helix of *Cr*ChR2 extends further into the cytosol, while in *Gt*ACR1, TM7 is followed shortly after exiting the membrane by an unordered tail that exhibits several hydrogen bonds to the rhodopsin domain, conferring structural stability (Kim *et al.*, 2018).

### Dimerization

While each protomer is a functional unit in microbial rhodopsins, all available structures show ChRs as dimers (Kato *et al.*, 2012; Volkov *et al.*, 2017; Kim *et al.*, 2018; Oda *et al.*, 2018; H. Li *et al.*, 2019). The microbial ion pumps are more diverse and have also been found in trimeric or pentameric configurations (Fudim *et al.*, 2019; Kouyama *et al.*, 2010; Kovalev *et al.*, 2019). In *Cr*ChR2, the dimer is mainly stabilized by hydrogen bonds between residues in TM2, TM4, and TM5, which are highly conserved among ChRs. Additionally, two cysteines, Cys34 and Cys36, form disulfide bridges that contribute to dimer stabilization (Volkov *et al.*, 2017) but are dispensable for dimerization (N. Krause *et al.*, 2013; Sattig *et al.*, 2013).

The contact surface between the two protomers forming the *Gt*ACR1 homodimer is much smaller compared to *Cr*ChR2. Here, only residues in TM3 and TM4 interact with each other, contributing to the dimerization. A disulfide bridge formed by Cys6 in the amino-terminus of the *Gt*ACR1 protomers is, in contrast to *Cr*ChR2, crucial for dimerization (Kim *et al.*, 2018).

### The retinal-binding pocket

Within the retinal-binding pocket of *Cr*ChR2 (Fig. 6 top right), the chromophore is sandwiched between two tryptophan residues, Trp124 and Trp223. Additionally, several phenylalanine residues are close to the chromophore. Furthermore, Cys128 and Asp156 are retinal-binding pocket-forming residues, stabilizing the protomer via a water-mediated hydrogen bond between TM3 and TM4 (Volkov *et al.*, 2017). This 'DC gate' or 'DC pair' (Nack *et al.*, 2010; Schneider *et al.*, 2015) is a characteristic and highly conserved motif of chlorophyte CCRs, connected to the Schiff base region via Thr127 (Ehrenberg *et al.*, 2019) and strongly affecting the open state lifetime (Berndt *et al.*, 2009; Bamann

*et al.*, 2010). Previously, Asp156 was proposed as a proton donor to the RSB during late photocycle intermediates (Lórenz-Fonfría *et al.*, 2013). However, the residue is too distant to the RSB for direct proton transfer (Volkov *et al.*, 2017).

In the *Gt*ACR1 structure, retinal was found exclusively in the all-*trans*, 15-*anti* configuration (Kim *et al.*, 2018). As in *Cr*ChR2, the chromophore is sandwiched by two tryptophan residues, Trp98 and Trp204. However, most aromatic residues of the retinal-binding pocket of *Cr*ChR2, are not conserved in *Gt*ACR1 (Fig. 7 top right; Kim *et al.*, 2018). Overall, these differences lead to a ground-state absorption at 520 nm in *Gt*ACR1 (Govorunova *et al.*, 2015; Kim *et al.*, 2018), which is red-shifted compared to *Cr*ChR2. Furthermore, the DC pair is not conserved in *Gt*ACR1. While the cysteine in TM3 is present, the TM4-aspartate is missing. Nonetheless, an extension of the open state lifetime is still possible upon mutation of the conserved cysteine (Govorunova *et al.*, 2018). Mutations of Ser130, the homolog of *Cr*ChR2-Asp156, did not affect the kinetics and functionality of *Gt*ACR1 (Sineshchekov *et al.*, 2016).

### The Schiff base region

In *Hs*BR, the $RSBH^+$ is connected to two counterions that stabilize the positive charge at the RSB via a water molecule (Sheves *et al.*, 1985). This water is not present in *Cr*ChR2. Instead, the two counterions, Glu123 and Asp253 (Ci1 and Ci2; Schneider *et al.*, 2015), are directly connected via salt bridges with the RSB (Volkov *et al.*, 2017). In cryptophyte CCRs, both Ci1 and Ci2 are aspartate residues, similar to *Hs*BR (Govorunova *et al.*, 2016b).

In *Gt*ACR1 and all other cryptophyte ACRs, Ci1 is replaced by alanine, threonine, or serine residues, similar to *Hs*HR (Váró, 2000; Govorunova *et al.*, 2017b). While in *Hs*HR, a $Cl^-$ was suggested to compensate for the lack of Ci1 (Kolbe *et al.*, 2000; Kanada *et al.*, 2011), a similar configuration is not found in *Gt*ACR1 (Fig. 7 top left; Kim *et al.*, 2018; H. Li *et al.*, 2019), raising the question of how the $RSBH^+$ is stabilized. Ci2 is conserved as an aspartate in *Gt*ACR1 and hydrogen-bonded to the $RSBH^+$, Tyr72, and Tyr207 (Kim *et al.*, 2018; H. Li *et al.*, 2019). The mutations D234N and Y207F both abolish channel function, but spectroscopic data also suggests that Asp234 is protonated in the dark state (Kim *et al.*, 2018), making it unlikely a counterion. Potentially, an extended hydrogen-bonding network around the RSB is involved in stabilizing its charge, but further experiments are required to elucidate this question.

In *Cr*ChR2, the counterions are further connected via a hydrogen bond network to Glu90, Lys93, Glu97, Try124, Thr127, and Pro227. The central gate is composed of the residues Ser63, Glu90, Asp253, and Asn258 (Fig. 6 top left; Volkov *et al.*, 2017). The central Glu90 was previously identified as a critical component for the ion selectivity in *Cr*ChR2 (Ruffert *et al.*, 2011; Kuhne *et al.*, 2019). Replacing it with either lysine or arginine (E90K, E90R) leads to anion-conductance (Wietek *et al.*, 2014; Berndt *et al.*, 2014).

### The putative ion conduction pathway

The ion conduction pathways of *Cr*ChR2 and *Gt*ACR1 are predicted to be formed by TM1, TM2, TM3, and TM7, but they show remarkable differences between the available structures (Volkov *et al.*, 2017; Kim *et al.*, 2018; H. Li *et al.*, 2019).

The proposed ion conduction pathway of *Cr*ChR2 shows four cavities separated by three constriction sites. In the extra- and intracellular half of the protomer, an outer and an inner cavity can be seen, respectively (Volkov *et al.*, 2017). They are separated by the extracellular gate (ECG; Fig. 6 bottom left), formed by Met107, Gln117, Tyr121, Trp124, Ser245, His249, and Arg120, and the intracellular gate (ICG; Fig. 6 bottom right), comprised of Tyr70, Glu82, Glu83, His134, Gly234, His265, and Arg268. Arg120 is a crucial component of the ECG, hydrogen-bonded to all other ECG-forming residues. The extra- and intracellular half of each protomer is separated by the Schiff base region acting as the central gate (Fig. 6 top left; Volkov *et al.*, 2017). Neutralization of Arg120 (R120A) as well as Glu97 (E97A) and Asp253 (D253A/N) nearly completely disrupts the ion channel function (Plazzo *et al.*, 2012; Lórenz-Fonfría *et al.*, 2013; Sugiyama *et al.*, 2009).

In the predicted ion conduction pathway of *Gt*ACR1, only one constriction site close to the Schiff base region is apparent. Gln46, Glu68, and Asn239 form this constriction site in the center of the proteins' conduction pathway (Fig. 7 top left). Furthermore, the extracellular entry point is shifted in *Gt*ACR1 compared to *Cr*ChR2. The predicted extracellular ion entry point of *Cr*ChR2 is blocked in *Gt*ACR1 by interactions of Tyr81, Arg94, and Glu223. However, due to stronger tilted TM1 and TM2, another entry point is formed (Kim *et al.*, 2018).

The putative pore and the intra- and extracellular surfaces of *Cr*ChR2 are lined with several carboxylic residues, resulting in an electronegative surface that prevents the passage of anions but not cations. The majority of these residues are not conserved in *Gt*ACR1. Many residues on the surface of the protein are replaced by the positively charged residues lysine or arginine, and pore-lining carboxylic residues are replaced by the nonpolar residues alanine or serine, resulting in a surface potential that is electropositive and excludes cations from entering the pore (Kim *et al.*, 2018). This exclusion principle is different from the selectivity filters of, for example, the well-described voltage-gated ion channels that allow for highly selective conduction of specific ions (Roux, 2017).

## 1.3.2. Electrophysiology and photocycle

Ionic currents evoked by activation of ChRs rise quickly at the onset of illumination and are inward- or outward-directed, depending on the membrane potential and gradients of the conducted ions (Fig. 8A; Nagel *et al.*, 2003; Bamann *et al.*, 2008). Upon continuous illumination, the photocurrents of most ChRs rise to a transient peak level ($I_p$), followed by desensitization to a stationary level ($I_s$). When the light is shut off, the photocurrents return

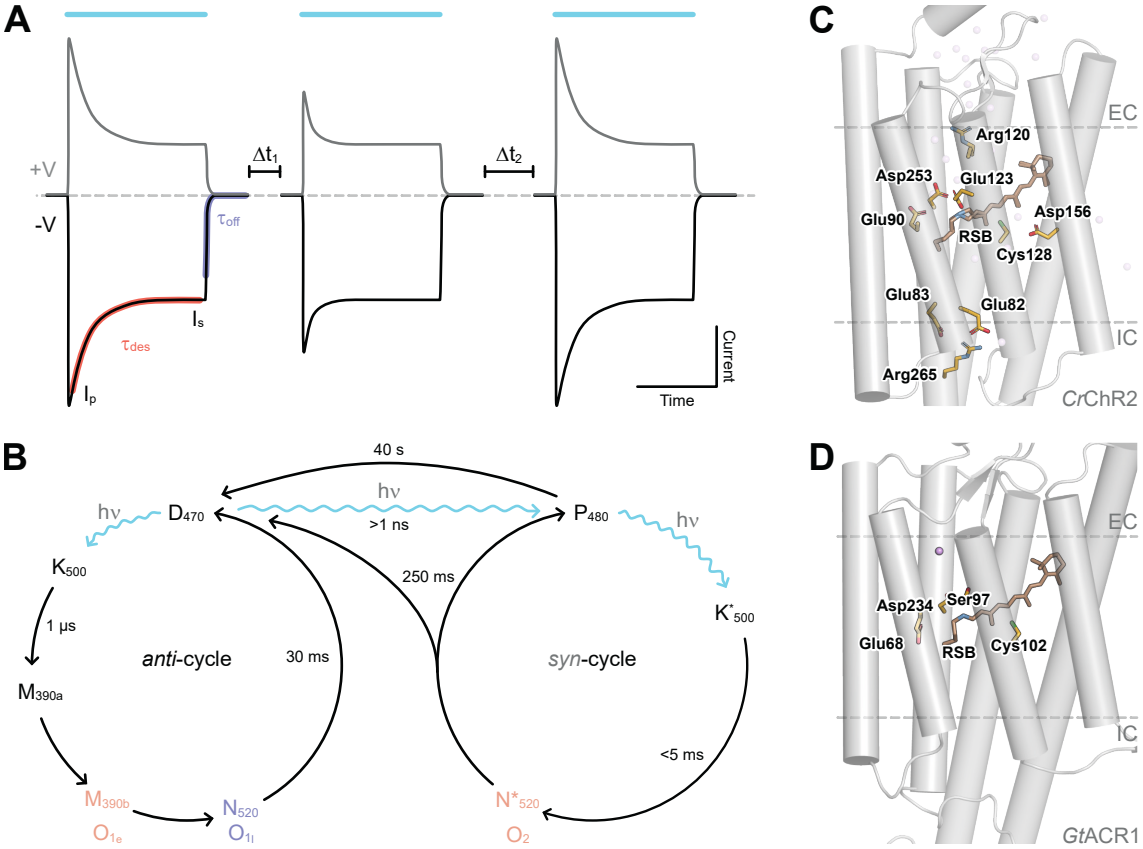


**Figure 8.: Photocurrents and photocycle of channelrhodopsins.** **A**, Representation of ChR photocurrents at positive (+V; gray traces) and negative (-V; black traces) membrane potentials. Transient and stationary photocurrents ($I_p$ and $I_s$) are indicated as well as typical kinetics ($\tau_{des}$ and $\tau_{off}$). Activation with only short dark periods ($\Delta t_1$) leads to a decrease of $I_p$. Extended dark periods ($\Delta t_2$) allow the full recovery of $I_p$. **B**, Photocycle of *Cr*ChR2, according to Kuhne *et al.* (2019). Fully dark-adapted *Cr*ChR2 populates the $D_{470}$ state of the *anti*-cycle. Upon absorption of blue light, the retinal chromophore isomerizes either to 13-*cis*,15-*anti*, initiating the *anti*-cycle, or to 13-*cis*,15-*syn*, the dark state of the *syn*-cycle ($P_{480}$), which is initiated by absorption of a second photon. The *anti*-cycle comprises an early ($O_{1e}$) and a late ($O_{1l}$) open/conducting state, while the *syn*-cycle comprises only one open state ($O_2$). **C, D**, Structures of *Cr*ChR2 (C; PDB: 6EID; Volkov *et al.*, 2017) and *Gt*ACR1 (D; PDB: 6CSM; Kim *et al.*, 2018). The protein backbone is shown in gray, with the retinal chromophore and residues relevant for open state formation as sticks, colored brown and yellow, respectively. Abbreviations: EC, extracellular; IC, intracellular; RSB, retinal Schiff base.

to the baseline. Activation with only a short dark period in between light pulses ($\Delta t_1$) causes $I_p$ to decrease while $I_s$ remains unchanged (Fig. 8A, middle trace), as the light-adapted form accumulates. Increasing the duration of the dark-periods ($\Delta t_2$) allows the protein to convert to its dark-adapted form, and $I_p$ recovers (Fig. 8A, right trace; Nagel *et al.*, 2003). The photocurrent amplitudes and their reversal potential[4], as well as the kinetics of the photocurrent desensitization ($\tau_{des}$), the return to the baseline ($\tau_{off}$), and the recovery of $I_p$ ($\tau_{rec}$) depend on the ChR, the membrane potential, light intensity, and ionic composition of the intra- and extracellular buffers (Schneider *et al.*, 2015).

[4]The membrane potential, where inward and outward ion flow negate each other at a certain ion gradient.

The underlying photocycle of *Cr*ChR2 has been controversially discussed over the past two decades, ranging from models with single and branched photocycles to models with two parallel photocycles (Ritter *et al.*, 2008; Nikolic *et al.*, 2009; Lórenz-Fonfría *et al.*, 2013; Kuhne *et al.*, 2019). Photocurrents of *Cr*ChR2 elicited by flash illumination can be sufficiently explained with a simple model comprising a single photocycle. In that model, illumination of the dark-adapted protein ($D_{470}$) results in retinal *trans-cis* isomerization, yielding a red-shifted intermediate ($K_{500}$) within ns. It is followed by the strongly blue-shifted intermediate $M_{390}$, marked by the transition of the RSB proton to Asp253 in a time frame of µs (Ritter *et al.*, 2008; Lórenz-Fonfría *et al.*, 2013). Within ms, the reprotonation of the RSB results in the formation of $N_{520}$; the suggested conducting state (Bamann *et al.*, 2008; Ritter *et al.*, 2008). After the conducting intermediate, it was further proposed that a long-lasting and non-conducting intermediate arises ($P_{480}$) that transitions into $D_{470}$ within 20 s to 40 s (Radu *et al.*, 2009; Ritter *et al.*, 2008; Lórenz-Fonfría *et al.*, 2013). However, the determined lifetimes, especially for the late photocycle intermediates, would cause stronger photocurrent desensitization during continuous illumination, suggesting that the photocycle of *Cr*ChR2 is more complicated (Hegemann *et al.*, 2005).

In a recent study, single-turnover electrophysiology and FTIR spectroscopy were combined to elucidate the *Cr*ChR2-photocycle in great detail (Kuhne *et al.*, 2019). Unlike previously reported, $P_{480}$ is not a late intermediate but arises very early upon illumination of the fully dark-adapted protein and in conjunction with the deprotonation of Glu90. Furthermore, three distinct conducting states were identified (Fig. 8B). Fully dark-adapted *Cr*ChR2 is entirely populated by all-*trans*,15-*anti* retinal (Bruun *et al.*, 2015), forming the dark state $D_{470}$ of the *anti*-cycle. Absorption of a photon may result in a single or a double isomerization of the retinal chromophore.

Single isomerization of the dark state retinal around $C_{13}$=$C_{14}$ yields 13-*cis*,15-*anti* retinal and initiates the transition through the *anti*-cycle, where the central Glu90 remains protonated. The *anti*-cycle proceeds with the above-described pattern, transitioning to $K_{500}$ within ns followed by deprotonation of the $RSBH^+$ within 1 µs, forming $M_{390a}$. Subsequently, $M_{390b}$, the early conducting state ($O_{1e}$) with high selectivity for $H^+$, is formed. Reprotonation of the RSB marks the appearance of $N_{520}$, the late conducting state ($O_{1l}$), with increased selectivity for $Na^+$. From $O_{1l}$, *Cr*ChR2 returns to $D_{470}$ within 30 ms. The different ion selectivities of the two conducting states result from a changing pore structure during the *anti*-cycle (Kuhne *et al.*, 2019).

The dark state $P_{480}$ of the *syn*-cycle comprises a 13-*cis*,15-*syn* retinal. $P_{480}$ is formed by isomerization around $C_{13}$=$C_{14}$ and $C_{15}$=N. This double isomerization is accompanied by Glu90 deprotonation. During the transition through the *syn*-cycle, Glu90 remains deprotonated. Absorption of a second photon initiates the *syn*-cycle. Retinal isomerizes to all-*trans*,15-*syn* by a single isomerization around $C_{13}$=$C_{14}$, and the $K^*_{500}$ intermediate is formed. The long-lived and weakly $H^+$-conducting $N^*_{520}$ ($O_2$) appears within 5 ms. $N^*_{520}$

relaxes to $P_{480}$ or $D_{470}$ within 250 ms (Kuhne *et al.*, 2019). Since thermal relaxation of $P_{480}$ to $D_{470}$ is slow, occurring within 40 s, and the weakly conducting $O_2$ has a long lifetime, these intermediates accumulate during continuous or high-frequency flash illumination, explaining the observed desensitization of *Cr*ChR2 (Kuhne *et al.*, 2019).

The structural changes that cause ion channel opening in ChRs are unknown as neither a crystal structure of the open state nor time-resolved crystal structures are available. Nevertheless, the available dark state structure (Fig. 8C) shows that the three constriction sites, on the extra- and intracellular side as well as centrally in the protein, need to restructure quickly together to allow the formation of a continuous conduction pathway (Volkov *et al.*, 2017).

The recently identified family of cryptophyte ACRs (Govorunova *et al.*, 2015; Wietek *et al.*, 2016; Govorunova *et al.*, 2017a) has not been investigated in as much detail yet in regards to the underlying photocycle. In the dark state, *Gt*ACR1 is populated by the all-*trans* retinal isomer with a protonated Schiff base (A. Yi *et al.*, 2016; Kim *et al.*, 2018). Furthermore, Ci1 is replaced by the non-carboxylic Ser97 (Fig. 8D) and Ci2 is supposedly protonated at neutral pH (Kim *et al.*, 2018). Therefore, these residues cannot function as counterions (A. Yi *et al.*, 2016; Kim *et al.*, 2018). Sineshchekov *et al.* (2016) found that upon photon absorption, a K-like photointermediate forms in *Gt*ACR1, transitioning within 1 µs into an L-like intermediate. In contrast to chlorophyte CCRs like *Cr*ChR2, this L-like state coincides with ion channel conduction (Sineshchekov *et al.*, 2016). Deprotonation of the $RSBH^+$, indicated by the rise of a strongly blue-shifted M-like intermediate within 20 ms, marks the closing of the ion channel and was similarly found in an ACR from *Proteomonas sulcata* (Wietek *et al.*, 2016; Govorunova *et al.*, 2016a; Hontani *et al.*, 2017). The initial dark state recovery of *Gt*ACR1 and *Ps*ACR1 occurs within 1.5 s and 3 s, respectively (Wietek *et al.*, 2016; Sineshchekov *et al.*, 2016), considerably faster than in *Cr*ChR2 but slower than the determined recovery kinetics of the transient photocurrents (Govorunova *et al.*, 2016a). Therefore, as for *Cr*ChR2, a single photocycle, albeit with faster recovery of the dark state, cannot sufficiently explain photocurrents of both ACRs during continuous illumination; the non-conducting intermediates will accumulate and cause more intense desensitization than observed (Govorunova *et al.*, 2015, 2016a; Wietek *et al.*, 2016). Therefore, a more complex photocycle, similar to *Cr*ChR2 (Kuhne *et al.*, 2019), seems more likely, but further experiments are required to elucidate its nature.

## 1.4. Optogenetics

The field of optogenetics is a multidisciplinary approach combining genetics, optics, and bioengineering to modify cells or organisms, subsequently allowing non-invasive and temporally precise control using light (Deisseroth *et al.*, 2006). Optogenetics has become a prominent method in the neurobiological sciences. Viruses can be used as vehicles to

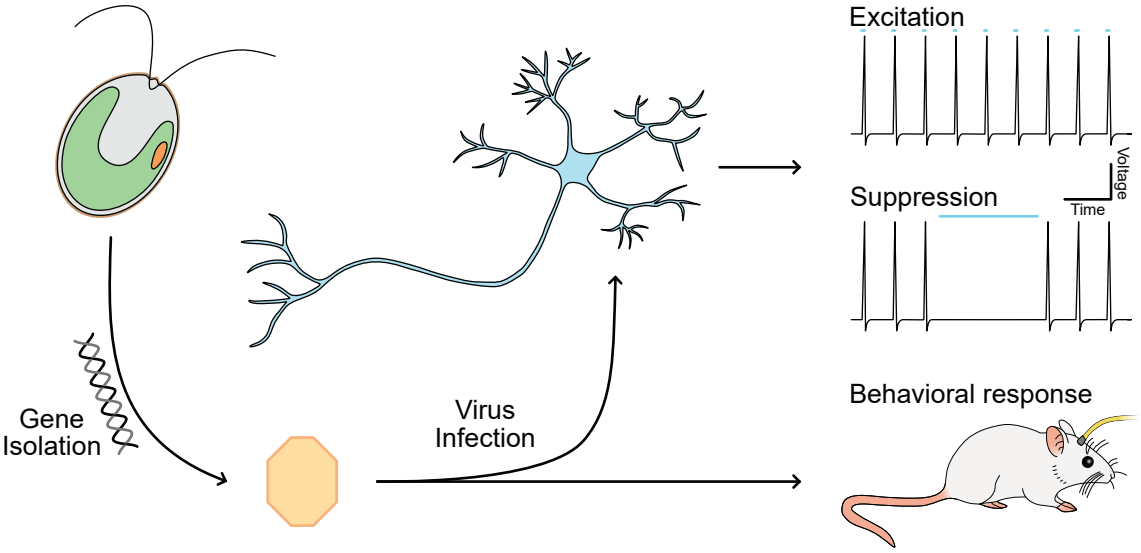


**Figure 9.: Optogenetic application of microbial rhodopsins.** Genes encoding for light-sensitive proteins are isolated from microbial organisms and used to generate viruses as a vehicle for delivering the gene via infection. Viral infection can be performed in cell culture (*in vitro*) or in the living animal (*in vivo*). Expression of the light-sensitive protein enables the non-invasive control of infected cells, e. g. excitation or suppression of action potentials in neurons, with high temporal precision, and the study of animal behavior in response to those manipulations.

deliver genes, coding for light-sensitive proteins. Subsequently, this allows the control of neuronal activity using light and enabling the study of neuronal circuits *in vitro*, *ex vivo*, or *in vivo* (Fig. 9).

Microbial rhodopsins have become important optogenetic tools, promoted by the discovery of ChRs (Nagel *et al.*, 2002, 2003) and their subsequent use in the modulation of cultured neurons activity (Boyden *et al.*, 2005; X. Li *et al.*, 2005; Ishizuka *et al.*, 2006). The first *in vivo* experiments demonstrated the possibilities of optogenetics by controlling the contractility in the nematode C. elegans (Nagel *et al.*, 2005) and restoration of rudimentary vision in blind mice (Bi *et al.*, 2006). The restoration of vision by Bi *et al.* (2006), with first clinical trials initiated recently (Kleinlogel *et al.*, 2020), is a prime example for optogenetics' high-impact potential. Optogenetics also proved useful for restoring auditory signaling (Mager *et al.*, 2018) and the heart's sinus rhythm upon atrial fibrillation (Nyns *et al.*, 2019). The discovery of enzymerhodopsins further increased the application of optogenetics, making the manipulation of secondary messengers such as cAMP or cGMP readily available (Stierl *et al.*, 2011; Scheib *et al.*, 2018; Mukherjee *et al.*, 2019).

The success and easy application of optogenetic tools spurred the search for new proteins viable for optogenetic application and extension of the optogenetic toolbox. For example, optogenetic tools have been targeted to sub-cellular organelles (Tkatch *et al.*, 2017; Asano *et al.*, 2018). Furthermore, the incorporation of retinal and the protein stability (Berndt *et al.*, 2011) as well as the acceleration of photocurrent kinetics (Gunaydin *et al.*, 2010) has been achieved by residue substitutions. The majority of microbial rhodopsins are most

active upon blue- or green-light absorption (Ernst *et al.*, 2014). The limited penetration depth of blue light in tissue (Weissleder, 2001) and the introduction of all-optical electrophysiology (Hochbaum *et al.*, 2014) encouraged the engineering of color-tuned variants of optogenetic tools, using mutational approaches (Prigge *et al.*, 2012) or synthetic retinal analogs (AzimiHashemi *et al.*, 2014). However, the furthest red-shifted absorption was not achieved by engineering but found naturally occurring in ChRs from algae (Klapoetke *et al.*, 2014; Govorunova *et al.*, 2020).

The shift of the ion selectivity of ChRs towards specific ions remains a focus in the field. For example, ChRs with high selectivity for $K^+$ would be useful as optogenetic tools to silence neuronal activity utilizing the naturally evolved system in neurons where voltage-gated ion channels open to repolarize the membrane potential after $Na^+$ ion channel activity. Furthermore, $Ca^{2+}$-conducting ChRs would offer the potential to manipulate the intracellular concentration of this essential cellular second messenger (Berridge *et al.*, 2003). Previously, ChR variants have been reported with supposedly increased $Ca^{2+}$ selectivity (Kleinlogel *et al.*, 2011; Pan *et al.*, 2014; Duan *et al.*, 2019). However, the engineering of a ChR with increased selectivity for potassium remains a challenge. Therefore, alternative tools have been engineered to indirectly increase the $K^+$-conductance of the membrane (Cosentino *et al.*, 2015; Alberio *et al.*, 2018; Bernal Sierra *et al.*, 2018). Recently, a promising substitution in the bacterial rhodopsin $Na^+$-pump KR2 was published. The pump was converted into an ion channel with increased selectivity for $K^+$ at alkaline pH (Vogt *et al.*, 2019). This report may pave the way towards the engineering of a directly light-gated potassium ion channel.

Since this inhibitory tool is not available yet, scientists have looked for alternative measures to suppress action potential-firing by applying light. Shortly after the first applications of *Cr*ChR2 as an excitatory tool, the inward-directed $Cl^-$ pump Halorhodopsin from *Natronomonas pharaonis* was used as an inhibitory tool, hyperpolarizing the membrane potential of neurons (Zhang *et al.*, 2007). However, ion pumps only transport one charge per absorbed photon and require continuously applied high light intensities, which can damage the sample. This problem was overcome by engineering anion-conducting variants of *Cr*ChR2 (Wietek *et al.*, 2014) and the chimera C1C2 (Berndt *et al.*, 2014), which were later improved (Wietek *et al.*, 2015; Berndt *et al.*, 2016). The used approaches could also be successfully applied to other ChRs (Wietek *et al.*, 2017), considerably increasing the number of available engineered inhibitory tools. These achievements were accompanied by the advent of natural anion-conducting ChRs (Govorunova *et al.*, 2015, 2017b), which have increased photocurrent amplitudes and accelerated photocycle turnover kinetics, compared to the engineered representatives. However, the inhibitory function of anion-conducting pumps or channels is dependent on the $Cl^-$ reversal potential, which can vary locally in a neuron (Mahn *et al.*, 2016, 2018) as well as during development (Sulis Sato *et al.*, 2017), making their application less practical and a potential $K^+$-conducting channel more

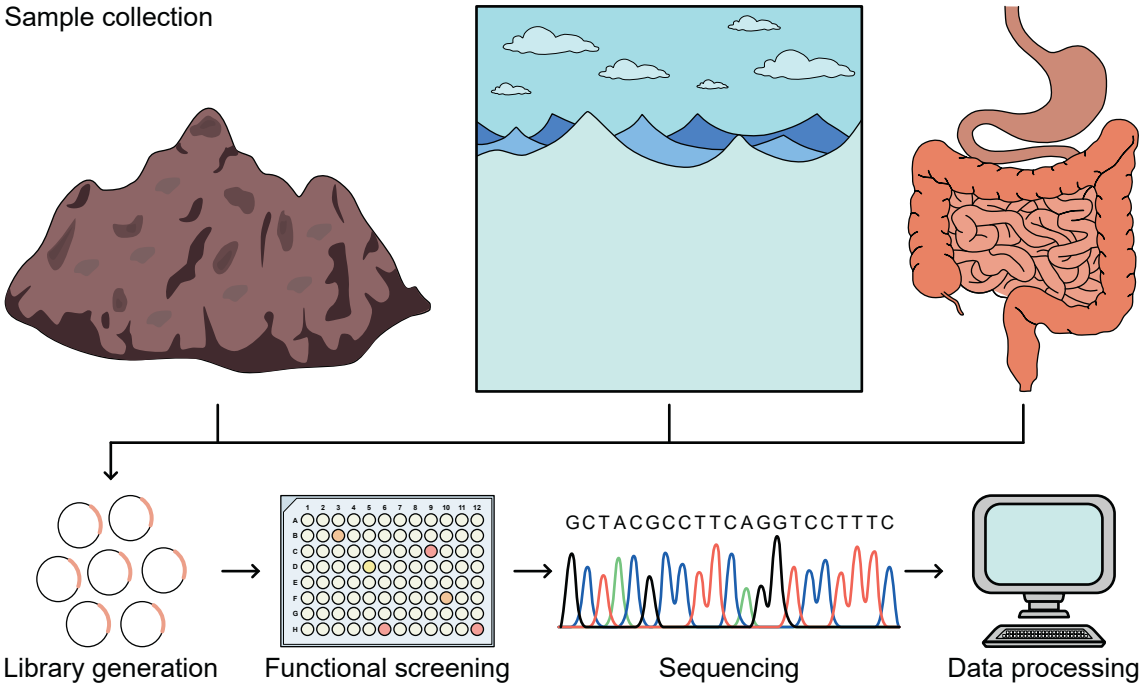


**Figure 10.: Metagenomic analysis of microbial communities.** To study the genetic diversity of microbial communities, samples are collected and the genetic material is directly isolated. The generation of a library, by inserting the fragmented genetic material into plasmids, enables optional functional screening. Subsequently, the complete library or parts of it are sequenced. The resulting data can then be processed using bioinformatic methods. The process shown here is referred to as environmental shotgun sequencing (Wooley *et al.*, 2010).

attractive.

## 1.5. Metagenomics

Microbial organisms make up a large fraction of life in every environment, and are essential for important ecological functions (Wooley *et al.*, 2010). The whole genome of many microbes is already available, yet single-organism genome studies are limited because most microbial organisms are not culturable in the laboratory (Amann *et al.*, 1995). The broad field of metagenomics aims to uncover all genetic diversity within a sample (Gilbert and Dupont, 2011). The cultivation of organisms is bypassed and the genetic material is isolated directly from environmental samples such as soil, water, or biological samples: e. g. intestine. To allow functional screenings, the DNA is fragmented and ligated into vectors. The sequencing data is further processed using bioinformatic methods (Fig. 10; Handelsman, 2004; Streit and Schmitz, 2004).

Shorter sequencing reads overlapping with each other are combined to longer contiguous sequences (contigs). Whole genomes of a species are usually not entirely covered by metagenomic studies. Nonetheless, with repeated collections of genomic material and subsequent sequencing, the coverage can be increased. However, due to this sequence fragmentation, identifying species is difficult. Furthermore, it can even lead to the generation

of interspecies chimeras. Nonetheless, metagenomics enables identifying the variability of genes in a microbial community and the interpretation of the acquired data in relation to environmental parameters such as water depth or nutrient composition (Wooley *et al.*, 2010).

In recent years, metagenomic studies have led to important discoveries, not only in regards to the human gut (Gill *et al.*, 2006; Jovel *et al.*, 2016) or soil microbiome (Andújar *et al.*, 2015) but also in regards to microbial rhodopsins. Most notable is the discovery of proteorhodopsins, bacterial proton pumps similar to the archaeal *Hs*BR, and their abundance in marine environments (Béjà *et al.*, 2000, 2001). More recently, the widely distributed heliorhodopsins have been identified by metagenomic means (Pushkarev *et al.*, 2018). However, while the crystal structure of heliorhodopsins has been solved (Shihoya *et al.*, 2019; Kovalev *et al.*, 2020) and despite extensive research (Otomo *et al.*, 2018; Singh *et al.*, 2018), their physiological function remains elusive so far.

## 1.6. Research objective

The discovery of ChRs (Nagel *et al.*, 2002, 2003) gave rise to the field of optogenetics, allowing a better understanding of the brain and other cellular systems (Deisseroth and Hegemann, 2017). Many ChRs had been identified and described at the beginning of this work (Govorunova *et al.*, 2017a), yet all in culturable chlorophyte and cryptophyte algae, excluding the majority of microorganisms (Amann *et al.*, 1995) and leading to a potential underrepresentation of ChRs within the family of microbial rhodopsins.

With metagenomic data sets, a large source of genetic material is available from organisms previously uncultured or unknown. To elucidate the viability of these data sets to identify new ChRs, a close collaboration with Prof. Dr. Oded Béjà was established. Prof. Dr. Béjà and his co-workers analyzed metagenomes of the *Tara* Oceans project (Sunagawa *et al.*, 2015; Brum *et al.*, 2015; Hingamp *et al.*, 2013) as well as transcriptomes of the One Thousand Plant Transcriptomes initiative (Initiative, 2019), identifying several promising sequences within two distinct phylogenetic groups.

Group 1 comprised seven members, all showing near complete photocurrent desensitization in continuous light. The elucidation of the underlying molecular mechanism is a central goal of this study. Therefore, a detailed characterization of the wild-type will be performed, using electrophysiology and spectroscopy. Functionally essential residues will be identified by amino acid exchange and subsequent functional analysis. Molecular dynamics simulations on a homology model will be performed to support the interpretation of the data.

The second group included two ChRs of viral origin as well as ChRs from their putative hosts. In the scope of this study, the ion channels will be characterized using electrophysiology.

# 2. Results

Metagenomic and transcriptomic data sets from the *Tara* Oceans project and 'One Thousand Plant Transcriptomes Initiative' (Sunagawa *et al.*, 2015; Brum *et al.*, 2015; Hingamp *et al.*, 2013; Initiative, 2019) were screened by Prof. Dr. Oded Béjà and colleagues, yielding many sequences with similarities to microbial rhodopsins. In total, eleven of the identified sequences showed ion channel-activity upon illumination. Here, the functional characterization of those new ChRs by electrophysiological and spectroscopic methods is described.

The MerMAIDs (**M**etagenomically discov**er**ed, **m**arine, **a**nion-conducting, and **i**ntensely **d**esensitizing ChR**s**) elicit nearly completely desensitizing photocurrents during continuous illumination and conduct anions.

The prasinophyte ChRs, comprised of green algal and viral sequences, elicit photocurrents with only minor desensitization and conduct anions as well. However, the viral ChRs are cytotoxic when expressed in mammalian cells and elicit photocurrents of considerably smaller amplitude than their algal homologs.

## 2.1. Sequence analysis

The metagenomically identified sequences show a sequence similarity between 40 % and 50 % compared to representatives of the three ChR subfamilies and microbial rhodopsin ion pumps (Fig. S1) using the Smith-Waterman algorithm for local sequence alignments (T. Smith and Waterman, 1981). The MerMAID1,3-5 sequences are 96 % to 98 % similar to each other and MerMAID2,6,7 76 % to 81 %. The viral and prasinophyte sequences show a similarity of 70 % to 74 %.

The MerMAID and prasinophyte ChRs separate into two distinct families in a phylogenetic analysis. Furthermore, they are more closely related to chlorophyte CCRs and cryptophyte ACRs than to cryptophyte CCRs and microbial rhodopsin ion pumps (Fig. 11A). The MerMAIDs are further split into two sub-branches comprised of MerMAID1,3-5 and MerMAID2,6,7, respectively. The family of prasinophyte ChRs shows closer relation to the chlorophyte CCRs. It comprises two sequences originating from prasinophyte algae, *Pyme*ACR1 from *Pyramimonas melkonianii* and *Py*2087ACR1 from *Pyramimonas spec.* CCMP 2087, which are homologous to two sequences found in the *Tara* Oceans viral metagenome, v*Py*ACR21821 and v*Py*ACR2164382. Due to their viral origin and relation to prasinophyte sequences, the prefix v*Py* is added to both. Their identifier is concluded by a series of numbers - their contig cluster identifiers (Rozenberg *et al.*, 2020).

Secondary structure prediction using the transmembrane helices hidden Markov model (TMHMM) algorithm (Sonnhammer *et al.*, 1998) suggests a heptahelical transmembrane

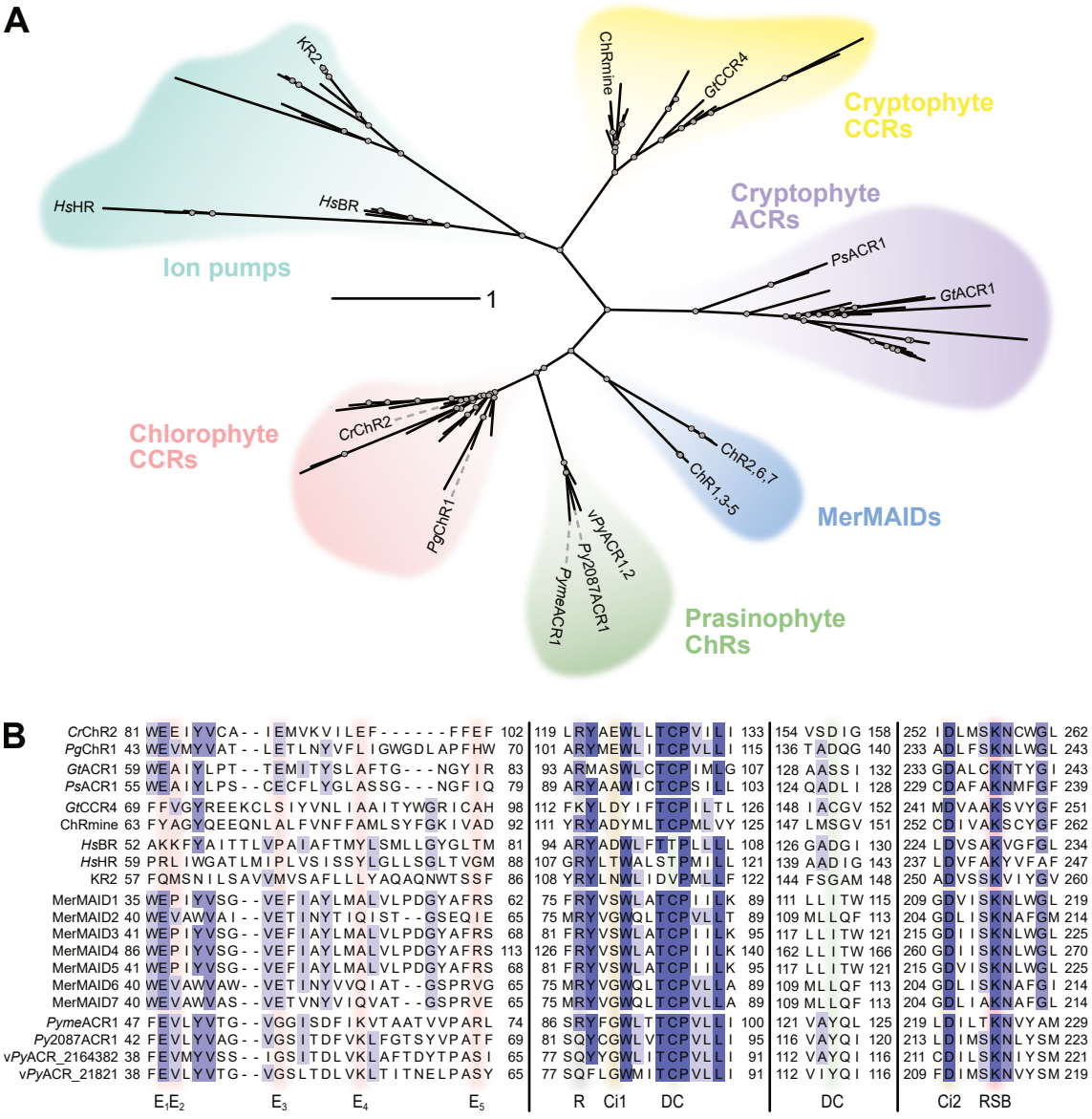


**Figure 11.: Phylogenetic comparison of metagenomically identified ChRs. A,** Unrooted phylogenetic tree of the channelrhodopsin superfamily and microbial ion pumps, including the metagenomically identified MerMAIDs and prasinophyte ChRs. Scale bar indicates the average number of residue substitutions per site. Representatives of each group are indicated. The tree was generated using ngphylogeny.fr (Lemoine *et al.*, 2019). v*Py*ACR2164382 and v*Py*ACR21821 are denoted as v*Py*ACR1 and v*Py*ACR2, respectively. **B,** Reduced sequence alignment of selected channelrhodopsins and ion pumps shown in A. The alignment was generated using ClustalW (Larkin *et al.*, 2007). Colored boxes indicate conservation. Abbreviations: ACRs, anion-conducting channelrhodopsins; CCRs, cation-conducting channelrhodopsins; Ci, Counterion; DC, DC pair-forming residues; E, Glutamates conserved in chlorophyte CCRs; MerMAIDs, Metagenomically discovered marine anion-conducting and intensely desensitizing channelrhodopsins; R, extracellular gate-forming arginine; RSB, Retinal Schiff base.

arrangement of the core segment, typical for microbial rhodopsins (Ernst *et al.*, 2014). While the amino- and carboxy-termini of the MerMAIDs are short, the prasinophyte ChRs have large carboxylic tails following the rhodopsin domain. These terminal regions are over 100 residues longer in the algal constructs than in the viral ones. Nonetheless, they

are all homologous to response regulator domains of histidine kinases (HKs). However, an aspartate residue, serving as a phosphorylation site in HKs (R. J. Lewis *et al.*, 1999; Bourret, 2010), is not conserved in the prasinophyte ChRs, suggesting a different role of these domains (Fig. S3; Rozenberg *et al.*, 2020). Large carboxy-terminal extensions have been identified previously in other ChRs. Although dispensable for ion channel function (Nagel *et al.*, 2003; Tashiro *et al.*, 2020), they might be involved in the trafficking of the protein (Greiner *et al.*, 2017).

In all sequences of the MerMAID and prasinophyte ChR families, the RSB-forming lysine in TM7 is conserved (RSB in Fig. 11B). In both MerMAID and prasinophyte ChRs, Ci1 is substituted by a serine or glycine residue, similar to cryptophyte ACRs and *Hs*HR (Váró, 2000; Govorunova *et al.*, 2017b). Ci2, on the other hand, is conserved as an aspartate residue in all sequences (Ci in Fig. 11B).

Five glutamate residues in TM2 form a highly conserved feature in chlorophyte CCRs (E in Fig. 11B). In *Cr*ChR2, the five glutamate residues are Glu82, Glu83, Glu90, Glu97, and Glu101 ($E_{1\text{-}5}$). Substitution of these glutamate residues with hydrophobic or uncharged residues reduces photocurrent amplitudes in *Cr*ChR2 (Sugiyama *et al.*, 2009; Watanabe *et al.*, 2012). Additionally, $E_3$ is associated with ion selectivity (Berndt *et al.*, 2014; Wietek *et al.*, 2014; Kuhne *et al.*, 2019). $E_1$ and $E_3$ are conserved in the MerMAIDs. In sub-branch 1 (MerMAID1,3-5), $E_2$ is replaced by a proline residue and $E_4$ by an alanine residue. On the other hand, in sub-branch 2 (MerMAID2,6,7), $E_2$ and $E_4$ are replaced with valine and glutamine residues, respectively. In the prasinophyte ChRs, only $E_1$ is conserved. $E_2$, $E_3$, and $E_5$ are replaced with non-polar residues, except for *Pyme*ACR1, where $E_5$ is an arginine residue. $E_4$, on the other hand, is replaced by a lysine residue in all prasinophyte ChRs. Interestingly, four residues C-terminally from $E_3$, about one $\alpha$-helix turn, the prasinophyte ChRs exhibit an aspartate residue, which may serve a similar function to its glutamate homolog in other ChRs (Fig. 11B).

In *Cr*ChR2 and other chlorophyte CCRs, the DC pair, composed of Cys128 and Asp156, confers intraprotomer stability via a water-mediated hydrogen bond connecting TM3 and TM4 (Volkov *et al.*, 2017). The cysteine residue is highly conserved in all ChR families, including the MerMAID and prasinophyte ChRs (DC in Fig. 11B). The aspartate residue, on the other hand, shows considerably less conservation outside the chlorophyte CCR family. In prasinophyte ChRs, a tyrosine residue is substituted for the aspartate residue, while in sub-branch 1 and sub-branch 2 of the MerMAIDs, Asp156 is replaced by an isoleucine and leucine residue, respectively.

The arginine residue critical for the formation of the ECG in *Cr*ChR2 (Arg120) is conserved in almost all microbial rhodopsins (R in Fig. 11B), and its substitution with an alanine residue renders *Cr*ChR2 nonfunctional (Plazzo *et al.*, 2012). A glutamine or alanine substitution of this residue in KR2, on the other hand, converted the $Na^+$-pump to an ion channel, conducting $K^+$ at alkaline $pH_e$ (Vogt *et al.*, 2019). In all MerMAIDs, the

arginine residue is conserved. However, in most prasinophyte ChRs, it is substituted with a glutamine residue (Fig. 11B).

## 2.2. MerMAID channelrhodopsins

### 2.2.1. Electrophysiological characterization

For a functional examination, human embryonic kidney (HEK) 293 cells were transiently transfected to express MerMAID1-7. After 24 h expression time, photocurrents were measured using whole-cell patch-clamp electrophysiology.

#### ChRs with a near-complete desensitization

Upon illumination with full-intensity (4 mW mm$^{-2}$) light, all seven constructs show large photocurrents that strongly desensitize in the light. Depending on the holding potential ($E_{\mathrm{hold}}$), the photocurrents have a positive or negative amplitude, typical for ChRs (Fig. 12A).

The spectral sensitivity of MerMAID1-7 was determined by recording action spectra from 390 nm to 680 nm, using 10 ms light pulses of low intensity and equal photon count. The action spectra have a distinct peak-activity ($\lambda_{\mathrm{max}}$) upon illumination with green light (Fig. 12B) ranging from 494.0 ± 0.8 nm (MerMAID6) to 502.0 ± 0.4 nm (MerMAID1; Fig. 12C). Therefore, for the following experiments, an excitation wavelength of 500 nm was chosen for all MerMAIDs.

$I_p$ at $E_{\mathrm{hold}} = -60$ mV ($I_{-60\,\mathrm{mV}}$) reaches between 0.3 ± 0.1 nA (MerMAID4) and 1.2 ± 0.2 nA (MerMAID6) upon illumination with full-intensity 500 nm-light (Fig. 12D). The transient photocurrent desensitization in continuous light reaches 98 % to 99 % (Fig. 12E). At low light intensities, $I_p$ of MerMAID1 is reduced or not apparent at all, while the stationary photocurrent amplitudes reach their maximum amplitude already at low light intensities. Furthermore, saturation of the transient photocurrents was not achieved at intensities up to 4 mW mm$^{-2}$ (Fig. S4), indicating a lower light sensitivity than other ACRs (Govorunova *et al.*, 2015; Wietek *et al.*, 2016).

#### MerMAIDs conduct anions

As pointed out above, the primary sequences of the MerMAIDs show similarities to cryptophyte ACRs, such as an uncharged Ci1 and substitutions of glutamate residues along the putative ion conduction pathway (Fig. 11B). While many other factors may contribute to ion selectivity, these similarities hint at an anion-conduction. Therefore, to investigate the ion selectivity, photocurrents were recorded at $E_{\mathrm{hold}}$ ranging from −80 mV to 40 mV (Fig. 13A). Between measurements, extracellular $Na^+$ or $Cl^-$ was replaced with various mono- or divalent cations or anions and liquid junction potentials (LJP) were corrected (Table 10).

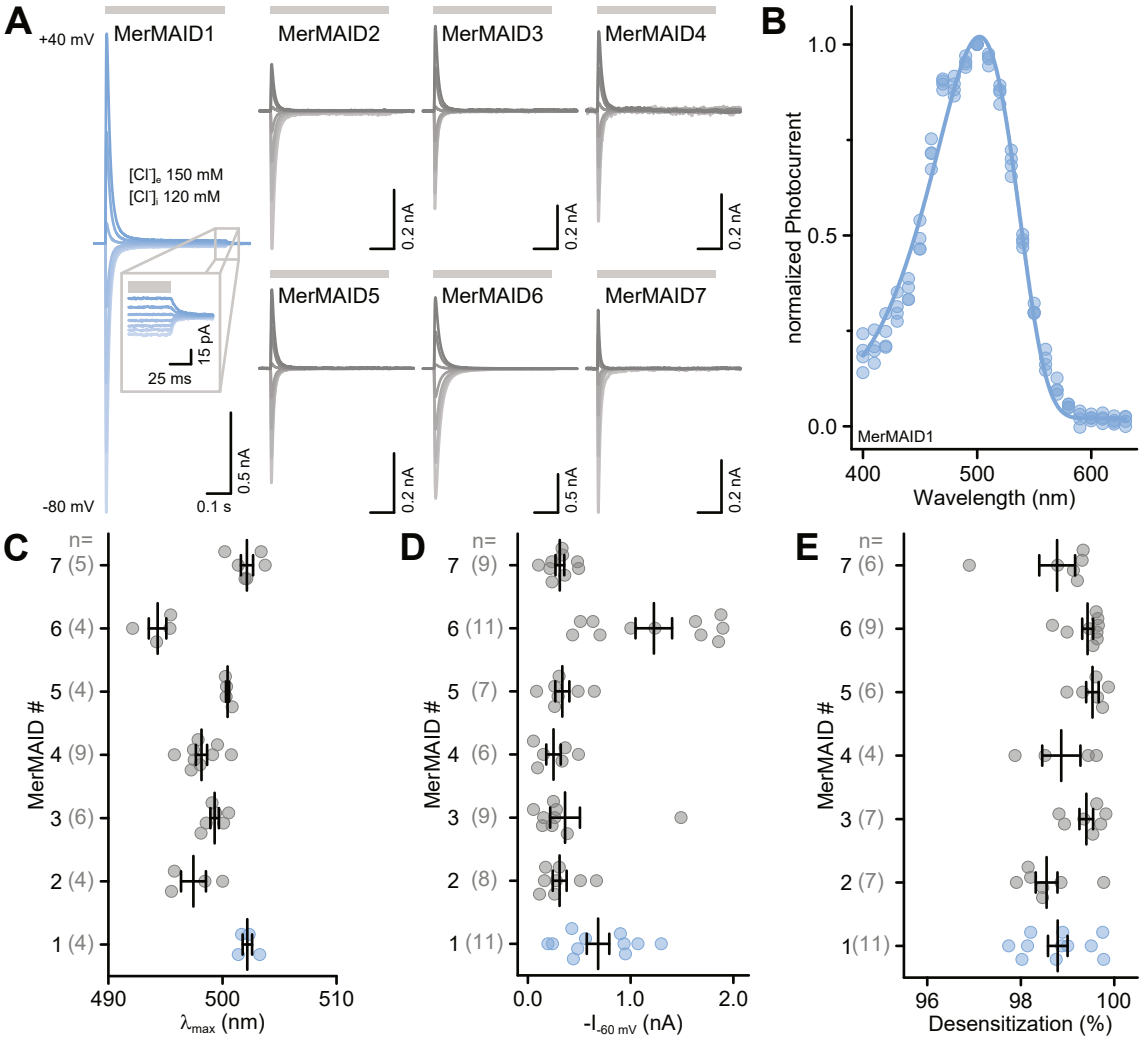


**Figure 12.: Photocurrents of MerMAIDs. A,** Photocurrents, evoked by 500 ms light pulses of 500 nm, were recorded in HEK293 cells at holding potentials between −80 mV to 40 mV with $[Cl^-]_i$ = 120 mM and $[Cl^-]_e$ = 150 mM. **B,** Action spectrum of MerMAID1. Low-intensity light between 390 nm to 680 nm in 10 nm steps was applied for 10 ms to induce photocurrents. Photocurrent amplitudes were normalized to the maximum amplitude and approximated with a three-parametric Weibull function (solid line) to determine the wavelength of the highest activity ($\lambda_{max}$). Single data points are shown as circles. **C,** $\lambda_{max}$ of all MerMAIDs. **D,** Amplitude of the transient photocurrent at −60 mV ($I_{-60\,mV}$) of all MerMAIDs upon excitation with 500 nm-light. **E,** Transient photocurrent desensitization of all MerMAIDs at −60 mV during excitation with 500 nm-light. In **C, D,** and **E,** single measurement data points are indicated as circles. Whiskers indicate standard error of the mean (SEM) with the mean indicated as a long line.

$I_p$ was determined, normalized to $I_{-80\,mV}$ in standard conditions and plotted against $E_{hold}$ (Fig. 13B). The ion selectivity was quantified by determining the reversal potential ($E_{rev}$) using a linear approximation. Changes in the concentration of conducted ions lead to shifts in the reversal potential ($\Delta E_{rev}$).

Upon reduction of the external $Cl^-$ concentration ($[Cl^-]_e$) to 10 mM by replacement with the non-conducted $Asp^-$, only negative-amplitude photocurrents remain (Fig. 13A) for all MerMAIDs. As the photocurrent amplitude sign is inverted for the negatively charged

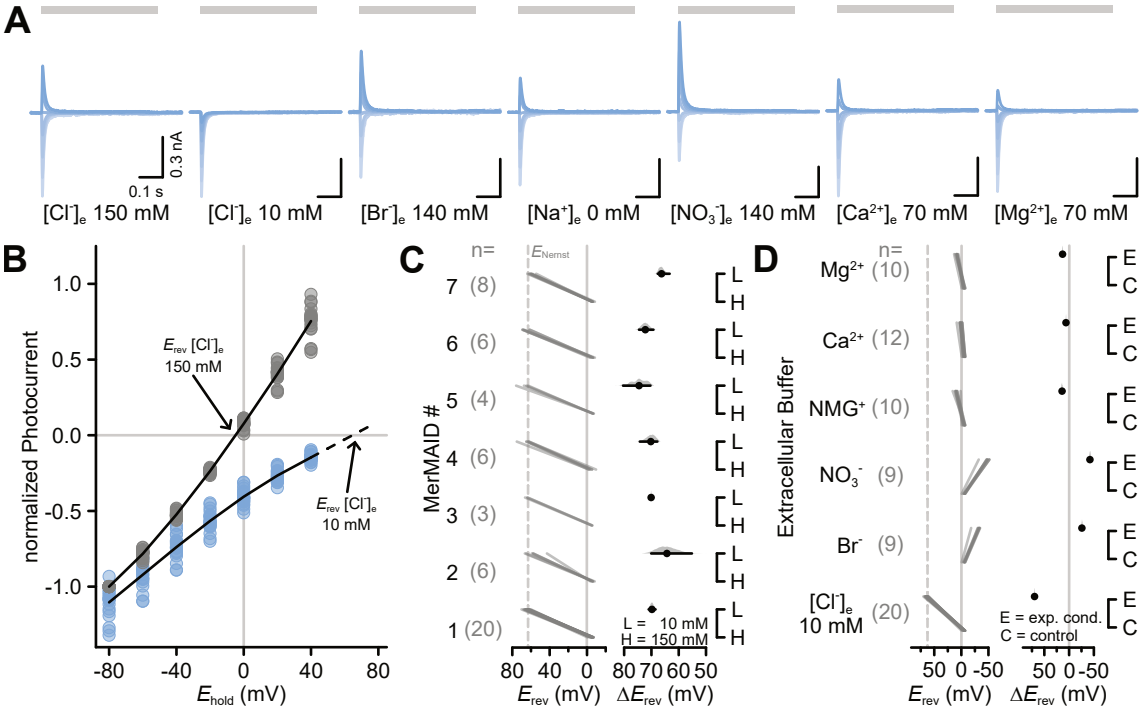


**Figure 13.: Ion selectivity of MerMAIDs. A,** Photocurrents, evoked by 500 ms light pulses of 500 nm recorded in HEK293 cells at holding potentials ($E_{hold}$) between −80 mV to 40 mV with $[Cl^-]_i$ = 120 mM. The extracellular buffer is indicated below the traces. **B,** Current-Voltage relationship of transient photocurrents of MerMAID1 recorded with 150 mM $Cl^-$ (gray circles) and 10 mM $Cl^-$ (blue circles) in the extracellular buffer. Arrows indicate the respective reversal potential ($E_{rev}$). **C,** Shifts of $E_{rev}$ ($\Delta E_{rev}$) for all MerMAIDs upon reduction of the extracellular $Cl^-$ concentration ($[Cl^-]_e$) from 150 mM to 10 mM. **D,** $\Delta E_{rev}$ of transient photocurrents of MerMAID1 upon replacement of the external buffer as indicated. The Nernst potential ($E_{Nernst}$) is indicated as a dashed line. Cumming estimation plots in **C and D** show the paired mean difference of the indicated comparisons. The raw data is plotted on the left axis, with each pair of observations connected by a line. The difference for the comparisons to the control ($[Cl^-]_e$ = 150 mM, $[Na^+]_e$ = 140 mM) is plotted on the right axis as a bootstrap sampling distribution, with the mean difference depicted as circles and the 95 % confidence interval indicated as a horizontal line.

anions, negative photocurrent amplitudes represent anion-efflux from the cell. In standard conditions, $E_{rev}$ ranges from −6.6 ± 0.6 mV (MerMAID6) to −4.7 ± 1.2 mV (MerMAID4). Upon $Cl^-$ reduction, $E_{rev}$ shifts significantly to positive values between 58.2 ± 3.4 mV (MerMAID2) and 67.9 ± 2.8 mV (MerMAID5) for all MerMAIDs (Fig. 13B, C). The theoretical Nernst potential ($E_{Nernst}$; Eq. 4.4) for $Cl^-$ at a concentration gradient of 120 mM intracellular and 10 mM extracellular is 63.2 mV.

The conduction of selected cations and anions was investigated for MerMAID1 (Fig. 13A, D). Replacement of $[Cl^-]_e$ with equivalent concentrations of either $Br^-$ or $NO_3^-$ shifts $E_{rev}$ significantly by 25.7 ± 1.1 mV and 41.9 ± 1.5 mV, respectively, to more negative values. In contrast to other ACRs (Govorunova *et al.*, 2015, 2016a), replacement of extracellular $Na^+$ with equivalent concentrations of mono- or divalent cations results in significant shifts of $E_{rev}$ as well. Replacing $Na^+$ with the non-conducted $NMDG^+$ results in a $\Delta E_{rev}$ of 14.5 ± 1.6 mV to more positive values, while replacing it with $Ca^{2+}$ or $Mg^{2+}$ shifts $E_{rev}$

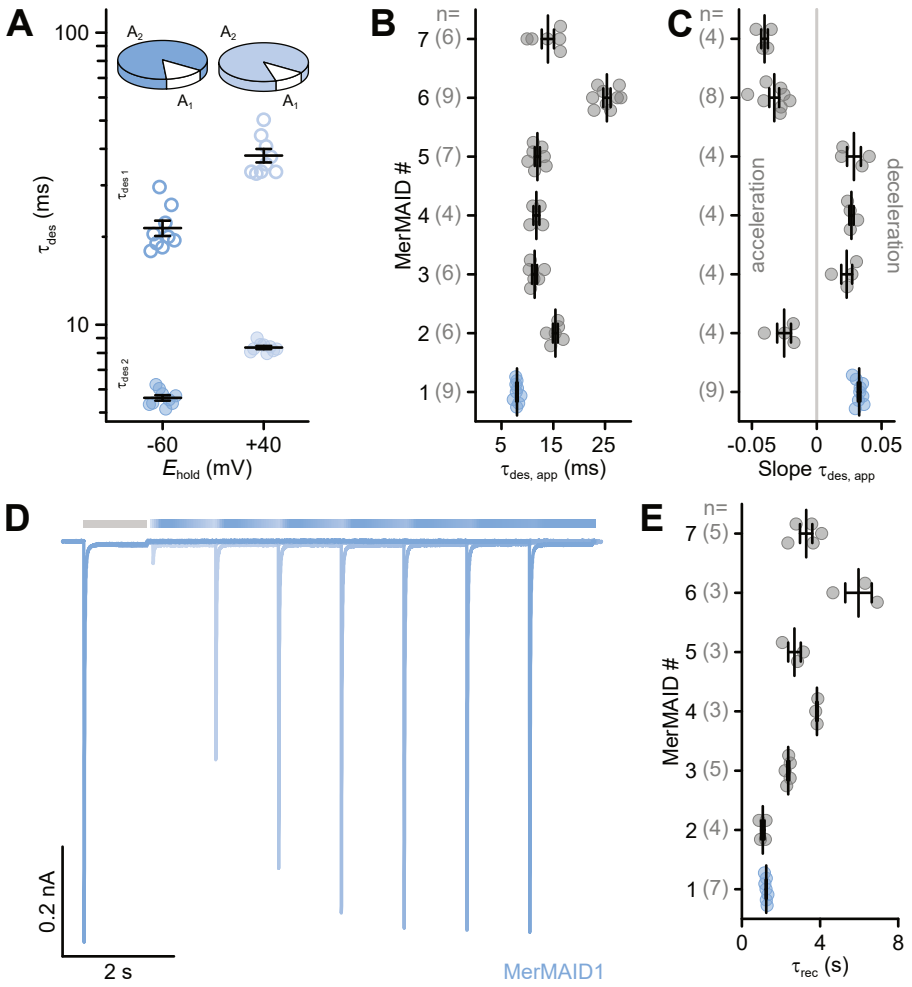


**Figure 14.: Photocurrent desensitization and recovery kinetics of MerMAIDs. A,** Time constants ($\tau_{\text{des}}1$ and $\tau_{\text{des}}2$) and their relative amplitudes (A1 and A2) of the bi-exponential desensitization of the transient photocurrents of MerMAID1 at holding potentials ($E_{\text{hold}}$) of −60 mV and 40 mV. **B,** Apparent kinetics of the transient photocurrent desensitization ($\tau_{\text{des, app}}$) for all MerMAIDs at $E_{\text{hold}} = -60$ mV. **C,** Voltage-dependence of the apparent kinetics of the transient photocurrent desensitization for all MerMAIDs with acceleration and deceleration indicated. **D,** Representative MerMAID1-photocurrent traces at −60 mV elicited by two light pulses of 500 nm with increasing dark intervals between them to determine the recovery kinetics ($\tau_{\text{rec}}$) of the transient photocurrents. **E,** $\tau_{\text{rec}}$ of all MerMAIDs. In **A, B, C, and E**, single measurement data points are indicated as circles. Whiskers indicate standard error of the mean (SEM) with the mean indicated as a long line.

more positive by 6.6 ± 0.6 mV and 13.6 ± 0.8 mV, respectively.

These results indicate that anions with a larger radius are better conducted than $Cl^-$, giving a relative permeability sequence of $NO_3^- > Br^- > Cl^-$. Nonetheless, the exchange of cations also affects $E_{\text{rev}}$, which may indicate a contribution of these ions to the photocurrents. However, the majority of the transported charge is carried by $Cl^-$ in standard conditions.

### The desensitization is voltage-dependent

The desensitization kinetics were approximated with a bi-exponential function, yielding a slow and a fast time component ($\tau_{\text{des 1}}$ and $\tau_{\text{des 2}}$) and their corresponding amplitudes ($A_1$ and $A_2$).

The photocurrent desensitization is dominated by the fast component and dependent on $E_{\text{hold}}$ (Fig. 14A). In MerMAID1, at a holding potential of −60 mV, 85.60 ± 0.01 % ($A_2$) of the $I_p$ decay with a time constant of 5.6 ± 0.1 ms ($\tau_{\text{des 2}}$), while 14.40 ± 0.01 % ($A_1$) decay with 21.4 ± 1.3 ms ($\tau_{\text{des 1}}$), roughly 4-fold slower than $\tau_{\text{des 2}}$. At a holding potential of 40 mV, $\tau_{\text{des 2}}$ decelerates to 8.4 ± 0.1 ms, accounting for the decay of 88.60 ± 0.01 % ($A_2$) of $I_p$. $\tau_{\text{des 1}}$, on the other hand, decelerates to 38.0 ± 2.0 ms with a relative amplitude of 11.40 ± 0.01 % ($A_1$).

For an easier comparison of the different MerMAIDs, the apparent kinetics of the transient photocurrent desensitization ($\tau_{\text{des, app}}$) were calculated (Eq. 4.5). At −60 mV, $\tau_{\text{des, app}}$ ranges from 8.0 ± 0.1 ms (MerMAID1) to 25.4 ± 0.7 ms (MerMAID6; Fig. 14B). The voltage-dependence of the desensitization apparent upon comparing the single components (Fig. 14A) was quantified as the slope of a linear approximation of $\tau_{\text{des, app}}$ at $E_{\text{hold}}$ between −80 mV and 40 mV. A negative slope represents an acceleration of the desensitization with $E_{\text{hold}}$ becoming more positive, while a positive slope indicates a deceleration of the desensitization. In measurements of MerMAID2,6,7, the desensitization accelerates, while in measurements of MerMAID1,3-5, the desensitization decelerates (Fig. 14C). This separation correlates well with the described phylogenetic relationship of the MerMAIDs, separating into two sub-branches in the phylogenetic tree (Fig. 11).

Repeated excitation of the MerMAIDs at $E_{\text{hold}} = -60$ mV in short succession strongly decreases $I_{-60\,\text{mV}}$, which only recovers with a longer duration of the dark intervals between the exciting light pulses (Fig. 14D), as described previously for ChRs (Nagel *et al.*, 2003; Schneider *et al.*, 2015). The kinetics of $I_{-60\,\text{mV}}$ recovery ($\tau_{\text{rec}}$) were determined by exciting the MerMAIDs with two light pulses, applied with increasing dark intervals (Fig. 14D). Subsequently, $\tau_{\text{rec}}$ was approximated using a mono-exponential function. $\tau_{\text{rec}}$ (Fig. 14E) ranges from 1.1 ± 0.1 s (MerMAID2) to 6.0 ± 0.7 s (MerMAID6), similar to chlorophyte CCRs (Schneider *et al.*, 2015), but considerably slower compared to cryptophyte ACRs (Govorunova *et al.*, 2016a).

### MerMAID photocurrents are unaffected by changes in the pH

The function of microbial rhodopsins is strongly coupled to de- and reprotonation of residues within the proteins (Lanyi, 2006; Kuhne *et al.*, 2019). Changes in the surrounding pH can significantly affect photocurrent amplitudes and kinetics (Schneider *et al.*, 2015).

All experiments shown in figures 12, 13, and 14 were performed at symmetrical pH of 7.2 on the inside and outside. The effect of pH on the MerMAIDs was assessed in measurements

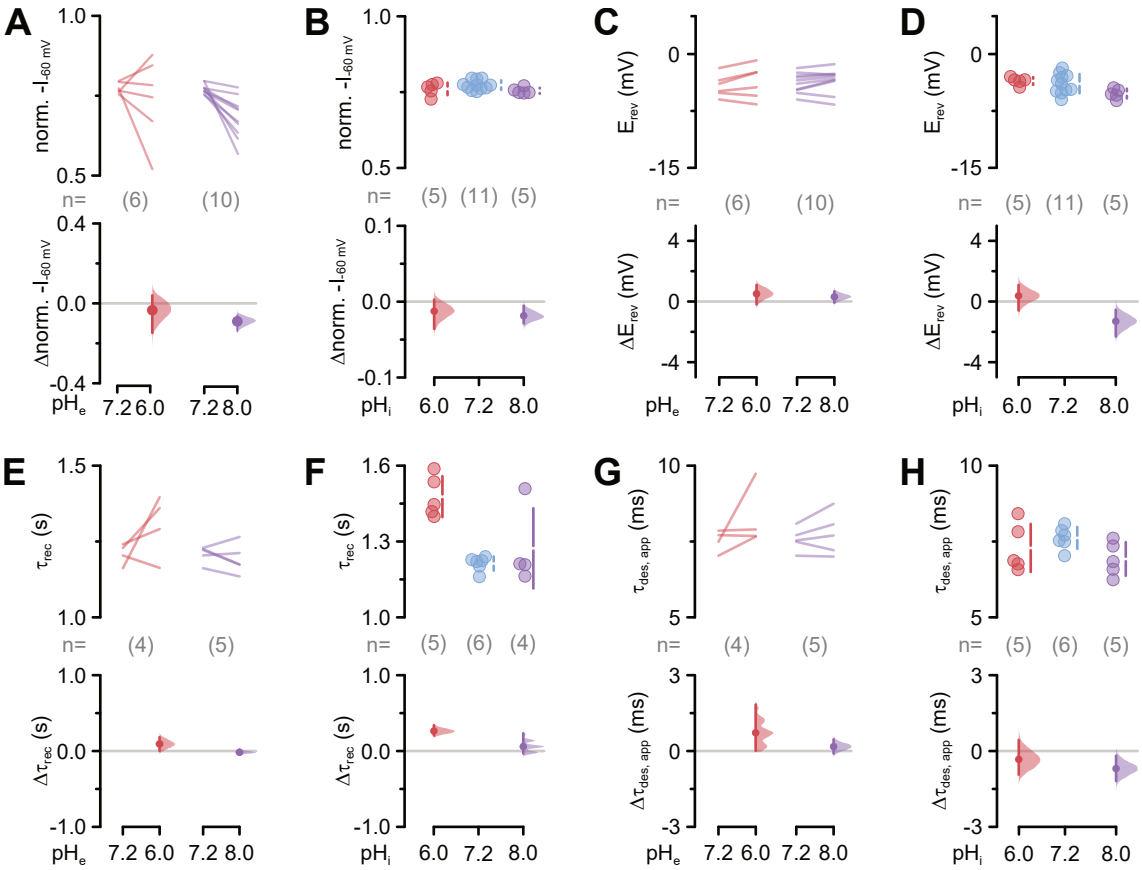


**Figure 15.: pH-dependence of electrophysiological parameters of MerMAID1.** Cumming estimation plots for the comparison of **A, B** transient photocurrent amplitudes at a holding potential of −60 mV ($I_{-60\,mV}$); **C, D,** reversal potentials ($E_{rev}$); **E, F,** recovery kinetics of the transient photocurrents ($\tau_{rec}$) at a holding potential of −60 mV; and **G, H,** kinetics of the transient photocurrent desensitization ($\tau_{des,\,app}$) at a holding potential of −60 mV at varied extracellular pH (A, C, E, and G) and intracellular pH (B, D, F, and H). In A, C, E, and G, the cumming estimation plots show the paired mean difference of comparisons, with the raw data plotted on the upper axes, with each pair of observations connected by a line. In B, D, F, and H, the cumming estimation plots show the mean difference of comparisons, with the raw data plotted as circles on the upper axes. The difference for the comparison to the control (pH 7.2) is plotted as a bootstrap sampling distribution on the lower axes, with the mean differences depicted as circles and the 95 % confidence interval indicated as vertical error bars.

of MerMAID1 in standard buffer with either the external pH ($pH_e$) or the internal pH ($pH_i$) adjusted to 6 or 8 and compared to measurements at symmetrical pH 7.2 (Fig. 15). As $\lambda_{max}$ is not drastically affected by changes in the pH in this range (Fig. S5A, B), 500 nm-light was used in all experiments, investigating the pH-dependence of MerMAID1.

The photocurrents evoked by applying light for 500 ms at $E_{hold}$ ranging from −80 mV to 40 mV are only marginally affected by changes in the pH and are always nearly completely desensitizing, independent of the intra- and extracellular pH (Fig. S5C, D).

Changing $pH_e$ from 7.2 to 6 decreases $I_{-60\,mV}$ by $3 \pm 5$ % on average, while increasing $pH_e$ from 7.2 to 8 decreases $I_{-60\,mV}$ significantly by $10 \pm 2$ %. However, single cases were detected in both conditions, where the transient photocurrents decreased by up to

25 % (Fig. 15A). With a mean difference of 1 % and 2 % upon changing $pH_i$ from 7.2 to 6 and 8, respectively, $I_{-60\,mV}$ was not affected (Fig. 15B).

$\tau_{des,\,app}$ at −60 mV mildly decelerates from $7.6 \pm 0.2$ ms at $pH_e$ 7.2 to $8.2 \pm 0.5$ ms at $pH_e$ 6. However, with $7.8 \pm 0.3$ ms, it remains unaffected at $pH_e$ 8 (Fig. 15G). In contrast, $\tau_{des,\,app}$ accelerates to $7.3 \pm 0.4$ ms at $pH_i$ 6 and significantly to $6.9 \pm 0.3$ ms at $pH_i$ 8 (Fig. 15H). The voltage-dependence of $\tau_{des,\,app}$ is unaffected by extra- or intracellular pH changes (Fig. S5E, F).

$E_{rev}$ is not affected by changes in $pH_e$ either (Fig. 15C), yet a mild pH-dependence becomes apparent upon modification of $pH_i$ (Fig. 15D). At an internal pH 7.2, $E_{rev}$ is $-3.9 \pm 0.4$ mV. Decreasing the internal pH shifts $E_{rev}$ slightly more positive to $-3.5 \pm 0.2$ mV, while, at a more alkaline internal pH, $E_{rev}$ shifts to more negative values of $-5.2 \pm 0.3$ mV.

Lastly, under symmetrical conditions, $\tau_{rec}$ is $1.20 \pm 0.01$ s. In a more acidic external environment, $\tau_{rec}$ decelerates to $1.30 \pm 0.05$ s, while with $1.20 \pm 0.02$ s $\tau_{rec}$ remains unaffected at $pH_e$ 8 (Fig. 15E). At a more acidic $pH_i$, $\tau_{rec}$ decelerates significantly to $1.50 \pm 0.04$ s. However, the recovery of $I_p$ remains unaffected with $1.30 \pm 0.08$ s at $pH_i$ 8 (Fig. 15F).

Overall the effects of changing the pH on the extra- or intracellular side are minimal and for most tested electrophysiological parameters not significant. Especially compared to other ChRs (Tsunoda and Hegemann, 2009; Wietek *et al.*, 2014), the effects of changes in the pH appear small. Therefore, the RSB proton possibly remains within the Schiff base region as suggested for heliorhodopsins (Pushkarev *et al.*, 2018), perhaps in a central proton cage as proposed for *Hs*BR (Friedrich *et al.*, 2020). $I_p$ and $E_{rev}$ do not change with the pH, indicating that $H^+$ is not contributing to the carried charge of MerMAID1. Interestingly, while $\tau_{des,\,app}$ is mostly unaffected as well, $\tau_{rec}$ consistently decelerates at more acidic pH in contrast to *Cr*ChR2 (Nagel *et al.*, 2003).

### 2.2.2. Spectroscopic characterization

To better understand the molecular processes in the MerMAIDs, a spectroscopic characterization is required. Therefore, a clone of *Pichia pastoris* was produced that recombinantly expressed MerMAID1 with a 6xHis-Tag for purification (Fig. S6A). The protein was obtained in high purity, as suggested by the protein-to-chromophore-ratio ($A_{280}/A_{502}$) of 1.9 (Fig. 16A). However, the gel filtration profile reveals that the sample is not homogeneous (Fig. S6B).

#### Fine-structured UV-light absorption upon illumination or alkalization

Steady-state UV/vis absorption spectra were recorded between 270 nm and 680 nm at a temperature of 281 K. The protein was dissolved in a buffer containing 100 mM NaCl in standard conditions, with the pH adjusted to 8. Dark-adapted MerMAID1 has a peak

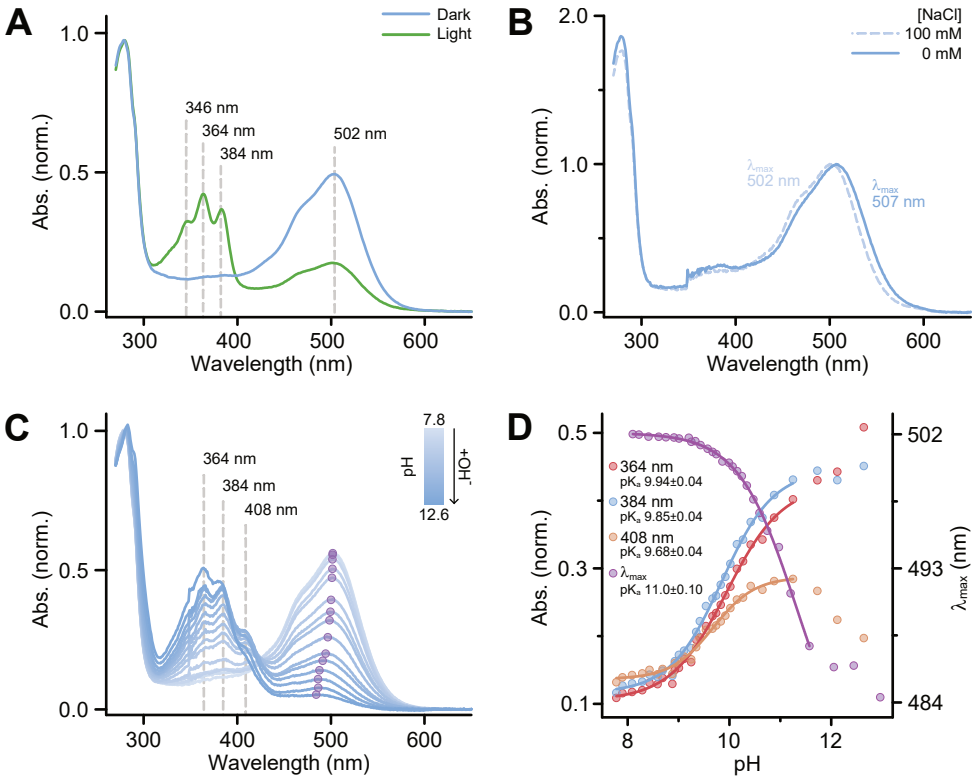


**Figure 16.: Steady-state absorption spectroscopy of purified MerMAID1.** **A,** Normalized UV/vis absorption spectra of dark-adapted MerMAID1 (green) and MerMAID1 during illumination (blue) are shown. Local absorption maxima are indicated. **B,** $Cl^-$-dependence of dark-adapted MerMAID1 absorption spectra. Normalized UV/vis absorption spectra of MerMAID1 with 100 mM NaCl (dashed line) and 0 mM NaCl (solid line) in the buffer are shown with the absorption maxima ($\lambda_{max}$) indicated. **C,** pH-dependence of dark-adapted MerMAID1 absorption spectra. UV/vis absorption spectra, normalized to $A_{280}$ at pH 7.8. The pH was titrated by adding small volumes of NaOH to the buffered protein solution. Dashed lines indicate local absorption maxima. Purple circles indicate $\lambda_{max}$ of the protonated retinal Schiff base ($RSBH^+$). **D,** Normalized absorption changes and $\lambda_{max}$ shift of the $RSBH^+$ upon titration of the pH. The respective p$K_a$ was determined using a Boltzmann function (solid lines).

absorption ($\lambda_{max}$) at 502 nm (Fig. 16A), similar to the measured action spectra (Fig. 12B, C). Furthermore, the absorption spectrum has a shoulder at approximately 470 nm (Fig. 12B, C). Between 350 nm and 400 nm, a slightly elevated absorption is visible (Fig. 16A) resembling the $\beta$-band absorption of the retinal chromophore originating from two-photon absorption (Kropf *et al.*, 1973; Stavenga *et al.*, 1993). Upon continuous illumination with $520 \pm 15$ nm-light, the RSB deprotonates, represented by the rise of a UV-light-absorbing species with three distinct local absorption maxima at 346 nm, 364 nm, and 384 nm (Fig. 16A).

Previous reports demonstrated the $Cl^-$ concentration affecting $\lambda_{max}$ of *Ps*ACR1 (Hontani *et al.*, 2017; Tsukamoto *et al.*, 2018). Furthermore, $Cl^-$ was proposed to compensate for the lack of a counterion in *Hs*HR (Kolbe *et al.*, 2000). Therefore, $Cl^-$ acting as a counterion in MerMAID1 was investigated, using UV/vis absorption spectroscopy. Spectra were recorded at pH 8 with 100 mM or 0 mM NaCl in the buffer, similar to experiments

performed for *Ps*ACR1 (Hontani *et al.*, 2017). Upon NaCl-depletion, the absorption of dark-adapted MerMAID1 shifts from 502 nm to 507 nm (Fig. 16B). Additionally, the $\beta$-band absorption shows a mild increase. Therefore, the absorption of MerMAID1 is mildly affected by changes in the ionic conditions, possibly indicating a weak contribution of $Cl^-$ to the stabilization of the RSB.

The pH-dependence of the absorption spectrum of dark-adapted MerMAID1 was investigated in the range of pH 7.8 to 12.6 (Fig. 16C). The pH was titrated and UV/vis absorption spectra were recorded. The absorption spectrum of dark-adapted MerMAID1 exhibits a maximum of 502 nm at pH 7.8, as observed before (Fig. 16C, D). Upon alkalization of the sample, the pronounced absorption peak of the $RSBH^+$ decreases, with the absorption maximum shifting to 484 nm, and giving rise to a UV-light-absorbing species with three distinct local maxima, similar to absorption spectra of light-adapted MerMAID1 (Fig. 16A), but shifted bathochromic with peaks at 364 nm, 384 nm, and 408 nm (Fig. 16C). With increasing pH (>11.3), $A_{408}$ decreases again, while $A_{364}$ and $A_{384}$ slightly increase or remain stable (Fig. 16C, D).

The p$K_a$ of the three UV-light-absorbing local maxima and the $RSBH^+$ was determined by plotting them against the pH and approximating their progression with a Boltzmann function between pH 7.8 and 11.3 (Fig. 16D). While the $RSBH^+$ absorption disappears with a p$K_a$ of $11.0 \pm 0.1$, the three local absorption maxima at 364 nm, 384 nm, and 408 nm appear with a p$K_a$ of $9.94 \pm 0.04$, $9.85 \pm 0.04$, and $9.68 \pm 0.04$, respectively. Exclusion of the absorption spectra recorded at pH >11.3 allows the determination of an isosbestic point ($\lambda_i$) at 425 nm (Fig. S7). An isosbestic point indicates that the reaction's stoichiometry remains unchanged (Jenkins and McNaught, 2014).

### Accumulation of a non-conducting photointermediate

The photocycle of MerMAID1 was investigated by recording single-turnover photocurrents and light-minus-dark UV/vis difference absorption spectra upon excitation with a ns-laser pulse of 500 nm at a temperature of 295 K (Fig. 17).

The transient photocurrent amplitudes, recorded after 24 h expression in HEK293 cells, reach their maximum 350 µs after excitation (Fig. 17A). The channel closing is biphasic with a dominating ($95 \pm 3$ %) fast component with a $\tau$ of $2.2 \pm 0.1$ ms at −60 mV. The remaining $5 \pm 3$ % of the photocurrent decayed with a kinetic of $26.5 \pm 15.0$ ms, yielding an apparent time constant for the photocurrent decay of $2.7 \pm 1.0$ ms.

In the UV/vis difference absorption spectra (Fig. 17B), the dark-state bleach (DSB) between 450 nm and 550 nm and an absorption increase at wavelengths <400 nm occurring within ms are most prominent. Excitation of purified MerMAID1 gives rise to an early photointermediate with a peak absorption at 570 nm ($P_{570}$). $P_{570}$ decays with a time constant of 173 ns and is followed by a photointermediate, weakly absorbing at 475 nm ($P_{475}$). With a time constant of 6 ms, $P_{475}$ transitions into a strongly blue-shifted photointermediate ($P_{366}$)

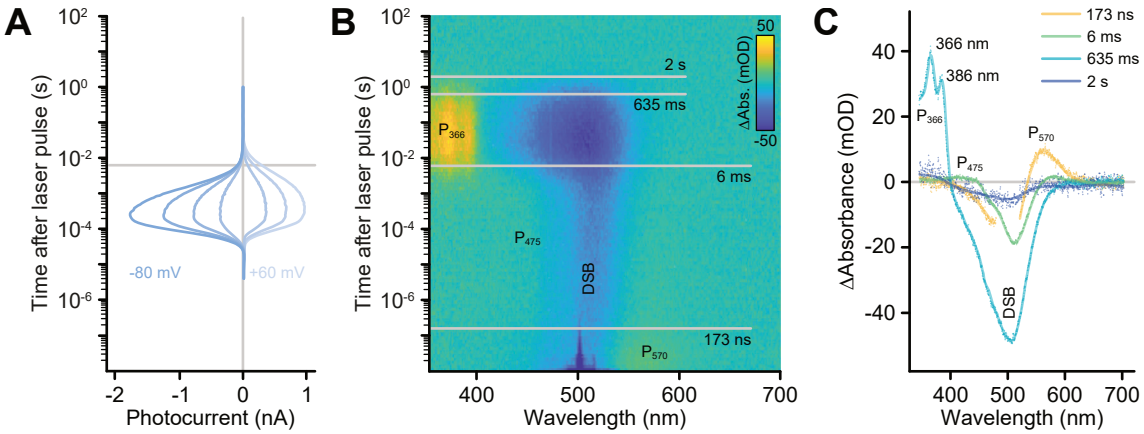


**Figure 17.: Temporal evolution of MerMAID1 photocurrents and absorption.** **A,** Photocurrents of MerMAID1 upon excitation with a ns-laser pulse, recorded at holding potentials between −80 mV to 60 mV in 20 mV steps and at symmetrical [$Cl^-$] of 120 mM intra- and extracellular. Photocurrents at 0 mV are not shown. The horizontal line indicates the time point of the $P_{475}$→$P_{366}$ photointermediate transition. **B,** Transient difference absorption spectra of MerMAID1 depicted as a contour plot. Photointermediates are indicated ($P_{570}$, $P_{475}$, and $P_{366}$) with their respective decay times given and indicated by gray lines. The dark-state bleach (DSB) decayed within 2 s. **C,** Evolution-associated difference spectra (EADS) of global fits of transient absorption spectra, presented as dots with lines for visual guidance. In the EADS at 173 ns, data points saturated from scattered laser light were excluded for global analysis. Photointermediates are indicated with their respective absorption maximum as subscript. Wavelengths of the local maxima of the $P_{366}$ EADS are given. Photocurrents and photocycle were induced by a 6 ns and 10 ns laser pulse of 500 nm, respectively. The data was collected and analyzed by Dr. Jonas Wietek (A) and Arita Silapetere (B, C). Adapted from Oppermann *et al.* (2019).

decaying with a time constant of 635 ms. The DSB recovers within 2 s, indicating the return of MerMAID1 to the initial dark state.

Evolution-associated difference spectra (EADS) were obtained from global fits of transient UV/vis absorption spectra of MerMAID1 (Fig. 17C). At 6 ms, the EADS shows two weak positive absorption changes at 475 nm and 590 nm. Furthermore, the EADS at 635 ms exhibits a substantial absorption increase <400 nm with a fine-structure similar to the steady-state UV/vis absorption spectrum obtained during illumination (Fig. 16A). However, in contrast, only two local maxima appear at 366 nm and 386 nm, since 346 nm is outside the measurement's spectral window.

The ns-laser pulse-induced transient photocurrents reach their maximum amplitudes at a timescale coinciding with the rise of $P_{475}$. Upon decay of $P_{475}$, the photocurrents decrease as well. With the accumulation of $P_{366}$, the ion channel becomes non-conducting (Fig. 17A, B).

### The RSB-linkage populates an *anti*-conformation

The appearance of three distinct local maxima in the UV/vis absorption spectra of MerMAID1 upon illumination as well as at alkaline conditions (Fig. 16A, C) might be an indicator for a heterogeneous dark state composition of the retinal chromophore in Mer-

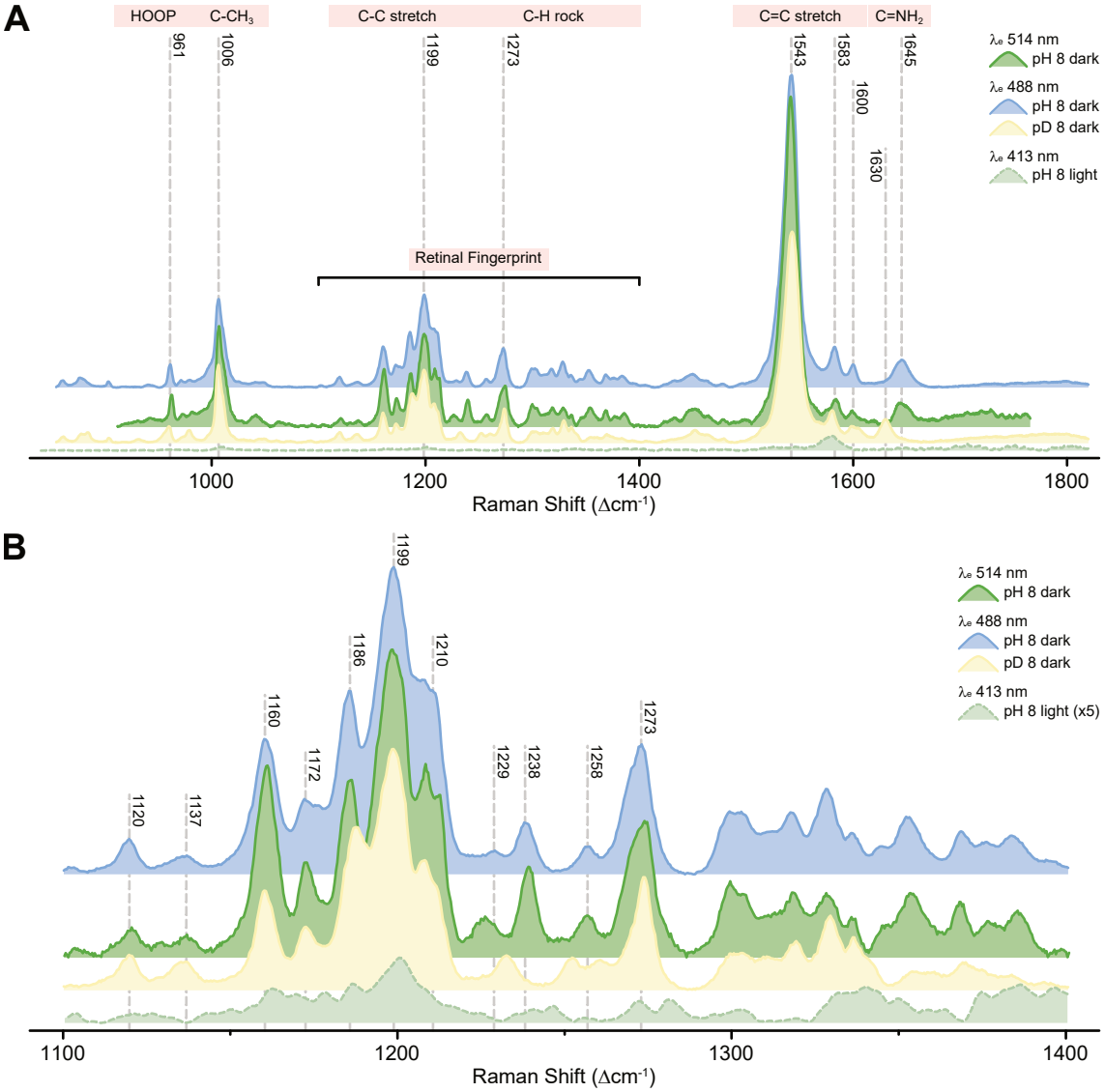


**Figure 18.: The chromophore structure of dark- and light-adapted MerMAID1. A,** Resonance Raman (RR) spectra of dark- and light-adapted MerMAID1. RR spectra of dark-adapted MerMAID1 at pH or pD 8 were probed with an excitation wavelength ($\lambda_e$) = 488 nm or 514 nm. Light-adapted MerMAID1 was probed with $\lambda_e$ = 413 nm. Regions of the RR spectrum indicating vibrations of specific chemical connections are labeled accordingly. **B,** Enlarged view of the retinal fingerprint region of RR spectra shown in A. The spectrum of light-adapted MerMAID1 recorded with $\lambda_e$ = 413 nm was scaled up by a factor of 5 to improve visibility. All RR spectra were accumulated for 30 min at 80 K with a laser power of 1 mW. Labeled frequencies refer to the RR spectrum of dark-adapted MerMAID1 at pH 8. The data was collected and prepared by Dr. Anke Keidel. Adapted from Oppermann *et al.* (2019).

MAID1 or the appearance of a retro-retinal as suggested before for the *Cr*ChR2-C128T mutant (Bruun *et al.*, 2011) and shown for *Hs*BR (Peters *et al.*, 1976; Schreckenbach *et al.*, 1977).

To further investigate the chromophore structure of MerMAID1, resonance Raman (RR) spectroscopy was performed with dark- or light-adapted samples, cryo-trapped at 80 K, with pH or pD 8 or 10. RR spectroscopy is an established method to analyze the chromophore

structure of microbial rhodopsins (Harbison *et al.*, 1984; S. O. Smith *et al.*, 1984; Luck *et al.*, 2012). The chromophore is excited by a laser within the chromophore's $\lambda_{max}$ and the Raman-scattered light[1] is detected. The difference between the frequency of the excitation laser and the scattered light corresponds to the vibrational frequencies of the chromophore (S. O. Smith *et al.*, 1985a; Chowdhury, 2018).

The dark state composition of the MerMAID1 chromophore was investigated by probing dark-adapted sample at pH 8 with an excitation wavelength ($\lambda_e$) of either 488 nm or 514 nm. The resulting RR spectra are very similar, with prominent vibrations not shifted more than 2 $cm^{-1}$, indicating that the chromophore is homogeneous in the sample (Fig. 18A).

Probing with $\lambda_e = 488$ nm yields a dominating ethylenic stretching vibration at 1543 $cm^{-1}$ ($\lambda_e = 514$ nm: 1541 $cm^{-1}$) in dark-adapted MerMAID1 (Fig. 18A). Additional C=C stretching vibrations appear at 1583 $cm^{-1}$ and 1600 $cm^{-1}$ ($\lambda_e = 514$ nm: 1584 $cm^{-1}$ and 1599 $cm^{-1}$). Furthermore, a prominent C=$NH_2$ stretching vibration is apparent at 1645 $cm^{-1}$ ($\lambda_e = 514$ nm: 1644 $cm^{-1}$). Deuteration of the sample exchanges accessible protons with deuterium (H/D exchange), leading to frequency shifts of protonation-sensitive vibrations. In the RR spectra of microbial rhodopsins, the C=$NH_2$ stretching vibration of the $RSBH^+$ is most affected by the H/D exchange (A. Lewis *et al.*, 1974). In deuterated MerMAID1, the C=$NH_2$ stretching vibration is downshifted by 15 $cm^{-1}$ to 1630 $cm^{-1}$, indicating protonation of the RSB in the dark state (Fig. 18A).

Illumination with $520 \pm 15$ nm-light and subsequent RR spectroscopy with $\lambda_e = 413$ nm reveals a substantial decrease of the detected Raman band intensities (Fig. 18A). The RR spectra of light-adapted MerMAID1 show a single prominent ethylenic stretching vibration at 1580 $cm^{-1}$. The ethylenic stretching vibration is inversely correlated with $\lambda_{max}$ of absorption spectra (Heyde *et al.*, 1971; Aton *et al.*, 1977), and an upshift of this vibration, therefore, correlates well with the hypsochromic shift of $\lambda_{max}$ in absorption spectra upon illumination (Fig. 16A). Furthermore, a C=$NH_2$ stretching vibration is not detected (Fig. 18A), indicating complete deprotonation of the RSB upon illumination.

All RR spectra show strong in-plane rocking vibrations at 1006 $cm^{-1}$ associated with the retinal methyl groups at $C_9$ and $C_{13}$ (S. O. Smith *et al.*, 1987b), which are only mildly affected by deuteration or illumination. At pH 8, three distinct hydrogen-out-of-plane (HOOP) vibrations are detected at 961 $cm^{-1}$, 972 $cm^{-1}$ and 980 $cm^{-1}$. Upon H/D exchange, they merge to form two HOOP vibrations with frequencies of 960 $cm^{-1}$ and 980 $cm^{-1}$ and, upon illumination, only a very weak HOOP vibration with a frequency of 961 $cm^{-1}$ is detected. These vibration modes may arise from strongly coupled hydrogens at double bonds of the retinal chromophore (S. O. Smith *et al.*, 1987b).

The retinal fingerprint region (Fig. 18B) comprises C−C stretching and C−H rocking vibrations sensitive to the retinal chromophore conformation, which enables the identification of the retinal isomer in the sample, based on previous studies on *Hs*BR (S. O. Smith *et al.*,

[1] inelastic scattering of photons, i. e. loss or increase of the frequency of the incident photon.

**Table 1.: Band assignments of C−C stretching vibrations in RR spectra of *Hs*BR and MerMAID1.** Assignments for *Hs*BR, according to S. O. Smith *et al.* (1987b,a). For details about the assignment of bands in the RR spectra of MerMAID1, please refer to the text. All values are given in $cm^{-1}$.

| | all-*trans* retinal | | 13-*cis* retinal | |
|---|---|---|---|---|
| | *Hs*BR | MerMAID1 | *Hs*BR | MerMAID1 |
| $C_6-C_7$ | 1122 | 1120 | 1122 | 1120 |
| $C_8-C_9$ | 1214 | 1210 | 1202 | 1202 |
| $C_{10}-C_{11}$ | 1169 | 1160/1172 | 1183 | 1186 |
| $C_{11}-C_{12}$ | 1248 | 1258 | 1234 | 1247 |
| $C_{14}-C_{15}$ | 1201 | 1199 | 1167 | 1178 |

1987b,a). Although it has to be noted that C−C stretching modes can be delocalized and mixed. Nonetheless, S. O. Smith and colleagues assigned the C−C stretching vibrations associated with $C_6-C_7$, $C_8-C_9$, $C_{10}-C_{11}$, $C_{11}-C_{12}$, and $C_{14}-C_{15}$ to 1122 $cm^{-1}$, 1214 $cm^{-1}$, 1169 $cm^{-1}$, 1248 $cm^{-1}$, and 1201 $cm^{-1}$ in the all-*trans* chromophore (S. O. Smith *et al.*, 1987b) and to 1122 $cm^{-1}$, 1202 $cm^{-1}$, 1183 $cm^{-1}$, 1234 $cm^{-1}$, and 1167 $cm^{-1}$ in the 13-*cis* chromophore (S. O. Smith *et al.*, 1987a). An overview of the band assignments for the C−C stretching vibrations of the all-*trans* and 13-*cis* retinal chromophore in *Hs*BR and MerMAID1 is given in table 1.

In the dark- and light-adapted MerMAID1, the vibration mode with a frequency of 1120 $cm^{-1}$ can be assigned to $C_6-C_7$ (Fig. 18B).

The $C_8-C_9$ stretching vibration in the dark-adapted sample is tentatively assigned to 1210 $cm^{-1}$ for dark-adapted MerMAID1, as it is only detected as a shoulder upon probing with $\lambda_e = 488$ nm, similar to *Hs*BR (S. O. Smith *et al.*, 1987b; A. Yi *et al.*, 2016), but more pronounced upon probing with $\lambda_e = 514$ nm. In light-adapted MerMAID1, the $C_8-C_9$ stretching vibration is assigned to 1202 $cm^{-1}$ (Fig. 18B), similar to *Hs*BR (S. O. Smith *et al.*, 1987a).

The $C_{10}-C_{11}$ stretching vibration in the dark-adapted sample shows a correlation with $\lambda_{max}$ of absorption spectra. Red-light-absorbing rhodopsins exhibit a single vibration mode that can be associated with this bond, while blue- or green-light-absorbing rhodopsins, such as GPR ($\lambda_{max} = 525$ nm) or BPR ($\lambda_{max} = 480$ nm), exhibit a downshifted vibration peak with an additional shoulder (A. Yi *et al.*, 2016). Therefore, in dark-adapted MerMAID1, the 1160 $cm^{-1}$ and 1172 $cm^{-1}$ are assigned to the $C_{10}-C_{11}$ stretching vibration (Fig. 18B). In the light-adapted sample, this vibration mode is upshifted to 1186 $cm^{-1}$. A vibration with this frequency is also detected in dark-adapted MerMAID1 and possibly resembles the formation of a 13-*cis* retinal photoproduct upon probing with $\lambda_e = 488$ nm.

The stretching of $C_{12}-C_{13}$ is assigned to 1258 $cm^{-1}$ in dark-adapted MerMAID1, similar to *Gt*ACR1 (A. Yi *et al.*, 2016). It exhibits a downshift to 1247 $cm^{-1}$ upon illumination.

Interestingly, this vibration mode appears to separate into two vibrations at 1252 $cm^{-1}$ and 1261 $cm^{-1}$ upon H/D exchange (Fig. 18B).

Lastly, the stretching of $C_{14}$−$C_{15}$ can be assigned to the most prominent peak in the retinal fingerprint region of the dark-adapted sample at 1199 $cm^{-1}$ (Fig. 18B). Upon isomerization to 13-*cis*, this vibration mode exhibits a pronounced downshift in *Hs*BR (S. O. Smith *et al.*, 1987a). In light-adapted MerMAID1, the $C_{14}$−$C_{15}$ stretching vibration is tentatively assigned to 1178 $cm^{-1}$. This band is also detected in the dark-adapted sample (Fig. 18B), further indicating photoproduct-formation upon probing with $\lambda_e = 488$ nm.

The assignment of C−C stretching bands in RR spectra of the dark- and light-adapted MerMAID1 suggests the transition of the retinal chromophore from the all-*trans* isomer in the dark to the 13-*cis* isomer upon illumination.

The effect of H/D exchange on the $C_{14}$−$C_{15}$ stretching vibration can be used as an indicator to determine the configuration of $C_{15}$=N (S. O. Smith *et al.*, 1987b; Fodor *et al.*, 1989). In dark-adapted MerMAID1, the $C_{14}$−$C_{15}$ stretching mode at 1199 $cm^{-1}$ is not affected by deuteration (Fig. 18B). For the 13-*cis* chromophore of *Hs*BR, a $C_{15}$=N-*syn* configuration was suggested based on a 41 $cm^{-1}$ upshift of the $C_{14}$−$C_{15}$ stretching mode (S. O. Smith *et al.*, 1987a). In RR spectra of MerMAID1, the C−C stretching region of the light-adapted sample at pH and pD 8 are very similar, indicating that no shift of the $C_{14}$−$C_{15}$ stretching mode occurs (Fig. S8B). While it cannot be entirely excluded that other vibration modes mask those upshifts, the apparent absence of band shifts indicates that $C_{15}$=N populates an *anti*-configuration for both the all-*trans* and the 13-*cis* chromophore.

In the RR spectra of dark-adapted MerMAID1, a distinct band is detected at 1238 $cm^{-1}$. Similar bands were previously detected in dark-adapted *Gt*ACR1, *Ca*ChR1, and *Cr*ChR2, but not in dark-adapted *Hs*BR (S. O. Smith *et al.*, 1987b; Nack *et al.*, 2009; A. Yi *et al.*, 2016). In *Hs*BR, a comparable band was detected for the 13-*cis* chromophore, sensitive to changes of $C_{12}$−$C_{13}$ and $C_{14}$−$C_{15}$ (S. O. Smith *et al.*, 1987a). In MerMAID1, this vibration is accompanied by a band at 1229 $cm^{-1}$, similar to *Cr*ChR2 (Nack *et al.*, 2009). A minor downshift to 1226 $cm^{-1}$ is observed upon probing with $\lambda_e = 514$ nm. Upon deuteration, the bands at frequencies of 1229 $cm^{-1}$ and 1238 $cm^{-1}$ merge and form a single band at 1232 $cm^{-1}$ (Fig. 18B), suggesting that the band at 1229 $cm^{-1}$ is a secondary mode to 1238 $cm^{-1}$. Upon illumination, both vibration modes shift up to 1241 $cm^{-1}$ and 1247 $cm^{-1}$.

Other distinct differences are detected in the retinal fingerprint region of light-adapted MerMAID1. A C−C stretching vibration, detected at 1137 $cm^{-1}$ in the dark-adapted sample, disappears upon illumination. Additionally, a C−H rocking vibration at 1281 $cm^{-1}$ appears, potentially representing an incomplete upshift of the band at 1273 $cm^{-1}$ (Fig. 18B).

### The chromophore remains in the all-*trans* conformation in alkaline conditions

Next, MerMAID1 was probed with $\lambda_e = 413$ nm and 488 nm in alkaline conditions. The resulting RR spectra are compared to dark- and light-adapted MerMAID1 at pH 8 (Fig. 19).

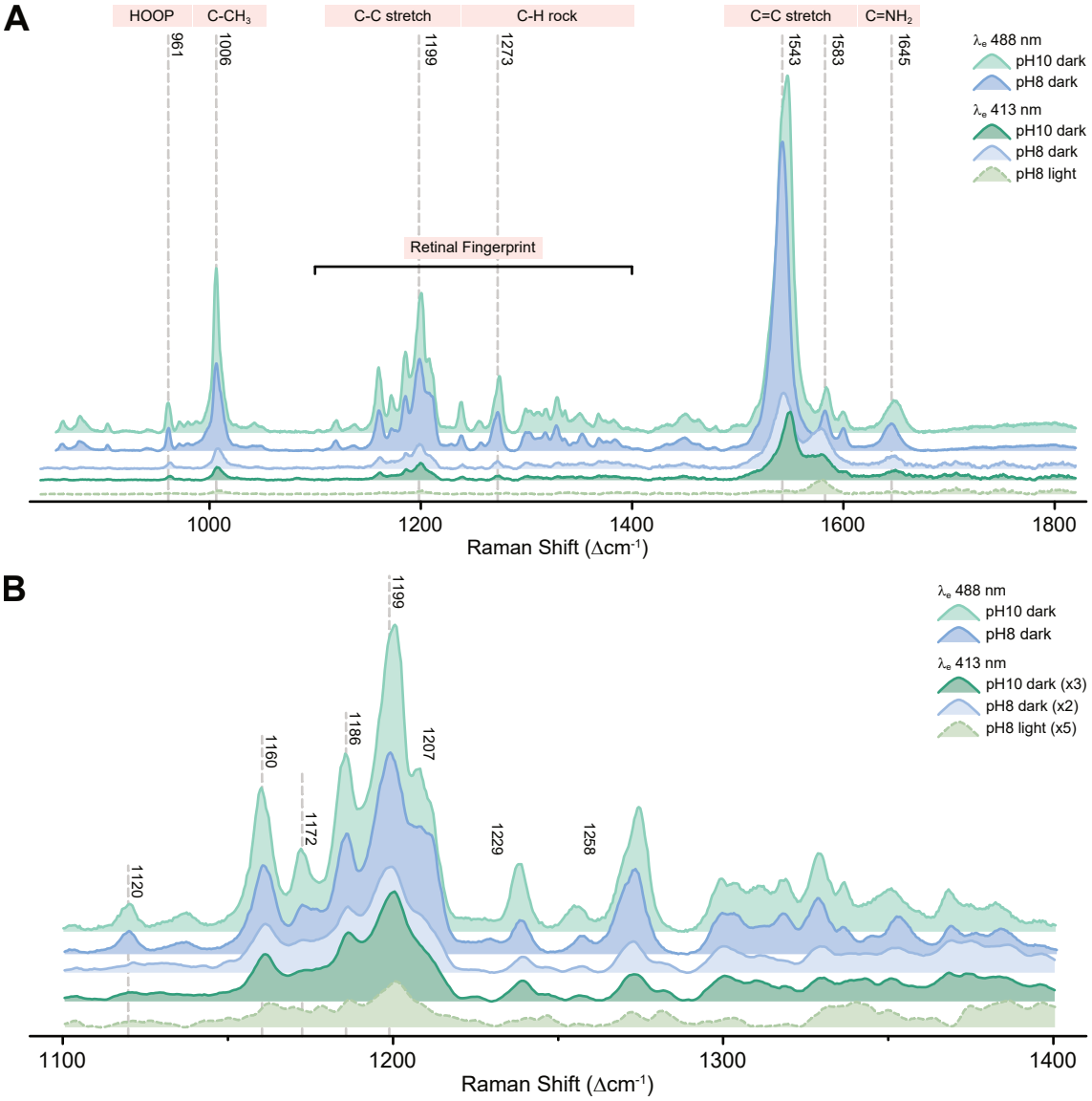


**Figure 19.: pH-dependence of the chromophore of dark-adapted MerMAID1. A,** Resonance Raman (RR) spectra of dark- and light-adapted MerMAID1 at pH 8 or 10 probed with $\lambda_e = 488$ nm or 413 nm. Regions of the RR spectrum indicating vibrations of specific chemical connections are labeled accordingly. **B,** Enlarged view of the retinal fingerprint region of RR spectra shown in A. RR spectra recorded with $\lambda_e = 413$ nm are scaled up as indicated to improve visibility. All RR spectra were accumulated for 30 min at 80 K with a laser power of 1 mW. Labeled frequencies refer to the RR spectrum of dark-adapted MerMAID1 at pH 8. The data was collected and prepared by Dr. Anke Keidel. Adapted from Oppermann *et al.* (2019).

The appearance of a C=$NH_2$ stretching vibration at 1648 $cm^{-1}$ indicates that a fraction of the RSB is still protonated, also seen in UV/vis absorption spectra at pH 10, where the peak of the absorption of the $RSBH^+$ (500 nm) is still approximately 50 % of the amplitude compared to pH 7.8 (Fig. 16C). Similar to RR spectra recorded at pH 8, also at pH 10, three different C=C stretching vibrations at 1547 $cm^{-1}$, 1584 $cm^{-1}$, and 1599 $cm^{-1}$ are detected (Fig. 19A). However, the prominent ethylenic vibration at 1547 $cm^{-1}$ is broadened due to three vibrations at 1540 $cm^{-1}$, 1542 $cm^{-1}$, and 1547 $cm^{-1}$ overlayed (Fig. 19A).

Upon probing MerMAID1 at pH 10 with $\lambda_e = 413$ nm, the prominent ethylenic vibration does not appear to be broadened.

The vibrations of the retinal methyl groups at 1006 $cm^{-1}$ are increased in intensity (compared to the intensity of the vibration at 1199 $cm^{-1}$) at pH 10 but not changed in frequency compared to pH 8. Furthermore, four instead of three distinct HOOP vibrations are detected at frequencies of 961 $cm^{-1}$, 971 $cm^{-1}$, 980 $cm^{-1}$, and 987 $cm^{-1}$ in the sample at pH 10. In RR spectra recorded with $\lambda_e = 413$ nm, only the most prominent HOOP vibration at 961 $cm^{-1}$ is detected at pH 8 and pH 10.

The retinal fingerprint region in RR spectra of dark-adapted MerMAID1 at pH 8 and 10 is very similar when probed with 413 nm and 488 nm but differs from the RR spectra of light-adapted MerMAID1 at pH 8 (Fig. 19B). Upon alkalization, the C−C stretching vibration of the $C_{14}$−$C_{15}$ upshifts slightly from 1199 $cm^{-1}$ to 1201 $cm^{-1}$ and is similarly broadened as the C=C stretching vibration at 1547 $cm^{-1}$ (Fig. 19A). As at pH 8, this vibration mode is unaffected by deuteration (Fig. S8B), indicating an *anti*-configuration (S. O. Smith *et al.*, 1987a). The vibration of $C_{12}$−$C_{13}$ broadens in shape and downshifts slightly from 1258 $cm^{-1}$ to 1255 $cm^{-1}$ (Fig. 19B). The vibrations of the other C−C stretching vibrations with frequencies of 1120 $cm^{-1}$ ($C_6$−$C_7$), 1210 $cm^{-1}$ ($C_8$−$C_9$), and 1160/1172 $cm^{-1}$ ($C_{10}$−$C_{11}$) are unaffected by changes in the pH. The vibration with a frequency of 1229 $cm^{-1}$, which previously was affected by deuteration and $\lambda_e$, is not detected at pH 10 (Fig. 19B).

These results indicate that upon alkalization, the chromophore remains in the all-*trans* conformation and that $C_{15}$=N appears to exclusively populate an *anti*-configuration (Fig. 3B) independent of illumination and pH.

### MerMAIDs have a single photocycle

A vibrational spectroscopic method, complementary to RR spectroscopy, is necessary to elucidate molecular processes occurring in the protein backbone upon illumination. FTIR spectroscopy has been established and used to analyze microbial rhodopsins in great detail (Ritter *et al.*, 2008; Lórenz-Fonfría *et al.*, 2013; Kuhne *et al.*, 2019). In FTIR spectroscopy, an FTIR absorption spectrum is generated from an interferogram of the detected light in relation to the position of a moving mirror using Fourier transformation (B. C. Smith, 2011). To investigate the molecular processes in MerMAID1, FTIR was performed in rapid-scan mode at pH or pD 8 and a temperature of 273 K. The sample was excited either by continuous illumination with green LEDs or by single-turnover illumination using a laser.

The resulting spectra were kinetically decomposed, revealing two spectral components upon single-turnover and continuous excitation (Fig. 20A). The fast component resembles the conducting state, and the slow component resembles the desensitized state, decaying mono-exponentially to the initial dark state with a kinetic of 3.9 s upon single-turnover excitation and 7.5 s upon continuous illumination (Fig. 20B). The decay of the desensitized

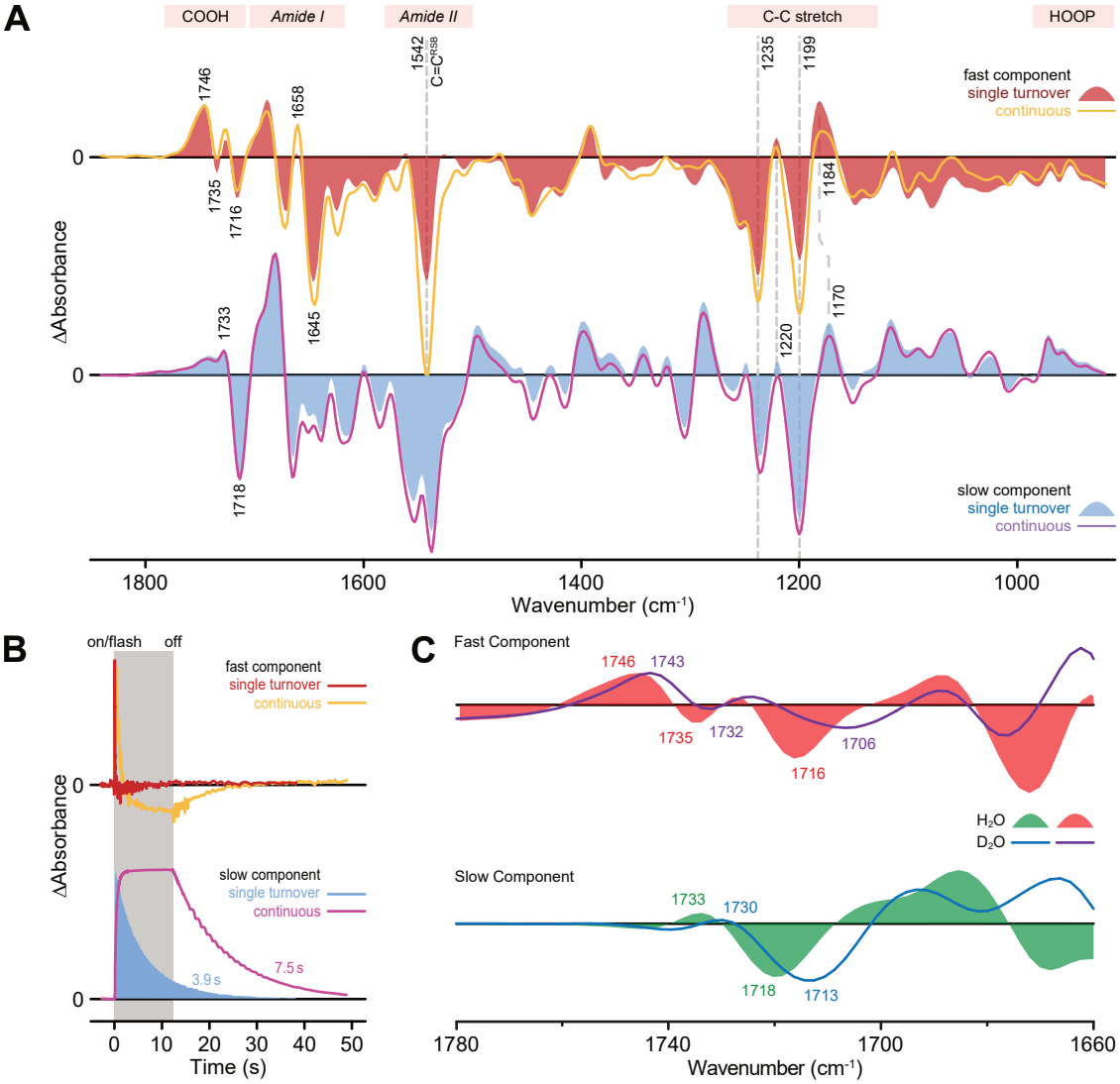


**Figure 20.: Protein backbone changes upon illumination of MerMAID1. A,** Fourier-transform infrared (FTIR) spectroscopy in single turnover and continuous excitation conditions. Two spectral components were obtained by global fit analysis for both conditions. Regions indicating absorption changes of certain protein elements are indicated above. Bands discussed in the text are labeled. **B,** Kinetics of the two spectral components in single turnover and continuous excitation conditions. **C,** Enlarged view of the COOH region of FTIR spectra with protonated and deuterated MerMAID1. Spectra were collected at 273 K. The data sets were collected and analyzed by Paul Fischer. Adapted from Oppermann *et al.* (2019).

state in single-turnover conditions is approximately 2-fold decelerated compared to transient UV/vis absorption spectra (Fig. 17B, C), most likely due to the temperature difference between the two sets of experiments. The light-minus-dark FTIR difference absorption spectra are very similar between the applied illumination protocols (Fig. 20A), indicating a single photocycle.

In both components, the fast and the slow, two prominent negative bands at 1199 $cm^{-1}$ and 1235 $cm^{-1}$ in the C−C stretching region are apparent, indicating depletion of the retinal all-*trans* isomer. The accompanying positive bands at 1184 $cm^{-1}$ and 1220 $cm^{-1}$ on the other hand show photoproduct formation. The band at 1184 $cm^{-1}$ has previously been

associated with 13-*cis* formation (Ames and Mathies, 1990; Braiman *et al.*, 1991). In the slow component, this vibration mode shifts to 1170 $cm^{-1}$, potentially indicating a change in the chromophore geometry. The band at 1220 $cm^{-1}$ has been observed before in *Hs*BR-T90A at pH ≤7 (Perálvarez-Marín *et al.*, 2004) but also in *Cr*ChR2-E123T (Lórenz-Fonfría *et al.*, 2015) as well as the *Cr*ChR2 wildtype (Lórenz-Fonfría *et al.*, 2013; Kuhne *et al.*, 2019). However, an exact assignment of this band is not possible.

Surprisingly, the bands in the amide I and amide II regions are of similar size as the bands mentioned above in the C−C stretching region, indicating small structural changes of the protein backbone, unusual compared to FTIR spectra of CCRs (N. Krause *et al.*, 2013; Kuhne *et al.*, 2019) and more similar to ion pumps (Gerwert *et al.*, 1989; Skopintsev *et al.*, 2020). Nevertheless, it should be noted that in FTIR spectra of *Gt*ACR1 peaks in the amide I and amide II regions are similarly small (A. S. Yi *et al.*, 2017; Kim *et al.*, 2018). This may be a feature typical for ACRs with only a single constriction site in the conduction pathway (Kim *et al.*, 2018; H. Li *et al.*, 2019), resulting in less molecular changes necessary to open the pathway. The amide II region is dominated by a negative band at 1542 $cm^{-1}$, associated with the C=C stretching mode of the retinal chromophore (Neumann-Verhoefen *et al.*, 2013) and correlates well with previously described RR spectra (Fig. 18A and 19A). Furthermore, in the amide I region of the fast component, a negative band at 1645 $cm^{-1}$ and a positive band at 1658 $cm^{-1}$ appear. However, in the slow component, these bands disappear and might resemble small structural changes necessary for conduction but reversed in the desensitized state.

In the fast component's carboxyl region, two negative bands appear at 1716 $cm^{-1}$ and 1735 $cm^{-1}$, and a positive band at 1746 $cm^{-1}$, which transition into a pronounced negative band at 1718 $cm^{-1}$ and a positive band at 1733 $cm^{-1}$ in the slow component. Upon H/D exchange (Fig. 20C), the bands in the fast component downshift to 1706 $cm^{-1}$, 1732 $cm^{-1}$, and 1743 $cm^{-1}$, respectively, while the bands in the slow component downshift to 1713 $cm^{-1}$ and 1730 $cm^{-1}$, respectively. These bands may therefore be the result of proton transfer processes or changes of a hydrogen-bonding network, similar to *Gt*ACR1 (A. S. Yi *et al.*, 2017). The early appearing negative 1735 $cm^{-1}$ band and the positive 1746 $cm^{-1}$ band have been similarly observed before in FTIR spectra of *Cr*ChR2 (Ritter *et al.*, 2008; Neumann-Verhoefen *et al.*, 2013) and *Hs*BR (Braiman *et al.*, 1988) and were assigned to hydrogen-bonding changes of an aspartate residue in TM4. The band at 1716 $cm^{-1}$, on the other hand, is associated with the deprotonation of a carboxylic residue (Shi *et al.*, 2006), possibly MerMAID1-Glu44, the homolog to *Cr*ChR2-Glu90, following reports for *Gt*ACR1 (A. S. Yi *et al.*, 2017).

### Photoactivity of late photocycle intermediates

Previously, it was shown that photon absorption by photocycle intermediates accelerates the back reaction to the initial dark state in ChRs such as *Vc*ChR1 and ReaChR (Ernst

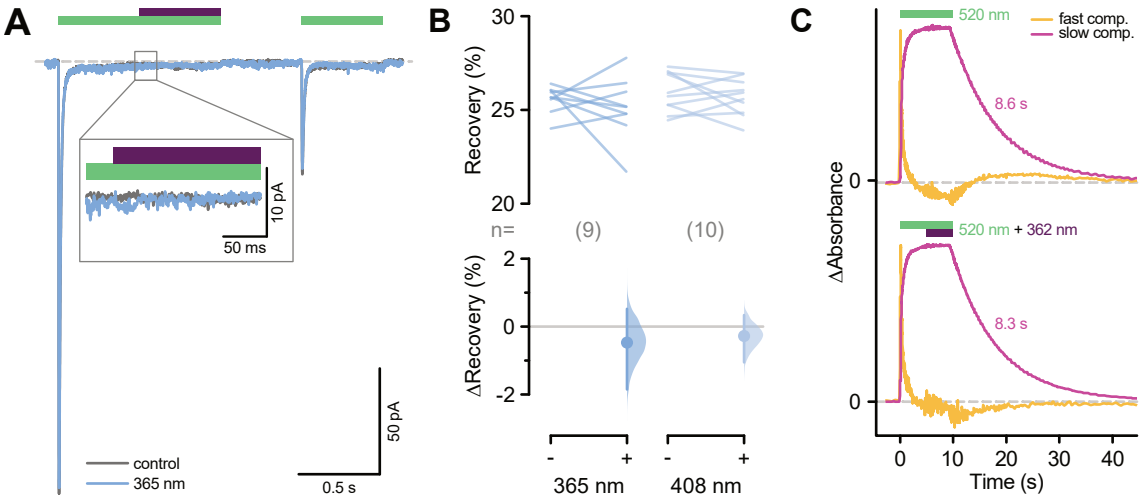


**Figure 21.: Photoactivity of the desensitized state in MerMAID1. A,** Representative photocurrent traces of MerMAID1 with additional UV-light illumination of the desensitized state. Photocurrents were recorded at −60 mV with a 500 nm-light pulse applied for 1 s. After 0.5 s, an additional light pulse of 365 nm and 0.5 s duration was applied. In control experiments, no additional light pulse was applied. The transient photocurrent recovery after 0.5 s darkness was examined by applying 500 nm light for 0.5 s. **B,** Cumming estimation plots for the paired mean difference of comparisons of the transient photocurrent recovery after additional illumination of the stationary photocurrents with 365 nm or 408 nm. The raw data is plotted on the upper axis, where a line connects each pair of observations. The difference of the comparison to the control is plotted as bootstrap sampling distribution on the right axis, with the mean difference shown as dot and the 95 % confidence interval indicated as error bars. **C,** Kinetics of the fast and slow FTIR spectral components. As a control, samples were continuously illuminated for 10 s using 520 nm-light (top). To probe the desensitized state's reactivity, additionally, 362 nm-light was applied for 5 s (bottom). The FTIR data was collected and analyzed by Paul Fischer. Note: Kinetics in panel C determined by J. Oppermann. Adapted from Oppermann *et al.* (2019).

*et al.*, 2008; B. S. Krause *et al.*, 2017). Therefore, the photoactivity of the desensitized state was investigated using whole-cell patch-clamp electrophysiology and FTIR spectroscopy (Fig. 21).

The photocurrents were recorded in standard conditions at $E_{\text{hold}} = -60$ mV and elicited by applying 500 nm-light for 1 s (Fig. 21A). After a 500 ms dark period, the recovered transient photocurrent was probed by applying a second 500 ms light pulse. Photoconversion of desensitized MerMAID1 to the dark state was tested by additional illumination with 365 nm or 408 nm light for 500 ms during the first 500 nm light pulse (Fig. 16A). Without additional application of 365 nm- or 408 nm-light, $25.9 \pm 0.2$ % and $26.0 \pm 0.3$ % of the transient photocurrents recovered, respectively (Fig. 21B). Upon application of 365 nm-light, the transient photocurrent recovery is $25.1 \pm 0.6$ %, while the application of 408 nm-light results in transient photocurrent recovery of $25.7 \pm 0.3$ %. Therefore, neither additional illumination with 365 nm nor with 408 nm significantly affects $I_p$ recovery.

The electrophysiological experiments were supplemented with FTIR spectroscopic measurements using a comparable illumination regime, and the kinetics of the fast and slow spectral component are compared (Fig. 21C). MerMAID1 was continuously illu-

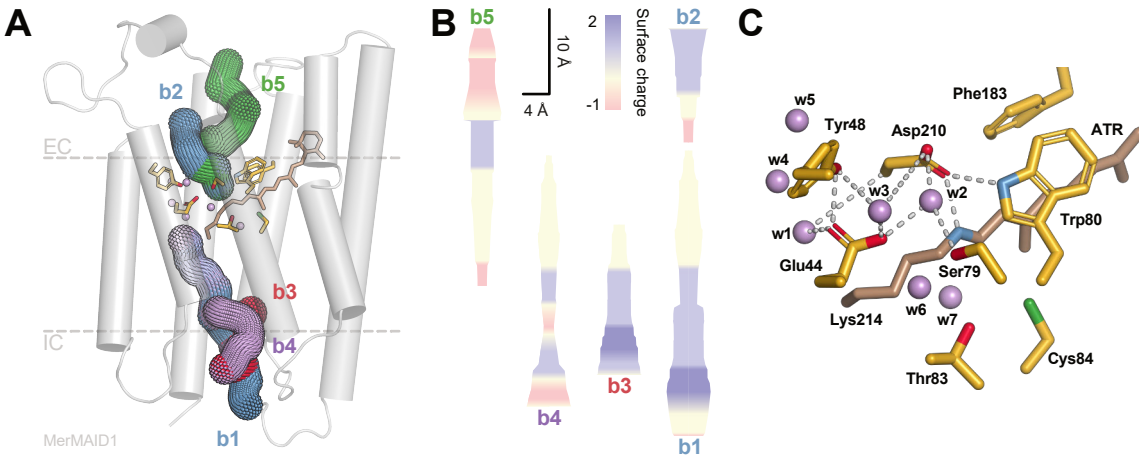


**Figure 22.: Homology model of MerMAID1. A,** Homology model based on the iC++ crystal structure (PDB: 6CSN; Kato *et al.*, 2018). The all-*trans* retinal chromophore (brown) and residues of the Schiff base region (yellow) are depicted as sticks. Water molecules are purple spheres. Cavities (b1 - b5), determined with MOLEonline (Pravda *et al.*, 2018), potentially acting as ion conduction pathways are shown as meshes. **B,** Electrostatic surface potential maps of predicted tunnels (b1 - b5) in the MerMAID1 homology model. **C,** Expanded view of the Schiff base region in the MerMAID1 homology model. All-*trans* retinal (ATR) and residues are shown as stick models in brown and yellow, respectively. Waters are shown as spheres. Possible interactions are indicated as gray, dashed lines. The MD calculations were performed by Enrico Peter and calculations of potential conduction pathways by Dr. Jonas Wietek. Adapted from Oppermann *et al.*, 2019.

minated for 10 s with 520 nm-light (Fig. 21C top). The photoactivity of late photocycle intermediates was investigated by additionally illuminating the sample for 5 s with 362 nm-light (Fig. 21C bottom). In control experiments, the slow spectral component recovers to the initial dark state with a kinetic of 8.6 s. Upon UV-light application, the dark state recovery accelerates to 8.3 s (Fig. 21C). While the extent of the acceleration is only mild, it may indicate low photoactivity of the late photointermediate that accumulates during the MerMAID photocycle (Fig. 17B). Nonetheless, neither the photocurrents nor the kinetics of the spectral components of FTIR difference spectra show any changes at the onset of the illumination with UV-light (Fig. 21A, C).

### 2.2.3. Homology model and residue substitutions

#### A single constriction site in the MerMAID anion-conduction pathway

Sequence alignments (Fig. 11B) are commonly used to identify homologous residues and possible candidates for single- or multi-residue substitutions. The selection of residues can be improved using homology models of the protein 3D protein structure, as they provide a better picture of the possible orientation of internal residues.

A homology model of MerMAID1 was constructed using the SWISS model server (Waterhouse *et al.*, 2018). The crystal structure of iC++ (PDB: 6CSN; Kato *et al.*, 2018) was chosen as a template because the best global model quality (GMQE) was predicted for this structure. After incorporating the all-*trans*-retinal chromophore, the homology model

was subjected to 100 ns of molecular dynamics (MD) simulations to allow relaxation of the side chains (Fig. 22A). For MD simulations, the homology model was embedded into a phospholipid bilayer surrounded by water.

Three water molecules entered the Schiff base region formed by Glu44, Tyr48, Ser79, Trp80, Asp210, and Lys214 (Fig. 22C). Furthermore, the homology model of MerMAID1 shows a highly conserved cysteine, Cys84, oriented towards the $RSBH^+$ and Phe183 oriented towards Asp210 (Fig. 22C).

Based on the homology model, potential ion conduction pathways were calculated (Fig. 22A) using MOLEonline (Pravda *et al.*, 2018), which calculates tunnels, cavities or pockets as well as their respective electrostatic surface potentials (Fig. 22B), allowing the consideration of the potential ion conduction pathways. In total, five putative tunnels were identified by MOLEonline that approach the Schiff base region in the center of the protein from the intra- or extracellular surface (b1 - b5 in Fig. 22A, B). For cavity b5, an electronegative surface potential was determined, excluding it as a potential anion conduction pathway because an electronegative surface potential would prohibit anions from entering (Rappleye and Berndt, 2019). Cavity b2, on the other hand, shows an electropositive surface potential, beneficial for the conduction of anions, and is, therefore, more likely to represent the extracellular half pore. In the intracellular half of the protomer, three cavities were identified. Cavity b4 is excluded as well because of its electronegative surface potential at the entry point. While the electrostatic surface potential of cavity b3 is suitable for anion-conduction, it must be excluded as it does not reach the Schiff base region. The vacity b1 is most plausible as ion conduction pathway from the intracellular surface to the Schiff base region. The positive electrostatic surface potential excludes cations from entering the pore, and the cavity is reaching the Schiff base region. According to these predictions and in agreement with solved crystal structures of *Gt*ACR1 (Kim *et al.*, 2018; H. Li *et al.*, 2019), the Schiff base region is the only constriction site prohibiting ion passage in MerMAID1.

**A conserved cysteine is critical for the near-complete photocurrent desensitization**

Sequence alignments showed that only Ci2 is conserved in the MerMAIDs (Asp210 in MerMAID1; Fig. 11B). Only one other carboxylic residue, Glu44, is found close to the Schiff base in MerMAID1, potentially acting as a counterion to the $RSBH^+$. In the homology model, Glu44 interacts with Tyr48 and via two water molecules (w1 and w2) with Ser79 and Asp210. Phe183 is oriented towards Asp210 (Fig. 22C).

The effect of single- or double-residue substitutions in MerMAID1 was assessed by whole-cell patch-clamp electrophysiology in HEK293 cells. The spectral sensitivity, transient photocurrent amplitudes, the extent of the photocurrent desensitization, the apparent kinetics of the desensitization, and the kinetics of the transient photocurrent recovery were analyzed (Fig. 23B to F).

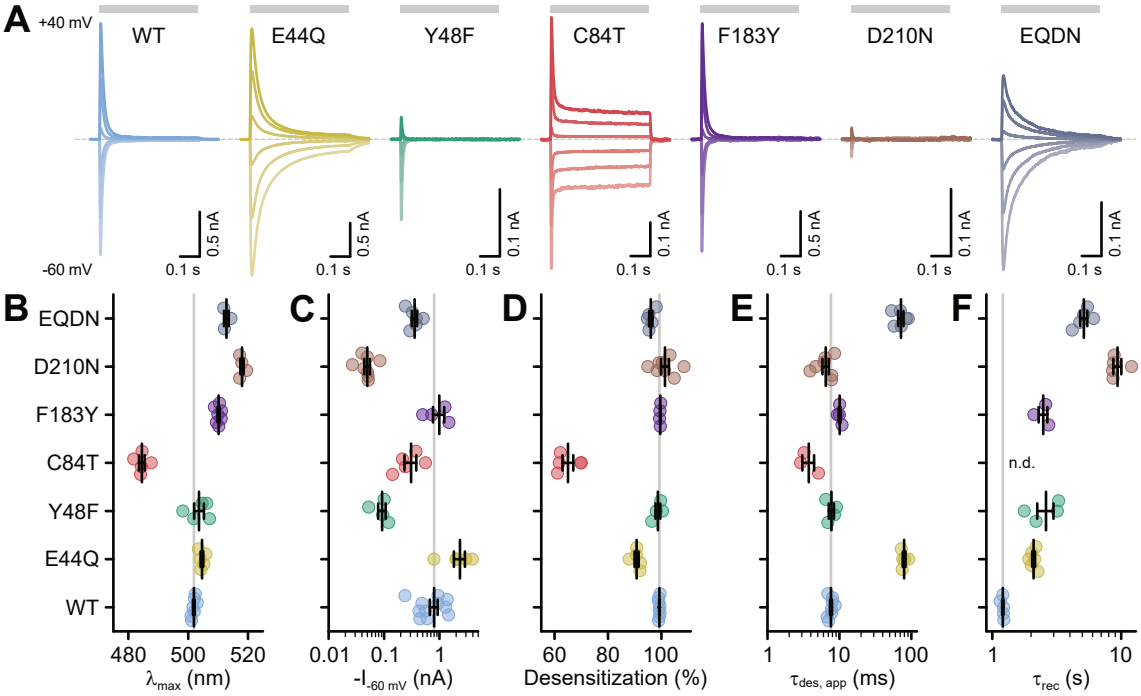


**Figure 23.: Effects of single- and double-residue substitutions in MerMAID1. A,** Representative photocurrent traces of MerMAID1 wildtype (WT) and mutants recorded at holding potentials from −60 mV to 40 mV in steps of 20 mV elicited by illumination with 500 nm light (470 nm for MerMAID1-C84T) indicated by a gray bar. **B-F,** Spectral sensitivity ($\lambda_{max}$, **B**), transient photocurrent amplitudes at −60 mV ($I_{-60\,mV}$) with 120 mM $[Cl^-]_i$ and 150 mM $[Cl^-]_e$ (**C**), extent of the desensitization (**D**), apparent kinetics of the desensitization ($\tau_{des,\,app}$) (**E**), and kinetics of the transient photocurrent recovery ($\tau_{rec}$) (**F**) of MerMAID1 WT and mutants shown in A. Circles represent single-measurement data points. Mean values ± SEM are indicated as black lines. See figure S9 for estimation statistics. Data for E44Q, D210N, and EQDN were acquired and analyzed by Bernhard Liepe. Adapted from Oppermann *et al.*, 2019.

Substitution of Glu44 with glutamine (E44Q) that would neutralize its charge if present as a carboxylate anion strongly impacts the photocurrent kinetics (Fig. 23A). $\tau_{des,\,app}$ is decelerated approximately 10-fold at −60 mV to 79.3 ± 3.5 ms, compared to 7.6 ± 0.2 ms in the wildtype (Fig. 23E), resulting in reduced $I_p$ desensitization of 90.7 ± 0.8 % during a 500 ms light pulse (Fig. 23D). $I_{-60\,mV}$ is 2- to 3-fold increased, reaching on average 2.3 ± 0.5 nA (Fig. 23C). These results contrast reports for *Gt*ACR1 where substitutions of the homolog Glu68 strongly decreased photocurrent amplitudes (Kim *et al.*, 2018). $\tau_{rec}$ is decelerated to 2.1 ± 0.1 s, 2-fold slower than the wildtype (Fig. 23F), while the wavelength sensitivity of MerMAID1 is only mildly affected by the substitution of Glu44, shifting $\lambda_{max}$ by 3 nm bathochromic to 504.6 ± 0.4 nm (Fig. 23B), similar to *Ps*ACR1 (Hontani *et al.*, 2017) and suggesting that Glu44 is protonated in the wildtype, as reported for *Gt*ACR2 (Kojima *et al.*, 2018).

Neutralization of Asp210 by substitution with asparagine (D210N) strongly affects $I_{-60\,mV}$, decreasing them to 49.9 ± 5.8 pA (Fig. 23C). However, the desensitization remains nearly complete (Fig. 23A, D). The transient photocurrents desensitize with an apparent

kinetic of 6.5 ± 0.7 ms (Fig. 23E), while $\tau_{rec}$ is strongly decelerated to 9.4 ± 0.7 s (Fig. 23F). Neutralization of Asp210 causes a substantial bathochromic shift of $\lambda_{max}$ by 16 nm to 518.0 ± 0.6 nm (Fig. 23B), indicating that it forms the primary counterion. These results are in contrast to cryptophyte ACRs, where neutralization of the homolog aspartate residue resulted in hypsochromic shifts of $\lambda_{max}$, indicating that it is protonated in the dark state and not directly acting as counterion (A. Yi *et al.*, 2016; Hontani *et al.*, 2017; Kim *et al.*, 2018).

Combining the D210N and E44Q substitution in EQDN rescues the ion channel activity, with $I_{-60\,mV}$ reaching 355.3 ± 37.6 pA (Fig. 23C). During a 500 ms light pulse, the transient photocurrents desensitize with an apparent kinetic of 71.6 ± 6.0 ms, similar to E44Q (Fig. 23E). The transient photocurrent desensitization is only slightly reduced compared to the wildtype and extends to 96.0 ± 0.6 % (Fig. 23D). The double mutant recovers from the desensitized state with $\tau_{rec}$ 5.1 ± 0.3 s, markedly decelerated compared to the wildtype though not as strongly affected as in the D210N single substitution (Fig. 23F). Similar to D210N, $\lambda_{max}$ is shifted bathochromic by 11 nm to 512.8 ± 0.8 nm (Fig. 23B).

The substitution of Tyr48, potentially interacting with Glu44, by a phenylalanine residue (Y48F), strongly decreases $I_{-60\,mV}$ to 92.4 ± 14.2 pA (Fig. 23C). Similar to E44Q, the spectral sensitivity is only mildly affected, shifting 2 nm bathochromic to 503.6 ± 1.6 nm (Fig. 23B). As in the wildtype, the transient photocurrents are strongly desensitizing by 98.7 ± 0.9 % (Fig. 23D) with an apparent kinetic of 7.7 ± 0.6 ms (Fig. 23E), but $\tau_{rec}$ is decelerated to 2.6 ± 0.4 s (Fig. 23F). Therefore, Tyr48 may participate in the reprotonation of the RSB.

Phe183 is highly conserved as either a phenylalanine or tyrosine residue in the MerMAIDs and other microbial rhodopsins (Fig. S2). Therefore, Phe183 was substituted with a tyrosine residue (F183Y). The transient photocurrent desensitization and amplitudes are comparable to the wildtype with 99.6 ± 0.1 % and 1.0 ± 0.2 nA, respectively (Fig. 23C, D), but $\tau_{des,\,app}$ is with 10.1 ± 0.3 ms slightly decelerated (Fig. 23E). The transient photocurrents of F183Y recover with 2.5 ± 0.2 s 2-fold slower than in the wildtype but similar to E44Q and Y48F (Fig. 23F). The spectral sensitivity upon introducing a tyrosine residue is similarly affected as in EQDN, shifting bathochromic by 8 nm to 510.2 ± 0.3 nm, suggesting an interaction with the RSB, possibly via Asp210.

As mentioned before, the homology model of MerMAID1 suggests that Cys84 in MerMAID1 is directed towards the $RSBH^+$ (Fig. 22C). Substitution of the homolog cysteine in *Cr*ChR2 by alanine, serine, or threonine strongly affects photocurrent decay kinetics after illumination, extending the time frame of ion conduction from milliseconds to several seconds (Berndt *et al.*, 2009; Bamann *et al.*, 2010). The substitution of Cys84 in MerMAID1 with threonine (C84T) shifts $\lambda_{max}$ hypsochromic by 17 nm to 484.5 ± 0.9 nm (Fig. 23B) and decreases $I_{-60\,mV}$ to 0.3 ± 0.1 nA (Fig. 23C). The transient photocurrents decay mono-exponentially instead of bi-exponentially with a $\tau_{des}$ of 3.7 ± 0.7 ms (Fig. 23E), strongly accelerated compared to the wildtype. The most notable

effect of the Cys84-substitution is a substantial reduction of the transient photocurrent desensitization to $65.0 \pm 2.0\,\%$ (Fig. 23D). $\tau_{rec}$ was longer than 200 s and could not be determined with the applied acquisition protocol. The substitution of Cys84 with serine in MerMAID1 affects the transient photocurrent desensitization similarly as substitution with threonine. However, the ion channel does not close completely. In MerMAID6, the transient photocurrent desensitization is considerably reduced upon substitution of Cys84 with a threonine residue as well (Fig. S10). These results suggest the highly conserved cysteine as a crucial factor for the strong desensitization in the MerMAIDs. Similar results were reported for cryptophyte CCRs with an almost complete transient photocurrent desensitization (Sineshchekov *et al.*, 2020b).

## 2.3. Viral and prasinophyte ChRs

Screening the viral *Tara* Oceans metagenome and transcriptomes of prasinophyte algae revealed four sequences that resemble ChRs and form a distinct sub-family (Fig. 11A). The proteins were investigated using whole-cell patch-clamp electrophysiology two days after transiently transfecting ND7/23 cells with the full-length sequences cloned into a vector in-frame with the fluorophore mCherry as an expression marker. The full-length algal proteins expressed well, and photocurrents could be evoked. The sequences originating from the viral metagenome, on the other hand, are cytotoxic when expressed in full-length. More importantly, the evoked photocurrents were noisy and had a small amplitude, hindering a thorough electrophysiological analysis. Therefore, it was first attempted to improve their membrane localization.

### 2.3.1. Improving membrane-targeting of viral ChRs

Confocal images of ND7/23 cells expressing full-length v*Py*ACR21821 (Fig. 24A) and v*Py*ACR2164382 (Fig. S11A) show that most of the protein is retained intracellularly. Previously, enhancing the membrane localization of microbial rhodopsin ion pumps improved their evoked photocurrent amplitudes (Gradinaru *et al.*, 2008; Grimm *et al.*, 2018). These modifications were, therefore, applied to both viral constructs to increase their photocurrent amplitudes.

A chimeric amino-terminus, consisting of parts from the amino-terminal regions of *Cr*ChR1 and *Cr*ChR2 (Rajasethupathy *et al.*, 2015), was added to both proteins. Furthermore, the fluorophore mCherry was replaced with the enhanced yellow fluorescent protein (eYFP) flanked by a membrane-trafficking signal sequence and an endoplasmic reticulum release sequence (Gradinaru *et al.*, 2008, 2010; Grimm *et al.*, 2018). Previously, photocurrents of *Cr*ChR2 were improved by truncation of a C-terminal extension (Nagel *et al.*, 2003). Therefore, the sizable carboxy-terminal domain with homology to response regulator domains of histidine-kinases (Fig. S3) was truncated after TM7.

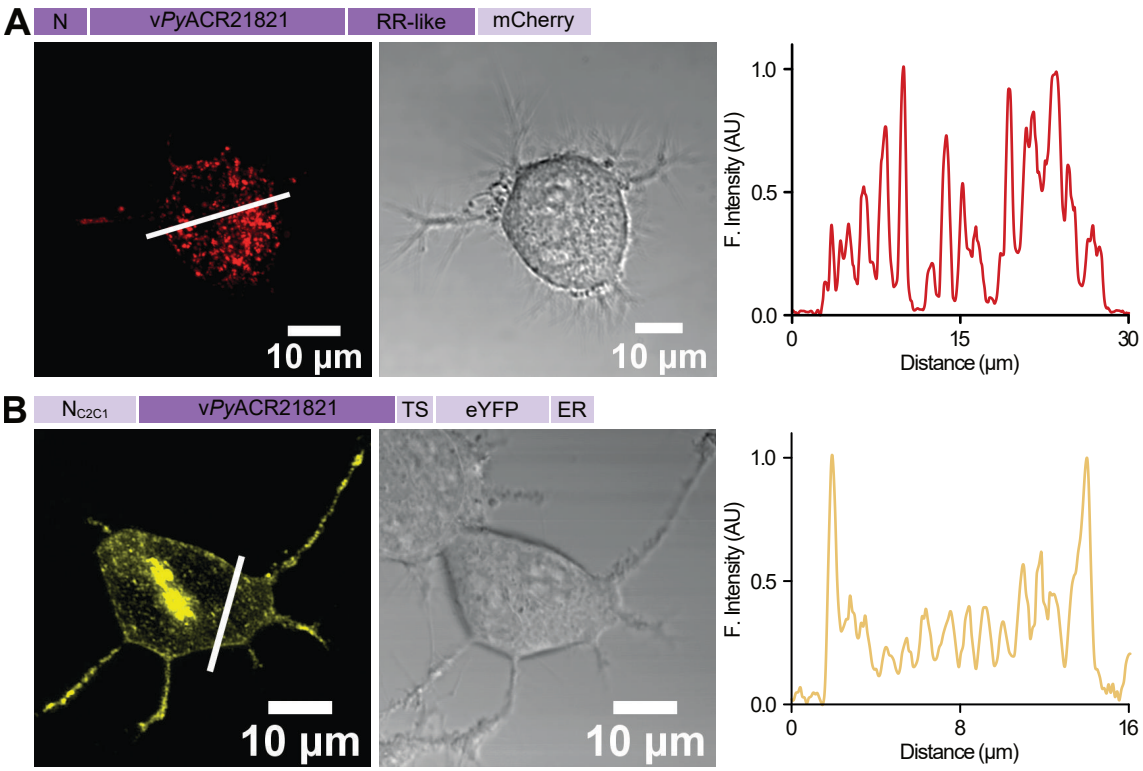


**Figure 24.: Membrane-targeting of a viral channelrhodopsin.** Confocal images of ND7/23 cells expressing full-length (**A**) or membrane-targeted (**B**) v*Py*ACR21821. Fluorescence (left) of mCherry is shown in red and of eYFP in yellow. Fluorescence intensity profiles (right) were measured at the locations indicated by the white line in the fluorescence image. A bright field picture (center) is shown. Measurements were repeated at least three times for each construct. Abbreviations: N, amino terminus; RR-like, Histidine-kinase response regulator-like; TS, membrane-trafficking signal; eYFP, enhanced yellow fluorescent protein; ER, endoplasmic reticulum release signal. Confocal microscopy was performed and analyzed by Rodrigo Gaston Fernandez Lahore. Adapted from Rozenberg *et al.* (2020).

Unfortunately, these modifications did not improve the expression or membrane-localization of v*Py*ACR2164382 (Fig. S11B), which remained cytotoxic. Therefore, only single measurements in standard conditions were acquired, not allowing a reliable analysis beyond its classification as a channelrhodopsin (Fig. S12). Attempts to exchange the external buffer were not successful.

For v*Py*ACR21821, on the other hand, the modifications enhanced the membrane localization (Fig. 24B). Even though the enhanced construct is still cytotoxic, the improvement of its membrane localization considerably increases the elicited photocurrent amplitudes and the stability of the whole-cell patch-clamp measurements.

### 2.3.2. Electrophysiological characterization

#### Spectral sensitivity

In the following, the electrophysiological characterization of v*Py*ACR21821, and the two algal homologs, *Pyme*ACR1 and *Py*2087ACR1, will be described.

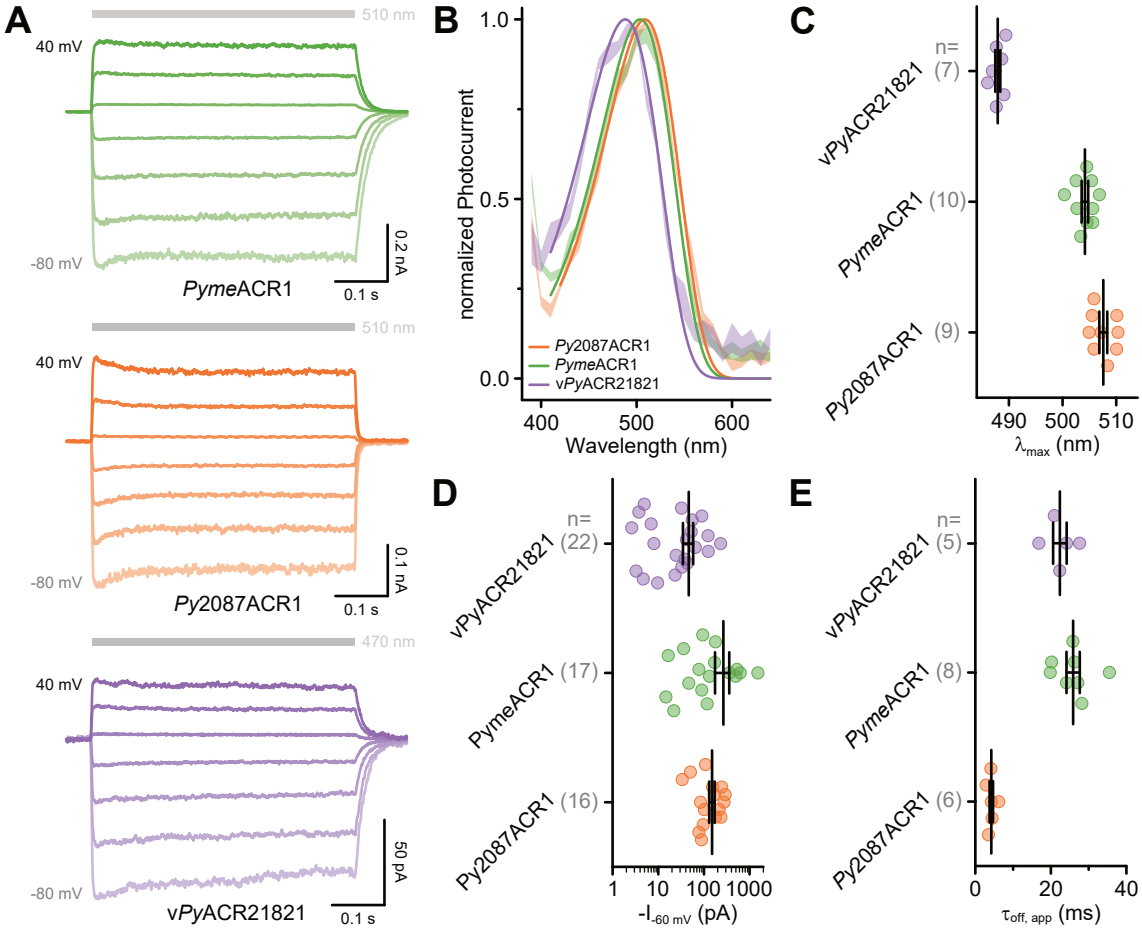


**Figure 25.: Wavelength sensitivity of prasinophyte and viral channelrhodopsins. A,** Representative photocurrent traces of *Pyme*ACR1 (top), *Py*2087ACR1 (center), and v*Py*ACR21821 (bottom). Photocurrents were evoked by 500 ms light pulses of 510 nm or 470 nm, indicated by a gray bar, and recorded at holding potentials between −80 mV to 40 mV in ND7/23 cells with $[Cl^-]_i$ of 120 mM and $[Cl^-]_e$ of 150 mM. **B,** Action spectra acquired by excitation with 10 ms light pulses of low intensity between 390 nm to 680 nm in 10 nm steps. Photocurrent amplitudes were normalized to the maximum amplitude and approximated with a three-parametric Weibull function (solid line) to determine the wavelength of the highest activity ($\lambda_{max}$). The shaded area indicates the mean ± SEM. **C,** $\lambda_{max}$ of the indicated channelrhodopsins. **D,** Stationary photocurrent amplitudes at a holding potential of −60 mV determined by averaging the photocurrent during the final 100 ms of the light pulse. **E,** Apparent kinetics of the bi-exponential photocurrent decay after the end of the 500 ms light pulse. In **C, D,** and **E,** single measurement data points are indicated as circles. Whiskers indicate standard error of the mean (SEM) with the mean indicated as a long line.

Upon illumination with full-intensity light and using high chloride concentration intra- and extracellularly, all three constructs show photocurrents that are, depending on $E_{hold}$, inward- or outward-directed indicating passive ion conduction (Fig. 25A). The photocurrents are weakly desensitizing during continuous illumination, but only at strongly negative or positive holding potentials.

The spectral sensitivity of all three constructs was determined by recording action spectra in the range of 390 nm to 680 nm and their subsequent approximation from 410 nm to 680 nm using a three-parametric Weibull function. The action spectra exhibit clear

peaks with maxima in the blue and green light region, though, interestingly, the action spectra of both the algal and the viral ChRs show increased photocurrents upon illumination with light <410 nm (Fig. 25B). $\lambda_{max}$ of *Pyme*ACR1 and *Py*2087ACR1 is 504.0 ± 0.6 nm and 508.0 ± 0.7 nm, respectively. With 488.0 ± 0.5 nm, v*Py*ACR21821 has a $\lambda_{max}$ shifted hypsochromically compared to its algal homologs (Fig. 25C). For subsequent experiments, an excitation wavelength of 510 nm was chosen for the algal ChRs, while v*Py*ACR21821 was excited with 470 nm-light.

During the final 100 ms of a 500 ms light pulse, the stationary photocurrent amplitudes show a large variance for all tested constructs. At −60 mV, the photocurrent amplitudes (Fig. 25D) reach 50 ± 10 pA (v*Py*ACR21821), 150 ± 20 pA (*Py*2087ACR1), and 380 ± 90 pA (*Pyme*ACR1). However, $I_{-60\,mV}$ of v*Py*ACR21821 and *Pyme*ACR1 show a broader range compared to *Py*2087ACR1.

The photocurrents of the three constructs decay bi-exponentially after the illumination ends. For v*Py*ACR21821 and *Pyme*ACR1, an apparent time constant of the photocurrent decay ($\tau_{off,\,app}$) of 22.4 ± 1.8 ms and 25.9 ± 1.7 ms was determined, respectively. Photocurrent decay of *Py*2087ACR1, on the other hand, is considerably accelerated, yielding a $\tau_{off,\,app}$ of 4.4 ± 0.5 ms (Fig. 25E), similar to ZipACR of *Proteomonas sulcata*, one of the fastest-closing ACRs available so far (Govorunova *et al.*, 2017b).

### Ion selectivity

Phylogenetically, the here described algal and viral ChRs seem closer related to the chlorophyte CCRs (Fig. 11A). However, their primary sequences are more similar to cryptophyte ACRs regarding the counterions and E1-E5 in TM2 (Fig. 11B), which may indicate anion selectivity.

The ion selectivity of the viral and algal ChRs was determined by recording photocurrents at $E_{hold}$ ranging from −80 mV to 40 mV. Between measurements, the external buffer was exchanged to contain varying concentrations of $Cl^-$ and other anions as well as $Na^+$. The intracellular buffer was not exchanged and continuously had a $Cl^-$-concentration of 120 mM and a $Na^+$ concentration of 110 mM (Table 10).

Upon reducing $[Cl^-]_e$ from 150 mM to 10 mM, only negative-amplitude photocurrents remain in all three constructs (Fig. 26A), most likely resembling anion-efflux from the cell. Interestingly, upon $[Cl^-]_e$ reduction, *Pyme*ACR1 photocurrents desensitize at $E_{hold}$ more negative than −60 mV. It can be further noted that the $Cl^-$-outward photocurrent amplitudes of *Pyme*ACR1 increase at low $[Cl^-]_e$, indicating outward-rectification. For *Py*2087ACR1 and v*Py*ACR21821, on the other hand, the photocurrent amplitudes decrease under the same conditions (Fig. 26A, B).

As a measure of ion selectivity, $E_{rev}$ was determined from current-voltage plots (Fig. 26B). The stationary photocurrents were normalized to the photocurrent amplitude at −80 mV with $[Cl^-]_e$ = 150 mM and plotted against $E_{hold}$ (Fig. 26B). The current-voltage relation-

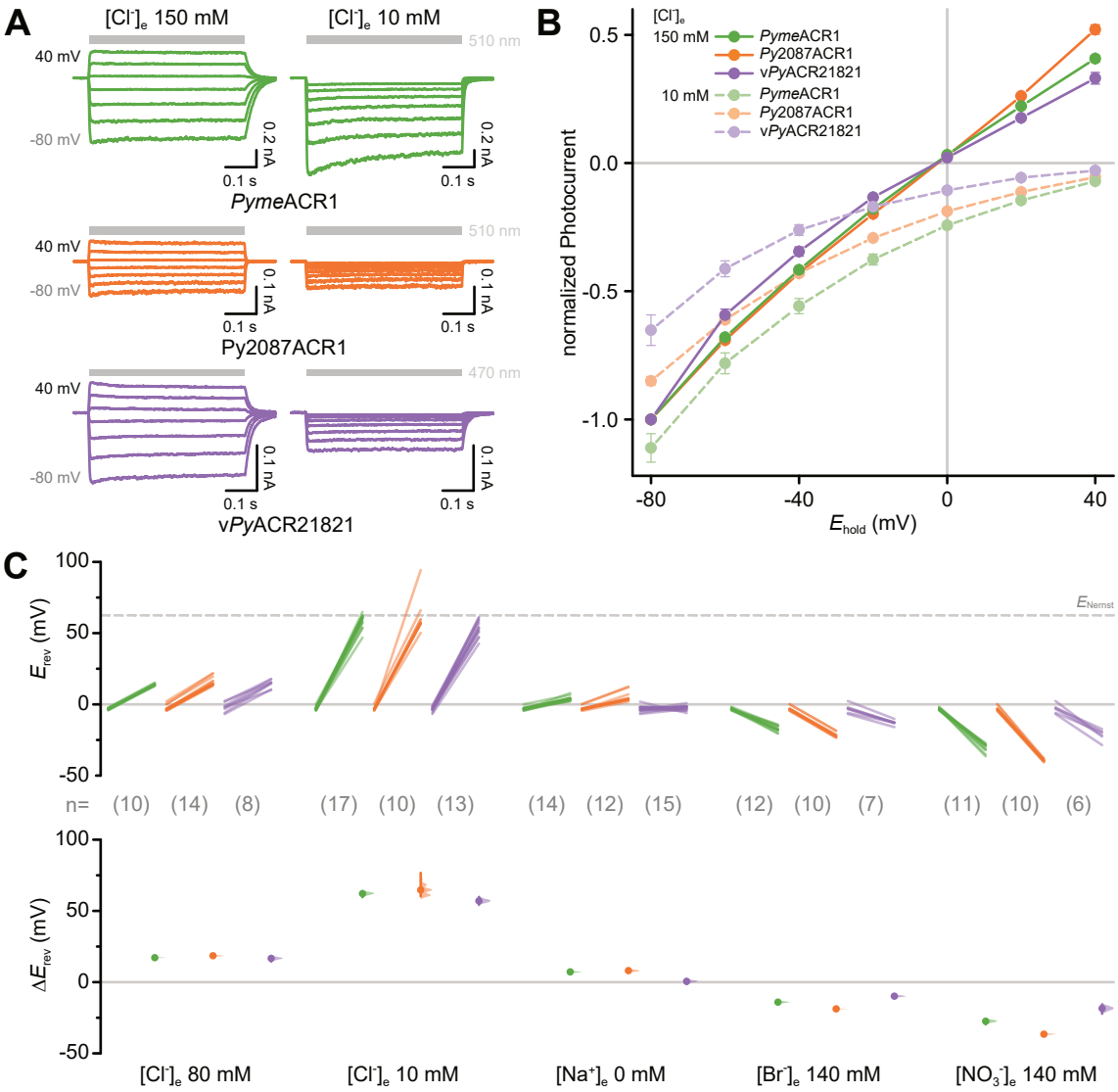


**Figure 26.: Ion selectivity of prasinophyte and viral channelrhodopsins. A,** Representative photocurrent traces of PymeACR1 (top), Py2087ACR1 (center), and vPyACR21821 (bottom). Photocurrents were evoked by 500 ms light pulses of 510 nm or 470 nm, indicated by a gray bar, and recorded at holding potentials ($E_{hold}$) between −80 mV to 40 mV in ND7/23 cells with $[Cl^-]_i$ of 120 mM and $[Cl^-]_e$ of 150 mM or 10 mM. **B,** Current-voltage relationship of stationary photocurrents of the indicated channelrhodopsins at $[Cl^-]_e$ of 150 mM and 10 mM. **C,** Cumming estimation plot showing the paired mean difference of comparisons of stationary photocurrent reversal potentials ($E_{rev}$) of *Pyme*ACR1 (green), *Py*2087ACR1 (orange), and v*Py*ACR21821 (purple) upon replacement of the external buffer as indicated. The raw data is plotted on the upper axis with paired data points connected by a line, and the Nernst potential ($E_{Nernst}$) is indicated as a dashed line. The difference for the comparison to the control ($[Cl^-]_e$ = 150 mM) is plotted as a bootstrap sampling distribution on the lower axis, with the mean differences depicted as dots and the 95 % confidence interval indicated as vertical error bars.

ship of the three ChRs is almost linear at $[Cl^-]_e$ = 150 mM but becomes exponential at $[Cl^-]_e$ = 10 mM.

In standard conditions $E_{rev}$ is −3.0 ± 0.3 mV, −2.5 ± 0.5 mV, and −2.6 ± 0.5 mV for *Pyme*ACR1, *Py*2087ACR1, and v*Py*ACR21821, respectively (Fig. 26C). Reducing the

external $Cl^-$ concentration to 80 mM or 10 mM shifts $E_{rev}$ significantly to more positive values for all three constructs. For *Pyme*ACR1, the determined reversal potentials at these conditions are $13.9 \pm 0.2$ mV and $59.2 \pm 1.0$ mV, respectively. For *Py*2087ACR1, $E_{rev}$ shifts more positive to $15.9 \pm 0.8$ mV and $61.5 \pm 3.8$ mV, respectively. At $[Cl^-]_e$ = 80 mM, $E_{rev}$ of v*Py*ACR21821 is with $14.6 \pm 1.0$ mV similar to the two algal constructs. However, upon $Cl^-$ reduction to 10 mM, $E_{rev}$ is with $53.7 \pm 1.6$ mV the least positive of the three investigated ChRs, indicating that it conducts anions less well. Nonetheless, $E_{rev}$ upon reduction of $[Cl^-]_e$ is close to $E_{Nernst}$ for $Cl^-$. Complete removal of $Na^+$ on the extracellular side results in small but significant reversal potential shifts to $4.1 \pm 0.4$ mV and $5.2 \pm 1.0$ mV for *Pyme*ACR1 and *Py*2087ACR1, respectively, while in photocurrents of v*Py*ACR21821 $E_{rev}$ was not significantly affected ($-2.5 \pm 0.4$ mV).

To test the conduction of other anions, $Cl^-$ was replaced on the extracellular side with $Br^-$ or $NO_3^-$, resulting in significant reversal potential shifts to more negative values (Fig. 26C). For v*Py*ACR21821, $E_{rev}$ shifts are not as pronounced as for the two algal ChRs, shifting to $-12.9 \pm 0.6$ mV and $-21.5 \pm 1.6$ mV with 140 mM $Br^-$ and 140 mM $NO_3^-$ on the extracellular side, respectively. In measurements of *Pyme*ACR1, $E_{rev}$ shifts to $-17.2 \pm 0.6$ mV and $-30.6 \pm 0.9$ mV, respectively. As before, the largest shifts are determined for *Py*2087ACR1. High $Br^-$-concentrations on the extracellular side result in an $E_{rev}$ shift to $-21.6 \pm 0.6$ mV, while a high extracellular $NO_3^-$-concentration shifts the reversal potential to $-39.4 \pm 0.3$ mV. High extracellular concentrations of $Br^-$ or $NO_3^-$ results in large inward-directed photocurrents in *Py*2087ACR1, while in *Pyme*ACR1 and v*Py*ACR21821, the inward currents at the same conditions are comparable to standard conditions (Fig. S13).

These results show that the viral construct and its algal homologs are ChRs, most active upon illumination with blue-green light, and selective for anions. However, $Na^+$ may contribute to the carried charge in the algal ion channels as observed in MerMAIDs.

# 3. Discussion

The ChR-family of microbial rhodopsins allows the flow of ions according to their electrochemical gradient through a conductive pore upon photon absorption (Schneider *et al.*, 2015). They are frequently used as optogenetic tools, enabling the non-invasive photocontrol of cells' electrical activity (Deisseroth and Hegemann, 2017). At the beginning of this project, various ChRs were known, conducting cations or anions (Govorunova *et al.*, 2017a). However, most were found in genomes of lab-cultured microbial algae, limiting the optogenetic application of ChRs and the understanding of their diversity. Metagenomic databases are a trove of genomic data and offer the potential to identify new types of ChRs.

Prof. Dr. Oded Béjà and colleagues identified many sequences[1] resembling ChRs in the microbial and viral metagenomes of the *Tara* Oceans project (Sunagawa *et al.*, 2015; Brum *et al.*, 2015; Hingamp *et al.*, 2013) and the One Thousand Plant Transcriptomes Initiative (Initiative, 2019). Among those sequences were the MerMAIDs and prasinophyte ChRs that form two distinct branches within the ChRs family (Fig. 11A). Their molecular characterization described in this thesis was conducted using electrophysiology and spectroscopy.

## 3.1. MerMAID channelrhodopsins

### 3.1.1. The MerMAIDs are ACRs

The MerMAIDs branch is comprised of seven members (Fig. 11A). All members are most active upon activation with 500 nm-light (Fig. 12C), reaching photocurrent amplitudes of up to 2 nA (Fig. 12D). Upon continuous illumination, the MerMAIDs elicit transient photocurrents that almost completely desensitize within 150 ms (Fig. 12A, E) in stark contrast to most other ChRs (Nagel *et al.*, 2003; Govorunova *et al.*, 2015, 2016b). However, recently, cryptophyte CCRs have been reported showing comparably strong $I_p$ desensitization (Sineshchekov *et al.*, 2020b).

Upon depletion of $[Cl^-]_e$, $E_{rev}$ shifts to positive values comparable to $E_{Nernst}$ for $Cl^-$ (Fig. 13B, C), indicating that at standard conditions, photocurrents are mainly carried by $Cl^-$. However, upon replacing $[Cl^-]_e$ with equal concentrations of $Br^-$ or $NO_3^-$, $E_{rev}$ shifts to negative values (Fig. 13D) demonstrating that anions other than $Cl^-$ are also conducted, as otherwise $E_{rev}$ similar to values reached upon depletion of $[Cl^-]_e$ would be expected. Equal conduction of $Br^-$, $NO_3^-$, and $Cl^-$ would result in similar $E_{rev}$. However, despite competing with $Cl^-$ on the intracellular side, inward-directed photocurrents occur at more negative $E_{hold}$. Therefore, both $Br^-$ and $NO_3^-$ are conducted better than $Cl^-$. Replacing of $[Cl^-]_e$ with $NO_3^-$ shifts $E_{rev}$ more negative than its replacement with $Br^-$ yielding a

[1] In total, extending the ChR-family to 875 members (Rozenberg *et al.*, 2020).

permeability sequence of $NO_3^- > Br^- > Cl^-$. Therefore, anions with a larger atomic radius are conducted better by MerMAIDs, as reported previously for cryptophyte ACRs (Govorunova *et al.*, 2015, 2017b).

Nonetheless, while changes in pH did not affect $E_{rev}$ (Fig. 15C, D), depletion of $[Na^+]_e$ as well as its replacement with divalent cations resulted in considerable $\Delta E_{rev}$ to more positive values (Fig. 13D). Therefore, cations may contribute to the elicited photocurrents contrasting ACRs reported previously (Govorunova *et al.*, 2015, 2017b). Such a contribution is surprising as the electrostatic surface potential of the predicted ion conduction pathways of CCRs and ACRs excludes anions and cations, respectively, from passing (Volkov *et al.*, 2017; Berndt *et al.*, 2016; Kim *et al.*, 2018; H. Li *et al.*, 2019). Furthermore, if $Na^+$ would be conducted, its extracellular depletion while maintaining high intracellular concentrations would result in shifts of $E_{rev}$ to more negative values. Therefore, $Na^+$ is most likely not contributing to the photocurrents elicited by MerMAIDs. The significant $\Delta E_{rev}$ upon its depletion might be attributable to $Na^+$ binding to negatively-charged residues on the protein surface, which may improve the conduction of anions as they are not repelled. The masking of these anionic residues may be less efficient by divalent cations. However, elevated concentrations of the divalent cations $Mg^{2+}$ and $Ca^{2+}$ would result in positive shifts of $E_{rev}$ if conducted. Therefore, their conduction cannot be excluded. Imaging of intracellular $Mg^{2+}$ (Trapani *et al.*, 2010) and $Ca^{2+}$ (J. Hess *et al.*, 1989) may be applied to investigate this question further.

Despite the effects upon changes in cation-concentration, the substantial $\Delta E_{rev}$ upon $Cl^-$-depletion and its replacement with $NO_3^-$ or $Br^-$ indicate that anions are the main contributor to the MerMAID-photocurrents justifying their classification as ACRs.

### 3.1.2. The photocycle of MerMAIDs

#### The photocycle intermediates

Three distinct photointermediates - $P_{570}$, $P_{475}$, and $P_{366}$ - were detected using transient UV/vis absorption spectroscopy (Fig. 17B). $P_{570}$, analogous to the K intermediate of *Hs*BR, appears on the ns-timescale and is only shortly detected in MerMAID1. Presumably, during the $D_{502}$-$P_{570}$ transition, the *trans-cis* isomerization of the retinal chromophore occurs in analogy to other microbial rhodopsins (Atkinson *et al.*, 1989). The *trans-cis* isomerization is also suggested by kinetically decomposed FTIR difference spectra (Fig. 20A), as well as RR spectra of the dark- and light-adapted sample (Fig. 18). In *Ps*ACR1, $P_{625}$ rises within 2.2 ps (Hontani *et al.*, 2017), suggesting that in the measurements performed with MerMAID1, with the earliest time point at 10 ns, only the decay of $P_{570}$ is detected, explaining its relatively low absorption (Fig. 17C). Femtosecond transient UV/vis absorption spectroscopy would be suitable to detect the evolution of $P_{570}$ and preceding photointermediates fully as well as excited state dynamics as shown for *Hs*BR (Nuss *et al.*, 1985; Mathies *et al.*, 1988)

and *Ps*ACR1 (Hontani *et al.*, 2017).

Next, $P_{475}$ appears and remains stable for milliseconds. However, the EADS may suggest an equilibrium with a $P_{590}$ photointermediate (Fig. 17C) similar to *Gt*ACR1 (Sineshchekov *et al.*, 2016) and *Ps*ACR1 (Wietek *et al.*, 2016; Hontani *et al.*, 2017). Like $P_{570}$ also $P_{475}$ shows only weak transient absorption changes, especially compared to $P_{366}$ (Fig. 17C), potentially reflecting the small absorption changes in the amide I and amide II regions in FTIR spectra (Fig. 20A). These may indicate small changes in the protein backbone, possibly due to the absence of constriction sites other than the Schiff base region in ACRs (Kim *et al.*, 2018; H. Li *et al.*, 2019).

**Accumulation of a late photocycle intermediate**

MerMAID photocurrents rise and decay on a similar timescale as $P_{475}$ and are fully decayed as $P_{366}$ reaches maximum absorption (Fig. 17A, B). In contrast, *Gt*ACR1 photocurrent-decay sustains throughout $P_{400}$, and the return to the baseline of the photocurrents and the photointermediate coincide (Sineshchekov *et al.*, 2016). Typical for ACRs (Sineshchekov *et al.*, 2016; Hontani *et al.*, 2017), the ion channel activity of MerMAID1 precedes the deprotonation of the RSB (Fig. 17A, B).

Interestingly, $\tau_{\mathrm{des,\,app}}$ is modulated by $E_{\mathrm{hold}}$ (Fig. 14A, C and 17A). A voltage-dependence of photocurrent decay kinetics has been reported previously for *Hs*BR (Geibel *et al.*, 2001). In *Hs*SRII, strongly negative membrane potentials prohibited the light-induced proton-transfer from the RSB to the primary proton acceptor due to the RSB proton dissociating and moving towards the cytoplasmic side (Jiang *et al.*, 2008). Furthermore, proton-transfer processes were also affected in *Cr*ChR1 (Hegemann *et al.*, 2005) and *Cr*ChR2 (Gradmann *et al.*, 2011). For MerMAID2,6,7, the desensitization accelerates with increasing membrane potential, while for MerMAID1,3-5, the desensitization decelerates at the same condition (Fig. 14C). Charged amino acids are known to respond to membrane potential changes, especially in voltage-gated ion channels (Aggarwal and MacKinnon, 1996; Seoh *et al.*, 1996). However, recently, depolarization-induced charge movements in the M2 muscarinic acetylcholine receptor were observed (Ben-Chaim *et al.*, 2006), and a new type of voltage-sensor, comprised of tyrosine residues, was described for this GPCR (Barchad-Avitzur *et al.*, 2016). Electrophysiological characterization paired with surface-enhanced infrared difference absorption spectroscopy (Jiang *et al.*, 2008) of single-residue substitutions could be applied to investigate voltage-dependent structural changes and identify the voltage-sensing residues in MerMAIDs.

The rise of $P_{366}$ in MerMAID1 marks the formation of the final spectroscopically detected photointermediate decaying bi-exponentially with 635 ms and 2 s to the initial dark state (Fig. 17B). In electrophysiological experiments, $I_p$ recovered within seconds in all MerMAIDs as well (Fig. 14E), similar to CCRs but not ACRs (Schneider *et al.*, 2015; Govorunova *et al.*, 2016a). However, MerMAID1 recovered faster in whole-cell patch-

clamp experiments than in transient UV/vis absorption spectra (compare Fig. 14E and 17B). However, as the photocurrents in patch-clamp experiments were not saturated (Fig. S4), this difference may be due to higher light intensities used to acquire transient UV/vis absorption spectra. The temperature can be excluded as a source for this discrepancy as both experiments were performed at room temperature.

$P_{366}$ comprises a 13-*cis* retinal chromophore with a deprotonated RSB (Fig. 18) and accumulates during the photocycle (Fig. 17B). The formation of $P_{366}$ may be accompanied by alteration of the chromophore geometry, indicated by the shift of a marker band for 13-*cis* retinal in FTIR difference spectra (Fig. 20A). Neither in electrophysiology nor FTIR spectroscopy measurements was the recovery of the initial dark state affected by UV-light illumination (Fig. 21), indicating that $P_{366}$ is not photoactive. Therefore, the chromophore may be rigidly enclosed within its binding pocket, preventing isomerization. A rigid retinal binding pocket was suggested before for *Hs*$BR_{570}$ and *Hs*$HR_{578}$, based on the similar half-width of resonance Raman bands (Alshuth *et al.*, 1985). This comparison cannot be made with the RR spectra recorded here because a control measurement of either *Hs*$BR_{570}$ or *Hs*$HR_{578}$ would be required. As no further photointermediates are detected after $P_{366}$ in MerMAID1, it can be concluded that the reisomerization of the chromophore and the reprotonation of the RSB, marking the return to the initial dark state, coincide (Fig. 17B). However, since $P_{366}$ decayed bi-exponentially, a spectroscopically silent photointermediate may follow $P_{366}$.

### $H^+$ and $Cl^-$ in the Schiff base region

Most investigated parameters of the MerMAID photocurrents were unaffected by changes in the intra- or extracellular pH (Fig. 15), suggesting that the RSB proton remains in the Schiff base region at physiological pH and is not in contact with the cytosol or extracellular space during the photocycle, similar to the recently reported heliorhodopsins (Pushkarev *et al.*, 2018). Instead, it may remain in a proton cage as suggested for *Hs*BR (Friedrich *et al.*, 2020).

While $\tau_{rec}$ is only slightly affected by changes in the pH compared to other ChRs (Nagel *et al.*, 2003), it markedly decelerates at increased intracellular $H^+$ concentrations, while decreased $H^+$ concentrations did not affect the photocurrent recovery (Fig. 15F). Similarly, extracellular changes of the $H^+$ concentration affected the photocurrent recovery, though to a lesser extent than changes on the intracellular side, upon elevation but not upon decrease (Fig. 15E). Therefore, the residues participating in the reprotonation of the RSB are, potentially, more accessible from the intracellular side than from the extracellular. At lower $pH_i$, these residues are potentially protonated, effectively blocking the reprotonation pathway and slowing down the recovery of the initial dark state. Changes in the pH did not affect $\tau_{des,\,app}$ (Fig. 15G, H), indicating, therefore, that the primary proton acceptor is unaffected at the tested pH range. In pH-titration experiments, $\lambda_{max}$ of UV/vis absorption

spectra shifted hypsochromic. Similar shifts were not observed in electrophysiological experiments, most likely due to the small pH range tested, but the lipid environment is also involved in stabilizing conformational states (Bhattarai *et al.*, 2020). Therefore, the accessibility of residues can differ between the cell membrane and detergent-purified protein.

Absorption spectra in the absence of NaCl shifted slightly bathochromic (Fig. 16B), potentially indicating $Cl^-$-binding to the protein and a mild contribution to stabilizing the dark state. This stabilization may occur via modification of the hydrogen bonding network within the Schiff base region, as suggested for *Hs*HR (Maeda *et al.*, 1985) and KR2 upon $Na^+$-binding (Otomo *et al.*, 2019). However, considering the mild bathochromic shift, the potential $Cl^-$-binding site is not close to the protonated RSB, as suggested for *Fulvimarina* rhodopsin (Inoue *et al.*, 2014). A similarly mild $Cl^-$-dependence has been reported for *Ps*ACR1 (Hontani *et al.*, 2017; Tsukamoto *et al.*, 2018), but not *Gt*ACR1, where the absorption maximum was unaffected by changes in the anion-concentration (Sineshchekov *et al.*, 2016). A contribution of $Na^+$ cannot be excluded for MerMAIDs, as both $Na^+$ and $Cl^-$ were removed entirely (Fig. 16B). For a detailed analysis of the $Cl^-$ contribution at the Schiff base region, the ionic strength of the buffer should be kept stable as done by Tsukamoto *et al.* (2018). Nonetheless, a substantial contribution of $Cl^-$ as a counterion in MerMAID1 can be excluded.

**Molecular determinants of the photocycle**

Only two carboxylic residues are located close to the RSB in MerMAID1, Glu44 and Asp210 (Fig. 22C). Neutralization of Asp210 and substitution of the close-by Phe183 with tyrosine shifted $\lambda_{max}$ bathochromic (Fig. 23A), indicating that Asp210 is the primary counterion, possibly coordinated by Phe183. However, it was suggested that in *Hs*BR, the homolog tyrosine residue is directly proton-bonded to the RSB in the dark state (Ding *et al.*, 2018). The substitution of this tyrosine residue with a phenylalanine residue resulted in a 7 nm hypsochromic shift. Therefore, the substitution of MerMAID1-Phe183 with a tyrosine residue may result in proton-bonding with the RSB, which could also explain the bathochromic shift. Neutralization of Glu44 resulted in only a mild bathochromic shift of $\lambda_{max}$ (Fig. 23A), suggesting it is protonated in the wildtype, in line with an unaffected $\tau_{des,\,app}$ upon changes in pH (Fig. 15G, H). Glu44 is, therefore, most likely not acting as a counterion, similarly suggested for *Gt*ACR2 (Kojima *et al.*, 2018).

Neutralization of Asp210, but also the substitution of Tyr48 with a phenylalanine residue, strongly reduced the transient photocurrent amplitudes and decelerated $\tau_{rec}$ (Fig. 23C, F). Therefore, RSB reprotonation seems to occur mainly via Asp210, as the impact on $\tau_{rec}$ is larger in MerMAID1-D210N, with the participation of Tyr48. However, $\tau_{des,\,app}$ is not affected by the substitution of either residue (Fig. 23E), indicating they are not involved in the deprotonation of the RSB and, hence, the formation of the desensitized state.

Substitution of Glu44 with glutamine, on the other hand, strongly decelerated $\tau_{\text{des, app}}$, but only mildly affected $\tau_{\text{rec}}$ (Fig. 23E, F), implying it is involved in the deprotonation of the RSB similarly proposed for *Gt*ACR1 (Sineshchekov *et al.*, 2015, 2016) and *Ps*ACR1 (Hontani *et al.*, 2017). Nonetheless, it may still affect the p$K_{\text{a}}$ of Asp210 and the RSB, which could explain the moderate deceleration of the dark state recovery of MerMAID1-E44Q (Fig. 23F).

The exact mechanism, how Glu44 accepts the proton, is not clear at the moment. However, it has to transiently deprotonate to accept the RSB proton considering its apparent protonated state in the wildtype. FTIR bands between 1716 $\text{cm}^{-1}$ and 1746 $\text{cm}^{-1}$ are supporting such a process (Fig. 20C). However, to determine which residues contribute to these FTIR bands, further experiments with MerMAID1-E44Q and MerMAID1-D210N are required.

Furthermore, the decelerated but not disrupted formation of the desensitized state upon substitution of Glu44 with glutamine suggests the existence of an alternative proton acceptor assuming Glu44 as the primary proton acceptor in the wildtype. Interestingly, the combination of E44Q and D210N strongly increased the transient photocurrent amplitudes compared to the D210N single substitution, while $\tau_{\text{des, app}}$ and $\tau_{\text{rec}}$ were comparable to both the E44Q and D210N single-residue substitutions, respectively (Fig. 23C, E, F). Therefore, alternative proton donor sites may become available upon the substitution of Glu44 as well. Alternatively, the substitution of Glu44 may prevent RSB deprotonation. However, to determine the molecular effects of the Glu44 and Asp210 substitutions, transient UV/vis absorption spectroscopy is necessary.

### A photocycle model

In summary, the collected data suggest that the MerMAID photocycle consists of three spectroscopically detectable photointermediates (Fig. 27A). Nonetheless, spectroscopically silent photointermediates and photointermediates rising and decaying at timescales below 10 ns may also contribute. $P_{570}$ most likely marks *trans-cis* isomerization of the retinal chromophore and precedes the formation of the conducting state $P_{475}$. With deprotonation of the RSB, the protein becomes non-conducting, and the photointermediate $P_{366}$ appears.

The RSB deprotonation is suggested to be mediated by Glu44, which would require its transient deprotonation to act as a proton acceptor (Fig. 27B). Upon return to the initial dark state $D_{502}$, RSB reprotonation seems to occur via the primary counterion Asp210 in conjunction with Tyr48. Virtually simultaneous, retinal isomerizes from the 13-*cis* to the all-*trans* conformation. MD simulations further suggest that the residues are connected and stabilized by a proton-binding network (Fig. 22C).

Interestingly, shortly after the MerMAIDs were reported (Oppermann *et al.*, 2019), Sineshchekov *et al.* (2020b) identified cryptophyte CCRs with striking similarities to the MerMAIDs. As the MerMAIDs, *Ra*CCR1 and *Rs*CCR1, identified in two *Rhodomonas* species, show nearly completely desensitizing photocurrents during continuous illumination.

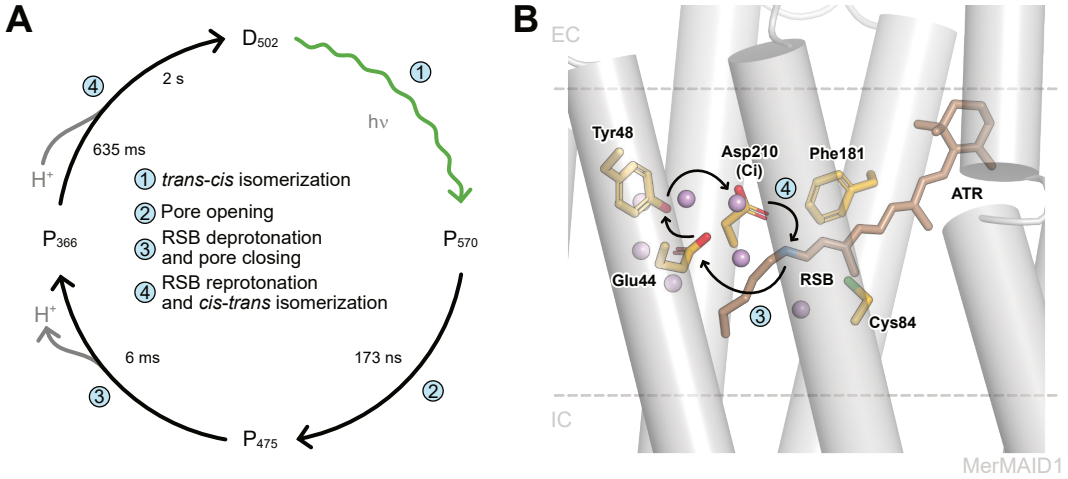


**Figure 27.: Suggested photocycle of MerMAID ChRs. A,** Model of the MerMAID1 photocycle comprised of the dark state $D_{502}$ and the three photointermediates $P_{570}$, $P_{475}$, and $P_{366}$. Subscript numbers indicate the maximum absorption wavelength of the photointermediate. The photocycle is initiated by the absorption of a photon (h$\nu$; green arrow). Circled numbers indicate steps of the photocycle with $H^+$ transitions indicated by gray arrows. Kinetics of the photointermediate transitions are given according to figure 17B, C. **B,** Homology model based on the iC++ crystal structure (PDB: 6CSN; Kato *et al.*, 2018). The all-*trans* retinal chromophore (brown) and residues of the Schiff base region (yellow) are depicted as sticks. Water molecules are purple dots. Suggested RSB proton circulation in the Schiff base region is indicated by arrows and circled numbers. Relevant residues (yellow) are depicted as sticks with oxygen (red) and nitrogen (blue) marked. Purple spheres are waters.

Typical for CCRs, photocurrents of *Ra*CCR1 and *Rs*CCR1 coincide with the deprotonation of the RSB, which is followed by accumulation of a late, strongly hypsochromic photocycle intermediate with a fine-structured absorption. The initial dark state is recovered within seconds in these cryptophyte CCRs (Sineshchekov *et al.*, 2020b).

Furthermore, among the recently reported labyrinthulea ACRs, two proteins show photocurrents similarly strong desensitizing as the MerMAIDs (Govorunova *et al.*, 2020). While a detailed study of these ChRs on the molecular level is not available at the moment, it suggests that ChRs with large-amplitude transient photocurrents and small-amplitude stationary photocurrents are more broadly distributed as expected.

### 3.1.3. Finestructured absorption of the deprotonated RSB

In steady-state UV/vis absorption spectra of MerMAID1, a fine-structured absorption with three distinct maxima was observed for the light-adapted protein (Fig. 16A). A similar fine-structure was observed upon the alkalization of the sample (Fig. 16C). Furthermore, in transient UV/vis absorption spectroscopy, a fine-structure with two absorption maxima appeared in EADS of $P_{366}$ (Fig. 17C), though the full fine-structure was most likely not observed due to the limit of the spectral detector.

**Fine-structured absorption spectra in other microbial rhodopsins**

Similar fine-structured UV absorption spectra have been observed before in light-adapted *Hs*BR (B. Hess and Kuschmitz, 1977; Birge *et al.*, 1989), though at a lesser intensity, and suggested to originate from a mixture of spectral species (B. Hess and Kuschmitz, 1977). Also, reduction of the Schiff base C=N to C−N using sodium borohydride ($NaBH_4$) produced a fine-structured UV-absorbing species which was pronounced at acidic pH and explained with retro-retinal formation where all ethylenic bonds are shifted towards the $\beta$-ionone ring by one position (Peters *et al.*, 1976). However, increased torsion of $C_6-C_7$ (Schreckenbach *et al.*, 1977), pronounced by interactions of the protein backbone with the chromophore (Schreckenbach *et al.*, 1978) have been suggested alternatively. In the *Cr*ChR2-C128T mutant, the appearance of a fine-structured UV-absorbing species was explained by transient hydrolysis of the Schiff base (Bruun *et al.*, 2011). UV-absorbing and fine-structured species were further observed in the engineered ACR iC++ (Kato *et al.*, 2018) and *Gt*ACR1 (Sineshchekov *et al.*, 2016) as well as upon residue substitutions in *Co*ChR and Chronos (B. S. Krause, 2017). However, all mentioned appearances of fine-structured UV absorption spectra were reported for the dark- and not the light-adapted proteins, contrasting MerMAID1 (Fig. 16A).

A mixture of dark states, which would populate different deprotonated states, is excluded for MerMAID1 by RR spectroscopy (Fig. 18). Probing the dark-adapted state with either 488 nm or 514 nm yielded almost identical RR spectra, except for one band showing a minimal shift and suggested to be a secondary mode to a vibration with a frequency of 1238 $cm^{-1}$. The consistency of the RR spectra upon probing with different $\lambda_e$ suggests a homogeneous dark state. However, some C−C marker bands of the 13-*cis* retinal isomer are detected in the RR spectra of the dark-adapted sample as well (Fig. 18B) though most likely due to isomerization induced by the probe pulse. Nevertheless, an isomer mixture of the chromophore in the dark state cannot be entirely excluded without additional data. For clarification, retinal extraction from dark- and light-adapted samples followed by high-performance liquid chromatography (HPLC) would yield additional information about the chromophore isomers and their ratios (Sato *et al.*, 2018). Furthermore, in pre-resonance Raman spectroscopy, a laser wavelength outside the absorption maximum of the chromophore is used. Hence, a conformation change induced by the probing laser is less likely, allowing for a more precise interpretation of the spectra.

Also, a retro-retinal populating the retinal binding pocket of the MerMAIDs can be excluded as an explanation for the fine-structured UV-absorption. The recorded RR spectra of dark-adapted MerMAID1 show a higher resemblance with the RR spectra of dark-adapted *Hs*BR (S. O. Smith *et al.*, 1985b) than with reduced retro-*Hs*BR (Bruun *et al.*, 2011), especially in the C−H-rocking region between 1300 $cm^{-1}$ and 1400 $cm^{-1}$.

Hydrolysis of the Schiff base linkage, as suggested by Bruun *et al.* (2011), can be

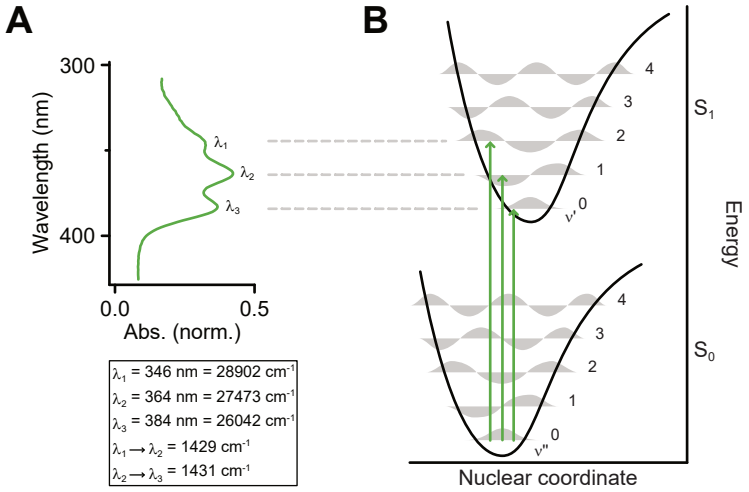


**Figure 28.: Illustration of the relation between absorption and vibrational levels. A,** Absorption spectrum of light-adapted MerMAID1. The fine-structured absorption of the UV-absorbing species is shown with the absorption maxima ($\lambda_1$-$\lambda_3$) indicated with the wavelength in nm and $cm^{-1}$ given in the box. Additionally, the difference between $\lambda_1 \rightarrow \lambda_2$ and $\lambda_2 \rightarrow \lambda_3$ is indicated as $\Delta cm^{-1}$. **B,** Potential energy diagram illustrating the origin of the fine-structure. Vibronic sub-states ($v$"0-4 and $v$'0-4) for the electronic ground state ($S_0$) and the first electronic excited state ($S_1$) are indicated as waves in gray. Note: $\lambda_1$-$\lambda_3$ are not necessarily reflecting $v$'0-2. The connections are made for illustration purposes.

dismissed for the MerMAIDs as well, based on the recovery kinetics of the transient photocurrents in electrophysiological experiments (Fig. 14D, E) as well as the kinetics of the return to the initial dark state in transient UV/vis and FTIR spectroscopic experiments (Fig. 17B and 20B). In all experiments, MerMAID1 returned to the initial state within seconds. On the other hand, Schiff base formation occurs in the time frame of several minutes, depending on the temperature and the pH (del Vado *et al.*, 1987), much slower than the observed dark state recovery.

### The MerMAIDs fine-structured absorption may result from vibronic coupling

Of the previously suggested causes of UV-absorbing fine-structures, the most plausible for the observed phenomenon in MerMAID1 is a rigid retinal binding pocket. Residues interacting with the chromophore may put a torsional strain on the molecule leading to absorption over a broad range with several distinct maxima (Schreckenbach *et al.*, 1977, 1978).

In an energy potential diagram, such torsional strain may be depicted as small shifts along the nuclear coordinate in the electronic ground state $S_0$ (start points of green arrows in Fig. 28B). As electronic transitions are faster than molecular motions (Luis *et al.*, 2003), the nuclear coordinate remains constant upon absorption of a photon and elevation to the first electronic excited state $S_1$, giving rise to additional vibronic excitation and population of vibronic sub-states (Fig. 28B). Such a vibronic coupling (Azumi and Matsuzaki, 1977) was suggested for *Hs*SRII and *Cr*ChR2, where a fine-structured absorption maximum of

the dark state chromophore was described (Takahashi *et al.*, 1990; Lórenz-Fonfría and Heberle, 2014). Vibronic excitation in polyenes similar to retinal shows a spacing in the range of 1450 $cm^{-1}$ in absorption spectra (Takahashi *et al.*, 1990).

Interestingly, the three local maxima of the UV-absorbing fine-structure of light-adapted MerMAID1 at $\lambda_1$ 346 nm, $\lambda_2$ 364 nm, and $\lambda_3$ 384 nm are at an almost equal distance of 1430 $cm^{-1}$ for $\lambda_1 \rightarrow \lambda_2$ and $\lambda_2 \rightarrow \lambda_3$ to each other (Fig. 28A, Box). Therefore, it can be argued that indeed the fine-structure of the UV-absorbing species originates from additional vibronic excitation.

The fine-structured absorption appeared not only upon illumination-induced 13-*cis* retinal formation and RSB deprotonation but also upon alkalization, though with the three local maxima $\lambda_1$-$\lambda_3$ shifted bathochromic (Fig. 16C). RR spectra of the chromophore at alkaline conditions indicate an all-*trans* conformation (Fig. 19), which is probably the reason for the shifted absorption. The absorption decrease of $\lambda_3$ at pH >11.3 (Fig. 16C, D) suggests the involvement of at least one titratable residue.

A possible candidate, causing the vibronic coupling, is a highly conserved cysteine in ChRs, Cys84 in MerMAID1 (Fig. 22C), which will be discussed in more detail in the following section. In the absorption spectra of the previously mentioned cryptophyte CCRs with near-complete desensitization, Sineshchekov *et al.* (2020b) observed a fine-structured UV-absorption as well but shifted hypsochromic compared to MerMAIDs. Upon substituting the conserved cysteine in *Ra*CCR1, the UV-absorbing species was not fine-structured anymore (Sineshchekov *et al.*, 2020b). Therefore, the vibronic coupling in MerMAIDs may originate from an interaction between the cysteine and the RSB. And indeed, the substantial hypsochromic shift of $\lambda_{max}$ in action spectra of MerMAID1-C84T (Fig. 23B) suggests a close connection of the RSB with the cysteine, though spectroscopic data of MerMAID1-C84T is needed to prove this hypothesis.

### 3.1.4. Photocurrent desensitization of MerMAIDs

Transient photocurrents of *Cr*ChR2 desensitize quickly to a stationary level during continuous illumination. Upon repeated excitation, the transient photocurrent amplitudes decrease while the stationary photocurrent amplitudes remain stable. The transient photocurrent amplitudes only recover after tens of seconds without photon exposure (Nagel *et al.*, 2003; Schneider *et al.*, 2015). A single photocycle cannot explain these photocurrents and, therefore, a model was developed with two parallel photocycles, each with its own closed and open states (Hegemann *et al.*, 2005), which was recently described in great detail (Kuhne *et al.*, 2019). Most ACRs show photocurrents that are similarly desensitizing as *Cr*ChR2 but exhibit rapid transient photocurrent recovery (Govorunova *et al.*, 2015, 2016a, 2017b). A single photocycle was suggested for *Gt*ACR1 (Sineshchekov *et al.*, 2016). However, the photocurrent desensitization, as well as the pigment recovery kinetic of 3 s determined for *Gt*ACR1 (Sineshchekov *et al.*, 2016), are incompatible with a single photocycle. Therefore,

a second photocycle may be populated in cryptophyte ACRs as well, similar to *Cr*ChR2 (Kuhne *et al.*, 2019). However, detailed investigations of the cryptophyte ACR-photocycle are required for the elucidation of this question.

**The photocycle model sufficiently explains MerMAIDs photocurrents**

In MerMAIDs, the fast and near-complete desensitization with transient photocurrents recovering within seconds can be sufficiently explained with a single photocycle where one conducting state converts quickly to a desensitized state that transits to the initial dark state within seconds (Fig. 27A). The low stationary photocurrent would, in this case, be explained by a minor population of the protein occupying the conducting state. An alternative explanation for the low-amplitude stationary photocurrents could be a low conductivity of the accumulating $P_{366}$. However, this can be excluded based on single-turnover electrophysiology, where no photocurrents were detected on similar timescales as the accumulation of $P_{366}$ (Fig. 17A).

In transient UV/vis absorption spectra, three distinct photointermediates were detected, comprising the MerMAID photocycle. $P_{366}$ accumulates during the photocycle and marks the deprotonation of the RSB (Fig. 27). Furthermore, the decay of photocurrents coincides with the rise of $P_{366}$ (Fig. 17). Kinetic decomposition of FTIR difference spectra revealed two spectral components for continuous and single turnover conditions. The spectra of both kinetic components show many similarities between the two illumination regimes, indicating that the same molecular changes occur in the rhodopsin independent of illumination duration. However, it has to be noted that the spectra of the fast spectral component, assigned to the conducting state, show more differences between the two illumination regimes, while the spectra of the slow component almost completely overlap (Fig. 20A). Therefore, during continuous illumination, the conducting state may be a mixture of different conducting states, transitioning to either the same or highly similar desensitized states. FTIR spectra were recorded in the rapid-scan mode. Alternatively, FTIR spectra can be recorded in the step-scan mode allowing a high temporal resolution (Manning *et al.*, 1991) and potentially offering additional information about the conducting state's nature.

FTIR spectra further indicate a change of the chromophore geometry upon transition from the conducting to the desensitized state (Fig. 20A). Since RR spectra were recorded with either the dark- and light-adapted protein (Fig. 18), the change in geometry cannot be confirmed from those experiments. However, time-resolved resonance Raman spectroscopy offers the potential to identify the proposed geometry changes and the time point of their occurrence (L. Zhu *et al.*, 1999).

A single photocycle model as an explanation for the strongly desensitizing photocurrents of MerMAIDs may further be supported by RR spectroscopy. Upon the exchange of accessible protons with deuterium, the marker bands of $C_{14}$–$C_{15}$ did not shift in the dark- nor light-adapted MerMAID1 protein (Fig. 18B). This insensitivity to deuteration is an

indicator for a $C_{15}$=N-*anti* configuration (S. O. Smith *et al.*, 1987b,a). It suggests that this bond remains structurally unchanged upon illumination. This result contrasts *Cr*ChR2, where $C_{15}$=N populates either an *anti*- or a *syn*-configuration (Fig. 3B), acting as the parent state for a parallel photocycle (Kuhne *et al.*, 2019). However, the assignment of Raman bands based on comparison to *Hs*BR is debatable as marker bands assigned in the ion pump may differ in a ChR. The most thorough method to identify and correctly assign bands of RR spectra to the various bonds of the retinal chromophore is the resubstitution of the opsin with retinal where single carbon positions are substituted with $^{13}$C as done previously for *Hs*BR (S. O. Smith *et al.*, 1987b,a). Yet, this approach is very cost- and time-intensive. Alternatively, since the clear identification of the vibration mode of $C_{14}$–$C_{15}$ of MerMAID1 would be most interesting to elucidate the question if $C_{15}$=N populates an *anti*-configuration exclusively, just $C_{14}$ and $C_{15}$ could be $^{13}$C-substituted. The interpretation of RR spectra can further be supported, as mentioned before, by extraction of the chromophore from dark- and light-adapted protein and subsequent HPLC analysis (Sato *et al.*, 2018). Furthermore, pre-resonance Raman spectroscopy should be applied, as it enables the analysis of the pure electronic ground state, as suggested before (Nack *et al.*, 2009).

Overall, the gathered data suggests that the population of a single photocycle causes MerMAID photocurrents. The quick and near-complete desensitization is explained by the accumulation of a late photointermediate with a deprotonated RSB, which takes seconds to decay to the initial dark state. Therefore, MerMAIDs offer the unique possibility to investigate the *anti*-photocycle, as suggested by RR spectroscopy, in near-pure conditions.

**Direct interaction between a conserved cysteine and the RSB**

It remains the question: what is causing the accumulation of the deprotonated RSB in the photocycle of MerMAIDs? Retro-retinal formation and RSB hydrolysis have been excluded before (Ch. 3.1.3). Substitution of Glu44 close to the RSB decelerates $\tau_{des,\,app}$ 10-fold and results in a 10 % reduced $I_p$ desensitization (Fig. 23A, D). However, it can be assumed that the extent of the desensitization would be similar to the wildtype upon extended illumination times since the photocurrents are still decaying after 500 ms (Fig. 23A). Therefore, the desensitized state $P_{366}$ is still formed, but its formation is decelerated.

The substitution resulting in the most pronounced effect on the desensitization level of transient photocurrents was MerMAID1-C84T (Fig. 23A, D). $I_p$ desensitization was similarly affected by a threonine-substitution of Cys84 in MerMAID6 (Fig. S10). Cys84 is the homologous residue to the DC-pair-forming *Cr*ChR2-Cys128 (Schneider *et al.*, 2015; Volkov *et al.*, 2017). Substitution of *Cr*ChR2-Cys128 with either threonine, alanine, or serine substantially extends the open state lifetime and also affects the $I_p$ desensitization (Berndt *et al.*, 2009; Bamann *et al.*, 2010; Hososhima *et al.*, 2015). The RSB of *Cr*ChR2-C128T favors a hydrogen-bonding network connecting it to the two counterions Glu123 and Asp253 via water molecules instead of a direct hydrogen-bond (Guo *et al.*, 2016). In

cryptophyte ACRs, the slow channel closing, as well as the dark-state recovery, is strongly affected by the substitution of the cysteine homologous to MerMAID1-Cys84, decelerating both parameters 100-fold and effectively extending the open-state lifetime (Govorunova *et al.*, 2018), due to an equilibrium between two photointermediates, comprising the conducting state and the deprotonated RSB (Sineshchekov *et al.*, 2015, 2016).

The strong effect of the substitutions of Cys84 on the photocurrent desensitization marks this cysteine as a critical factor for the molecular mechanism underlying the near-complete photocurrent desensitization in MerMAIDs. Moreover, also in the previously mentioned cryptophyte CCRs with almost complete desensitization induces substitution of this highly conserved cysteine substantially reduced photocurrent desensitization. Transient UV/vis absorption spectra could further clarify which spectral photointermediates are affected by this substitution. A prolonged $P_{475}$ and accelerated decay of $P_{366}$ to the initial dark state are both excluded by the acquired electrophysiological data, which shows accelerated desensitization and a decelerated recovery of the transient photocurrents (Fig. 23E, F).

Potentially, Cys84 suppresses the formation of $C_{15}$=N-*syn* in the wildtype. Its substitution may, therefore, allow the isomerization of $C_{15}$=N and the branching of the photocycle, as determined for *Cr*ChR2 (Kuhne *et al.*, 2019). For *Cr*ChR2-C128T, hydrolysis of the RSB was suggested (Bruun *et al.*, 2011). In CCRs, the conducting state coincides with the deprotonated RSB (Kuhne *et al.*, 2019). A hydrolyzed RSB cannot reprotonate and takes a long time to reform itself, therefore extending the open state in a CCR past the end of the exciting light pulse. The possibility to accelerate channel closing in *Cr*ChR2-C128S/A/T by a second illumination pulse of a different wavelength (Berndt *et al.*, 2009) may be a counterargument to the suggested hydrolysis though, as it is not clear how additional illumination would promote the formation of the RSB. The recovery kinetics of MerMAID1-C84T are severely decelerated, with the transient photocurrents not completely recovering in a time frame of 200 s (Fig. 23F). The stationary photocurrent amplitudes remained stable over this time, though, and channel closure after the illumination was quick and complete. However, a hydrolyzed RSB should also affect the stationary photocurrents since ACRs require a protonated RSB to form the conducting state. Therefore, hydrolysis of the RSB in MerMAID1-C84T can be excluded as a potential explanation for the strongly decreased desensitization. Instead, the strongly decelerated recovery to the initial dark state indicates the formation of a second photocycle.

A thorough investigation of MerMAID1-C84T may help elucidate the molecular mechanism by which Cys84 is suppressing the reprotonation of the RSB in the wildtype, which is still elusive at this moment. One possibility could be the formation of a thio-adduct during the MerMAID photocycle, as recently reported for the vertebrate non-visual opsin Opn5L1 (Sato *et al.*, 2018). Thio-adduct formation is further known from LOV domains between a cysteine residue and the flavin chromophore, forming in a µs-timeframe but decaying with time constants of tens of seconds (Swartz *et al.*, 2001; J. Zhu *et al.*, 2016). While

the µs-timeframe for a thio-adduct formation seems to fit reasonably with the kinetics of the MerMAID photocycle, the decay of a thio-adduct is too long to accommodate for the MerMAID desensitization, as the transient photocurrents recover within 1 s to 6 s (Fig. 14E). Furthermore, thio-adduct formation in Opn5L1 leads to the formation of a photointermediate $P_{270}$ without deprotonation of the RSB (Sato *et al.*, 2018). Neither was detected for MerMAIDs (Fig. 16A). Nonetheless, a thio-adduct formation could be additionally tested by FTIR spectroscopy, extending the spectral range to the S−H stretching region (2500 $cm^{-1}$ to 2620 $cm^{-1}$), where thio-adduct formation can be observed as S−H-stretching bands disappear (Iwata *et al.*, 2003).

## 3.2. Viral and prasinophyte ChRs

In addition to the MerMAIDs, a second sub-family of ChRs was metagenomically identified. This branch in the ChR-family of microbial rhodopsins comprises sequences from green algae and marine giant viruses. Their electrophysiological characterization described here supplements the bioinformatic analysis performed by Dr. Andrey Rozenberg (Rozenberg *et al.*, 2020).

### 3.2.1. Membrane-targeting of viral ChRs

While the algal constructs expressed well in mammalian cells, the viral constructs were cytotoxic and the photocurrent amplitudes too small for an electrophysiological characterization. Confocal images further showed that most of the protein was not located in the cell membrane (Fig. 24A and S11A). Similar expression patterns have been observed before for microbial rhodopsins such as *Np*HR (Gradinaru *et al.*, 2008) and KR2 (Grimm *et al.*, 2018). For those proteins, it was possible to improve the membrane-targeting and the elicited photocurrent amplitudes. Therefore, the viral constructs were modified according to previous successful approaches (Grimm *et al.*, 2018) and truncated C-terminally. These modifications improved the membrane-localization of v*Py*ACR21821 (Fig. 24B) but not v*Py*ACR2164382 (Fig. S11B).

Considering the chosen modifications were only semi-successful, further studies of the viral ACRs should be preceded by a thorough membrane-targeting approach, testing various available amino-terminal fusions as well as different fluorophores and assessing the protein localization with confocal imaging, as done here, but additionally using fluorescent markers for the cell membrane. Previously, N-terminal extension using a fragment of the rat gastric $H^+/K^+$-ATPase $\beta$-subunit ($\beta$HK; Shull, 1990) improved photocurrents of the microbial rhodopsin ion pumps *Hs*BR (Geibel *et al.*, 2001) and KR2 (Vogt *et al.*, 2019). However, also the addition of protein kinase C conserved 1 and protein kinase C conserved 2 domains may improve the membrane-targeting (Cho, 2001). Furthermore, Grimm *et al.* (2018) found that the choice of the fluorophore can dramatically impact the aggregation

and intracellular retention of a fusion protein. Therefore, a range of available fluorophores should be evaluated for their impact on the membrane-localization of the viral ACRs.

A contrasting approach to the one chosen here would be exchanging the carboxyl-terminus in the viral ChRs instead of its truncation. Even though the C-terminal regions of *Pyme*ACR1 and *Py*2087ACR1 are over 100 residues longer than in the viral representatives, both algal ChRs express well and elicit photocurrents without the addition of signaling sequences or truncation. Therefore, it may be argued that functionally essential parts of this domain are missing in the viral constructs. Exchanging the C-terminal domain in the viral constructs for their algal representative could, potentially, render the viral ChRs functional again.

### 3.2.2. Photoactivity of viral and prasinophyte ChRs

The photocurrents of the three tested viral and prasinophyte ChRs showed no desensitization during continuous illumination in standard conditions and were inward- or outward-directed, depending on the membrane potential (Fig. 25A). While the characterization of v*Py*ACR2164382 was not possible due to intracellular retention of the protein and its cytotoxicity, single measurements in standard conditions were acquired, demonstrating its ion channel activity (Fig. S12). Nonetheless, v*Py*ACR2164382 is referred to as an anion-conducting ChR due to its sequence similarity with v*Py*ACR21821 (Fig. S1 and Ch. 2.1).

The highest photocurrent amplitudes were achieved upon illumination with blue-green light (Fig. 25B, C), but the photocurrent amplitudes of the viral construct were approximately five times smaller compared to the algal constructs (Fig. 25D). This indicates an overall reduced ion conductance for v*Py*ACR21821, though impaired protein expression and reduced membrane localization compared to the algal constructs may contribute.

#### Increased activity in UV-light

All three ChRs show a decrease in activity at 400 nm compared to 390 nm, though this is more prominent for the prasinophyte ChRs than for the viral ACR (Fig. 25B). The origin of this increased activity is currently unclear. Recently, Förster energy resonance transfer (FRET) from the fluorophore to the rhodopsin was demonstrated for labyrinthulea and haptophyte ACRs (Govorunova *et al.*, 2020). Both *Pyme*ACR1 and *Py*2087ACR1 were expressed as fusion construct with mCherry added as a fluorescent tag after the carboxy-terminal domain, while v*Py*ACR21821 was associated with eYFP, following directly after the rhodopsin domain. The maximum excitation wavelength of mCherry and eYFP is 590 nm and 510 nm, respectively, but both fluorophores are sensitive to UV-light as well, although only to a small extent (Ormö *et al.*, 1996; Shaner *et al.*, 2004; Kremers *et al.*, 2006; Lambert, 2019). Therefore, if the FRET would be this efficient albeit illumination

with a wavelength so far off the excitation maximum of the fluorophore, a much larger effect has to be expected upon illumination with wavelengths close to the excitation maximum. However, all three constructs show almost no activity upon illumination with wavelengths >580 nm (Fig. 25B), excluding FRET as a possible explanation.

Therefore, the increased activity upon illumination with 390 nm-light seems to originate from the rhodopsins themselves. Action spectra were recorded after pre-illumination of the constructs to ensure that all proteins in the cell membrane are subsequently activated from the same state. Therefore, it is unlikely that only a fraction of the proteins transitions to an inactivated state upon UV-light illumination. Nonetheless, action spectra should be recorded in the reverse direction from 680 nm to 390 nm to confirm the absence of inactivation. The action spectra may suggest a second species with ion channel activity in the prasinophyte and viral ACRs, potentially rendering them the most blue-shifted ChRs currently known.

Additionally, investigation of the photocycle of these new ChRs would be interesting. The acquisition of transient UV/vis absorption spectra upon excitation with UV-light and blue or green light could yield information if two different photocycles are activated by excitation with different wavelengths or the same photocycle.

**First green algal and viral ACRs**

The photocurrents of the viral and prasinophyte ChRs showed no or only very weak desensitization during continuous illumination. However, a depletion of the extracellular $Cl^-$ results in transient photocurrents in *Pyme*ACR1 at strongly negative $E_{hold}$ that mildly desensitize (Fig. 26A). The increased electrochemical driving force for $Cl^-$ at low extracellular $Cl^-$ concentrations most likely pronounce the desensitization in *Pyme*ACR1 below −60 mV. Alternatively, due to the larger photocurrent amplitudes of *Pyme*ACR1, $Cl^-$ may deplete locally on the intracellular side, leading to an apparent decrease in photocurrents. However, considering the photocycle model for *Cr*ChR2 by Kuhne *et al.* (2019), the transient and the stationary photocurrents could be interpreted as two different open and closed states, C1/O1 and C2/O2, each with their separate photocycle, in the viral and prasinophyte ChRs. At symmetrical conditions, the conductance of both open states may be equal or not differentiable, but at low $[Cl^-]_e$, a mild outward-rectification of O1 may become apparent, visible as desensitization as the population of O2 increases. The bi-exponential decay of the photocurrents after illumination further supports two open states (Fig. 25E).

Extracellular $Cl^-$ depletion shifted the reversal potential strongly to positive values in all tested constructs, indicating $Cl^-$ conduction (Fig. 26). However, while for *Pyme*ACR1 outward-directed photocurrent amplitudes increased under these conditions, as typically observed for ACRs (Govorunova *et al.*, 2016a), they decreased for *Py*2087ACR1 and v*Py*ACR21821 (Fig. 26A, B and S13). This suggests an outward-rectification of *Pyme*ACR1 photocurrents. It is further noticeable that the photocurrent amplitudes in all three ChRs

are decreased upon depletion of $[Na^+]_e$ and restoration of $[Cl^-]_e$ (Fig. S13) while $E_{rev}$ was not or only mildly affected (Fig. 26C). Therefore, the conducting pore may get blocked by aspartate, which is used to compensate $Cl^-$ in measurements with low $[Cl^-]_e$. However, in ion selectivity measurements, $Cl^-$ depletion was always performed first. Exchange of the external buffer in random order would be required to allow a proper interpretation of a potential ion channel block. Nonetheless, the decreasing photocurrent amplitudes may be attributable to a drift over time, as previously described for *Cr*ChR2 (Gradmann *et al.*, 2011; Schneider, 2013).

Interestingly, in *Py*2087ACR1 were inward-directed photocurrents strongly increased at high $[Br^-]_e$ and $[NO_3^-]_e$, while they were comparable to standard conditions for v*Py*ACR21821 and *Pyme*ACR1 (Fig. S13). However, $E_{rev}$ was strongly affected in all three ChRs. Nonetheless, $\Delta E_{rev}$ was more negative for *Py*2087ACR1 than for v*Py*ACR21821 and *Pyme*ACR1 (Fig. 26C). Therefore, while $Cl^-$ conduction is equal in all three ChRs, conduction of larger anions such as $Br^-$ and $NO_3^-$ is better in *Py*2087ACR1. These results demonstrate that both the prasinophyte ChRs and their viral homolog are anion-conducting and, hence, the prasinophyte ChRs are the first green algal ACRs.

Microbial rhodopsins of viral origin have been demonstrated previously (Philosof and Béjà, 2013; López *et al.*, 2017; Needham *et al.*, 2019a,b), and for some, an ion channel activity was suggested (Bratanov *et al.*, 2019) or demonstrated (Zabelskii *et al.*, 2020). However, these viral rhodopsins with channel activity belong to a separate family phylogenetically close to microbial rhodopsin ion pumps and sensory rhodopsins (Yutin and Koonin, 2012; López *et al.*, 2017). The here described viral ACRs are the first viral rhodopsins showing a close phylogenetic relationship with the family of ChRs. Nonetheless, investigation of the origin and the distribution of viral rhodopsins with ion channel activity may yield a better understanding of the evolutionary advantage viruses may gain from incorporating these proteins.

## 3.3. Potential for optogenetic application

ChRs are widely used as tools to manipulate the activity of excitable cells within the discipline of optogenetics (Deisseroth and Hegemann, 2017).

Since MerMAIDs are only exhibiting large photocurrents for a short time before reaching the accumulating desensitized state under continuous illumination, they are not suitable to silence AP-firing over longer times as other ACRs (Govorunova *et al.*, 2015, 2018). Nevertheless, their unique biophysical properties enable temporally precise single AP-suppression at the onset of illumination without affecting subsequent neuronal activity as demonstrated in experiments with MerMAID6 (Fig. 29; Oppermann *et al.*, 2019), which was chosen as it exhibits the largest transient photocurrent amplitudes in HEK293 cells (Fig. 12D).

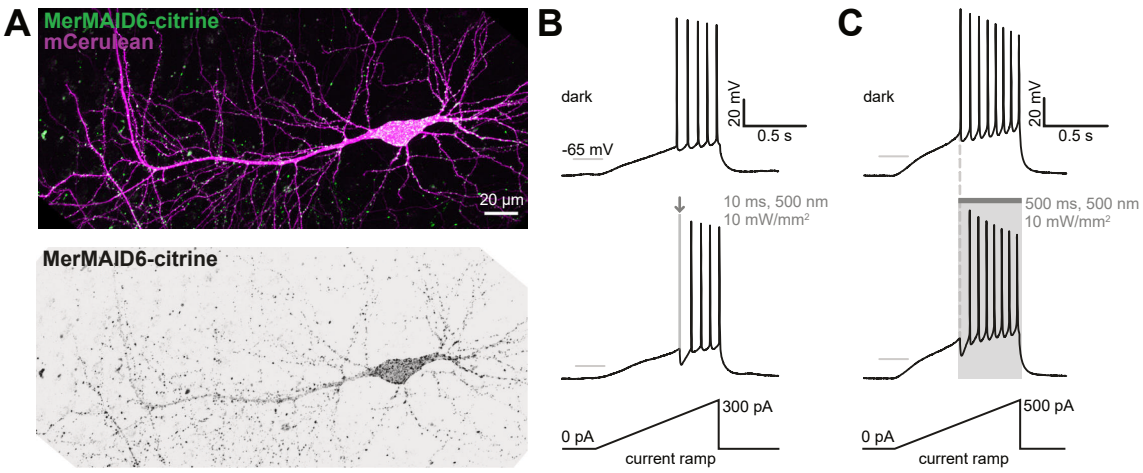


**Figure 29.: Optogenetic application of MerMAID6. A,** (left) Stitched maximum intensity projections of two-photon images of a CA1 pyramidal neuron expressing MerMAID6 fused to Citrine (green) five days after electroporation. mCerulean (magenta) was co-electroporated and is located intracellularly. (right) Inverted gray value of the left image to indicate fluorescence intensity. **B, C,** Voltage responses to injection of a depolarizing current ramp. MerMAID6 was activated 5 ms before action potential onset by application of 500 nm-light (10 mW mm$^{-2}$) for 10 ms (B) or 500 ms (C), indicated by a gray line or arrow above and gray background, to shunt single action potential spikes. The data was collected by Silvia Rodriguez-Rozada. Adapted from Oppermann *et al.* (2019).

MerMAID6 was fused to Citrine and co-electroporated with mCerulean as a cytosol marker in CA1 pyramidal neurons of hippocampal slices. The ChR expressed well, although the membrane-localization was spotty (Fig. 29A) as observed for other ACRs (Mahn *et al.*, 2018). After determining the rheobase[2] in the dark, a 500 nm-light pulse of 10 ms (Fig. 29B) or 500 ms (Fig. 29C) was applied, synchronized with the first action potential (AP). Both treatments resulted in the suppression of the first AP without affecting subsequent spiking (Fig. 29B, C). These experiments demonstrate that MerMAIDs are suitable for temporally precise inhibition of AP-firing at the onset of illumination.

The prasinophyte ACRs, on the other hand, have larger photocurrents applicable for optogenetic silencing of neuronal or cardiac action potentials over extended periods. Especially *Py*2087ACR1 might offer an advantage compared to other ACRs, as its fast off-kinetics (Fig. 25E) allow for inhibition of electrical activity at higher frequencies, similar to ZipACR (Govorunova *et al.*, 2017b), but less disturbing for the chloride balance due to smaller photocurrent amplitudes.

With optogenetics becoming more and more established, optogenetic experiments become increasingly sophisticated, and experimenters may want to use optical actuators such as microbial rhodopsin ion pumps or ChRs as well as optical reporters simultaneously. A general obstacle in pairing up actuators and reporters is their spectral overlap. Ideally, the actuator is not activated by the light used for the reporter, as otherwise, the read-out results are not conclusive due to overlapping activity, drastically limiting the available options for

[2]the current injection needed to elicit action potential firing

actuators and reporters.

The accumulation of the desensitized state in MerMAIDs, resulting in a short period of electrical activity, enables experiments that require temporally precise suppression of AP-firing with a subsequent read-out of reporters over longer times to analyze neuronal activity. Additionally, spectrally overlapping reporters can be used, as MerMAIDs would not be constitutively active. Similar experiments could also be possible with the strongly desensitizing cryptophyte CCRs (Sineshchekov *et al.*, 2020b).

The low electrical activity of MerMAIDs during continuous illumination may further allow their use to manipulate the cellular resting potential at a sub-threshold level. The resting potential is known to regulate, among many things, cell proliferation, cell migration and differentiation, as well as cell-cell-communication (Sachs *et al.*, 1974; Adams and Levin, 2013; Levin, 2014; Abdul Kadir *et al.*, 2018). It is affected by the ionic composition on the intra- and extracellular side. Therefore, an easy way to manipulate the resting membrane potential in cell culture is to exchange the extracellular buffer (Bonzanni *et al.*, 2020). However, *in vivo*, this is difficult. Hence, light-activated ion-conducting proteins with low electrical activity may offer the potential to manipulate the resting membrane potential in the living animal non-invasively.

## 3.4. Physiological function of algal and viral ACRs

Predictions of the physiological function of metagenomically identified proteins are generally tricky and highly speculative as information about the organism the proteins are found in is scarce, and sequences may be incomplete. Nonetheless, for metagenomic data sets, environmental info is gathered and can be helpful for interpretations.

Findings by Govorunova *et al.* (2020) and Andrey Rozenberg (Rozenberg *et al.*, 2020) indicate stramenopiles as the carrier of MerMAID-like rhodopsins, a diverse group of phototrophic picoeukaryotes abundant in marine environments (Massana *et al.*, 2004).

MerMAID-like rhodopsins were mainly found in samples gathered at stations of the *Tara* Oceans project in the Atlantic and Pacific oceans close to the equator (Fig. 30A). The sea surface temperatures (SST) in these regions range from approximately 20 °C to 28 °C (Emery, 2015). However, MerMAID-like sequences were also found close to the Antarctic and in the Mediterranean sea (Fig. 30A), where SSTs are approximately 5 °C and 18 °C, respectively (Emery, 2015). Most MerMAID-like sequences were identified in surface-level water in depths of up to 200 m (Fig. 30B). MerMAIDs show the highest activity upon illumination with green light of approximately 500 nm (Fig. 12B, C) and are therefore optimized to light perception in shallow and deep water, where blue and green light penetrates deepest (Pinhassi *et al.*, 2016). In surface seawater, $Cl^-$ is the most abundant anion (Pilson, 2013), suggesting it as the primary contributing ion to MerMAIDs photocurrents in the marine environment, following the here observed high selectivity for

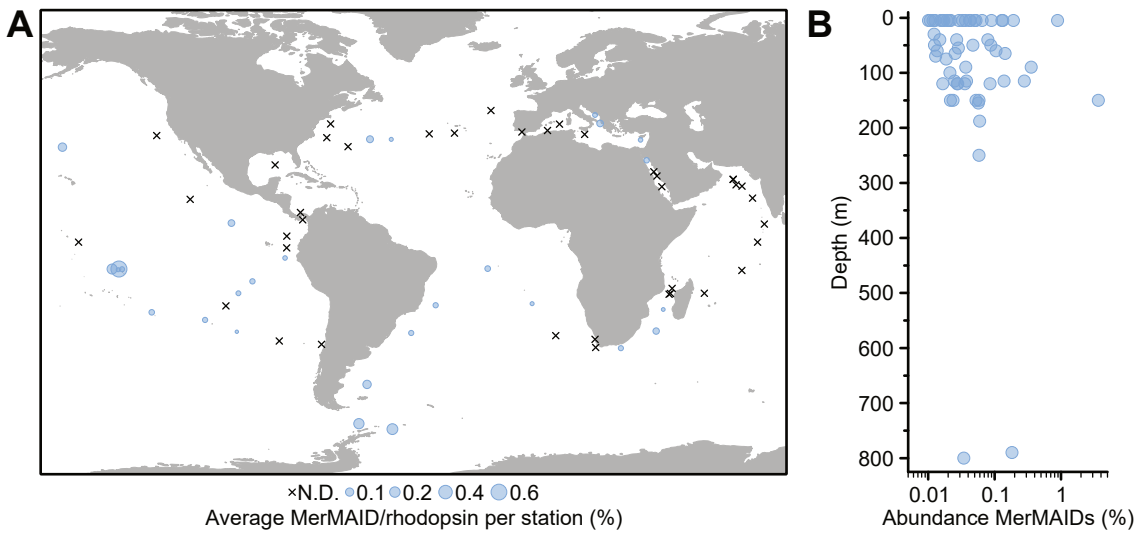


**Figure 30.: Global distribution and depth profile of MerMAIDs. A,** Global distribution and relative abundance of MerMAID-like rhodopsins. Different-sized circles indicate the estimated average MerMAID/rhodopsin ratio at stations of the *Tara* Oceans project. Crosses mark stations where MerMAID-like rhodopsins were not detected (N.D.). **B,** Depth profile of MerMAIDs. The abundance of MerMAID-like proteins (MerMAID-like/total rhodopsins) was paired with environmental metadata of the *Tara* Oceans samples to produce depth profiles. Circles indicate individual data points. The data was collected and analyzed by José Flores-Uribe. Adapted from Oppermann *et al.* (2019).

anions (Fig. 13C, D).

ChRs were first identified in *C. reinhardtii* (Nagel *et al.*, 2002, 2003), a chlorophyte freshwater algae, where they are associated with phototactic and -phobic responses (Sineshchekov *et al.*, 2002). The proteins are accumulated in the cell membrane of the algae above the eyespot (Kreimer, 2009; Engel *et al.*, 2015). Cation-influx through the ChRs at the eyespot triggers flagellar currents when exceeding a threshold level, modulating the flagellar beating (Holland *et al.*, 1996). While swimming, the alga rotates around its axis (Foster and Smyth, 1980), resulting in an oscillating activation of the ChRs, which are blocked from the light from one side by a layer of carotenoid granules (Kreimer, 2009).

However, the photocurrents of MerMAIDs are unique compared to most described ChRs regarding the transient photocurrent desensitization. While in other ChRs, the desensitized stationary photocurrents are of considerable size (Nagel *et al.*, 2003; Schneider *et al.*, 2015; Govorunova *et al.*, 2015), they are almost not existent in MerMAIDs (Fig. 12A, E). Therefore, the question is, what the physiological function of a quickly and nearly completely desensitizing light-activated ion channel could be in a marine organism.

When discussing potential physiological functions, it has to be considered that the sunlight's intensity decreases strongly in seawater with increasing depth (Jewson, 1977). However, single-photon absorption may be sufficient for directional changes (Foster and Smyth, 1980). At low light intensities, MerMAIDs exhibit non-desensitizing photocurrents of low amplitude, and for transient photocurrents to appear, high light intensities are

required (Fig. S4). Therefore, in the natural environment, between 5 m and 200 m in seawater, the stationary currents are the relevant part of MerMAID photocurrents.

### 3.4.1. ACRs and phototaxis

Surface seawater has a $Cl^-$-concentration of approximately 560 mM (Pilson, 2013). Intracellular chloride concentrations vary between 30 mM and 50 mM in the halotolerant alga *Daniella salina* resilient to a concentration of up to 5.5 M NaCl (Karni and Avron, 1988) but are lower in algae of less saline environments (Findlay, 1959; E. a. C. MacRobbie, 1970; Tazawa *et al.*, 1974).

Even when assuming a high $[Cl^-]_i$ of 50 mM for the MerMAID-expressing species (MES), an equilibrium potential for $Cl^-$ of approximately $-62$ mV can be calculated using the Nernst equation (Eq. 4.4). However, as the MES are found in a less saline environment than *D. salina*, $[Cl^-]_i$ is probably lower and, therefore, $E_{\mathrm{Nernst}}$ more negative.

For *D. salina*, a resting membrane potential (RP) of approximately $-100$ mV was estimated (Oren-Shamir *et al.*, 1990). However, the RP can be even more negative (Findlay, 1959) and reaches up to $-170$ mV in *Acetabularia crenulata* (Gradmann, 1970). Assuming similar RPs for the MES, the electrochemical driving force acting on $Cl^-$ would be approximately $-20$ mV to $-100$ mV, leading to its efflux from the cell. Outward $Cl^-$ flow leads to a membrane potential depolarization and can initiate an action potential in algae. However, an active transport system for $Cl^-$ and other AP-contributing ions would be required to maintain their gradients across the plasmalemma as proposed for other algae (Gutknecht, 1965; E. A. C. MacRobbie and Dainty, 1958).

In *Nitella* and *Chara* algae, $Ca^{2+}$ influx triggers depolarizing outward currents of $Cl^-$ (Lunevsky *et al.*, 1983; Shiina and Tazawa, 1987; Shiina and Tazawa, 1988). Potentially, a similar mechanism could explain the observed delayed flagellar currents in *C. reinhardtii* (Harz *et al.*, 1992). The following amplifying ion transporter may be voltage- or ligand-gated. $Cl^-$ currents across the membrane of *C. reinhardtii* cells were previously shown at low $[Cl^-]_e$ (Ehlenbeck, 2002; Hegemann and Berthold, 2009). The possible contribution of these $Cl^-$ currents to the phototactic behavior of the alga could be evaluated in measurements of the phototaxis using a light scattering system (Uhl and Hegemann, 1990) and adding for example 9-anthracenecarboxylic acid or ethacrynic acid to the cell culture to block the activity of $Cl^-$ ion channels.

Considering the outlined assumptions of a highly negative RP paired with a $Cl^-$ reversal potential that is more positive than the RP, ACRs are well-suited to initiate phototactic responses. Neither post-synaptic currents (Pankratov and Krishtal, 2003) nor photoreceptor currents at the eyespot of *C. reinhardtii* (Harz *et al.*, 1992) exceed a few pA. Therefore, the low stationary activity of MerMAIDs could be sufficient as an AP-trigger at an electrochemical driving force as large as $-100$ mV. As identified in the marine diatome *Odontella sinensis* (Taylor, 2009), voltage-gated ion channels may subsequently activate and amplify

the signal.

In prasinophytes, the appearance of ACRs coincides with that of putative and proven CCRs, as previously reported for cryptophyte algae (Govorunova *et al.*, 2015, 2016b). Furthermore, only species with an eyespot carried genes coding for ChRs (Rozenberg *et al.*, 2020). Therefore, in some prasinophyte species, CCRs and ACRs may both participate in the phototaxis. However, simultaneous activation of CCRs and ACRs would negate any de- or hyperpolarizing shifts of the membrane potential. Therefore, their activation most likely occurs at different time points.

Activity regulation can either occur on the expression level by controlling the transcription of genes or based on the proteins' properties, such as spectral sensitivity or photocurrent rectification. A potential regulation may also arise from the carboxy-terminal domain as reported for *Cr*ChR1, where it was critical for reversible phosphorylation in response to changing light intensities (Böhm *et al.*, 2019). The carboxy-terminal domain of prasinophyte ACRs shows homology to HK response regulator domains (Fig. S3) but is, supposedly, rendered nonfunctional due to the substitution of an aspartate residue critical for autophosphorylation (Fig. S3; Rozenberg *et al.*, 2020). However, the phosphorylation-independent activity of response regulators has been demonstrated several times (Perron-Savard *et al.*, 2005; Ruiz *et al.*, 2008; Desai and Kenney, 2017). Furthermore, the domain could be a trafficking signal in the algae, regulating the cellular localization of the ACRs (Awasthi *et al.*, 2016).

### 3.4.2. Beyond the action potential

Nevertheless, ACRs and CCRs coinciding in the same species may indicate the participation of ChRs in physiological functions beyond the generation of action potentials for phototactic responses. Furthermore, for MerMAIDs to act as phototactic light sensors, potentially, unreasonably high expression levels would be required to generate pA-photocurrents in an alga.

However, the regulation of the $Cl^-$-flux is vital for other physiological functions as well. A hyperpolarization- and $pH_e$-sensitive chloride efflux across the plasmalemma was suggested to maintain the proton-motive force in *Chara inflata* cells, enabling the cells to uphold ATP-production at varying external pH (Tyerman *et al.*, 1986a,b). In *Conocephalum conicum*, the liverwort, action potentials upon damaging and non-damaging stimuli triggered increased $O_2$-consumption by respiration, supposedly increasing the available ATP levels for a short time (Dziubinska *et al.*, 1989).

Though $Cl^-$-conducting ion channels are not only located in the plasmalemma of algae and other plant cells but also membranes of the tonoplast and other organelles (Tester, 1990). Passive and active $Cl^-$ fluxes across the tonoplast are associated with the regulation of turgor and osmosis (Bisson and Gutknecht, 1977; Wendler *et al.*, 1983) and were found to be dependent on $Ca^{2+}$ fluxes (Lunevsky *et al.*, 1983; Kikuyama, 1986, 1989). While

these insights were mostly gathered from multicellular algae and even a moss, they allow us to appreciate the many-fold importance of $Cl^-$ in the cellular physiology of plant and algal cells.

Light-dependent $Cl^-$ currents could indirectly help maintain the proton-motive force for ATP production and other cellular mechanisms similar to the active regulation via *Hs*BR-mediated $H^+$ currents (Oesterhelt and Stoeckenius, 1973; Matsuno-Yagi and Mukohata, 1977). Furthermore, a light-dependent cell size regulation via light-activated $Cl^-$ currents across the tonoplast membrane could benefit the organism as it could allow the increase of photosynthetic surface in optimal conditions.

### 3.4.3. Viruses and microbial rhodopsins

Viruses are considered to be the most abundant biological entities (Brum *et al.*, 2015; Wigington *et al.*, 2016; Schulz *et al.*, 2020), impacting microbial communities on a large scale as they change the host's metabolism, transfer genes (a driver of evolution), and reduce population sizes (Suttle, 2007; Zimmerman *et al.*, 2020). Previously, viruses infecting marine cyanobacteria have been found to carry Photosystem-coding genes, suggesting a direct intervention of the viruses in their hosts' photosynthesis to ensure energy production (Mann *et al.*, 2003; Lindell *et al.*, 2004; Sharon *et al.*, 2009). Moreover, viral proteorhodopsins and other viral-like rhodopsins were found abundant in marine metagenomes (Yutin and Koonin, 2012; Philosof and Béjà, 2013; López *et al.*, 2017; Needham *et al.*, 2019a), suggesting not only interference with the energy production but also potentially behavioral responses to light of the host. While so far reported viral-like rhodopsins are similar to microbial rhodopsin ion pumps (Yutin and Koonin, 2012; López *et al.*, 2017; Needham *et al.*, 2019b), recently, a potential function as ion channels was suggested for some of them (Bratanov *et al.*, 2019; Zabelskii *et al.*, 2020).

Here, the initial electrophysiological characterization of a viral-like rhodopsin from marine giant viruses with high similarity to ChRs, v*Py*ACR21821, has been described, and its function as an ion channel was demonstrated, as well as for the closely related v*Py*ACR2164382 (Ch. 2.3). Andrey Rozenberg demonstrated the acquisition of the ChR genes by the marine giant viruses from their prasinophyte hosts via lateral gene transfer (Rozenberg *et al.*, 2020).

However, why do these viruses carry genes coding for ChRs in their genome? Their algal homologs are probably part of the prasinophytes' visual system (Rozenberg *et al.*, 2020). Therefore, expression of the viral ChRs in the algal host would interfere with the phototactic behavior, guiding the host organism towards environments advantageous for the replication of the virus, as indicated by the action spectrum of the v*Py*ACR21821 shifted hypsochromic compared to the prasinophyte ChRs (Fig. 25B, C).

In animal viruses such as influenza A virus, HIV-1, or coronaviruses, viroporins are essential parts of the virus life cycle. Viroporins are short proteins that oligomerize in the

host cell membrane, forming pores, ultimately leading to the host organism's demise and release of virus particles (Gonzalez and Carrasco, 2003; Nieva *et al.*, 2012). Considering the cytotoxicity observed in mammalian cells for the full-length and, to some degree, also the truncated viral ACRs (Fig. 24 and S11), a function similar to viroporins seems plausible. This process's light-dependence may offer a selective advantage for the virus as the cell lysis would be initiated in light conditions where potentially an abundance of host organisms is available.

## 3.5. Outlook

While the here described characterization of the MerMAIDs demonstrates the critical function of a conserved cysteine residue for the near-complete desensitization, it is still unclear what the underlying molecular mechanism is. Nevertheless, the recently described cryptophyte CCRs with similar properties to the MerMAIDs (Sineshchekov *et al.*, 2020b) indicate a universal function of the residue in strongly desensitizing ChRs. As also among the labyrinthulea and haptophyte ACRs representatives with strongly desensitizing transient photocurrents were reported (Govorunova *et al.*, 2020), this phenomenon may occur more often than expected. Therefore, the elucidation of the molecular mechanism of near-complete desensitization should be a focus of future studies.

The cysteine may suppress conformational changes of $C_{15}$=N by direct interaction with the RSB in the wildtype, as suggested by electrophysiology and RR spectroscopy. However, direct evidence is missing for this hypothesis. Therefore, a spectroscopic investigation of MerMAID1-C84T should be conducted, applying UV/vis absorption and vibrational spectroscopy for a complete characterization of this substitution's effects. MD calculations should be performed to simulate the photoactivation in the wildtype and cysteine-substituted protein to gather insight into this residue's function in the wildtype protein. These calculations may be hampered, though, as currently, only homology models are available for strongly desensitizing ChRs, which may not resemble the actual structure. Therefore, efforts may be made to resolve the 3D structure of a MerMAID channelrhodopsin and a cryptophyte CCR counterpart, as well as their cysteine-substituted variants. While this approach is time- and cost-intensive, it would be beneficial for simulation studies to acquire the real configuration of these proteins' Schiff base region.

The identification of the MerMAIDs and prasinophyte ChRs demonstrates the value of functional metagenomics for the study of ChRs. Not only can the understanding of these proteins be advanced, but also their applicability in optogenetic studies is increased as ChRs with new properties are identified. While many CCRs are already available, ChRs preferably conducting $K^+$ or $Ca^{2+}$ are still highly requested. Furthermore, a general goal for the engineering of optogenetic tools is to shift their absorption towards red or infrared light, as the penetration of tissue is greatly enhanced at wavelengths above 600 nm, allowing to

activate optogenetic tools deeper within the brain (Barun *et al.*, 2007). Therefore, future metagenome studies could focus on identifying not only ChRs in general but also ChRs with specific properties. While this may be more difficult for specific ion selectivities, red-light-absorbing ChRs could potentially be identified by using a consensus sequence of available rhodopsins absorbing light >580 nm as a query for searches in metagenomic databases. Acquired sequences could be further evaluated and selected, using machine-learning-based approaches established to predict absorption wavelengths (Karasuyama *et al.*, 2018).

ACRs have seen much attention since their discovery (Govorunova *et al.*, 2015), but mainly as optogenetic tools to shunt neuronal activity (Mahn *et al.*, 2018). However, while the investigation of the physiological function of especially *Cr*ChR1 and *Cr*ChR2 is steadily, albeit slowly, progressing (Govorunova *et al.*, 2004; Berthold *et al.*, 2008; Böhm *et al.*, 2019), only little is known about phototaxis in marine algae and the role ACRs play in it (Sineshchekov *et al.*, 2005). The apparent abundance of ACRs in marine microbial algae may increase interest in the elucidation of their physiological function. Therefore, it would be advantageous to establish the CRISPR/Cas method in *G. theta*, as done previously for *C. reinhardtii* (Greiner *et al.*, 2017), enabling the knock-out of ACR genes in the alga. However, the abundance of rhodopsin genes in *G. theta* would obstruct the interpretation of data gathered from knock-outs. Therefore, it might be advantageous to establish a new model organism for the elucidation of ACR-function *in vivo*. The effect of the gene knock-out could subsequently be analyzed by electrophysiology on the organism (Sineshchekov *et al.*, 2020a).

Furthermore, despite the progress made in elucidating the physiological function of ChRs in *C. reinhardtii*, the potentiating signaling cascade following activation of ChRs is still not clear. A $Ca^{2+}$-activated $Cl^-$ channel seems plausible as a potentiator. Therefore, future experiments may include identification of genes coding for such ion channels and their knock-out in *C. reinhardtii*, followed by an investigation of the phototaxis paired with electrophysiology of the alga.

# 4. Methods

## 4.1. Sequences

Metagenomically identified sequences (Tab. 2) were codon-optimized (human and mouse) and synthesized (GenScript, Piscataway, NJ). For use in experiments, sequences were sub-cloned into various plasmid backbones (Tab. 3) using restriction cloning (Ch. 4.3.3) or Gibson assembly (Ch. 4.3.2). All used sequences are available at GenBank (NCBI, Bethesda, MD) and Addgene (Watertown, MA).

**Table 2.: List of used constructs and their availability.** Constructs used in this study have been made available at GenBank (NCBI) and Addgene and can be accessed via the indicated accession numbers.

| Construct | GenBank | Addgene |
|---|---|---|
| MerMAID1 | MK914541 | 126513 |
| MerMAID2 | MK914542 | 126514 |
| MerMAID3 | MK914543 | 126515 |
| MerMAID4 | MK914544 | 126516 |
| MerMAID5 | MK914545 | 126517 |
| MerMAID6 | MK914546 | 126518 |
| MerMAID7 | MK914547 | 126519 |
| *Pyme*ACR1 | MT353682 | 153031 |
| *Py*2087ACR1 | MT353681 | 153032 |
| v*Py*ACR2164382 | MT353684 | 153029 |
| v*PY*ACR21821 | MT353683 | 153030 |

**Table 3.: List of used plasmids.** Included antibiotics resistance and intended experimental use are indicated.

| Plasmid | Resistance | Intended use |
|---|---|---|
| pmCherry-C1 | Kanamycin | Heterologous expression in HEK293 and ND7/23 cells |
| pEYFP-N1 | Kanamycin | Heterologous expression in HEK293 and ND7/23 cells |
| pAAV2 | Ampicilin | Heterologous expression in neurons |
| pPiC-Z | Zeocin™ | Heterologous expression in *Pichia pastoris* |

## 4.2. Plasmid amplification

Plasmids were amplified using chemocompetent XL1-Blue *Escherichia coli* cells (Agilent Technologies, Santa Clara, CA). Growth media used for *E. coli* cultures were prepared (Tab. 4) and thermally sterilized (121 °C, 30 min). For LB agar plates, 15 ml to 25 ml liquid LB agar were poured into Petri dishes. When used for selection, growth media were supplemented with the appropriate antibiotic (Tab. 3). For the amplification of constructs in the pPiC-Z plasmid backbone, low-salt LB and low-salt LB agar was used. If not stated otherwise, cultures were grown at 37 °C. Liquid cultures were additionally rotated at 180 rpm.

**Table 4.: Growth media for the cultivation of *E. coli*.**

| Medium | Recipe | Source |
|---|---|---|
| LB | 2 % Lennox LB broth | Carl Roth |
| | 0.05 % NaCl | Carl Roth |
| | $ddH_2O$ | |
| | pH 7.5 (NaOH) | |
| low-salt LB | 2 % Lennox LB Broth | Carl Roth |
| | $ddH_2O$ | |
| | pH 7.5 (NaOH) | |
| (low-salt) LB agar | (low-salt) LB with | |
| | 1.5 % Agar | Carl Roth |

### 4.2.1. Preparation of chemocompetent *E. coli*

Chemocompetent XL1-Blue *E. coli* cells were prepared using TfbI and TfbII buffers (Tab. 5). The buffers were sterile filtered, and stored at 4 °C until further use. Chemicals were acquired from Carl Roth (Karlsruhe, Germany), Fluka (Buchs, Switzerland), Merck (Darmstadt, Germany), and Sigma-Aldrich (Munich, Germany). All further steps were performed under sterile conditions.

Chemocompetent cells from the previous batch were spread on an LB agar plate without antibiotics and grown overnight. Colonies were picked to grow in 4 ml LB without antibiotics overnight. From the preculture, 2 ml were used to inoculate 200 ml LB without antibiotics in a 1 l flask with baffles. The main culture was grown to an optical density at 600 nm ($OD_{600}$) of 0.5. Subsequently, the culture was incubated for 15 min on ice, transferred into centrifuge buckets and harvested (10 min, 3000 *g*, 4 °C). The supernatant was discarded, and the cell pellet resuspended in 30 ml ice-cold TfbI buffer per 100 ml main culture by slowly shaking for 30 min on ice. After pelleting the cells in 50 ml falcons (10 min, 3000 *g*, 4 °C), cell pellets were carefully resuspended in 3.3 ml ice-cold TfbII

**Table 5.: Buffers for the preparation of chemocompetent XL1-Blue *E. coli* cells.**

| Medium | Recipe | Source |
|---|---|---|
| TfbI | 30 mM Potassium acetate | Merck |
| | 100 mM RbCl | Sigma-Aldrich |
| | 2 mM $CaCl_2$ 2 $H_2O$ | Carl Roth |
| | 15 % Glycerol | Carl Roth |
| | $ddH_2O$ | |
| | pH 5.8 (acetic acid) | |
| | 50 mM $MnCl_2$ | Fluka |
| TfbII | 10 mM MOPS | Carl Roth |
| | 10 mM RbCl | Sigma-Aldrich |
| | 75 mM $CaCl_2$ 2 $H_2O$ | Carl Roth |
| | 15 % Glycerol | Carl Roth |
| | $ddH_2O$ | |
| | pH 6.8 (KOH) | |

buffer. Aliquots of 50 µl were prepared, immediately frozen in liquid nitrogen, and stored at −80 °C until further use.

### 4.2.2. Transformation of *E. coli*

Chemocompetent XL1-Blue *E. coli* were transformed with plasmid DNA using the heat shock method. Therefore, aliquots of competent cells were thawed on ice. After adding 5 µl plasmid DNA, the cells were incubated for 7 min on ice, followed by a heat shock (42 °C for 1 min). The transformation mix was left on ice for at least 7 min before 500 µl LB without antibiotics were added. After 1 h incubation at 37 °C under continuous shaking, the cells were harvested and resuspended in a small volume LB. The cell suspension was spread out on LB agar plates supplemented with antibiotics, and incubated overnight.

### 4.2.3. DNA extraction

Single colonies of transformed *E. coli* clones were selected and grown in 4 ml to 250 ml LB medium supplemented with antibiotics. After incubation overnight, liquid cultures were harvested by centrifugation, and the plasmid DNA was purified using commercially available kits (NuceloSpin Plasmid EasyPure or NuceloBond Xtra Midi, Macherey-Nagel, Düren, Germany). The DNA concentration was determined using a photometer (BioPhotometer Plus, Eppendorf, Hamburg, Germany), and samples were stored at −20 °C.

## 4.3. Plasmid modification

Sequences were sub-cloned into different plasmid backbones for expression in various cell systems (Tab. 3) using restriction cloning (Cohen *et al.*, 1973) or Gibson assembly (Gibson *et al.*, 2009). Single residues were substituted using site-directed mutagenesis (Carter, 1986). Plasmid modifications were verified by sequencing (LGC Genomics, Berlin, Germany) and GENtle v1.9.4 or SnapGene v4.3 (GSL Biotech LLC, Chicago, IL) were used to inspect sequencing results. Enzymes were acquired from Thermo Fisher Scientific (Waltham, MA), New England Biolabs (Ipswich, MA), and Agilent Technologies. For electrophysiological experiments and confocal imaging, ChRs were expressed as fusion constructs with the fluorophores mCherry (Shaner *et al.*, 2004) or eYFP (Kremers *et al.*, 2006). For neuronal recordings, the fluorophore was exchanged for Citrine (Griesbeck *et al.*, 2001).

### 4.3.1. PCR Primer design

Gibson assembly and site-directed mutagenesis are polymerase chain reaction (PCR)-based and therefore require the design of specific, short DNA sequences serving as PCR primers. For Gibson assembly, overlapping primers were designed using NEBuilder v2.1.0 (New England Biolabs). PCR primer for site-directed mutagenesis were designed using GENtle v1.9.4 or SnapGene v4.3 to have a melting temperature ($T_m$) of approximately 62 °C, calculated using the OligoAnalyzer v3.1 (Integrated DNA Technologies, Leuven, Belgium). Primer pairs were designed to overlap at the substitution-position, flanking it by at least 9 base pairs 3' and 5'. All primers were ordered from Integrated DNA Technologies.

### 4.3.2. Gibson Assembly

For the assembly of larger DNA fragments, the Gibson assembly method was used (Gibson *et al.*, 2009). DNA fragments were generated by PCR (Tab. 6) using either an S1000 Thermal Cycler (Bio-Rad Laboratories GmbH Deutschland, München, Germany) or a peqSTAR thermal cycler (VWR Life Science Competence Center, Erlangen, Germany). A temperature gradient was applied for the annealing step to ensure efficient fragment amplification. Four aliquots of the PCR mix (Tab. 6) were subjected to a different temperature, respectively. After the PCR, methylated template DNA was removed, if necessary, by incubation of the PCR mix with 1 µl DpnI (30 min, 37 °C).

Amplification of the DNA fragments was verified by gel electrophoresis (15 min, 120 V) using 1.0 % to 1.2 % w/v agarose gels prepared with TAE buffer (Carl Roth). The amplified DNA was mixed with 5 µl SYBR-Green (Thermo Fisher Scientific) for staining and loaded onto the gel together with a DNA ladder (O'GeneRuler DNA Ladder Mix, Thermo Fisher Scientific). DNA fragments of expected sizes were purified from the gel using a commercial

**Table 6.: Standard protocol for amplification of Gibson-ready DNA fragments.** Components of the PCR reaction were mixed as indicated (left) and were divided into four aliquots. The mix was subjected to a temperature protocol in a thermocycler (right). Steps 2 to 4 of the temperature protocol were repeated 25 to 30 times. For step 3, a temperature gradient was set, and each aliquot was subjected to a different temperature. Dimethyl sulfoxide (DMSO) was added to the PCR mix when the target site had a high guanine and cytosine content.

| Mix | | Protocol | | |
|---|---|---|---|---|
| Component | Volume | Step | Temperature | Duration |
| 5x HighFidelity (HF) buffer | 20 µl | 1 | 95 °C | 5 min |
| 2 mM dNTPs | 10 µl | 2 | 95 °C | 45 s |
| 10 µM Primer mix | 10 µl | 3 | 56 °C to 66 °C | 30 s |
| 40 ng µl$^{-1}$ Template DNA | 2 µl | 4 | 72 °C | 6 min |
| Phusion DNA Polymerase | 1 µl | 5 | 72 °C | 10 min |
| $ddH_2O$ | ad. 100 µl | 6 | 4 °C | ∞ |

**Table 7.: Recipes for ISO buffer and master mix used in Gibson assemblies.** Aliquots of the buffer and the master mix were prepared and stored at −20 °C until further use. Abbreviations: DTT, dithiothreitol; ISO, isothermal; NAD, nicotinamide adenine dinucleotide; PEG, polyethylene glycol.

| 5x ISO buffer | | Gibson Master Mix | |
|---|---|---|---|
| Component | Volume | Component | Volume |
| 1 M Tris-HCl pH 7.5 | 3 ml | 5x ISO buffer | 320 µl |
| 2 M $MgCl_2$ | 150 µl | 10 U/µl T5 exonucelase | 0.64 µl |
| 100 mM dNTPs | 240 µM | 2 U/µl Phusion DNA polymerase | 20 µl |
| 1 M DTT | 300 µM | 40 U/µl *Taq* ligase | 160 µl |
| PEG-8000 | 1.5 g | $ddH_2O$ | ad 1.2 ml |
| 100 mM NAD | 300 µM | | |
| $ddH_2O$ | ad 6 ml | | |

kit (Macherey-Nagel).

For the assembly the DNA fragments, 60 ng of the plasmid backbone and 120 ng of each insert were mixed with the Gibson assembly master mix (Tab. 7) and incubated (20 min, 50 °C). Subsequently, the assembly mix was transformed into chemocompetent *E. coli* cells (Ch. 4.2.2), followed by isolation of the plasmid DNA from liquid cultures (Ch. 4.2.3).

### Membrane-targeting of constructs

Membrane-targeting and expression of vPyACR21821, vPyACR2164382 were improved by subcloning them in frame with eYFP into the pEYFP-N1 plasmid backbone. Furthermore, additional sequences were added to the constructs as previously reported (Grimm

**Table 8.: Standard mix for restriction digest of plasmid DNA.** Abbreviations: AP, alkalic phosphatase; FD, fast digest.

| Digestion | | Ligation | |
|---|---|---|---|
| Plasmid DNA | 1 µg | Vector | 100 ng |
| 10x FD Buffer Green | 3 µl | Insert | 100 ng |
| FD Restriction enzyme | each 1 µl | 10x T4 DNA Ligase Buffer | 2 µl |
| Fast AP (if necessary) | 2 µl | T4 DNA Ligase | 1 µl |
| $ddH_2O$ | ad. 30 µl | $ddH_2O$ | ad. 20 µl |

*et al.*, 2018). The fluorophore eYFP was flanked by a membrane trafficking (KSRITSEGEYIPLDQIDINV; Gradinaru *et al.*, 2010) and an ER export (FCYENEV; Gradinaru *et al.*, 2008) sequence. The amino-terminus was extended by a C2C1-chimeric sequence (MDYGGALSAVGLFQTSYTLENNGSVICIPNNGQCFCLAWLKSNG; Rajasethupathy *et al.*, 2015) and the last 131 amino acids of the carboxy-terminus were truncated.

### 4.3.3. Restriction cloning

For digestion with restriction enzymes, plasmid DNA or PCR fragments were mixed (Tab. 8) and incubated (30 min, 37 °C). Generally, sequences ordered from GenScript were digested using FastDigest (FD) NheI and FD BshTI/AgeI (Thermo Fisher Scientific).

DNA digestion was verified by gel electrophoresis as described before (Ch. 4.3.2), and DNA fragments of expected sizes were purified from the gel using a commercial kit (Macherey-Nagel).

Ligation reactions were mixed (Tab. 8) and incubated for 30 min at room temperature. For amplification of ligated plasmid DNA, chemocompetent *E. coli* were transformed with 5 µl of the ligation reaction (Ch. 4.2.2) followed by isolation of the plasmid DNA from liquid cultures (Ch. 4.2.3).

### 4.3.4. Site-directed Mutagenesis

Amino acid substitutions in the proteins were achieved by the site-directed mutagenesis method (Carter, 1986). PCRs were performed using thermal cyclers (Tab. 9). Following PCR, the methylated template DNA was DpnI-digested (30 min, 37 °C). Subsequently, chemocompetent *E. coli* cells were transformed (Ch. 4.2.2), and the plasmid DNA was purified from liquid cultures (Ch. 4.2.3).

**Table 9.: Standard protocol for site-directed mutagenesis.** Components of the PCR reaction were mixed as indicated (left) and subjected to a temperature protocol in a thermocycler (right). Steps 2 to 4 of the temperature protocol were repeated 25 to 30 times. Dimethyl sulfoxide (DMSO) was added to the PCR mix when the target site had a high guanine and cytosine content.

| Mix | | Protocol | | |
|---|---|---|---|---|
| Component | Volume | Step | Temperature | Duration |
| 10x Pfu buffer | 2.5 µl | 1 | 95 °C | 5 min |
| 2 mM dNTPs | 2.5 µl | 2 | 95 °C | 45 s |
| 10 µM Primer mix | 2 µl | 3 | $T_m$ −5 °C | 30 s |
| 40 µg µl$^{-1}$ Template DNA | 1 µl | 4 | 72 °C | 6 min |
| Pfu DNA Polymerase | 1 µl | 5 | 72 °C | 10 min |
| dd$H_2O$ | ad. 25 µl | 6 | 4 °C | ∞ |
| DMSO (if necessary) | 1 µl | | | |

## 4.4. Mammalian cell culture

### 4.4.1. Cell cultivation

Human embryonic kidney (HEK) 293 cells (ECACC: 85120602; Sigma-Aldrich) or neuroblastoma-derived ND7/23 cells (ECACC: 92090903; Sigma-Aldrich) were used for all electrophysiology experiments. Before the measurements, the cells were handled under a laminar flow hood in sterile conditions. Mammalian cells were cultured 5 ml culture medium in sterile T25 cell culture flasks (TPP, Trasadingen, Switzerland) in incubators (HERAcell 240, Thermo Scientific; CB 60, Binder, Tuttlingen, Germany) at 37 °C and 5 % $CO_2$. Culture medium was prepared by supplementing Dulbeccos modified eagle medium (DMEM) with 5 % or 10 % fetal calf serum (FCS) for culturing of ND7/23 or HEK293 cells, respectively. Furthermore, 1 % penicillin/streptomycin (100 µg ml$^{-1}$) were added. DMEM, FCS and antibiotics were all acquired from Biochrome (Berlin, Germany).

When cells were 90 % confluent, they were passed into new culture flasks. Therefore, cells were detached by washing twice with phosphate buffered saline (PBS, Biochrome) and lightly tapping the flasks. After resuspending the cells in 5 ml culture medium, cells were counted using a Luna automated cell counter (Logos Biosystems, Villeneuve d'Ascq, France) and seeded with a concentration of $2.5 \times 10^5$ cells in 5 ml culture medium until passage 30 was reached.

### 4.4.2. Long term storage

For long-term storage of mammalian cells, $2 \times 10^6$ cells were transferred into 1.5 ml DMEM supplemented with 20 % FCS and 10 % DMSO, frozen at a rate of −1 °C min$^{-1}$ using a CoolCell (Biozym Scientific GmbH, Hessisch Oldendorf, Germany) and stored at −80 °C

or in liquid nitrogen for storage times exceeding 2 years.

To recover stored cells, they were rapidly thawed at 37 °C in a water bath and transferred to 10 ml recovery medium (DMEM with 20 % FCS). After centrifugation for 5 min at 25 *g* to remove DMSO, cells were resuspended carefully in 5 ml recovery medium and cultured in sterile T25 cell culture flasks. After one day, the recovery medium was replaced with culture medium to remove residual DMSO and dead cells.

### 4.4.3. Coating of coverslips

For experiments, cells were seeded on 15 mm coverslips (Thermo Fisher Scientific), coated with sterile-filtered poly-D-lysine (PDL; Sigma-Aldrich) to improve cell attachment and growth. Therefore, up to 400 coverslips were covered with 1 N HCl and incubated (72 h, 120 rpm). The pH was neutralized by thoroughly washing with $ddH_2O$. Subsequently, the coverslips were incubated with 70 % EtOH (24 h, 120 rpm), which was then replaced with a small volume of 95 % EtOH.

The following steps were performed under sterile conditions using a laminar flow hood. Each coverslip was flamed and allowed to cool down, followed by at least 1 h incubation at room temperature in a 50 µg ml$^{-1}$ PDL solution. After washing with sterile $ddH_2O$, the coverslips were spread on sterile tissue to dry under UV-illumination for 30 min and stored until further use in a sterile Petri dish in the dark.

### 4.4.4. Seeding and transfection

Two to three days before the experiments, up to three PDL-coated coverslips were placed in 35 mm Petri dishes (TPP). Between $0.5 \times 10^5$ to $1.0 \times 10^5$ cells were seeded in 2 ml culture medium with 1 µM all-*trans* retinal. One day after seeding, cells were transiently transfected by lipofection (Felgner *et al.*, 1987) using the FuGENE HD transfection reagent (Promega, Madison, WI). After 15 min incubation at room temperature, a mixture of 250 µl DMEM, 6 µl transfection reagent, and 2 µg plasmid DNA was added in drops to each Petri dish. The cells were incubated with the transfection mixture for at least one day before measurements were performed.

### 4.4.5. Preparation of retinal stock solution

Stock solutions of all-*trans* retinal were prepared at dim light as follows. Powdered all-*trans* retinal (1 g, 98 % purity; Sigma-Aldrich) was diluted in 10 ml isopropanol. The concentration $c$ was determined from UV/vis absorption spectra ($\lambda_{max} = 380$ nm) according to equation 4.1, where $\epsilon$ is the molar extinction coefficient of all-*trans* retinal (42 880 M$^{-1}$ cm$^{-1}$). Aliquots of 1 ml were prepared and stored at −80 °C until further use.

$$c = \frac{A}{\epsilon} \tag{4.1}$$

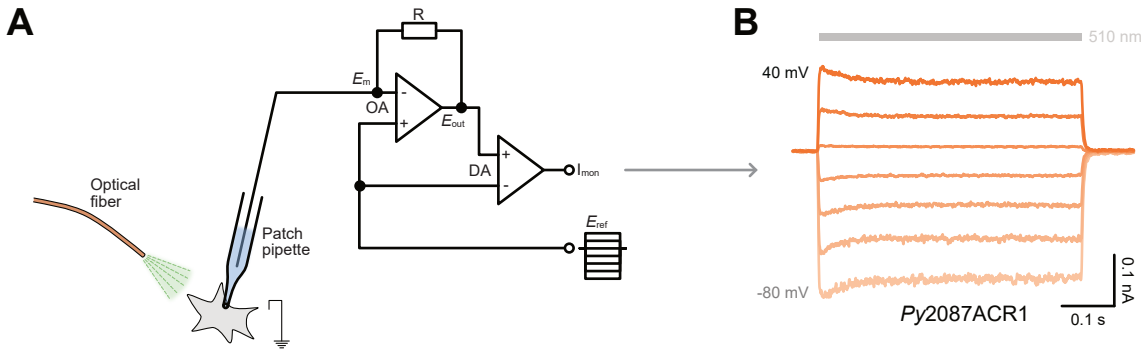


**Figure 31.: Whole-cell patch-clamp method. A,** A patch-clamp circuit for voltage-clamp measurements in the whole-cell mode. The electrode is connected to a cell via a patch pipette filled with the intracellular buffer and attached to a patch-clamp amplifier. The system is grounded via a bath electrode. The patch electrode measures the membrane potential ($E_m$), which is passed to the operational amplifier (OA) and compared to a reference potential ($E_{ref}$). The potential difference ($E_{out}$) results in a current passed through a resistor (R) into the cell and the differential amplifier (DA). In the DA, $E_{ref}$ and the output of OA are used to calculate current flowing over the membrane ($I_{mon}$). Photocurrents are elicited by light application to the patched cell via an optical fiber. Modified from Ogden and Stanfield (1994). **B,** Representative photocurrent trace of *Py*2087ACR1 to illustrate $I_{mon}$. Photocurrents were measured at membrane potentials between −80 mV to 40 mV and elicited by applying 510 nm-light.

## 4.5. Electrophysiology

Electrophysiological experiments were performed using the patch-clamp method in the whole-cell configuration (Neher *et al.*, 1978; Hamill *et al.*, 1981; Sakmann and Neher, 1984). The application of various temporally precise illumination protocols combined with different ionic conditions and holding potentials enabled the analysis of biophysical properties of elicited photocurrents.

### 4.5.1. Patch-clamp electrophysiology

The patch-clamp method was developed by Erwin Neher and Bert Sakmann and subsequently improved to measure current flowing over the membrane of single cells or patches of the membrane (Neher and Sakmann, 1976; Neher *et al.*, 1978; Hamill *et al.*, 1981). While various configurations for the patch-clamp method are available, such as excised patch variations (Hamill *et al.*, 1981), here, the whole-cell mode was used exclusively, with the membrane potential clamped (Fig. 31A).

A single chlorinated silver-wire electrode (Science Products, Hofheim, Germany) is used as a patch electrode to measure the membrane potential ($E_m$) and inject current. A second chlorinated silver-wire electrode is connected to the extracellular buffer serving as the ground electrode. A 1.5 % agar bridge (140 mM NaCl) was used to prevent $Cl^-$-leakage, potential jumps upon bath exchange, and redox reactions at the bath electrode.

Electrodes were prepared from a polished silver wire with a diameter of 0.64 mm for bath and 0.25 mm for patch electrodes. For an even AgCl-coating, enabling reversible electron

flow in $Cl^-$-containing buffers (Eq. 4.2), electrodes were connected to a power supply, and dipped into a 3 M KCl buffer. Subsequently, 1.2 V was applied for at least 10 min.

$$Ag + Cl^- \longleftrightarrow AgCl + e^- \tag{4.2}$$

The electrode is connected to the cell via a patch pipette pulled from borosilicate glass capillaries with filament (Warner Instruments, Hamden, CT) to resistances between 1.5 MΩ and 3 MΩ, using a P1000 micropipette puller (Sutter Instruments, Novato, CA). Patch pipettes were fire-polished using a microforge and filled with intracellular buffer (Tab. 10).

The patch electrode is connected to a patch-clamp amplifier consisting of an operational and a differential amplifier (OA and DA), each with an inverting and a non-inverting terminal (Fig. 31A). The OA receives a reference potential ($E_{ref}$) on the non-inverting terminal and the measured membrane potential ($E_m$) on the inverting terminal. The potential difference ($E_{out}$) is passed on by the OA, resulting in current through a resistance (R) into the cell, thereby reducing the difference between $E_{ref}$ and $E_m$. The DA outputs the difference between $E_{out}$ and $E_{ref}$ from which the current flow over the membrane ($I_{mon}$) is calculated using R (Fig. 31B).

Here, a patch-clamp setup was used described elsewhere (Grimm *et al.*, 2017). An Axopatch 200B amplifier was used and connected to a DigiData 1440A digitizer (both Molecular Devices, Sunnyvale, CA) to convert analog and digital signals. A patch pipette and electrode holder (PPH-1P-AXU-0-1.5, ALA Scientific Instruments, Farmingdale, NY) was attached to a headstage (CV203BU, Molecular Devices). The headstage was mounted on a micromanipulator (PatchStar, Scientifica, Uckfield, United Kingdom) and connected to the patch-clamp amplifier.

For experiments, the coverslips with ChR-expressing cells were placed in a custom-made measuring chamber and placed on the stage of a microscope (Axiovert 100, Carl Zeiss, Jena, Germany). A water immersion objective (W Plan-Apochromat 40x/1.0, 0.066 $mm^2$, Carl Zeiss) was used for selection of cells. The microscope's built-in illumination system was connected to an external power supply (HCS-3202, Manson, Hong Kong, China).

The microscope and micromanipulator were placed on a vibration isolation table (M-VW-3636-OPT-01, Newport, Irvine, CA) to reduce disturbances. Furthermore, the setup was enclosed by a Faraday cage and astrally grounded.

A custom-made water column was used to apply and hold positive or negative pressure, generated via a mouthpiece. The extracellular buffer was exchanged manually or using an MPCU bath handler (Lorentz Messgerätebau, Katlenburg-Lindau, Germany).

The primary light source to excite the fused fluorophores as well as the ChRs was a Polychrome V (TILL Photonics, Victor, NY) set to a bandwidth of 7 nm. For the acquisition of action spectra, the light intensity was regulated in 10 % steps using the built-in electronically controllable aperture of the Polychrome. A motorized and circular variable ND filter

**Table 10.: Intra- and extracellular buffers used in electrophysiological measurements.** All ion concentrations are given in mM and all LJPs in mV. Abbreviations: Asp, Aspartate; EGTA, ethylene glycol tetraacetic acid; HEPES, 4.(2-hydroxyethyl)-1-piperazineethanesulfonic acid; LJP, liquid junction potential; NMDG, N-methyl-D-glucamine.

| Buffer | | NaCl | KCl | $MgCl_2$ | $CaCl_2$ | CsCl | NaAsp | NMDG | HCl | NaBr | $NaNO_3$ | HEPES | EGTA | LJP |
|---|---|---|---|---|---|---|---|---|---|---|---|---|---|---|
| Intra | NaCl | 110 | 1 | 2 | 2 | 1 | - | - | - | - | - | 10 | 10 | - |
| Extra | NaCl | 140 | 1 | 2 | 2 | 1 | - | - | - | - | - | 10 | - | 0.6 |
| | NaAsp | - | 1 | 2 | 2 | 1 | 140 | - | - | - | - | 10 | - | −12.6 |
| | NMGCl | 1 | 1 | 2 | 2 | 1 | - | 140 | 140 | - | - | 10 | - | 6.3 |
| | $CaCl_2$ | 1 | 1 | 2 | 70 | 1 | - | - | - | - | - | 10 | - | 4.3 |
| | $MgCl_2$ | 1 | 1 | 70 | 2 | 1 | - | - | - | - | - | 10 | - | 5.0 |
| | NaBr | - | 1 | 1 | 2 | 2 | 1 | - | - | 140 | - | 10 | - | 1.0 |
| | $NaNO_3$ | - | 1 | 1 | 2 | 2 | 1 | - | - | - | 140 | 10 | - | −0.3 |

wheel (50Q04AV.1 mounted on an NSR1, Newport) was used in action spectra recordings to achieve equal photon flux. For light titration experiments, a motorized 12-position filter wheel (FW212C, Thorlabs, Newton, NJ) equipped with various neutral density (ND) filters was used. The light application was controlled with a shutter system (VS25, Vincent Associates, Rochester, NY). For additional light application, a 150 W xenon lamp (Ushido, Tokyo, Japan) was coupled into the light path, using a 30/70 beam splitter (Chroma, Bellows Falls, VT) and filtered to the desired wavelength using bandwidth filters. The additional light application was controlled with a separate VS25 shutter system.

Single-turnover electrophysiology was performed by Dr. Jonas Wietek. Therefore, a pulsed Opolette HE 355 LD Nd:YAG laser was used as pump-source for an optical parametric oscillator (OPO; both Opotek, Carlsbad, CA) with a pulse length of 6 ns. The laser was coupled into the microscope.

### 4.5.2. Intra- and extracellular buffers

All intra- and extracellular buffers for electrophysiological experiments were prepared with chemicals obtained from Carl Roth, Merck, and Sigma-Aldrich. Chemicals were dissolved in dd$H_2O$ to final concentrations summarized in table 10. The pH was measured with a 765 Calimetric pH-meter (Knick, Berlin, Germany) and adjusted using either citric acid or N-methyl-D-glucamine ($NMDG^+$). The osmolarity was measured with an OM 815 osmometer (Vogel, Fernwald, Germany) or an Osmomat 3000basic osmometer (Gonotec, Berlin, Germany), and adjusted to 290 mOsm and 320 mOsm for intra- and extracellular buffers, respectively, using glucose. After sterile filtration using 0.22 µm filters, buffers were stored at 4 °C for short-term or at −20 °C for long-term.

When the ionic compositions of intra- and extracellular buffers differ, a liquid junction potential (LJP) arises due to differences in ion mobilities at interfaces of different buffers

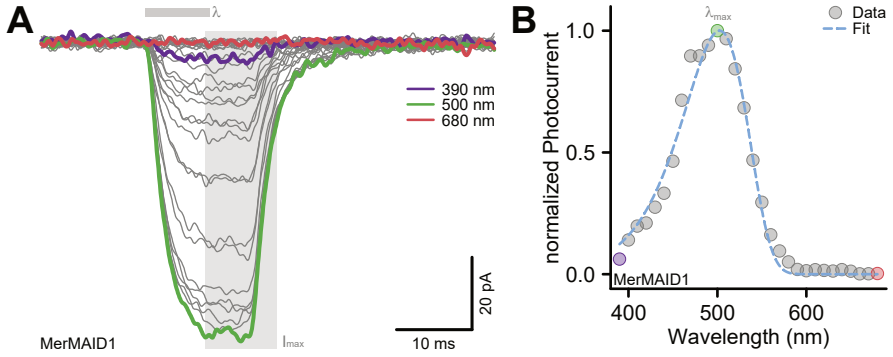


**Figure 32.: Acquisition of action spectra. A,** Representative photocurrent trace of MerMAID1 upon excitation with a 10 ms low-intensity light pulse ($\lambda$) between 390 nm and 680 nm at $E_{hold} = -60$ mV. The maximum photocurrent amplitude ($I_{max}$) of each trace was determined in the gray-shaded area. **B,** Action spectrum determined from measurement in A. All $I_{max}$ (gray circles) were normalized to the overall maximum amplitude and approximated with a three-parametric Weibull function (dashed blue line) to determine the wavelength of highest activity ($\lambda_{max}$).

(Neher, 1992). LJPs for the used buffers were calculated using the build-in JPCalc function (Barry, 1994) of Clampex 10.4 (Molecular Devices) for 23 °C and a 140 mM NaCl reference electrode. The LJPs were corrected before or after measurements. If not stated otherwise, measurements were performed in standard conditions with NaCl buffers intra- and extracellular.

### 4.5.3. Acquisition protocols and data analysis

The acquisition of electrophysiological data was controlled using Clampex 10.4. The data analysis was performed using Clampfit 10.4 (Molecular Devices) and Origin 2018 (OriginLab, Northampton, MA). Before establishing a patch, the potential offset was corrected. Patches were established with a membrane resistance ($R_m$) >1 GΩ. Measurements were carried out at room temperature, with $R_m$ >500 MΩ and an access resistance ($R_a$) <10 MΩ. During acquisition, data was filtered at 2 kHz using a Bessel filter.

#### Action spectra

Action spectra were recorded in 10 nm steps at $E_{hold} = -60$ mV using low-intensity, 10 ms light pulses between 390 nm and 680 nm (Fig. 32A). The maximum photocurrent amplitude ($I_{max}$) of each trace was determined and normalized to the overall maximum photocurrent amplitude. $\lambda_{max}$ was determined by applying a three-parametric Weibull function (Fig. 32B) implemented in Origin 2018.

A circular ND filter wheel was placed in the light path and controlled by a LabVIEW program written by Dr. Jonas Wietek (Wietek, 2018) to maintain equal photon count at different wavelengths during recordings of action spectra. The filter wheel positions were determined by calibration. Therefore, light intensities were determined using an optometer (P9710, Gigahertz Optik, Türkenfeld, Germany) in the cell's plane and calculated for the

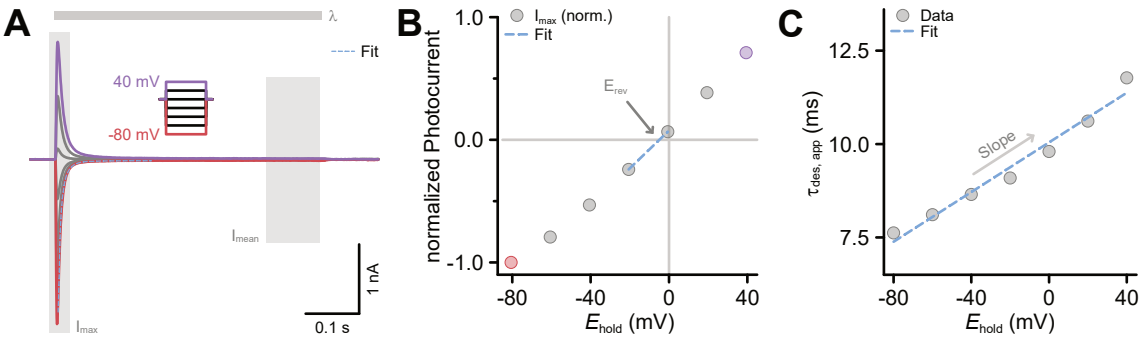


**Figure 33.: Current-voltage measurements. A,** Representative photocurrent trace of MerMAID1. Photocurrents were recorded at membrane potentials between −80 mV and 40 mV and elicited for 500 ms by applying 500 nm light ($\lambda$). The maximum photocurrent amplitude ($I_{max}$) and the mean photocurrent amplitude ($I_{mean}$) were determined in the gray-shaded areas. **B,** The reversal potential ($E_{rev}$) was determined by normalization of $I_{max}$ and linear approximation between the two data points where the sign changes. **C,** The voltage-dependence of the apparent kinetics of the transient photocurrent desensitization ($\tau_{des,\,app}$) was determined as the slope of a linear approximation.

illuminated field of the objective. Subsequently, filter wheel positions were determined for each wavelength to match the desired photon fluxes Φ, calculated according to equation 4.3, where $H$ is the light intensity, $\lambda$ the wavelength, $h$ the Planck constant, and $c$ the speed of light.

$$\Phi = H * \frac{\lambda}{h * c} \tag{4.3}$$

### Current-voltage relationship

Photocurrents at $E_{hold}$ between −80 mV and 40 mV were elicited by applying full-intensity light close to $\lambda_{max}$ for 500 ms. Transient photocurrent amplitudes were determined as $I_{max}$ at the onset of the illumination. Stationary photocurrents were determined as the mean of the terminal 100 ms of the light pulse ($I_{mean}$; Fig. 33A). The photocurrent desensitization was determined by calculating the ratio between transient and stationary photocurrents.

$E_{rev}$ was approximated using a linear regression between the two data points where photocurrent amplitudes switched the sign, or between 20 mV and 40 mV if photocurrents did not switch sign (Fig. 33B). $\Delta E_{rev}$ was determined by subtracting $E_{rev}$ at standard conditions from $E_{rev}$ of experimental condition. $E_{rev}$ for a purely $Cl^-$-conducting ion channel was calculated as $E_{Nernst}$ for $Cl^-$ using the Nernst equation (Eq. 4.4) where $R$ is the universal gas constant, $T$ the temperature in kelvin, $z$ the ionic valence, $F$ Faraday's constant, and $[Cl^-]_{e/i}$ the extra- and intracellular $Cl^-$ concentration.

$$E_{Cl^-,\,Nernst} = \frac{RT}{zF} * ln\frac{[Cl^-]_e}{[Cl^-]_i} \tag{4.4}$$

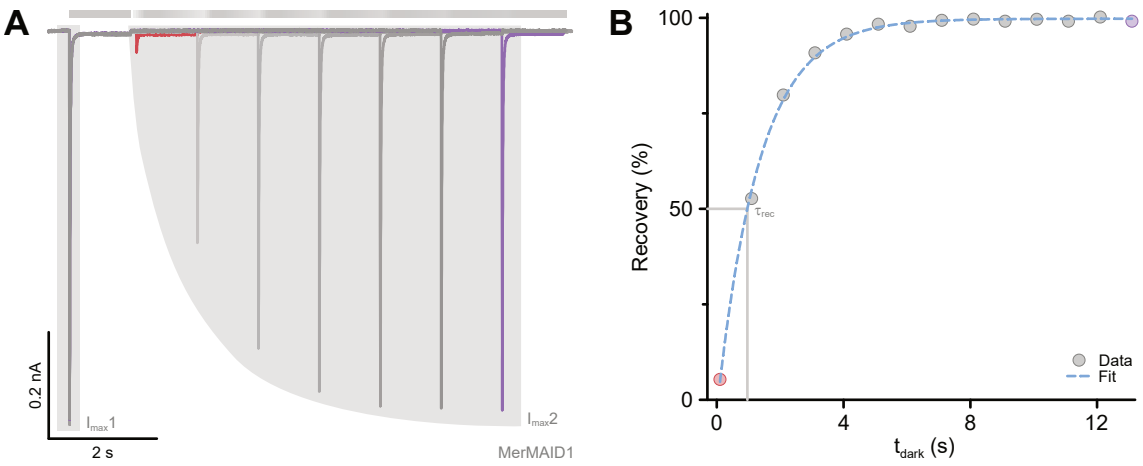


**Figure 34.: Transient photocurrent recovery.** **A,** Representative photocurrent trace of MerMAID1 at a membrane potential of −60 mV. Photocurrents were elicited with two 1 s light pulses of 500 nm, applied with increasing time intervals. The maximum photocurrent amplitude of the first and the second light pulse ($I_{max}$ 1 and $I_{max}$ 2) was determined in the gray-shaded areas. **B,** The ratio of $I_{max}$ 2-to-$I_{max}$ 1 represents the recovery of the transient photocurrents. The kinetics of the recovery ($\tau_{rec}$) were determined by approximation using a mono-exponential function. $\tau_{rec}$ represents the half-maximal photocurrent recovery.

### Kinetics of photocurrent decay

The kinetics of the photocurrent decay, $\tau_{des}$ or $\tau_{off}$, were approximated using a bi-exponential function applied to the photocurrent decay of the transient or stationary photocurrents (dashed blue line in Fig. 33A), yielding the time constants and amplitudes of a slow and a fast kinetic component ($\tau_2$, $\tau_1$, A2 and A1). The apparent kinetics of the photocurrent decay ($\tau_{des,\,app}$ and $\tau_{off,\,app}$) were calculated according to Eq. 4.5.

$$\tau_{app} = \frac{(A1 * \tau_1) + (A2 * \tau_2)}{A1 + A2} \tag{4.5}$$

The voltage-dependence of the apparent photocurrent decay kinetics was determined as the slope of a linear approximation of $\tau_{des,\,app}$ or $\tau_{off,\,app}$ at $E_{hold}$ between −80 mV and 40 mV (Fig. 33C).

### Kinetics of photocurrent recovery

The transient photocurrent recovery was determined at $E_{hold} = -60$ mV by applying two 1 s light pulses with increasing dark intervals. Transient photocurrent amplitudes were determined as $I_{max}$ and normalized to the photocurrent amplitude of the first light pulse ($I_{max}$ 1). $\tau_{rec}$ was approximated by applying a mono-exponential function to the normalized photocurrents.

### 4.5.4. Neuronal recordings

Neuronal recordings of MerMAID6 were performed and analyzed by Silvia Rodriguez-Rozada. Rat hippocampal slice cultures were transfected by single-cell electroporation after 14 to 16 days *in vitro* (DIV). At DIV 19 to 21, whole-cell patch-clamp experiments were performed. Patch pipettes with resistances of 3 MΩ to 4 MΩ were filled with a buffer consisting of (in mM): 135 K-gluconate, 4 $MgCl_2$, 4 $Na_2$-ATP, 0.4 Na-GTP, 10 $Na_2$-phosphocreatine, 3 ascorbate, 0.2 EGTA, and 10 HEPES, adjusted to pH 7.2. Slices were kept in a buffer consisting of (in mM): 135 NaCl, 2.5 KCl, 2 $CaCl_2$, 1 $MgCl_2$, 10 Na-HEPES, 12.5 D-glucose, and 1.25 $NaH_2PO_4$, adjusted to pH 7.4 and supplemented with 10 µM CPPene, 10 µM NBQX, and 100 µM picrotoxin (Tocris, Bristol, UK). A pE-4000 LED system (CoolLED, Andover, UK) was used for excitation. Data were analyzed using IgorPro 8.0 (Wavemetrics, Lake Oswego, OR).

## 4.6. Imaging techniques

Confocal imaging of ND7/23 cells expressing v*Py*ACR21821 or v*Py*ACR2164382 was performed by Rodrigo Gaston Fernandez Lahore. Cells were seeded at a density of $0.2 \times 10^5$ in polymerbottom dishes (ibidi, Gräfelfing, Germany). A confocal laser scanning microscope (FV1000, Olympus, Shinjuku, Tokyo, Japan) with a water immersion objective (UPlanSApo, Olympus) was used for image acquisition. A diode laser set to 559 nm or an argon laser set to 515 nm were used to excite mCherry or eYFP, respectively. The acquired z stacks were analyzed using ImageJ (Rueden *et al.*, 2017) and relevant z-planes were z-projected for representative images of membrane fluorescence.

Two-photon microscopy imaging of neurons expressing MerMAID6 was performed by Silvia Rodriguez-Rozada at DIV 19 to 21 using a microscope (BX-51WI, Olympus) with a DF-scope multiphoton imaging package (Sutter Instruments). The setup was controlled by, and data was collected with ScanImage 2017b (Vidrio Technologies, Ashburn, VA). The system was equipped with a tuneable laser (Ti:Sapphire Chameleon Vision-S, Coherent, Santa Clara, CA) and a fiber laser (Fidelity-2, Coherent).

## 4.7. Protein expression in *Pichia pastoris*

The protein sample of MerMAID1 for spectroscopic analysis was acquired by heterologous expression in *Pichia pastoris* and subsequent protein purification. Therefore, the MerMAID1 gene fused to a 6xHis-tag was cloned into the pPiC-Z vector using the Gibson assembly method. *P. pastoris* cells were transformed by electroporation and selected by Zeocin™ (InvivoGen, Toulouse, France) resistance. Positive clones were stored as cryocultures. After induction of the protein expression, cells were harvested, lyzed and the

**Table 11.:** Growth media for the cultivation of *P. pastoris*. Abbreviations: BMGY, buffered medium w/ glycerole for yeast; BMMZ, buffered medium w/ methanol for yeast; KP, potassium phosphate; YNB, yeast-nitrogen-base; YPD, yeast-extract peptone dextrose; YPDS, YPD with sorbitol.

| Medium | Recipe | Source |
|---|---|---|
| YPD | 2 % tryptone | Carl Roth |
| | 1 % yeast extract | Carl Roth |
| | 2 % glucose | Carl Roth |
| YPD Agar | YPD with | |
| | 2 % Agar | Carl Roth |
| YPDS | YPD with | |
| | 18 % sorbitol | |
| KP buffer | 9.5 ml 1 M $K_2HPO_4$ | Carl Roth |
| | 90.5 ml 1 M $KH_2PO_4$ | Carl Roth |
| | pH 6 | |
| BMGY | 2 % tryptone | Carl Roth |
| | 1 % yeast extract | Carl Roth |
| | 1 % glycerole | Carl Roth |
| | 1.5 % YNB | Carl Roth |
| | Zeocin™ | |
| BMMY | 2 % tryptone | Carl Roth |
| | 1 % yeast extract | Carl Roth |
| | 100 mM KP buffer | |
| | 1.5 % YNB | Carl Roth |
| | 2.5 % methanole | Carl Roth |
| | 1 % BME vitamins | Sigma-Aldrich |
| | 5 µM all-*trans* retinal | Sigma-Aldrich |

membrane fraction was separated. After solubilization of the proteins in the membrane fraction, MerMAID1 was purified using an Äkta system.

If not stated otherwise, *P. pastoris* cultures were were incubated at 30 °C. Liquid cultures were additionally rotated at 200 rpm.

### 4.7.1. Transformation of *Pichia pastoris*

#### Plasmid linearization

The transformation of competent *P. pastoris* cells requires linearized DNA. Therefore, 10 µg plasmid DNA was mixed with 5 µl buffer and 15 µl of either MssI, SacI, or BstXI (Thermo Fisher Scientific) and filled to a total volume of 50 µl using $ddH_2O$. After incubation (1 h,

37 °C), the DNA was precipitated by adding 50 µl 3 M sodium acetate (pH 5.6), 500 µl ice-cold isopropanol, and 400 µl $ddH_2O$. The mix was incubated (30 min, −80 °C) and, subsequently, the precipitated DNA was pelleted by centrifugation (20 min, full speed, 4 °C). After discarding the supernatant, the pellet was washed with ice-cold 70 % EtOH, and the DNA was pelleted again by centrifugation (30 min, full speed, 4 °C). The supernatant was discarded, and the pellet was dried in a heated vacuum centrifuge (DNA120 SpeedVac, Thermo Savant, Holbrook, NY). Afterward, the DNA was dissolved in 10 µl $ddH_2O$ and stored at 4 °C until further use but not longer than 24 h.

### Preparation of *P. pastoris* for electroporation

For each transformation, a new culture of cryoconserved *P. pastoris* (clone SMD1168H, Thermo Fisher Scientific) was prepared by inoculating 50 ml YPD medium and incubating overnight in a flask without chicanery. 500 ml YPD medium was inoculated with $OD_{600}$ 1.3 to 1.5 from the pre-culture and incubated overnight in a flask without chicanery. The main culture was harvested by centrifugation (1500 *g*, 4 °C) at $OD_{600}$ 1.4. After discarding the supernatant, the cells were repeatedly dissolved and pelleted by centrifugation (1500 *g*, 4 °C) in 500 ml ice-cold $ddH_2O$, followed by 250 ml ice-cold $ddH_2O$, and 20 ml ice-cold 1 M sorbitol (Carl Roth). Finally, the cells were resuspended in 1 ml ice-cold 1 M sorbitol.

### Electroporation

For electroporation, 80 µl cell suspension was mixed with the previously linearized DNA in an ice-cold electroporation cuvette (EquiBio, UK) and incubated for 5 min on ice. After electroporation (1500 V, 200 Ω, and 25 µF; ECM630, BTX Harvard Bioscience, Holliston, MA), the cells were immediately diluted in 1 ml ice-cold 1 M sorbitol and incubated for 3 h. Subsequently, 50 µl, 100 µl, and 200 µl of the cell suspension were spread out on freshly prepared YPDS agar plates with a Zeocin™ concentration of 100 µg $ml^{-1}$ and incubated for up to three days until colonies were visible.

### Clone selection

A combinatorial test was performed to select clones with an expected high protein yield. Therefore, 16 colonies were picked, and of each, one third was transferred to YPDS agar plates with Zeocin™ concentrations of 100 µg $ml^{-1}$, 1000 µg $ml^{-1}$, and 2000 µg $ml^{-1}$, respectively. After two days of incubation, four to eight colonies showing the most substantial growth at all three Zeocin™ concentrations were chosen for a test expression.

For this purpose, 10 ml BMGY medium was inoculated with a single clone and incubated overnight. To induce protein expression, 50 ml BMMY medium was inoculated with $OD_{600}$ 1.0 from the preculture and incubated overnight. The cells were harvested by centrifugation at 4000 *g*, and the rhodopsin expression was evaluated by the color of the

cell pellet. The clone with the strongest red-colored cell pellet was chosen for large scale expression.

#### Cryocultures

Selected clones were preserved in cryoculture. To this purpose, 10 ml BMGY medium was inoculated. After incubation overnight and a subsequent check for contamination, 86 % glycerol was added to a final concentration of 17.2 %. Aliquots of 400 µl were prepared and snap-frozen in liquid nitrogen before long-term storage at −80 °C.

### 4.7.2. Protein purification

#### Protein expression

For large-scale protein expression, 250 ml BMGY were inoculated and incubated overnight. After checking for contamination, at least 500 ml BMMY medium were inoculated with $OD_{600}$ 1.0 from the preculture and incubated for 24 h to 36 h. The cells were harvested by centrifugation (10 min, 4000 *g*). The supernatant was discarded, the cells resuspended in breaking buffer, and collected in a 50 ml falcon. After centrifugation at 4000 *g*, the supernatant was again discarded, and the cell pellet was snap-frozen in liquid nitrogen and stored at −80 °C until further use.

#### Membrane isolation

The membrane of *P. pastoris* cells was isolated first to purify the channelrhodopsin. The stored cell pellets were prepared by resuspending them in 50 ml breaking buffer and homogenization in a tissue grinder. Subsequently, a French press (G. Heinemann Ultraschall und Labortechnik, Schwäbisch Gmünd, Germany) was used to disrupt the cells using high pressure (20 000 pounds per square inch). The membrane fraction was collected by centrifugation (10 min, 4 °C, 16 000 *g*). The pellet was discarded and the supernatant centrifuged (1 h, 4 °C, 40 000 rpm) in a vacuum. The supernatant was discarded and the pellet resuspended in 10 ml buffer (20 mM Tris, 100 mM NaCl, pH 8) and homogenized in a tissue grinder. The protein concentration was determined using a commercially available Pierce BCA protein assay (Thermo Fisher Scientific).

#### Protein solubilization and purification

The membrane proteins were diluted to a concentration of 10 mg ml$^{-1}$ in solubilization buffer and, subsequently, solubilized by stirring gently overnight at 4 °C. Non-solubilized proteins were removed by centrifugation (40 000 rpm, 1 h, 4 °C). The recombinant rhodopsin was purified by affinity chromatography, using an Äkta pure system (GE Healthcare Life Science, Chicago, IL) with a 5 ml HisTrap$^{TM}$ FF crude column (GE Healthcare Life

**Table 12.: Buffer for protein purification.** PMSF was added right before use. Abbreviations: ATR, all-*trans* retinal; DDM, *n*-Dodecyl $\beta$-D-maltoside; EDTA, Ethylenediaminetetraacetic acid; PMSF, Phenylmethanesulfonyl fluoride

| Buffer | Recipe | Source |
|---|---|---|
| Breaking Buffer | 50 mM $NaPO_4$ | Merck |
| | 1 mM EDTA | Carl Roth |
| | 1 mM PMSF | Carl Roth |
| | DNAseI | Roche |
| | pH 7.4 | |
| Solubilization Buffer | 20 mM Tris | Carl Roth |
| | 100 mM NaCl | Carl Roth |
| | 20 mM Imidazole | Sigma-Aldrich |
| | 2 % DDM | Glycon Biochemicals |
| | 5 µM ATR | Sigma-Aldrich |
| | pH 8 | |
| Washing Buffer | 20 mM Tris | Carl Roth |
| | 100 mM NaCl | Carl Roth |
| | 20 mM Imidazole | Sigma-Aldrich |
| | 0.05 % DDM | Glycon Biochemicals |
| | pH 8 | |
| Elution Buffer | 20 mM Tris | Carl Roth |
| | 100 mM NaCl | Carl Roth |
| | 500 mM Imidazole | Sigma-Aldrich |
| | 0.05 % DDM | Glycon Biochemicals |
| | pH 8 | |
| Storing Buffer | 20 mM Tris | Carl Roth |
| | 100 mM NaCl | Carl Roth |
| | 0.05 % DDM | Glycon Biochemicals |
| | pH 8 | |

Science). Non-specifically bound protein was removed by applying the washing buffer to the column. Before elution of the rhodopsin from the column, an additional wash step was performed with the washing buffer containing 50 mM imidazole. After elution, the purified protein was concentrated in storing buffer using Amikon falcons with a cutoff of 100 kDa (Merck). The protein concentration $c$ in mg ml$^{-1}$ was determined from absorption spectra (Eq. 4.6), assuming an approximate molecular weight (MW) of the rhodopsin of 30 000 Da. Gel filtration was performed using the Äkta pure system with a HiPrep$^{TM}$ 26/10

desalting column (GE Healthcare Life Science).

$$c = (\frac{A_{502}}{\epsilon}) * MW \tag{4.6}$$

## 4.8. Spectroscopy

For spectroscopic experiments, samples were diluted in standard or titration buffer (Tab. 13). For the exchange of accessible protons with deuterium, samples were dissolved in standard buffer at pD 8 or 10. The pD was adjusted under consideration of Krezel and Bal (2004). Excess buffer was removed using Amikon tubes (Merck). The procedure was repeated three times to ensure complete exchange.

### 4.8.1. Steady-state UV/vis absorption spectroscopy

Steady-state UV/vis absorption spectra were collected at a spectral resolution of 1 nm using either a Cary 300 (Varian Inc., Palo Alto, USA) or a UV-2600 (Shimadzu, Kyōto, Japan) UV/vis spectrophotometer with the appropriate software, Varian UV v3.0 software (Varian) and UVProbe v2.34 software (Shimadzu), respectively. Analysis of steady-state UV/vis absorption spectra was performed using Origin 2018. Absorption spectra of light-adapted MerMAID1 were acquired in standard buffer during illumination of the sample with a 530 nm LED filtered to 520 ± 15 nm. The temperature was adjusted to 281 K.

For pH-titration experiments, the sample was diluted in titration buffer (Tab. 13). Small volumes (0.25 µl to 1.00 µl) of 1 M NaOH were added to the buffered sample to increase the pH. After thoroughly mixing, the pH was measured using pH microelectrodes (SI Analytics, Mainz, Germany). Subsequently, spectra were collected.

### 4.8.2. Transient UV/vis absorption spectroscopy

Transient UV/vis absorption spectra were acquired and analyzed by Arita Silapetere at room temperature in single-turnover conditions from $10^{-8}$ s to $10^{2}$ s with 120 s between excitations at a spectral resolution of 0.4 nm. For experiments, a modified LKS.60 flash-photolysis system (Applied Photophysics Ltd., Leatherhead, UK) was used. An Nd:YAG laser (BrilliantB, Quantel, Les Ulis, France) was used as pump-source for an OPO (MagicPrism, Opotek) set to 500 nm for the sample excitation. The laser energy was adjusted to 5 mJ per pulse, with a pulse duration of 10 ns. Transient absorption changes were monitored using a 150 W xenon lamp (Osram, München, Germany) and an Andor iStar ICCD camera (DH734; Andor Technology Ltd, Belfast, Ireland) and recorded using custom-written software. The analysis was performed using Octave 4.2 (Eaton, 2002) and Matlab R2016b (MathWorks, Natick, MA) as well as Glotaran 1.5.1 (Mullen and van Stokkum, 2007; Snellenburg *et al.*, 2012).

**Table 13.: Buffers for spectroscopic experiments.** Abbreviations: BTP, bis-tris propane; CAPS, 3-(cyclohexylamino)-1-propanesulfonic acid; DDM, *n*-Dodecyl $\beta$-D-maltoside.

| Buffer | Recipe | Source |
|---|---|---|
| Std. buffer | 100 mM NaCl | Carl Roth |
| | 20 mM Tris | Carl Roth |
| | 0.05 % DDM | Glycon Biochemicals |
| | pH or pD 8 or 10 | |
| Titration buffer | 100 mM NaCl | Carl Roth |
| | 10 mM BTP | Sigma-Aldrich |
| | 10 mM CAPS | Sigma-Aldrich |
| | 0.05 % DDM | Glycon Biochemicals |
| | pH 7.5 | |

### 4.8.3. Fourier-transform infrared spectroscopy

FTIR spectra were collected and analyzed by Paul Fischer at 273 K in forward-backward rapid-scan mode using a Vertex 80 v FTIR spectrometer (Bruker Optics, Karlsruhe, Germany) with an MCT detector (Kolmar Technologies, Newburyport, MA) cooled using liquid nitrogen, and operated with the OPUS 7.5 software (Bruker Optics). The spectral resolution was 8 $cm^{-1}$, and the data acquisition rate 300 kHz. The time resolution was 6 ms. An optical cutoff filter at 1850 $cm^{-1}$ was used.

Samples were prepared by drying 10 µl sample with a concentration of >20 mg $ml^{-1}$ dissolved in standard buffer on a $BaF_2$ window. The chamber was sealed with a second $BaF_2$ window after rehydration. Samples were equilibrated for 1 h. For continuous illumination conditions, 520 nm-LEDs were used, and for additional UV-light illumination, 362 nm-LEDs. For single-turnover conditions, an Nd:YAG laser (Powerlite 9010, Continuum, San Jose, CA) served as the pump-source for an OPO (Horizon II, Continuum) set to 530 nm. The laser energy was approximately 60 mJ with a pulse duration of $5 \pm 2$ ns. The acquired data was analyzed using Octave 4.2 (Eaton, 2002) and fitted using a sum of exponential functions.

### 4.8.4. Resonance Raman spectroscopy

RR spectra were collected and corrected by Dr. Anke Keidel at 80 K (Linkam cryostat; Linkam Scientific Instruments, Surrey, UK) with a spectral resolution of 2 $cm^{-1}$ and $\lambda_e$ 514 nm, 488 nm, or 413 nm using $Ar^+$ or $Kr^+$ laser (Coherent). Signals were detected in the backscattering configuration using a confocal LabRamHR spectrometer (Horiba, Villeneuve, France) and recorded using the LabSpec Spectroscopy Suite software (Horiba). Signals were accumulated over 30 min with a laser power of 1 mW. Data was background-

subtracted with custom-written software and analyzed using the LabSpec Spectroscopy Suite (Horiba) or Origin 2018.

## 4.9. Molecular dynamics simulations

A homology model of MerMAID1 was constructed based on the iC++ structure (PDB: 6CSN; Kim *et al.*, 2018) using the SWISS model server (Waterhouse *et al.*, 2018). The monomeric model was subjected to MD simulations, performed and analyzed by Enrico Peter using CHARMM-GUI (Jo *et al.*, 2008) with the model embedded in a homogeneous 1,2-dimyristoyl-sn-glycero-3-phosphocholine bilayer surrounded by water. Simulations were performed with 2 fs time steps at 303 K and the CHARMM36 force field (MacKerell *et al.*, 1998). Prediction of tunnels serving as potential ion conduction pathways was performed by Dr. Jonas Wietek using MOLEonline (Pravda *et al.*, 2018).

## 4.10. Data presentation and Statistics

Electrophysiology and spectroscopy data was plotted in Origin 2018.

Sequence identity and similarity of microbial rhodopsins (Fig. S1) were calculated with the Snapgene software using the Smith-Waterman algorithm (T. Smith and Waterman, 1981) for local sequence alignments with BLOSUM62 (S. Henikoff and J. G. Henikoff, 1992) as substitution matrix. A gap open penalty of 10 and a gap extension penalty of 1 were applied.

Phylogenetic trees were generated using NGPhylogeny.fr (Lemoine *et al.*, 2019) and adjusted using Interactive Tree Of Life (iTOL) v4 (Letunic and Bork, 2019).

PDB files were visualized using PyMol 2.4.oao (Schrödinger, NY). All figures were combined and aesthetically adjusted using Affinity Designer 1.8 (Serif, Nottingham, UK).

### 4.10.1. Estimation statistics

If not otherwise stated, data is given as mean ± SEM. Where applicable, the data was statistically evaluated using estimation statistics (Ho *et al.*, 2019). Cumming estimation plots for paired or unpaired data were generated using Estimation Stats[1] (Fig. 35).

Cumming estimation plots combine the visualization of the observed data and the effect size. Paired data are presented as connect lines (Fig. 35A) and unpaired data as a swarm plot of single data points for control and test group (Fig. 35B). The presentation of unpaired data is further extended by plotting the mean (white dot) ± SEM (line). On a separate axis, the effect size is presented as the mean difference (circle) with its bootstrap sampling distribution (curve) and the 95 % confidence interval (line). In bootstrap methods (Efron,

[1] http://www.estimationstats.com/

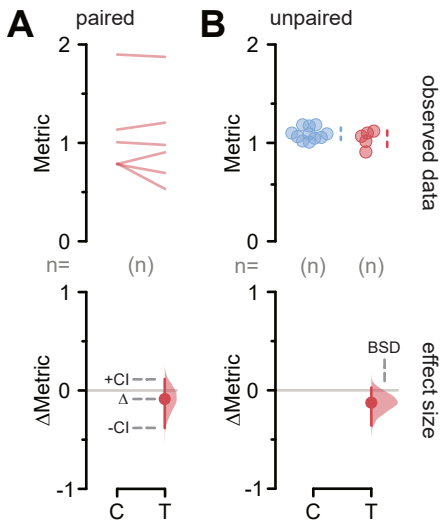


**Figure 35.: Estimation statistics.** Paired **(A)** and unpaired **(B)** data plotted as Cumming estimation plots using Estimation Stats. Experimental data of control (C) and test (T) group are plotted separately, with paired data connected by lines while unpaired data is plotted as single data points (top). The effect size of a comparison is plotted (bottom) as mean difference (Δ) with its 95 % confidence interval (CI) and bootstrap sampling distribution (BSD) indicated by a solid line and a curve, respectively.

1979), the observed data is used as a pool for resampling, yielding the difference in means for resampled control and test groups, which approaches normal distribution (Ho *et al.*, 2019). The 95 % confidence interval is the central 95 % of the resampled mean difference, i. e. between the 125$^{th}$ and the 4875$^{th}$ value of 5000 resamples. Bootstrap resampling distributions are additionally bias-corrected (Efron, 1987).

# A. Supplement

## A.1. Supplementary figures

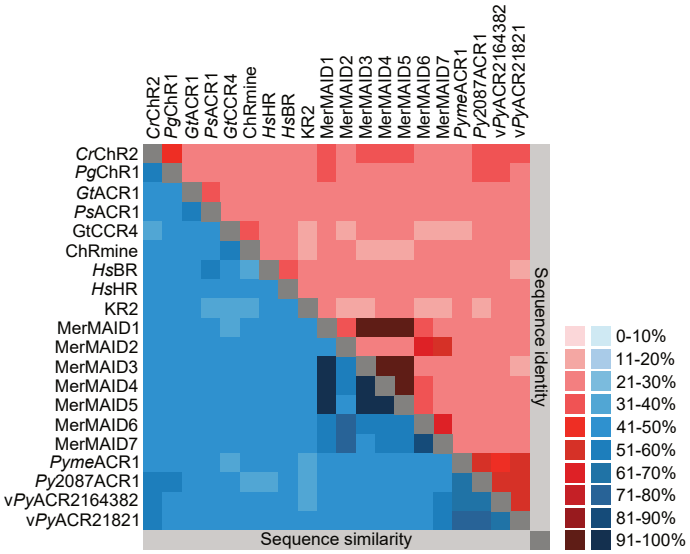


**Figure S1.: Heat map of sequence identity and similarity of selected microbial rhodopsins.** Sequence identity and similarity were determined using the Smith-Waterman algorithm for local alignments (T. Smith and Waterman, 1981) with BLOSUM62 (S. Henikoff and J. G. Henikoff, 1992).

| | | | |
|---|---|---|---|
| *Cr*ChR2 | 217 | WLFFVSWGMFP | 227 |
| *Pg*ChR1 | 198 | YMFFLSWMCFP | 208 |
| *Gt*ACR1 | 198 | IVFYVSWMAYP | 208 |
| *Ps*ACR1 | 194 | WIFIVSWCVYP | 204 |
| *Gt*CCR4 | 208 | TLYFSIWCGYP | 218 |
| ChRmine | 217 | FTFSMLWILFP | 227 |
| *Hs*BR | 189 | NVTVVLWSAYP | 199 |
| *Hs*HR | 201 | VLTVVLWLGYP | 211 |
| KR2 | 209 | ILFLISWTLYP | 219 |
| MerMAID1 | 174 | ALLMVSWIVFP | 184 |
| MerMAID2 | 169 | LYFMTSWLVFP | 179 |
| MerMAID3 | 180 | ALLMVSWILFP | 190 |
| MerMAID4 | 225 | SLLMVSWILFP | 235 |
| MerMAID5 | 180 | SLLMVSWILFP | 190 |
| MerMAID6 | 169 | MYFMASWLVFP | 179 |
| MerMAID7 | 169 | LYFMGSWLVFP | 179 |
| *Pyme*ACR1 | 184 | GIFYGGWAAFG | 194 |
| *Py*2087ACR1 | 178 | VIFYGSWSGFG | 188 |
| v*Py*ACR2164382 | 176 | IVFYSSWSGFG | 186 |
| v*Py*ACR21821 | 174 | FVFYVSWSGFG | 184 |

**Figure S2.: Sequence alignment of selected microbial rhodopsins.** Aligned are residues around Phe183 of MerMAID1. The alignment was generated using ClustalW (Larkin *et al.*, 2007). Shades of blue indicate conservation.

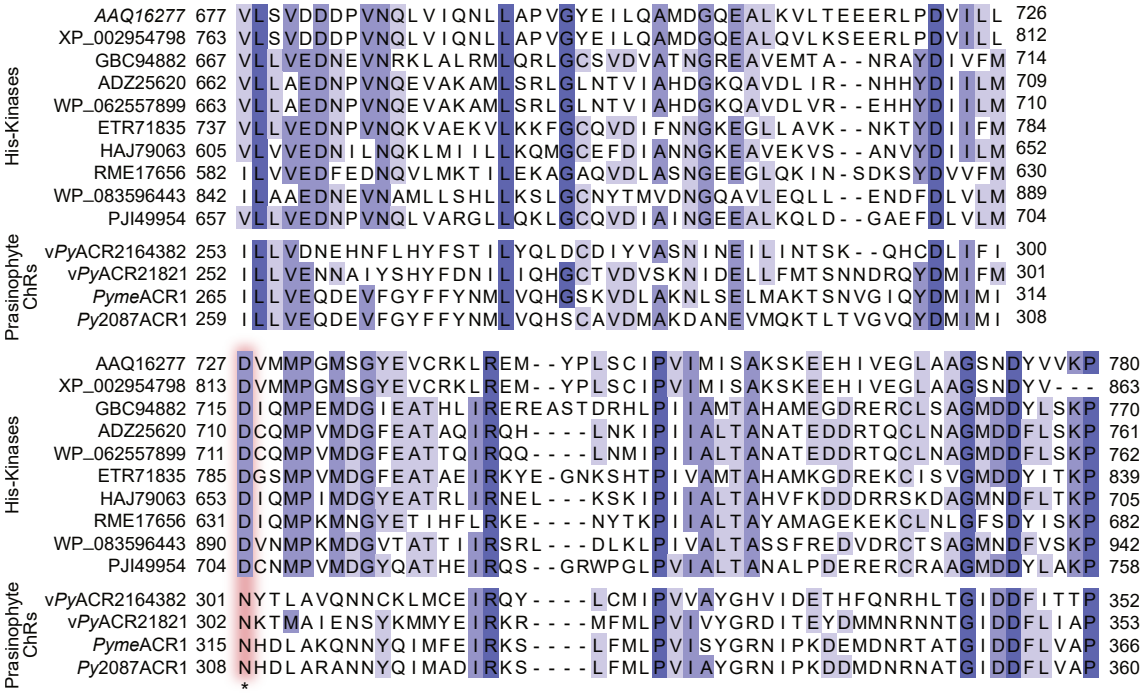


**Figure S3.: Sequence alignment of response regulator domains.** Carboxy-terminal domain of prasinophyte ChRs aligned to response regulator domains of histidine-kinases. response regulator domains are referenced as GeneBank accession numbers. Residues marked with red background and asterisk are conserved phosphorylation site of HKs. The alignment was generated using ClustalW (Larkin *et al.*, 2007). Shades of blue indicate conservation.

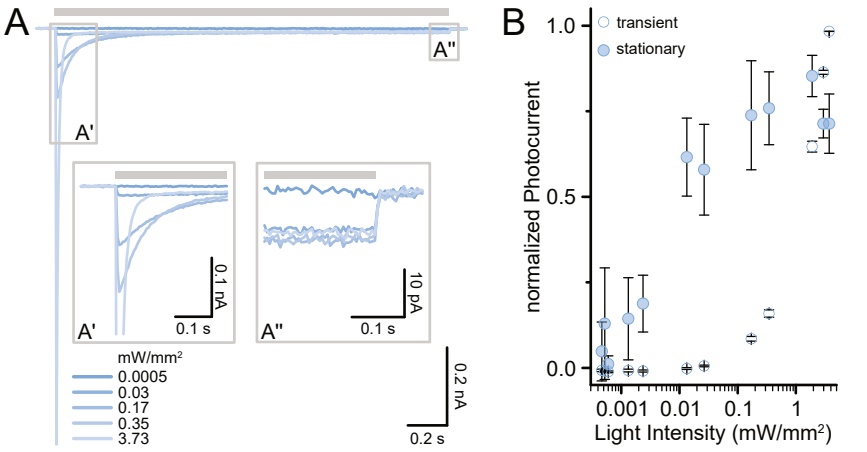


**Figure S4.: Light titration of MerMAID1. A,** Exemplary photocurrent trace of MerMAID1 upon illumination with 500 nm-light of indicated intensities in mW mm$^{-2}$ recorded at a membrane potential of −60 mV. Transient (A') and stationary (A") photocurrents are additionally magnified and shown as separate zoom-ins. **B,** Light titration plots for transient (circle) and stationary (filled circle) photocurrents. Photocurrents were normalized to the largest amplitude and plotted against the light intensity (mW mm$^{-2}$).

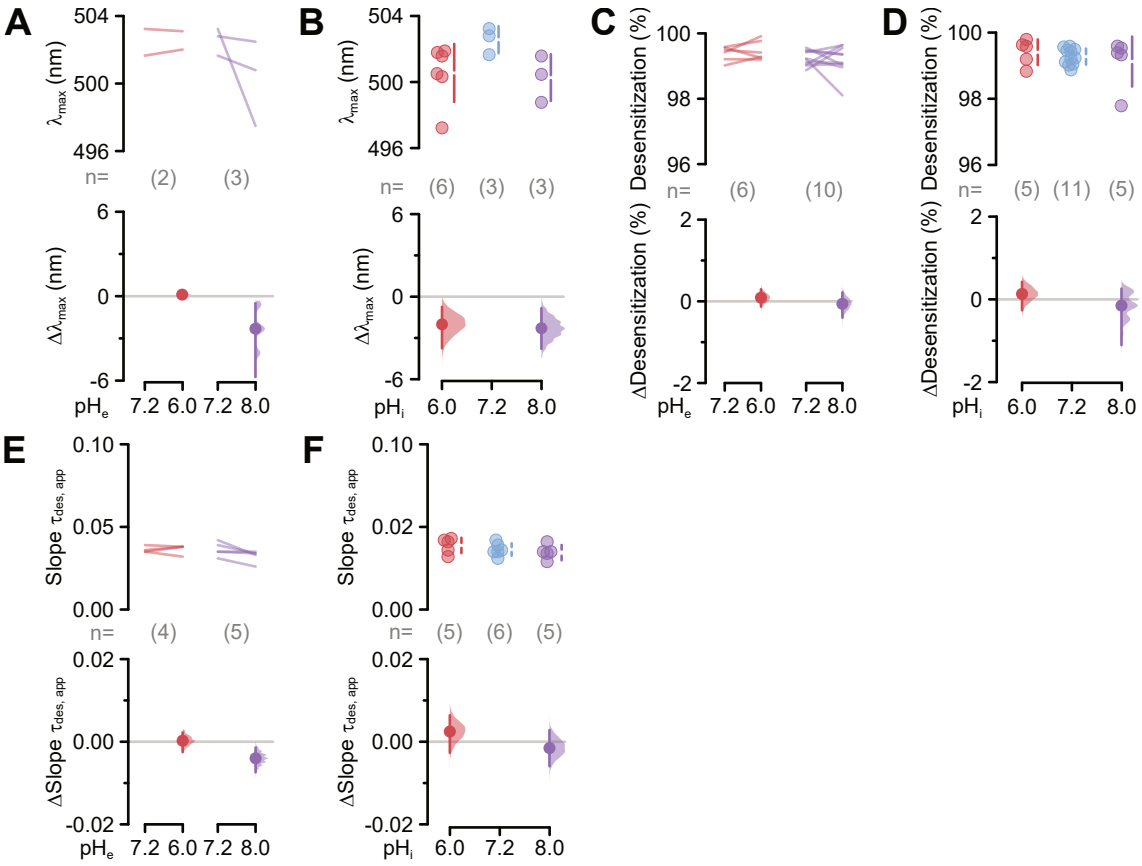


**Figure S5.: pH-dependence of additional electrophysiological parameters of MerMAID1.** Cumming estimation plots for the comparison of **A, B** the maximal spectral sensitivity $\lambda_{max}$; **C, D,** the level of transient photocurrent desensitization; **E, F,** and the voltage-dependence of the transient photocurrent desensitization at varied extracellular pH (A, C, E, and G) and intracellular pH (B, D, F, and H). In **A, C, and E,** the cumming estimation plots show the paired mean difference of comparisons, with the raw data plotted on the upper axes, where each paired set of observations connected by a line. In **B, D, and F,** the cumming estimation plots show the mean difference of comparisons, with the raw data plotted as dots on the upper axes. The difference for the comparison to the control (pH 7.2) is plotted as a bootstrap sampling distribution on the lower axes, with the mean differences depicted as dots and the 95 % confidence interval indicated as vertical error bars.

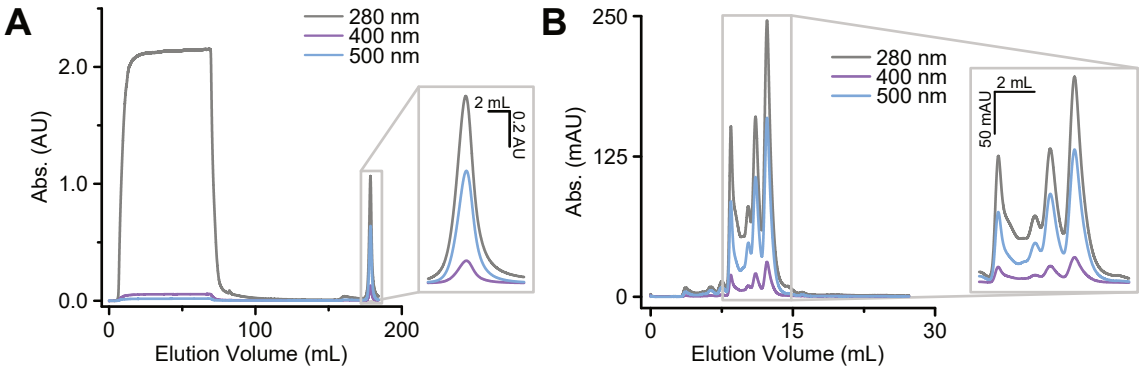


**Figure S6.: Purification of MerMAID1. A,** Elution profile of 6xHis-Tag-purified MerMAID1. Between 0 mL and 100 mL, weakly bound protein was eluted, using a buffer with 50 mM imidazole. The peak representing the elution of MerMAID1 is magnified on the right. **B,** Elution profile after gel filtration of previously purified MerMAID1. The absorption of the total protein (280 nm, gray), deprotonated MerMAID1 (400 nm, purple), and protonated MerMAID1 (500 nm, blue) were detected in both experiments, using an absorption detector.

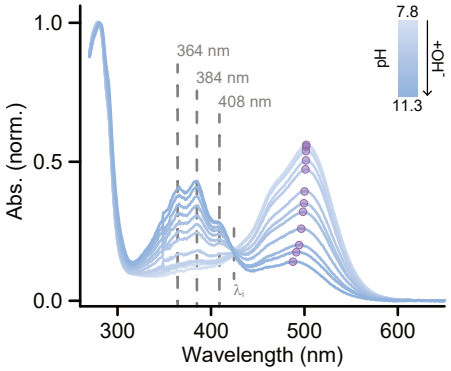


**Figure S7.: Isosbestic point of MerMAID1.** pH-dependence of dark-adapted MerMAID1 absorption spectra between pH 7.8 and 11.3. UV/vis absorption spectra, normalized to $A_{280}$ at pH 7.8. The pH was titrated by adding small volumes of NaOH to the buffered protein. Local absorption maxima and the isosbestic point ($\lambda_i$) are indicated by dashed lines. Purple dots indicate $\lambda_{max}$ of the protonated retinal Schiff base ($RSBH^+$). Adapted from Oppermann *et al.* (2019).

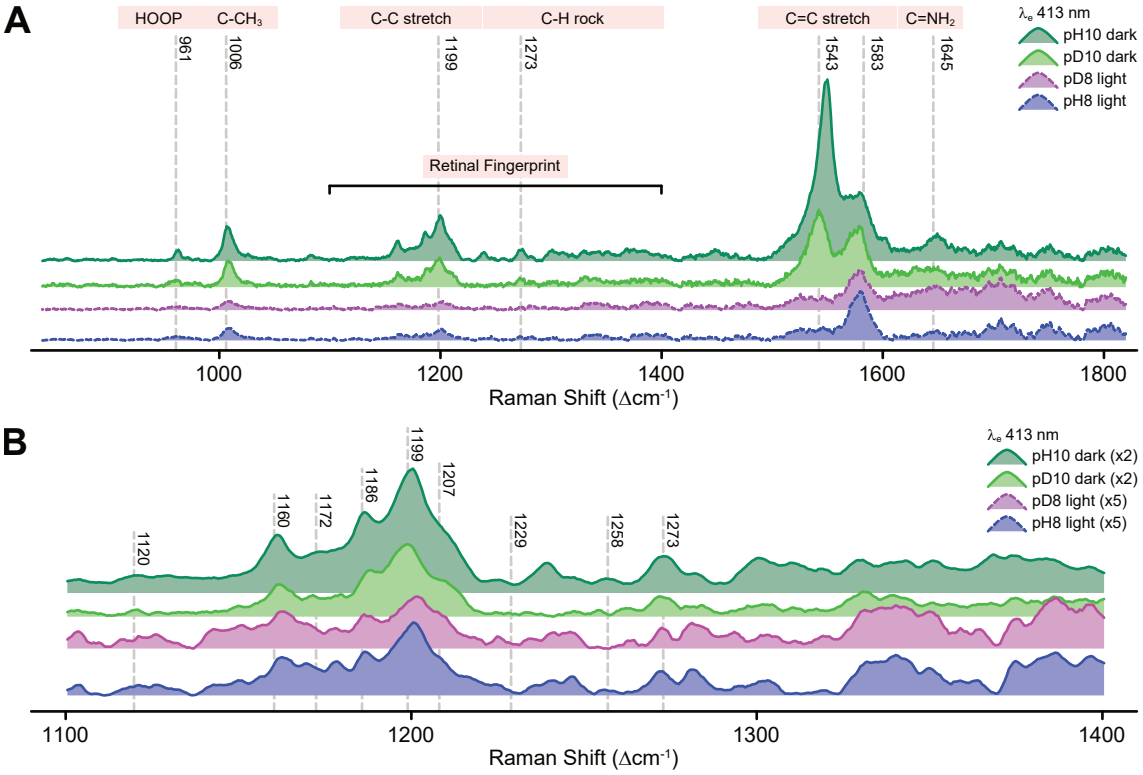


**Figure S8.: pH-dependence of the chromophore of dark-adapted MerMAID1. A,** Resonance Raman (RR) spectra of dark-adapted and illuminated MerMAID1 at pH 8 or 10 probed with $\lambda_e$ = 413 nm. Regions of the RR spectrum indicating vibrations of certain chemical connections are labeled accordingly. **B,** Enlarged view of the retinal fingerprint region of RR spectra shown in A, scaled up as indicated to improve visibility. All RR spectra were accumulated for 30 min at 80 K with a laser power of 1 mW. Labeled frequencies refer to the RR spectrum of dark-adapted MerMAID1 at pH 8. The data was collected and analyzed in collaboration with Dr. Anke Keidel. Adapted from Oppermann *et al.* (2019).

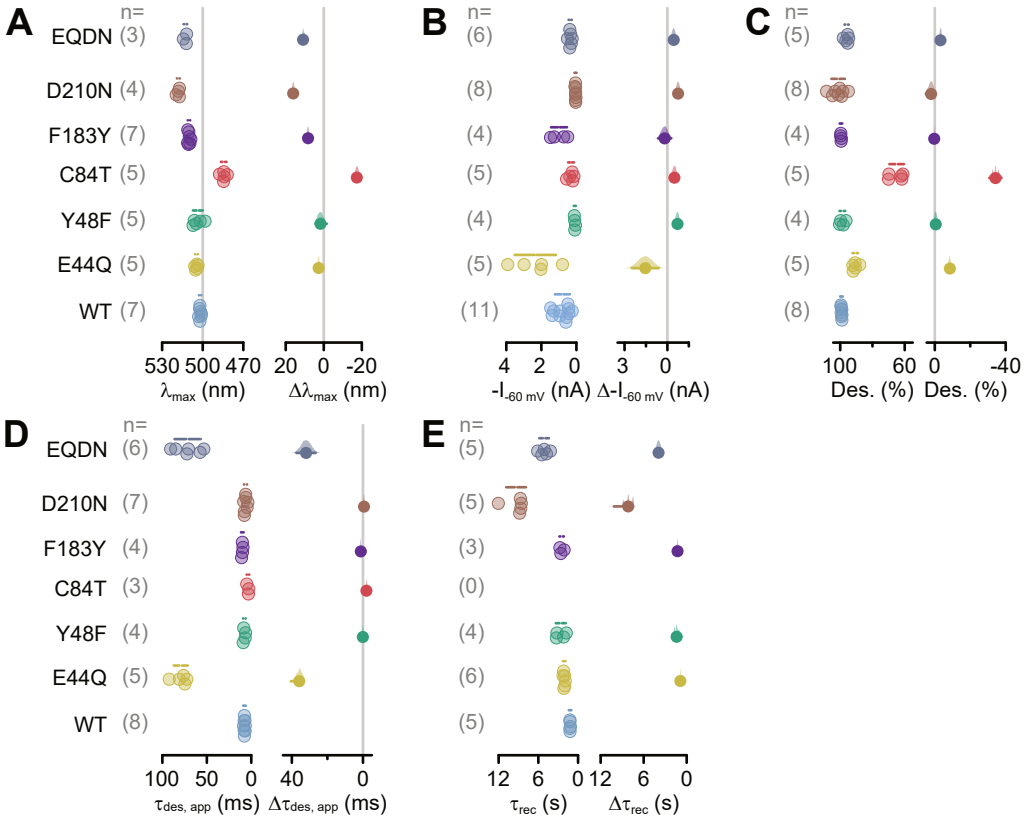


**Figure S9.: Estimation statistics of single- and double-residue substitutions in MerMAID1.** Cumming estimations plots comparing **A,** the maximal spectral sensitivity, **B,** the transient photocurrent amplitude at a membrane potential of −60 mV, **C,** the level of transient photocurrent desensitization, **D,** the apparent kinetics of the transient photocurrent desensitization, and **E,** the kinetics of the transient photocurrent recovery of single- or double-residue substitutions in MerMAID1 to the wildtype (WT), as shown in figure 23. The cumming estimation plots show the mean difference of comparisons, with the raw data plotted as dots on the left axes. The difference for the comparison to the WT is plotted as a bootstrap sampling distribution on the right axes, with the mean differences depicted as dots and the 95 % confidence interval indicated as vertical error bars.

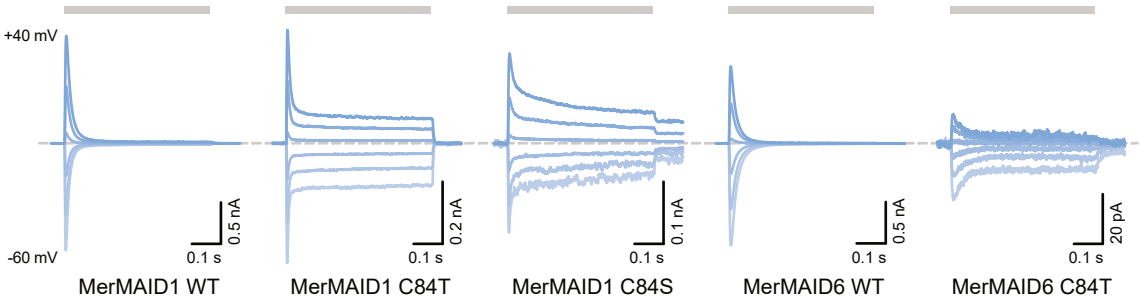


**Figure S10.: Representative photocurrent traces of Cys84 substitutions in MerMAID1 and MerMAID6.** Photocurrents were recorded at membrane potentials from −60 mV to 40 mV in steps of 20 mV and induced by illumination with 500 nm-light for the wildtype (WT) and 470 nm-light for Cys84 substitutions. Illumination is indicated by gray bar.

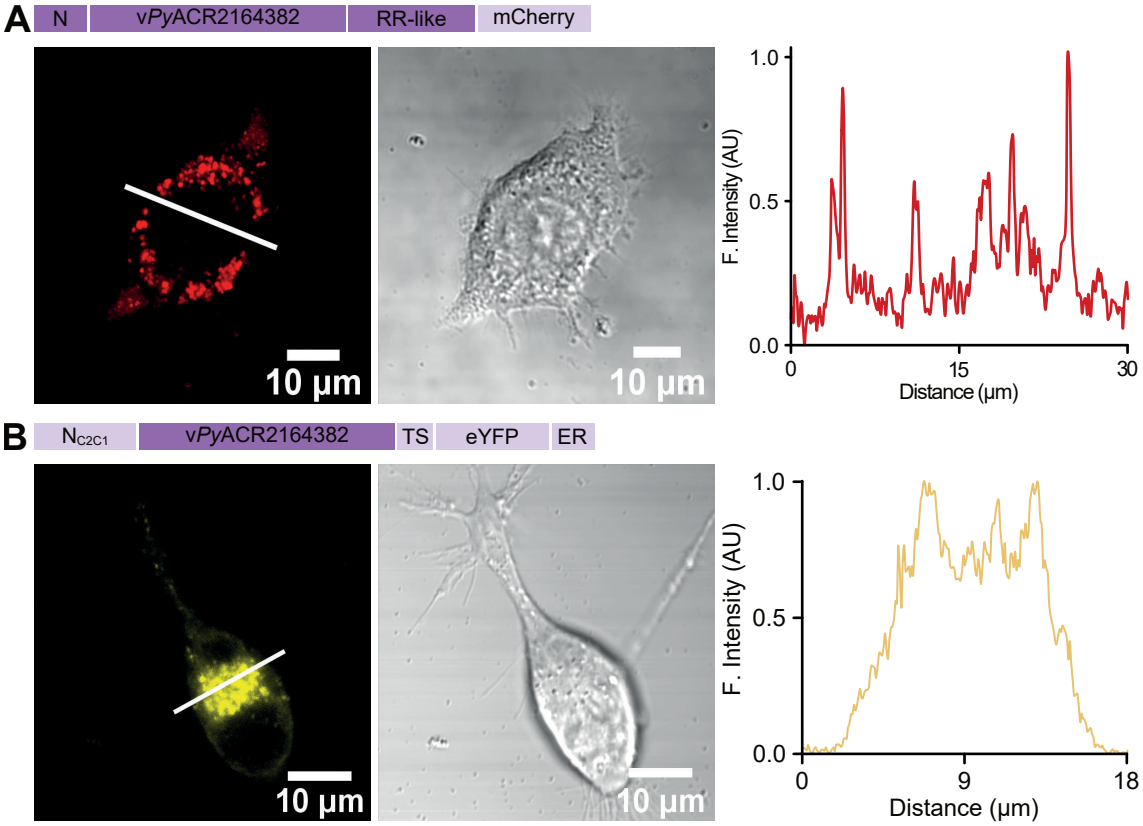


**Figure S11.: Membrane localization of v*Py*ACR2164382.** Confocal images of ND7/23 cells expressing full-length (**A**) or membrane-targeted (**B**) v*Py*ACR2164382. Fluorescence (left) of mCherry is shown in red and of eYFP in yellow. Fluorescence intensity profiles (right) were measured at the locations indicated by the white line in the fluorescence image. A bright field picture (center) is shown. Measurements were repeated at least three times for each construct. Abbreviations: N, amino terminus; RR-like, Histidine-kinase response regulator-like; TS, membrane-trafficking signal; eYFP, enhanced yellow fluorescent protein; ER, endoplasmic reticulum release signal. Confocal microscopy was performed and analyzed by Rodrigo Gaston Fernandez Lahore.

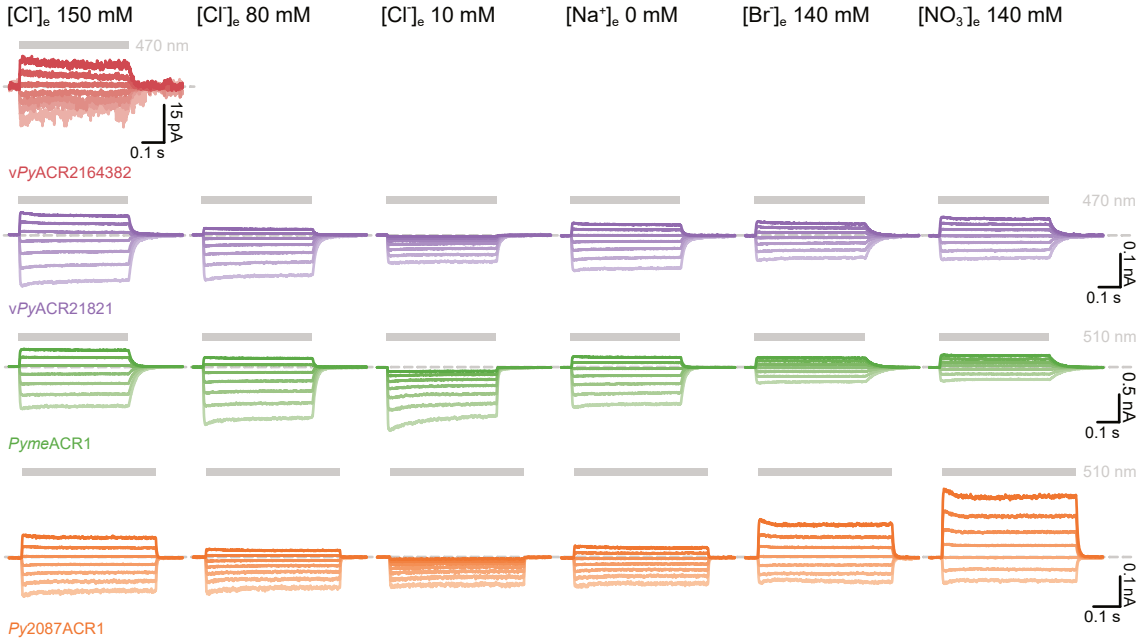


**Figure S12.: Representative photocurrent traces of viral and prasinophyte ChRs.** Photocurrents were evoked by 500 ms light pulses of 510 nm or 470 nm, indicated by a gray bar, and recorded at membrane potentials between −80 mV to 40 mV in ND7/23 cells with $[Cl^-]_i = 120$ mM and $[Na^+]_i = 110$ mM and with the extracellular buffer as indicated above.

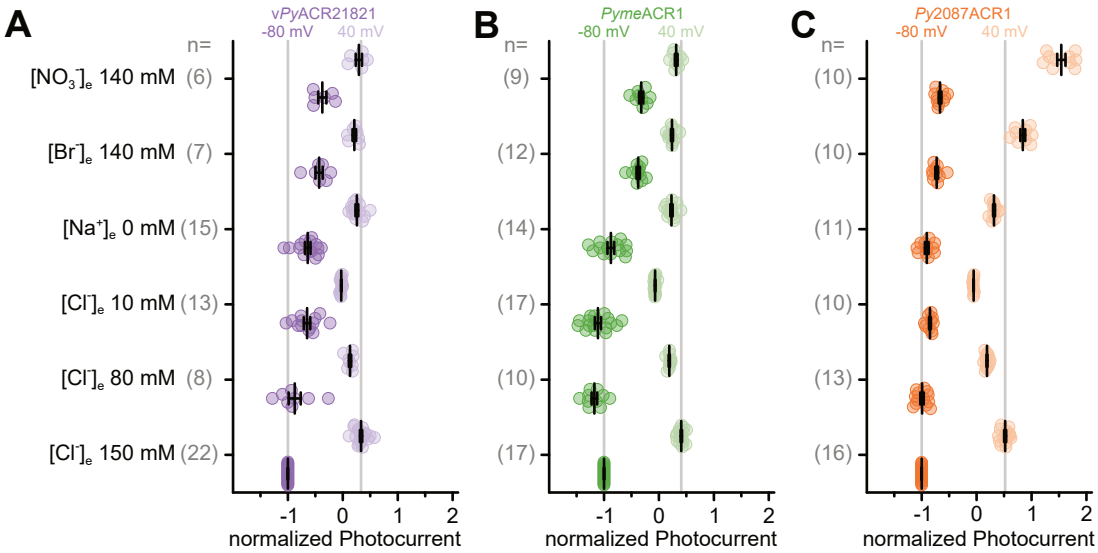


**Figure S13.: Normalized photocurrent amplitudes of viral and prasinophyte ChRs.** Photocurrent amplitudes of v*Py*ACR21821 (**A**), *Pyme*ACR1 (**B**), and *Py*2087ACR1 (**C**) were normalized to $I_{-80\,mV}$ in standard conditions. Normalized photocurrent amplitudes at −80 mV and 40 mV in indicated external ionic conditions were plotted.

## A.2. Supplementary tables

**Table S1.: Sequences used for phylogenetic trees and alignments.** GenBank accession numbers, PubMed identifier, and usage are indicated. Abbreviations: MASTs, marine uncultured stramenopiles; n. c., not classified; NCLDV, nucleo-cytoplasmic large DNA viruses; PMID, PubMed identifier.

| Name | Species | GenBank | PMID | in Fig. |
|---|---|---|---|---|
| MerMAID1 | MASTs | MK914541 | 31346176 | 11A, B |
| MerMAID2 | MASTs | MK914542 | 31346176 | 11A, B |
| MerMAID3 | MASTs | MK914543 | 31346176 | 11A, B |
| MerMAID4 | MASTs | MK914544 | 31346176 | 11A, B |
| MerMAID5 | MASTs | MK914545 | 31346176 | 11A, B |
| MerMAID6 | MASTs | MK914546 | 31346176 | 11A, B |
| MerMAID7 | MASTs | MK914547 | 31346176 | 11A, B |
| *Pyme*ACR1 | *Pyramimonas melkonianii* | MT353682 | 33065010 | 11A, B |
| *Py*2087ACR1 | *Pyramimonas spec.* | MT353681 | 33065010 | 11A, B |
| v*Py*ACR2164382 | NCLDV | MT353684 | 33065010 | 11A, B |
| v*Py*ACR21821 | NCLDV | MT353683 | 33065010 | 11A, B |
| *Cr*ChR1 | *Chlamydomonas reinhardtii* | AAM44039 | 12089443 | 2B; 5D; 11A |
| *Cr*ChR2 | *Chlamydomonas reinhardtii* | AAM44040 | 14615590 | 2B; 5D; 11A, B |
| *Vc*ChR1 | *Volvox carteri* | ABZ90900 | 19641026 | 2B; 5D; 11A |
| *Vc*ChR2 | *Volvox carteri* | ABZ90902 | 19641026 | 2B; 5D; 11A |
| *Bs*ChR1 | *Brachiomonas submarina* | AHH02152 | 24509633 | 5D; 11A |
| *Bs*ChR2 | *Brachiomonas submarina* | AHH02100 | 24509633 | 5D; 11A |
| *Cb*ChR1 | *Chlamydomonas bilatus-A* | AHH02128 | 24509633 | 5D; 11A |
| Chrimson | *Chlamydomonas noctigama* | AHH02126 | 24509633 | 2B; 5D; 11A |
| *Cn*ChR2 | *Chlamydomonas noctigama* | AHH02139 | 24509633 | 5D; 11A |
| *Cs*ChR | *Chloromonas subdivisa* | AHH02144 | 24509633 | 5D; 11A |
| *Co*ChR | *Chloromonas oogama* | AHH02107 | 24509633 | 5D; 11A |
| *Ds*ChR1 | *Dunaliella salina* | AEY68833 | 22196724 | 5D; 11A |
| *Ps*ChR2 | *Platymonas subcordiformis* | AGF84747 | 23995841 | 5D; 11A |
| *Sd*ChR | *Scherffelia dubia* | AHH02138 | 24509633 | 5D; 11A |
| *Tc*ChR | *Tetraselmis cordiformis* | AHH02123 | 24509633 | 5D; 11A |
| *Ts*ChR | *Tetraselmis striata* | AHH02155 | 24509633 | 5D; 11A |
| *Ag*ChR | *Asteromonas gracilis-B* | AHH02104 | 24509633 | 5D; 11A |
| Chronos | *Stigeoclonium helveticum* | AHH02106 | 24509633 | 5D; 11A |
| *Hd*ChR | *Haematococcus droebakensis* | AHH02125 | 24509633 | 5D; 11A |

**Table S1.:** (continued)

| Name | Species | GenBank | PMID | in Fig. |
|---|---|---|---|---|
| *Mv*ChR | *Mesostigma viride* | AEI83869 | 21693637 | 5D; 11A |
| *Ns*ChR | *Neochlorosarcina spec.* | AHH02120 | 24509633 | 5D; 11A |
| *Pg*ChR1 | *Pyramimonas gelidicola* | JQ241366 | 22196724 | 11A, B |
| *Gt*ACR1 | *Guillardia theta* | AKN63094 | 26113638 | 2B; 5D; 11A, B |
| *Gt*ACR2 | *Guillardia theta* | AKN63095 | 26113638 | 2B; 5D; 11A |
| *Gc*ACR-457 | *Geminigera cryophila* | APZ76704 | 28256618 | 5D; 11A |
| *Gc*ACR-439 | *Geminigera cryophila* | APZ76706 | 28256618 | 5D; 11A |
| C1ACR-887 | n. c. (CCMP2293) | APZ76721 | 28256618 | 5D; 11A |
| ZipACR | *Proteomonas sulcata* | APZ76709 | 28256618 | 2B; 5D; 11A |
| R1ACR-367 | *Rhodomonas spec.* | APZ76714 | 28256618 | 5D; 11A |
| R1ACR-447 | *Rhodomonas spec.* | APZ76716 | 28256618 | 5D; 11A |
| R1ACR-799 | *Rhodomonas spec.* | APZ76718 | 28256618 | 5D; 11A |
| R2ACR-853 | *Rhodomonas spec.* | APZ76719 | 28256618 | 5D; 11A |
| R1ACR-877 | *Rhodomonas spec.* | APZ76715 | 28256618 | 5D; 11A |
| *Gc*ACR-145 | *Geminigera cryophila* | APZ76705 | 28256618 | 5D; 11A |
| G1ACR-203 | *Geminigera spec.* | APZ76707 | 28256618 | 5D; 11A |
| G1ACR-243 | *Geminigera spec.* | APZ76708 | 28256618 | 5D; 11A |
| R2ACR-142 | *Rhodomonas spec.* | APZ76720 | 28256618 | 5D; 11A |
| C1ACR-023 | n. c. (CCMP2293) | APZ76722 | 28256618 | 5D; 11A |
| *Psu*ACR-003 | *Proteomonas sulcata* | APZ76711 | 28256618 | 5D; 11A |
| *Rl*ACR-477 | *Rhodomonas lens* | APZ76712 | 28256618 | 5D; 11A |
| *Rs*ACR-995 | *Rhodomonas salina* | APZ76713 | 28256618 | 5D; 11A |
| *Ps*ACR1 | *Proteomonas sulcata* | AHH02140 | 26740624 | 2B; 5D; 11A, B |
| *Psu*ACR-433 | *Proteomonas sulcata* | APZ76710 | 28256618 | 5D; 11A |
| *Gt*CCR1 | *Guillardia theta* | ANC73520 | 27233115 | 2B; 5D; 11A |
| *Gt*CCR2 | *Guillardia theta* | ANC73518 | 27233115 | 2B; 5D; 11A |
| *Gt*CCR3 | *Guillardia theta* | ANC73519 | 27233115 | 5D; 11A |
| *Gt*CCR4 | *Guillardia theta* | ARQ20888 | 28630812 | 5D; 11A, B |
| *Ps*CCR2 | *Proteomonas sulcata* | AHH02122 | 24509633 | 2B; 5D; 11A |
| ChRmine | *Rhodomonas lens* | QDS02893 | 31320556 | 5D; 11A, B |
| *Ra*CCR1 | *Rhodomonas abbreviata* | QIU80793 | 32317325 | 5D; 11A |
| *Ra*CCR2 | *Rhodomonas abbreviata* | QIU80796 | 32317325 | 2B; 5D; 11A |
| *Ra*CCR3 | *Rhodomonas abbreviata* | QIU80794 | 32317325 | 5D; 11A |
| *Rs*CCR1 | *Rhodomonas salina* | QIU80800 | 32317325 | 5D; 11A |

**Table S1.:** (continued)

| Name | Species | GenBank | PMID | in Fig. |
|---|---|---|---|---|
| *Rs*CCR2 | *Rhodomonas salina* | QIU80801 | 32317325 | 5D; 11A |
| *Psu*CCR2 | *Proteomonas sulcata* | QIU80791 | 32317325 | 5D; 11A |
| *Hp*CCR | *Hanusia phi* | QIU80788 | 32317325 | 5D; 11A |
| *Gc*CCR2 | *Geminigera cryophila* | QIU80786 | 32317325 | 5D; 11A |
| *Bf*CCR1 | *Baffinella frigidus* | QIU80783 | 32317325 | 5D; 11A |
| KR1 | *Krokinobacter eikastus* | BAN14807 | 23575682 | 2B; 11A |
| *Nd*R | *Nonlabens dokdonensis* | AGC76155 | 23292138 | 2B; 11A |
| XR | *Salinibacter ruber* | WP011404249 | 27630250 | 2B; 11A |
| GR | *Gloeobacter violaceus* | BAC88139 | 14621292 | 2B; 11A |
| *Cb*ClR | *Citromicrobium bathyomarinum* | WP010235302 | 27630250 | 2B; 11A |
| *Cs*ClR | *Citromicrobium sp.* | WP010414786 | 27630250 | 2B; 11A |
| FR | *Fulvimarina pelagi* | BAT31066 | 26534993 | 2B; 11A |
| *Nm*ClR | *Nonlabens marinus* | WP052476770 | 27630250 | 2B; 11A |
| KR2 | *Krokinobacter eikastus* | BAN14808 | 23575682 | 2B; 11A, B |
| *Gl*NaR | *Gillisia limnaea* | WP040506994 | 27630250 | 2B; 11A |
| *Ia*NaR | *Indibacter alkaliphilus* | WP009036080 | 27630250 | 2B; 11A |
| *Hw*BR | *Haloquadratum walsbyi* | CAJ51144 | 16820047 | 2B; 11A |
| *Hs*BR | *Halobacterium salinarum* | CAA23744 | 12049093 | 2B; 11A, B |
| AR1 | *Halorubrum chaoviator* | P69051 | 2833260 | 2B; 11A |
| AR2 | *Halobacterium sp.* | P29563 | 1654776 | 2B; 11A |
| AR3 | *Halorubrum sodomense* | ADB03110 | 9878396 | 2B; 11A |
| *Np*HR | *Natronomonas pharaonis* | P15647 | 2104837 | 2B; 11A |
| *Hs*HR | *Halobacterium salinarum* | WP010902090 | 24409552 | 2B; 11A, B |
| *Sr*HR | *Salinibacter ruber* | ABC44173 | 16330755 | 2B; 11A |
| *Hs*SRII | *Halobacterium salinarum* | WP010903286 | 2591367 | 2B |
| *Hh*SRII | *Halobacterium hubeiense* | CQH59952 | | 2B |
| *Np*SRII | *Natronomonas pharaonis* | CAI50508 | 16169924 | 2B |
| *Cs*R | *Coccomyxa subellipsoidea* | XP005646688 | 22630137 | 2B |
| *Aa*RI | *Acetabularia acetabulum* | AEF12206 | 21780504 | 2B |
| *Aa*RII | *Acetabularia acetabulum* | AEF12207 | | 2B |
| *Be*RhGC | *Blastocladiella emersonii* | AIC07007 | 24835457 | 2B |
| *Ca*RhGC | *Catenaria anguillulae* | AVZ03094 | 29799525 | 2B |

# References

**Abdul Kadir**, **L.**; **M. Stacey**; **R. Barrett-Jolley** (2018). "Emerging roles of the membrane potential: Action beyond the action potential". *Frontiers in Physiology* 9, 1661. DOI: 10.3389/fphys.2018.01661.

**Adams**, **D. S.**; **M. Levin** (2013). "Endogenous voltage gradients as mediators of cell-cell communication: Strategies for investigating bioelectrical signals during pattern formation". *Cell and Tissue Research* 352, 1, pp. 95–122. DOI: 10.1007/s00441-012-1329-4.

**Aggarwal**, **S. K.**; **R. MacKinnon** (1996). "Contribution of the S4 segment to gating charge in the Shaker $K^+$ channel". *Neuron* 16, 6, pp. 1169–1177. DOI: 10.1016/S0896-6273(00)80143-9.

**Ahmad**, **M.**; **A. R. Cashmore** (1993). "HY4 gene of *A. thaliana* encodes a protein with characteristics of a blue-light photoreceptor". *Nature* 366, 6451, pp. 162–166. DOI: 10.1038/366162a0.

**Alberio**, **L.** *et al.* (2018). "A light-gated potassium channel for sustained neuronal inhibition". *Nature Methods* 15, 11. DOI: 10.1038/s41592-018-0186-9.

**Alshuth**, **T.**; **M. Stockburger**; **P. Hegemann**; **D. Oesterhelt** (1985). "Structure of the retinal chromophore in Halorhodopsin: A resonance Raman study". *FEBS Letters* 179, 1, pp. 55–59. DOI: 10.1016/0014-5793(85)80190-3.

**Amann**, **R. I.**; **W. Ludwig**; **K.-H. Schleifer** (1995). "Phylogenetic identification and *in situ* detection of individual microbial cells without cultivation". *Microbiological and Molecular Biology Reviews* 59, 1, pp. 143–169.

**Ames**, **J. B.**; **R. A. Mathies** (1990). "The role of back-reactions and proton uptake during the N-O transition in Bacteriorhodopsins photocycle: A kinetic resonance Raman study". *Biochemistry* 29, 31, pp. 7181–7190. DOI: 10.1021/bi00483a005.

**Ames**, **J. B.**; **J. Raap**; **J. Lugtenburg**; **R. A. Mathies** (1992). "Resonance Raman study of Halorhodopsin photocycle kinetics, chromophore structure, and chloride-pumping mechanism". *Biochemistry* 31, 50, pp. 12546–12554. DOI: 10.1021/bi00165a002.

**Anders**, **K.**; **L.-O. Essen** (2015). "The family of phytochrome-like photoreceptors: Diverse, complex and multi-colored, but very useful". *Current Opinion in Structural Biology* 35, pp. 7–16. DOI: 10.1016/j.sbi.2015.07.005.

**Andersen**, **L. H.**; **I. B. Nielsen**; **M. B. Kristensen**; **M. O. A. El Ghazaly**; **S. Haacke**; **M. B. Nielsen**; **M. Å. Petersen** (2005). "Absorption of Schiff-base retinal chromophores *in vacuo*". *Journal of the American Chemical Society* 127, 35, pp. 12347–12350. DOI: 10.1021/ja051638j.

**Anderson**, **S.**; **S. Crosson**; **K. Moffat** (2004). "Short hydrogen bonds in Photoactive Yellow Protein". *Acta Crystallographica Section D: Biological Crystallography* 60, 6, pp. 1008–1016. DOI: 10.1107/S090744490400616X.

**Andújar**, **C.**; **P. Arribas**; **F. Ruzicka**; **A. Crampton-Platt**; **M. J. T. N. Timmermans**; **A. P. Vogler** (2015). "Phylogenetic community ecology of soil biodiversity using mitochondrial metagenomics". *Molecular Ecology* 24, 14, pp. 3603–3617. DOI: 10.1111/mec.13195.

**Asano**, **T.**; **H. Igarashi**; **T. Ishizuka**; **H. Yawo** (2018). "Organelle optogenetics: Direct manipulation of intracellular $Ca^{2+}$-dynamics by light". *Frontiers in Neuroscience* 12, 8, pp. 1–8. DOI: 10.3389/fnins.2018.00561.

**Atkinson**, **G. H.**; **T. L. Brack**; **D. Blanchard**; **G. Rumbles** (1989). "Picosecond time-resolved resonance Raman spectroscopy of the initial *trans* to *cis* isomerization in the Bacteriorhodopsin photocycle". *Chemical Physics* 131, 1, pp. 1–15. DOI: 10.1016/0301-0104(89)87077-6.

**Aton**, **B.**; **A. G. Doukas**; **R. H. Callender**; **B. Becher**; **T. G. Ebrey** (1977). "Resonance Raman studies of the purple membrane". *Biochemistry* 16, 13, pp. 2995–2999. DOI: 10.1021/bi00632a029.

**Avelar**, **G. M.**; **R. I. Schumacher**; **P. A. Zaini**; **G. Leonard**; **T. A. Richards**; **S. L. Gomes** (2014). "A rhodopsin-guanylyl cyclase gene fusion functions in visual perception in a fungus". *Current Biology* 24, 11, pp. 1234–1240. DOI: 10.1016/j.cub.2014.04.009.

**Awasthi**, **M.**; **P. Ranjan**; **K. Sharma**; **S. K. Veetil**; **S. Kateriya** (2016). "The trafficking of bacterial-type rhodopsins into the *Chlamydomonas* eyespot and flagella is IFT-mediated". *Scientific Reports* 6, 1, p. 34646. DOI: 10.1038/srep34646.

**AzimiHashemi**, **N.** *et al.* (2014). "Synthetic retinal analogues modify the spectral and kinetic characteristics of microbial rhodopsin optogenetic tools". *Nature Communications* 5, 1, p. 5810. DOI: 10.1038/ncomms6810.

**Azumi**, **T.**; **K. Matsuzaki** (1977). "What does the term vibronic coupling mean?" *Photochemistry and Photobiology* 25, 3, pp. 315–326. DOI: 10.1111/j.1751-1097.1977.tb06918.x.

**Babourina**, **O.**; **I. Newman**; **S. Shabala** (2002). "Blue light-induced kinetics of $H^+$ and $Ca^{2+}$ fluxes in etiolated wild-type and phototropin-mutant *Arabidopsis* seedlings". *Proceedings of the National Academy of Sciences* 99, 4, pp. 2433–2438. DOI: 10.1073/pnas.042294599.

**Bamann**, **C.**; **R. Gueta**; **S. Kleinlogel**; **G. Nagel**; **E. Bamberg** (2010). "Structural guidance of the photocycle of Channelrhodopsin-2 by an interhelical hydrogen bond". *Biochemistry* 49, 2, pp. 267–278. DOI: 10.1021/bi901634p.

**Bamann**, **C.**; **T. Kirsch**; **G. Nagel**; **E. Bamberg** (2008). "Spectral characteristics of the photocycle of Channelrhodopsin-2 and its implication for channel function". *Journal of Molecular Biology* 375, 3, pp. 686–694. DOI: 10.1016/j.jmb.2007.10.072.

**Barchad-Avitzur**, **O.**; **M. F. Priest**; **N. Dekel**; **F. Bezanilla**; **H. Parnas**; **Y. Ben-Chaim** (2016). "A novel voltage sensor in the orthosteric binding site of the M2 muscarinic receptor". *Biophysical Journal* 111, 7, pp. 1396–1408. DOI: 10.1016/j.bpj.2016.08.035.

**Barry**, **P. H.** (1994). "JPCalc, a software package for calculating liquid junction potential corrections in patch-clamp, intracellular, epithelial and bilayer measurements and for correcting junction potential measurements". *Journal of Neuroscience Methods* 51, 1, pp. 107–116. DOI: 10.1016/0165-0270(94)90031-0.

**Barun**, **V. V.**; **A. P. Ivanov**; **A. V. Volotovskaya**; **V. S. Ulashchik** (2007). "Absorption spectra and light penetration depth of normal and pathologically altered human skin". *Journal of Applied Spectroscopy* 74, 3, pp. 430–439. DOI: 10.1007/s10812-007-0071-2.

**Béjà**, **O.**; **J. K. Lanyi** (2014). "Nature's toolkit for microbial rhodopsin ion pumps". *Proceedings of the National Academy of Sciences* 111, 18, pp. 6538–6539. DOI: 10.1073/pnas.1405093111.

**Béjà**, **O.**; **E. N. Spudich**; **J. L. Spudich**; **M. Leclerc**; **E. F. DeLong** (2001). "Proteorhodopsin phototrophy in the ocean". *Nature* 411, 6839, pp. 786–789. DOI: 10.1038/35081051.

**Béjà**, **O.** *et al.* (2000). "Bacterial rhodopsin: Evidence for a new type of phototrophy in the sea". *Science* 289, 5486, pp. 1902–1906.

**Ben-Chaim**, **Y.**; **B. Chanda**; **N. Dascal**; **F. Bezanilla**; **I. Parnas**; **H. Parnas** (2006). "Movement of 'gating charge' is coupled to ligand binding in a G-protein-coupled receptor". *Nature* 444, 7115, pp. 106–109. DOI: 10.1038/nature05259.

**Bernal Sierra**, **Y. A.** *et al.* (2018). "Potassium channel-based optogenetic silencing". *Nature Communications* 9, 1, p. 4611. DOI: 10.1038/s41467-018-07038-8.

**Berndt**, **A.**; **S. Y. Lee**; **C. Ramakrishnan**; **K. Deisseroth** (2014). "Structure-guided Transformation of channelrhodopsin into a light-activated chloride channel". *Science* 344, 6182, pp. 420–424. DOI: 10.1126/science.1252367.

**Berndt**, **A.**; **P. Schoenenberger**; **J. Mattis**; **K. M. Tye**; **K. Deisseroth**; **P. Hegemann**; **T. G. Oertner** (2011). "High-efficiency channelrhodopsins for fast neuronal stimulation at low light levels". *Proceedings of the National Academy of Sciences* 108, 18, pp. 7595–7600. DOI: 10.1073/pnas.1017210108.

**Berndt**, **A.**; **O. Yizhar**; **L. A. Gunaydin**; **P. Hegemann**; **K. Deisseroth** (2009). "Bi-stable neural state switches". *Nature Neuroscience* 12, 2, pp. 229–234. DOI: 10.1038/nn.2247.

**Berndt**, **A.** *et al.* (2016). "Structural foundations of optogenetics: Determinants of channelrhodopsin ion selectivity". *Proceedings of the National Academy of Sciences* 113, 4, pp. 822–829. DOI: 10.1073/pnas.1523341113.

**Berridge**, **M. J.**; **M. D. Bootman**; **H. L. Roderick** (2003). "Calcium signalling: Dynamics, homeostasis and remodelling". *Nature Reviews Molecular Cell Biology* 4, 7, pp. 517–529. DOI: 10.1038/nrm1155.

**Berthold**, **P.**; **S. P. Tsunoda**; **O. P. Ernst**; **W. Mages**; **D. Gradmann**; **P. Hegemann** (2008). "Channelrhodopsin-1 initiates phototaxis and photophobic responses in *Chlamydomonas* by immediate light-induced depolarization". *The Plant Cell* 20, 6, pp. 1665–1677. DOI: 10.1105/tpc.108.057919.

**Bhattarai**, **A.**; **J. Wang**; **Y. Miao** (2020). "G-protein-coupled receptor-membrane interactions depend on the receptor activation state". *Journal of Computational Chemistry* 41, 5, pp. 460–471. DOI: 10.1002/jcc.26082.

**Bhoo**, **S.-H.**; **S. J. Davis**; **J. Walker**; **B. Karniol**; **R. D. Vierstra** (2001). "Bacteriophytochromes are photochromic histidine kinases using a biliverdin chromophore". *Nature* 414, 6865, pp. 776–779. DOI: 10.1038/414776a.

**Bi**, **A.**; **J. Cui**; **Y.-P. Ma**; **E. Olshevskaya**; **M. Pu**; **A. M. Dizhoor**; **Z.-H. Pan** (2006). "Ectopic expression of a microbial-type rhodopsin restores visual responses in mice with photoreceptor degeneration". *Neuron* 50, 1, pp. 23–33. DOI: 10.1016/j.neuron.2006.02.026.

**Birge**, **R. R.**; **T. M. Cooper**; **A. F. Lawrence**; **M. B. Masthay**; **C. Vasilakis**; **C. F. Zhang**; **R. Zidovetzki** (1989). "A spectroscopic, photocalorimetric, and theoretical investigation of the quantum efficiency of the primary event in Bacteriorhodopsin". *Journal of the American Chemical Society* 111, 11, pp. 4063–4074. DOI: 10.1021/ja00193a044.

**Bisson**, **M. A.**; **J. Gutknecht** (1977). "Osmotic regulation in the marine alga *Codium decorticatum*". *The Journal of Membrane Biology* 37, 1, pp. 85–98. DOI: 10.1007/BF01940925.

**Blatz**, **P. E.**; **J. H. Mohler**; **H. V. Navangul** (1972). "Anion-induced wavelength regulation of absorption maxima of Schiff bases of retinal". *Biochemistry* 11, 5, pp. 848–855. DOI: 10.1021/bi00755a026.

**Bogomolni**, **R. A.**; **J. L. Spudich** (1982). "Identification of a third rhodopsin-like pigment in phototactic *Halobacterium halobium*". *Proceedings of the National Academy of Sciences* 79, 20, pp. 6250–6254. DOI: 10.1073/pnas.79.20.6250.

**Böhm**, **M.** *et al.* (2019). "Channelrhodopsin-1 phosphorylation changes with phototactic behavior and responds to physiological stimuli in *Chlamydomonas*". *The Plant Cell* 31, 4, pp. 886–910. DOI: 10.1105/tpc.18.00936.

**Bonzanni**, **M.**; **S. L. Payne**; **M. Adelfio**; **D. L. Kaplan**; **M. Levin**; **M. J. Oudin** (2020). "Defined extracellular ionic solutions to study and manipulate the cellular resting membrane potential". *Biology Open* 9, 1. DOI: 10.1242/bio.048553.

**Bouly**, **J.-P.** *et al.* (2007). "Cryptochrome blue light photoreceptors are activated through interconversion of flavin redox states". *Journal of Biological Chemistry* 282, 13, pp. 9383–9391. DOI: 10.1074/jbc.M609842200.

**Bourret**, **R. B.** (2010). "Receiver domain structure and function in response regulator proteins". *Current Opinion in Microbiology* 13, 2, pp. 142–149. DOI: 10.1016/j.mib.2010.01.015.

**Bousché**, **O.**; **S. Sonar**; **M. P. Krebs**; **H. G. Khorana**; **K. J. Rothschild** (1992). "Time-resolved Fourier transform infrared spectroscopy of the Bacteriorhodopsin mutant Tyr-185-Phe: Asp-96 reprotonates during O formation; Asp-85 and Asp-212 deprotonate during O decay". *Photochemistry and Photobiology* 56, 6, pp. 1085–1095. DOI: 10.1111/j.1751-1097.1992.tb09732.x.

**Boyden**, **E. S.**; **F. Zhang**; **E. Bamberg**; **G. Nagel**; **K. Deisseroth** (2005). "Millisecond-timescale, genetically targeted optical control of neural activity". *Nature Neuroscience* 8, 9, pp. 1263–1268. DOI: 10.1038/nn1525.

**Braatsch**, **S.**; **G. Klug** (2004). "Blue light perception in bacteria". *Photosynthesis Research* 79, 1, pp. 45–57. DOI: 10.1023/B:PRES.0000011924.89742.f9.

**Braiman**, **M. S.**; **O. Bousché**; **K. J. Rothschild** (1991). "Protein dynamics in the Bacteriorhodopsin photocycle: Submillisecond Fourier transform infrared spectra of the L, M, and N photointermediates." *Proceedings of the National Academy of Sciences* 88, 6, pp. 2388–2392. DOI: 10.1073/pnas.88.6.2388.

**Braiman**, **M. S.**; **T. M. Mogi**; **T. M. Marti**; **L. J. Stern**; **H. G. Khorana**; **K. J. Rothschild** (1988). "Vibrational spectroscopy of Bacteriorhodopsin mutants: Light-driven proton transport involves protonation changes of aspartic acid residues 85, 96, and 212". *Biochemistry* 27, 23, pp. 8516–8520. DOI: 10.1021/bi00423a002.

**Braiman**, **M. S.**; **T. J. Walter**; **D. M. Briercheck** (1994). "Infrared spectroscopic detection of light-induced change in chloride-arginine interaction in Halorhodopsin". *Biochemistry* 33, 7, pp. 1629–1635. DOI: 10.1021/bi00173a003.

**Bratanov**, **D.** *et al.* (2019). "Unique structure and function of viral rhodopsins". *Nature Communications* 10, 1, pp. 1–13. DOI: 10.1038/s41467-019-12718-0.

**Brown**, **B. A.**; **C. Cloix**; **G. H. Jiang**; **E. Kaiserli**; **P. Herzyk**; **D. J. Kliebenstein**; **G. I. Jenkins** (2005). "A UV-B-specific signaling component orchestrates plant UV protection". *Proceedings of the National Academy of Sciences* 102, 50, pp. 18225–18230. DOI: 10.1073/pnas.0507187102.

**Brown**, **L. S.**; **Y. Gat**; **M. Sheves**; **Y. Yamazaki**; **A. Maeda**; **R. Needleman**; **J. K. Lanyi** (1994). "The retinal Schiff base-counterion complex of Bacteriorhodopsin: Changed geometry during the photocycle is a cause of proton transfer to aspartate 85". *Biochemistry* 33, 40, pp. 12001–12011. DOI: 10.1021/bi00206a001.

**Brum**, **J. R.** *et al.* (2015). "Patterns and ecological drivers of ocean viral communities". *Science* 348, 6237, pp. 1261498–1261498. DOI: 10.1126/science.1261498.

**Brunet**, **T.**; **B. T. Larson**; **T. A. Linden**; **M. J. A. Vermeij**; **K. McDonald**; **N. King** (2019). "Light-regulated collective contractility in a multicellular choanoflagellate". *Science* 366, 6463, pp. 326–334. DOI: 10.1126/science.aay2346.

**Bruun**, **S.**; **H. Naumann**; **U. Kuhlmann**; **C. Schulz**; **K. Stehfest**; **P. Hegemann**; **P. Hildebrandt** (2011). "The chromophore structure of the long-lived intermediate of the C128T Channelrhodopsin-2 variant". *FEBS Letters* 585, 24, pp. 3998–4001. DOI: 10.1016/j.febslet.2011.11.007.

**Bruun**, **S.** *et al.* (2015). "Light-dark adaptation of channelrhodopsin involves photoconversion between the all-*trans* and 13-*cis* retinal isomers". *Biochemistry* 54, 35, pp. 5389–5400. DOI: 10.1021/acs.biochem.5b00597.

**Butler**, **W. L.**; **K. H. Norris**; **H. W. Siegelman**; **S. B. Hendricks** (1959). "Detection, assay, and preliminary purification of the pigment controlling photoresponsive development of plants". *Proceedings of the National Academy of Sciences* 45, 12, pp. 1703–1708.

**Carter**, **P.** (1986). "Site-directed mutagenesis". *Biochemical Journal* 237, 1, pp. 1–7. DOI: 10.1042/bj2370001.

**Checover**, **S.**; **E. Nachliel**; **N. A. Dencher**; **M. Gutman** (1997). "Mechanism of proton entry into the cytoplasmic section of the proton-conducting channel of Bacteriorhodopsin". *Biochemistry* 36, 45, pp. 13919–13928. DOI: 10.1021/bi9717542.

**Cho**, **W.** (2001). "Membrane targeting by C1 and C2 domains". *Journal of Biological Chemistry* 276, 35, pp. 32407–32410. DOI: 10.1074/jbc.R100007200.

**Chon**, **Y.-S.**; **H. Kandori**; **J. Sasaki**; **J. K. Lanyi**; **R. Needleman**; **A. Maeda** (1999). "Existence of two L photointermediates of Halorhodopsin from *Halobacterium salinarum*, differing in their protein and water FTIR bands". *Biochemistry* 38, 29, pp. 9449–9455. DOI: 10.1021/bi9903042.

**Chowdhury**, **J.** (2018). "Resonance Raman spectroscopy: Principles and applications". *Molecular and Laser Spectroscopy*. Ed. by **V. P. Gupta**, pp. 147–164. ISBN: 978-0-12-849883-5. DOI: 10.1016/B978-0-12-849883-5.00007-3.

**Christie**, **J. M.** (2007). "Phototropin blue-light receptors". *Annual Review of Plant Biology* 58, 1, pp. 21–45. DOI: 10.1146/annurev.arplant.58.032806.103951.

**Christie**, **J. M.**; **P. Reymond**; **G. K. Powell**; **P. Bernasconi**; **A. A. Raibekas**; **E. Liscum**; **W. R. Briggs** (1998). "*Arabidopsis* NPH1: A flavoprotein with the properties of a photoreceptor for phototropism". *Science* 282, 5394, pp. 1698–1701. DOI: 10.1126/science.282.5394.1698.

**Christie**, **J. M.** *et al.* (2012). "Plant UVR8 photoreceptor senses UV-B by tryptophan-mediated disruption of cross-dimer salt bridges". *Science* 335, 6075, pp. 1492–1496. DOI: 10.1126/science.1218091.

**Cohen**, **S. N.**; **A. C. Y. Chang**; **H. W. Boyer**; **R. B. Helling** (1973). "Construction of biologically functional bacterial plasmids *in vitro*". *Proceedings of the National Academy of Sciences* 70, 11, pp. 3240–3244. DOI: 10.1073/pnas.70.11.3240.

**Cosentino**, **C.** *et al.* (2015). "Engineering of a light-gated potassium channel". *Science* 348, 6235, pp. 707–710. DOI: 10.1126/science.aaa2787.

**Davis**, **S. J.**; **A. V. Vener**; **R. D. Vierstra** (1999). "Bacteriophytochromes: Phytochrome-like photoreceptors from nonphotosynthetic eubacteria". *Science* 286, 5449, pp. 2517–2520. DOI: 10.1126/science.286.5449.2517.

**Deisseroth**, **K.**; **G. Feng**; **A. K. Majewska**; **G. Miesenböck**; **A. Ting**; **M. J. Schnitzer** (2006). "Next-generation optical technologies for illuminating genetically targeted brain circuits". *Journal of Neuroscience* 26, 41, pp. 10380–10386. DOI: 10.1523/JNEUROSCI.3863-06.2006.

**Deisseroth**, **K.**; **P. Hegemann** (2017). "The form and function of channelrhodopsin". *Science* 357, 6356, eaan5544. DOI: 10.1126/science.aan5544.

**del Vado**, **M. A. G.**; **J. Donoso**; **F. Muñoz**; **G. R. Echevarria**; **F. G. Blanco** (1987). "Kinetic and thermodynamic parameters for Schiff's base formation between Pyridoxal 5'-Phosphate and n-Hexylamine". *Journal of the Chemical Society, Perkin Transactions 2*, 4, pp. 445–448. DOI: 10.1039/P29870000445.

**Dellago**, **C.**; **M. M. Naor**; **G. Hummer** (2003). "Proton transport through water-filled carbon nanotubes". *Physical Review Letters* 90, 10, p. 105902. DOI: 10.1103/PhysRevLett.90.105902.

**Dencher**, **N. A.**; **G. Papadopoulos**; **D. Dresselhaus**; **G. Büldt** (1990). "Light- and dark-adapted Bacteriorhodopsin, a time-resolved neutron diffraction study". *Biochimica et Biophysica Acta (BBA) - Biomembranes* 1026, 1, pp. 51–56. DOI: 10.1016/0005-2736(90)90331-H.

**Desai**, **S. K.**; **L. J. Kenney** (2017). "To ∼P or not to ∼P? Non-canonical activation by two-component response regulators". *Molecular Microbiology* 103, 2, pp. 203–213. DOI: 10.1111/mmi.13532.

**Di Wu** *et al.* (2012). "Structural basis of Ultraviolet-B perception by UVR8". *Nature* 484, 7393, pp. 214–219. DOI: 10.1038/nature10931.

**Ding**, **X.** *et al.* (2018). "Functional roles of tyrosine 185 during the Bacteriorhodopsin photocycle as revealed by *in situ* spectroscopic studies". *Biochimica et Biophysica Acta (BBA) - Bioenergetics* 1859, 10, pp. 1006–1014. DOI: 10.1016/j.bbabio.2018.05.011.

**Dioumaev**, **A. K.**; **L. S. Brown**; **R. Needleman**; **J. K. Lanyi** (1999). "Fourier-transform infrared spectra of a late intermediate of the Bacteriorhodopsin photocycle suggest transient protonation of Asp-212". *Biochemistry* 38, 31, pp. 10070–10078. DOI: 10.1021/bi990873+.

**Dobler**, **J.**; **W. Zinth**; **W. Kaiser**; **D. Oesterhelt** (1988). "Excited-state reaction dynamics of Bacteriorhodopsin studied by femtosecond spectroscopy". *Chemical Physics Letters* 144, 2, pp. 215–220. DOI: 10.1016/0009-2614(88)87120-3.

**Doig**, **S. J.**; **P. J. Reid**; **R. A. Mathies** (1991). "Picosecond time-resolved resonance Raman spectroscopy of Bacteriorhodopsin's J, K, and KL intermediates". *The Journal of Physical Chemistry* 95, 16, pp. 6372–6379. DOI: 10.1021/j100169a054.

**Duan**, **X.**; **G. Nagel**; **S. Gao** (2019). "Mutated channelrhodopsins with increased sodium and calcium permeability". *Applied Sciences* 9, 4, p. 664. DOI: 10.3390/app9040664.

**Dunn**, **R.**; **J. McCoy**; **M. Simsek**; **A. Majumdar**; **S. H. Chang**; **U. L. Rajbhandary**; **H. G. Khorana** (1981). "The Bacteriorhodopsin gene". *Proceedings of the National Academy of Sciences* 78, 11, pp. 6744–6748. DOI: 10.1073/pnas.78.11.6744.

**Dziubinska**, **H.**; **K. Trebacz**; **T. Zawadzki** (1989). "The effect of excitation on the rate of respiration in the liverwort *Conocephalum conicum*". *Physiologia Plantarum* 75, 3, pp. 417–423. DOI: 10.1111/j.1399-3054.1989.tb04648.x.

**Eaton**, **J. W.** (2002). *GNU Octave manual*. Network Theory Limited. ISBN: 0-9541617-2-6.

**Efron**, **B.** (1979). "Bootstrap methods: Another look at the jackknife". *The Annals of Statistics* 7, 1, pp. 1–26. DOI: 10.1214/aos/1176344552.

**Efron**, **B.** (1987). "Better bootstrap confidence intervals". *Journal of the American Statistical Association* 82, 397, pp. 171–185. DOI: 10.1080/01621459.1987.10478410.

**Ehlenbeck**, **S.** (2002). "Licht-induzierte $H^+$- und $Cl^-$-Ströme in *Chlamydomonas reinhardtii*". Dissertation. Regensburg: University of Regensburg.

**Ehrenberg**, **D.** *et al.* (2019). "Atomistic insight into the role of threonine 127 in the functional mechanism of Channelrhodopsin-2". *Applied Sciences* 9, 22, p. 4905. DOI: 10.3390/app9224905.

**Emery**, **W. J.** (2015). "Sea surface temperature". *Encyclopedia of Atmospheric Sciences*. Ed. by **G. R. North**; **J. Pyle**; **F. Zhang**. Second. Air Sea Interactions. Oxford: Academic Press, pp. 136–143. ISBN: 978-0-12-382225-3. DOI: 10.1016/B978-0-12-382225-3.00065-7.

**Engel**, **B. D.**; **M. Schaffer**; **L. Kuhn Cuellar**; **E. Villa**; **J. M. Plitzko**; **W. Baumeister** (2015). "Native architecture of the *Chlamydomonas* chloroplast revealed by *in situ* cryo-electron tomography". *eLife* 4. Ed. by **J. Chory**, e04889. DOI: 10.7554/eLife.04889.

**Ernst**, **O. P.**; **D. T. Lodowski**; **M. Elstner**; **P. Hegemann**; **L. S. Brown**; **H. Kandori** (2014). "Microbial and animal rhodopsins: Structures, functions, and molecular mechanisms". *Chemical Reviews* 114, 1, pp. 126–163. DOI: 10.1021/cr4003769.

**Ernst**, **O. P.**; **P. A. Sánchez Murcia**; **P. Daldrop**; **S. P. Tsunoda**; **S. Kateriya**; **P. Hegemann** (2008). "Photoactivation of channelrhodopsin". *Journal of Biological Chemistry* 283, 3, pp. 1637–1643. DOI: 10.1074/jbc.M708039200.

**Essen**, **L.-O.** (2002). "Halorhodopsin: Light-driven ion pumping made simple?" *Current Opinion in Structural Biology* 12, 4, pp. 516–522. DOI: 10.1016/S0959-440X(02)00356-1.

**Essen**, **L.-O.**; **J. Mailliet**; **J. Hughes** (2008). "The structure of a complete phytochrome sensory module in the Pr ground state". *Proceedings of the National Academy of Sciences* 105, 38, pp. 14709–14714. DOI: 10.1073/pnas.0806477105.

**Fankhauser**, **C.**; **D. Staiger** (2002). "Photoreceptors in *Arabidopsis thaliana*: Light perception, signal transduction and entrainment of the endogenous clock". *Planta* 216, 1, pp. 1–16. DOI: 10.1007/s00425-002-0831-4.

**Felgner**, **P. L.** *et al.* (1987). "Lipofection: A highly efficient, lipid-mediated DNA-transfection procedure". *Proceedings of the National Academy of Sciences* 84, 21, pp. 7413–7417. DOI: 10.1073/pnas.84.21.7413.

**Findlay**, **G. P.** (1959). "Studies of action potentials in the vacuole and cytoplasm of *Nitella*". *Australian Journal of Biological Sciences* 12, 4, pp. 412–426. DOI: 10.1071/bi9590412.

**Finkel**, **O. M.**; **O. Béjà**; **S. Belkin** (2013). "Global abundance of microbial rhodopsins". *The ISME Journal* 7, 2, pp. 448–451. DOI: 10.1038/ismej.2012.112.

**Fodor**, **S. P.**; **R. Gebhard**; **J. Lugtenburg**; **R. A. Bogomolni**; **R. A. Mathies** (1989). "Structure of the retinal chromophore in Sensory Rhodopsin I from resonance Raman spectroscopy". *Journal of Biological Chemistry* 264, 31, pp. 18280–18283.

**Foster**, **K. W.**; **J. Saranak**; **N. Patel**; **G. Zarilli**; **M. Okabe**; **T. Kline**; **K. Nakanishi** (1984). "A rhodopsin is the functional photoreceptor for phototaxis in the unicellular eukaryote *Chlamydomonas*". *Nature* 311, 5988, pp. 756–759. DOI: 10.1038/311756a0.

**Foster**, **K. W.**; **R. D. Smyth** (1980). "Light antennas in phototactic algae". *Microbiology Reviews* 44, 4, pp. 572–630.

**Freier**, **E.**; **S. Wolf**; **K. Gerwert** (2011). "Proton transfer via a transient linear water-molecule chain in a membrane protein". *Proceedings of the National Academy of Sciences* 108, 28, pp. 11435–11439. DOI: 10.1073/pnas.1104735108.

**Friedrich**, **D.**; **F. N. Brünig**; **A. J. Nieuwkoop**; **R. R. Netz**; **P. Hegemann**; **H. Oschkinat** (2020). "Collective exchange processes reveal an active site proton cage in Bacteriorhodopsin". *Communications Biology* 3, 1, pp. 1–9. DOI: 10.1038/s42003-019-0733-7.

**Fudim**, **R.** *et al.* (2019). "Design of a light-gated proton channel based on the crystal structure of *Coccomyxa* Rhodopsin". *Science Signaling* 12, 573, eaav4203. DOI: 10.1126/scisignal.aav4203.

**Gai**, **F.**; **K. C. Hasson**; **J. C. McDonald**; **P. A. Anfinrud** (1998). "Chemical dynamics in proteins: The photoisomerization of retinal in Bacteriorhodopsin". *Science* 279, 5358, pp. 1886–1891. DOI: 10.1126/science.279.5358.1886.

**Galvão**, **V. C.**; **C. Fankhauser** (2015). "Sensing the light environment in plants: Photoreceptors and early signaling steps". *Current Opinion in Neurobiology* 34, pp. 46–53. DOI: 10.1016/j.conb.2015.01.013.

**Garavelli**, **M.** (2006). "Computational organic photochemistry: Strategy, achievements and perspectives". *Theoretical Chemistry Accounts* 116, 1, pp. 87–105. DOI: 10.1007/s00214-005-0030-z.

**Garczarek**, **F.**; **L. S. Brown**; **J. K. Lanyi**; **K. Gerwert** (2005). "Proton binding within a membrane protein by a protonated water cluster". *Proceedings of the National Academy of Sciences* 102, 10, pp. 3633–3638. DOI: 10.1073/pnas.0500421102.

**Geibel**, **S.**; **T. Friedrich**; **P. Ormos**; **P. G. Wood**; **G. Nagel**; **E. Bamberg** (2001). "The voltage-dependent proton pumping in Bacteriorhodopsin is characterized by optoelectric behavior". *Biophysical Journal* 81, 4, pp. 2059–2068. DOI: 10.1016/S0006-3495(01)75855-9.

**Gergely**, **C.**; **C. Ganea**; **G. Váró** (1994). "Combined optical and photoelectric study of the photocycle of 13-*cis* Bacteriorhodopsin". *Biophysical Journal* 67, 2, pp. 855–861. DOI: 10.1016/S0006-3495(94)80545-4.

**Gerwert**, **K.**; **B. Hess**; **J. Soppa**; **D. Oesterhelt** (1989). "Role of aspartate-96 in proton translocation by Bacteriorhodopsin". *Proceedings of the National Academy of Sciences* 86, 13, pp. 4943–4947. DOI: 10.1073/pnas.86.13.4943.

**Getzoff**, **E. D.**; **K. N. Gutwin**; **U. K. Genick** (2003). "Anticipatory active-site motions and chromophore distortion prime photoreceptor PYP for light activation". *Nature Structural & Molecular Biology* 10, 8, pp. 663–668. DOI: 10.1038/nsb958.

**Gibson**, **D. G.**; **L. Young**; **R.-Y. Chuang**; **J. C. Venter**; **C. A. Hutchison**; **H. O. Smith** (2009). "Enzymatic assembly of DNA molecules up to several hundred kilobases". *Nature Methods* 6, 5, pp. 343–345. DOI: 10.1038/nmeth.1318.

**Gilbert**, **J. A.**; **C. L. Dupont** (2011). "Microbial metagenomics: Beyond the genome". *Annual Review of Marine Science* 3, 1, pp. 347–371. DOI: 10.1146/annurev-marine-120709-142811.

**Gill**, **S. R.** *et al.* (2006). "Metagenomic analysis of the human distal gut microbiome". *Science* 312, 5778, pp. 1355–1359. DOI: 10.1126/science.1124234.

**Gomelsky**, **M.**; **S. Kaplan** (1998). "AppA, a redox regulator of photosystem formation in *Rhodobacter sphaeroides* 2.4.1, is a flavoprotein - Identification of a novel FAD binding domain". *Journal of Biological Chemistry* 273, 52, pp. 35319–35325. DOI: 10.1074/jbc.273.52.35319.

**Gomelsky**, **M.**; **G. Klug** (2002). "BLUF: A Novel FAD-binding domain involved in sensory transduction in microorganisms". *Trends in Biochemical Sciences* 27, 10, pp. 497–500. DOI: 10.1016/S0968-0004(02)02181-3.

**Gong**, **J.** *et al.* (2016). "The *C. elegans* taste receptor homolog LITE-1 is a photoreceptor". *Cell* 167, 5, 1252–1263.e10. DOI: 10.1016/j.cell.2016.10.053.

**Gonzalez**, **M. E.**; **L. Carrasco** (2003). "Viroporins". *FEBS Letters* 552, 1, pp. 28–34. DOI: 10.1016/S0014-5793(03)00780-4.

**Govorunova**, **E. G.**; **K.-H. Jung**; **O. A. Sineshchekov**; **J. L. Spudich** (2004). "*Chlamydomonas* Sensory Rhodopsins A and B: Cellular content and role in photophobic responses". *Biophysical Journal* 86, 4, pp. 2342–2349. DOI: 10.1016/S0006-3495(04)74291-5.

**Govorunova**, **E. G.**; **O. A. Sineshchekov**; **R. Janz**; **X. Liu**; **J. L. Spudich** (2015). "Natural light-gated anion channels: A family of microbial rhodopsins for advanced optogenetics". *Science* 349, 6248, pp. 647–650. DOI: 10.1126/science.aaa7484.

**Govorunova**, **E. G.**; **O. A. Sineshchekov**; **H. Li**; **J. L. Spudich** (2017a). "Microbial rhodopsins: Diversity, mechanisms, and optogenetic applications". *Annual Review of Biochemistry* 86, 1, pp. 845–872. DOI: 10.1146/annurev-biochem-101910-144233.

**Govorunova**, **E. G.**; **O. A. Sineshchekov**; **H. Li**; **Y. Wang**; **L. S. Brown**; **J. L. Spudich** (2020). "RubyACRs, nonalgal anion channelrhodopsins with highly red-shifted absorption". *Proceedings of the National Academy of Sciences*. DOI: 10.1073/pnas.2005981117.

**Govorunova**, **E. G.**; **O. A. Sineshchekov**; **J. L. Spudich** (2016a). "*Proteomonas Sulcata* ACR1: A fast anion channelrhodopsin". *Photochemistry and Photobiology* 92, 2, pp. 257–263. DOI: 10.1111/php.12558.

— (2016b). "Structurally distinct cation channelrhodopsins from cryptophyte algae". *Biophysical Journal* 110, 11, pp. 2302–2304. DOI: 10.1016/j.bpj.2016.05.001.

**Govorunova**, **E. G.** *et al.* (2017b). "The expanding family of natural anion channelrhodopsins reveals large variations in kinetics, conductance and spectral sensitivity". *Scientific Reports* 7, 1, p. 43358. DOI: 10.1038/srep43358.

**Govorunova**, **E. G.** *et al.* (2018). "Extending the time domain of neuronal silencing with cryptophyte anion channelrhodopsins". *eNeuro* 5, 3. DOI: 10.1523/ENEURO.0174-18.2018.

**Gradinaru**, **V.**; **K. R. Thompson**; **K. Deisseroth** (2008). "eNpHR: A *Natronomonas* Halorhodopsin enhanced for optogenetic applications". *Brain Cell Biology* 36, 1, pp. 129–139. DOI: 10.1007/s11068-008-9027-6.

**Gradinaru**, **V.** *et al.* (2010). "Molecular and cellular approaches for diversifying and extending optogenetics". *Cell* 141, 1, pp. 154–165. DOI: 10.1016/j.cell.2010.02.037.

**Gradmann**, **D.** (1970). "Einfluss von Licht, Temperatur und Aussenmedium auf das elektrische Verhalten von *Acetabularia crenulata*". *Planta* 93, pp. 323–353.

**Gradmann**, **D.**; **A. Berndt**; **F. Schneider**; **P. Hegemann** (2011). "Rectification of the channelrhodopsin early conductance". *Biophysical Journal* 101, 5, pp. 1057–1068. DOI: 10.1016/j.bpj.2011.07.040.

**Greiner**, **A.**; **S. Kelterborn**; **H. Evers**; **G. Kreimer**; **I. Sizova**; **P. Hegemann** (2017). "Targeting of photoreceptor genes in *Chlamydomonas reinhardtii* via zinc-finger nucleases and CRISPR/Cas9". *The Plant Cell* 29, 10, pp. 2498–2518. DOI: 10.1105/tpc.17.00659.

**Griesbeck**, **O.**; **G. S. Baird**; **R. E. Campbell**; **D. A. Zacharias**; **R. Y. Tsien** (2001). "Reducing the environmental sensitivity of yellow fluorescent protein". *Journal of Biological Chemistry* 276, 31, pp. 29188–29194. DOI: 10.1074/jbc.M102815200.

**Grigorieff**, **N.**; **T. A. Ceska**; **K. H. Downing**; **J. M. Baldwin**; **R. Henderson** (1996). "Electron-crystallographic refinement of the structure of Bacteriorhodopsin". *Journal of Molecular Biology* 259, 3, pp. 393–421. DOI: 10.1006/jmbi.1996.0328.

**Grimm**, **C.**; **A. Silapetere**; **A. Vogt**; **Y. A. Bernal Sierra**; **P. Hegemann** (2018). "Electrical properties, substrate specificity and optogenetic potential of the engineered light-driven sodium pump eKR2". *Scientific Reports* 8, 1, p. 9316. DOI: 10.1038/s41598-018-27690-w.

**Grimm**, **C.**; **J. Vierock**; **P. Hegemann**; **J. Wietek** (2017). "Whole-cell patch-clamp recordings for electrophysiological determination of ion selectivity in channelrhodopsins". *Journal of Visualized Experiments*, 123. DOI: 10.3791/55497.

**Gruia**, **A. D.**; **A.-N. Bondar**; **J. C. Smith**; **S. Fischer** (2005). "Mechanism of a molecular valve in the Halorhodopsin chloride pump". *Structure* 13, 4, pp. 617–627. DOI: 10.1016/j.str.2005.01.021.

**Gunaydin**, **L. A.**; **O. Yizhar**; **A. Berndt**; **V. S. Sohal**; **K. Deisseroth**; **P. Hegemann** (2010). "Ultrafast optogenetic control". *Nature Neuroscience* 13, 3, pp. 387–392. DOI: 10.1038/nn.2495.

**Guo**, **Y.** *et al.* (2016). "Active site structure and absorption spectrum of Channelrhodopsin-2 wild-type and C128T mutant". *Chemical Science* 7, 6, pp. 3879–3891. DOI: 10.1039/C6SC00468G.

**Gutknecht**, **J.** (1965). "Sodium, potassium, and chloride transport and membrane potentials in *Valonia ventricosa*". *The Biological Bulletin* 130, 3, pp. 331–344. DOI: 10.2307/1539728.

**Hamill**, **O. P.**; **A. Marty**; **E. Neher**; **B. Sakmann**; **F. J. Sigworth** (1981). "Improved patch-clamp techniques for high-resolution current recording from cells and cell-free membrane patches". *Pflügers Archiv - European Journal of Physiology* 391, 2, pp. 85–100. DOI: 10.1007/BF00656997.

**Handelsman**, **J.** (2004). "Metagenomics: Application of genomics to uncultured microorganisms". *Microbiology and Molecular Biology Reviews* 68, 4, pp. 669–685. DOI: 10.1128/MMBR.68.4.669-685.2004.

**Harbison**, **G. S.** *et al.* (1984). "Dark-adapted Bacteriorhodopsin contains 13-*cis*, 15-*syn* and all-*trans*, 15-*anti* retinal Schiff bases". *Proceedings of the National Academy of Sciences* 81, 6, pp. 1706–9. DOI: 10.1073/pnas.81.6.1706.

**Harbison**, **G. S.** *et al.* (1985). "Solid-state carbon-13 NMR detection of a perturbed 6-s-*trans* chromophore in Bacteriorhodopsin". *Biochemistry* 24, 24, pp. 6955–6962. DOI: 10.1021/bi00345a031.

**Harz**, **H.**; **P. Hegemann** (1991). "Rhodopsin-regulated calcium currents in *Chlamydomonas*". *Nature* 351, 6326, pp. 489–491. DOI: 10.1038/351489a0.

**Harz**, **H.**; **C. Nonnengässer**; **P. Hegemann** (1992). "The photoreceptor current of the green alga *Chlamydomonas*". *Philosophical Transactions: Biological Sciences* 338, 1283, pp. 39–52.

**Heberle**, **J.**; **J. Fitter**; **H. J. Sass**; **G. Büldt** (2000). "Bacteriorhodopsin: The functional details of a molecular machine are being resolved". *Biophysical Chemistry* 85, 2, pp. 229–248. DOI: 10.1016/S0301-4622(99)00154-4.

**Hegemann**, **P.** (1997). "Vision in microalgae". *Planta* 203, 3, pp. 265–274. DOI: 10.1007/s004250050191.

**Hegemann**, **P.**; **P. Berthold** (2009). "Sensory photoreceptors and light control of flagellar activity". *The Chlamydomonas Sourcebook*. Ed. by **E. H. Harris**; **D. B. Stern**; **G. B. Witman**. Second. London: Academic Press, pp. 395–429. ISBN: 978-0-12-370873-1. DOI: 10.1016/B978-0-12-370873-1.00050-2.

**Hegemann**, **P.**; **S. Ehlenbeck**; **D. Gradmann** (2005). "Multiple photocycles of channelrhodopsin". *Biophysical Journal* 89, 6, pp. 3911–3918. DOI: 10.1529/biophysj.105.069716.

**Hegemann**, **P.**; **W. Gärtner**; **R. Uhl** (1991). "All-*trans* retinal constitutes the functional chromophore in *Chlamydomonas* rhodopsin". *Biophysical Journal* 60, 6, pp. 1477–1489. DOI: 10.1016/S0006-3495(91)82183-X.

**Hegemann**, **P.**; **D. Oesterhelt**; **M. Steiner** (1985). "The photocycle of the chloride pump Halorhodopsin. I: Azide-catalyzed deprotonation of the chromophore is a side reaction of photocycle intermediates inactivating thepump". *The EMBO Journal* 4, 9, pp. 2347–2350. DOI: 10.1002/j.1460-2075.1985.tb03937.x.

**Henderson**, **R.**; **J. M. Baldwin**; **T. A. Ceska**; **F. Zemlin**; **E. Beckmann**; **K. H. Downing** (1990). "Model for the structure of Bacteriorhodopsin based on high-resolution electron cryo-microscopy". *Journal of Molecular Biology* 213, 4, pp. 899–929. DOI: 10.1016/S0022-2836(05)80271-2.

**Henikoff**, **S.**; **J. G. Henikoff** (1992). "Amino acid substitution matrices from protein blocks". *Proceedings of the National Academy of Sciences* 89, 22, pp. 10915–10919. DOI: 10.1073/pnas.89.22.10915.

**Herbst**, **J.**; **K. Heyne**; **R. Diller** (2002). "Femtosecond infrared spectroscopy of Bacteriorhodopsin chromophore isomerization". *Science* 297, 5582, pp. 822–825. DOI: 10.1126/science.1072144.

**Hess**, **B.**; **D. Kuschmitz** (1977). "The photochemical reaction of the 412 nm chromophore of Bacteriorhodopsin". *FEBS Letters* 74, 1, pp. 20–24. DOI: 10.1016/0014-5793(77)80743-6.

**Hess**, **J.**; **C. V. Jensen**; **N. H. Diemer** (1989). "Calcium-imaging with Fura-2 in isolated cerebral microvessels". *Acta Histochemica* 87, 2, pp. 107–114. DOI: 10.1016/S0065-1281(89)80011-X.

**Heyde**, **M. E.**; **D. Gill**; **R. G. Kilponen**; **L. Rimai** (1971). "Raman spectra of Schiff bases of retinal (Models of visual photoreceptors)". *Journal of the American Chemical Society* 93, 25, pp. 6776–6780. DOI: 10.1021/ja00754a012.

**Hingamp**, **P.** *et al.* (2013). "Exploring nucleo-cytoplasmic large DNA viruses in *Tara* Oceans microbial metagenomes". *The ISME Journal* 7, 9, pp. 1678–1695. DOI: 10.1038/ismej.2013.59.

**Ho**, **J.**; **T. Tumkaya**; **S. Aryal**; **H. Choi**; **A. Claridge-Chang** (2019). "Moving beyond P values: Everyday data analysis with estimation plots". *Nature Methods* 16, 7, pp. 565–566. DOI: 10.1101/377978.

**Hochbaum**, **D. R.** *et al.* (2014). "All-optical electrophysiology in mammalian neurons using engineered microbial rhodopsins". *Nature Methods* 11, 8, pp. 825–833. DOI: 10.1038/nmeth.3000.

**Hoffmann**, **M.** *et al.* (2006). "Color tuning in rhodopsins: The mechanism for the spectral shift between Bacteriorhodopsin and Sensory Rhodopsin II". *Journal of the American Chemical Society* 128, 33, pp. 10808–10818. DOI: 10.1021/ja062082i.

**Holland**, **E.-M.**; **F.-J. Braun**; **C. Nonnengässer**; **H. Harz**; **P. Hegemann** (1996). "The nature of rhodopsin-triggered photocurrents in *Chlamydomonas*. I. Kinetics and influence of divalent ions". *Biophysical Journal* 70, 2, pp. 924–931. DOI: 10.1016/S0006-3495(96)79635-2.

**Hontani**, **Y.**; **M. Broser**; **A. Silapetere**; **B. S. Krause**; **P. Hegemann**; **J. T. M. Kennis** (2017). "The femtosecond-to-second photochemistry of red-shifted fast-closing anion channelrhodopsin *Ps*ACR1". *Physical Chemistry Chemical Physics* 19, 45, pp. 30402–30409. DOI: 10.1039/C7CP06414D.

**Hososhima**, **S.**; **S. Sakai**; **T. Ishizuka**; **H. Yawo** (2015). "Kinetic evaluation of photosensitivity in bi-stable variants of chimeric channelrhodopsins". *PLOS ONE* 10, 3, e0119558. DOI: 10.1371/journal.pone.0119558.

**Houjou**, **H.**; **Y. Inoue**; **M. Sakurai** (2001). "Study of the opsin shift of Bacteriorhodopsin: Insight from QM/MM calculations with electronic polarization effects of the protein environment". *The Journal of Physical Chemistry B* 105, 4, pp. 867–879. DOI: 10.1021/jp0032863.

**Huang**, **K.**; **C. F. Beck** (2003). "Phototropin is the blue-light receptor that controls multiple steps in the sexual life cycle of the green alga *Chlamydomonas reinhardtii*". *Proceedings of the National Academy of Sciences* 100, 10, pp. 6269–6274. DOI: 10.1073/pnas.0931459100.

**Hughes**, **J.**; **T. Lamparter**; **F. Mittmann**; **E. Hartmann**; **W. Gärtner**; **A. Wilde**; **T. Börner** (1997). "A prokaryotic phytochrome". *Nature* 386, 6626, pp. 663–663. DOI: 10.1038/386663a0.

**Ihee**, **H.**; **S. Rajagopal**; **F. Schotte**; **P. A. Anfinrud**; **M. Wulff**; **K. Moffat** (2005). "Visualizing reaction pathways in photoactive yellow protein from nanoseconds to seconds". *Proceedings of the National Academy of Sciences* 102, 20, p. 6. DOI: 10.1073/pnas.0409035102.

**Inaguma**, **A.** *et al.* (2015). "Chimeras of Channelrhodopsin-1 and -2 from *Chlamydomonas reinhardtii* exhibit distinctive light-induced structural changes from Channelrhodopsin-2". *Journal of Biological Chemistry* 290, 18, pp. 11623–11634. DOI: 10.1074/jbc.M115.642256.

**Initiative**, **O. T. P. T.** (2019). "One thousand plant transcriptomes and the phylogenomics of green plants". *Nature* 574, 7780, pp. 679–685. DOI: 10.1038/s41586-019-1693-2.

**Inoue**, **K.**; **Y. Kato**; **H. Kandori** (2015). "Light-driven ion-translocating rhodopsins in marine bacteria". *Trends in Microbiology* 23, 2, pp. 91–98. DOI: 10.1016/j.tim.2014.10.009.

**Inoue**, **K.**; **F. H. M. Koua**; **Y. Kato**; **R. Abe-Yoshizumi**; **H. Kandori** (2014). "Spectroscopic study of a light-driven chloride ion pump from marine bacteria". *The Journal of Physical Chemistry B* 118, 38, pp. 11190–11199. DOI: 10.1021/jp507219q.

**Inoue**, **K.**; **H. Ono**; **R. Abe-Yoshizumi**; **S. Yoshizawa**; **H. Ito**; **K. Kogure**; **H. Kandori** (2013). "A light-driven sodium ion pump in marine bacteria". *Nature Communications* 4, 1, pp. 1–10. DOI: 10.1038/ncomms2689.

**Ishizuka**, **T.**; **M. Kakuda**; **R. Araki**; **H. Yawo** (2006). "Kinetic evaluation of photosensitivity in genetically engineered neurons expressing green algae light-gated channels". *Neuroscience Research* 54, 2, pp. 85–94. DOI: 10.1016/j.neures.2005.10.009.

**Iwata**, **T.**; **D. Nozaki**; **S. Tokutomi**; **T. Kagawa**; **M. Wada**; **H. Kandori** (2003). "Light-induced structural changes in the LOV2 domain of *Adiantum* Phytochrome3 studied by low-temperature FTIR and UV-visible spectroscopy". *Biochemistry* 42, 27, pp. 8183–8191. DOI: 10.1021/bi0345135.

**Jan**, **L. Y.** (1975). "The isomeric configuration of the Bacteriorhodopsin chromophore". *Vision Research* 15, 10, pp. 1081–1086. DOI: 10.1016/0042-6989(75)90004-8.

"Isosbestic point" (2014). *IUPAC. Compendium of Chemical Terminology* Online Version (2019-). Ed. by **A. Jenkins**; **A. McNaught**. DOI: 10.1351/goldbook.I03310.

**Jewson**, **D. H.** (1977). "Light penetration in relation to phytoplankton content of the euphotic zone of Lough Neagh, N. Ireland". *Oikos* 28, 1, pp. 74–83. DOI: 10.2307/3543325.

**Jiang**, **X.** *et al.* (2008). "Resolving voltage-dependent structural changes of a membrane photoreceptor by surface-enhanced IR difference spectroscopy". *Proceedings of the National Academy of Sciences* 105, 34, pp. 12113–12117. DOI: 10.1073/pnas.0802289105.

**Jo**, **S.**; **T. Kim**; **V. G. Iyer**; **W. Im** (2008). "CHARMM-GUI: A web-based graphical user interface for CHARMM". *Journal of Computational Chemistry* 29, 11, pp. 1859–1865. DOI: 10.1002/jcc.20945.

**Jovel**, **J.** *et al.* (2016). "Characterization of the gut microbiome using 16S or shotgun metagenomics". *Frontiers in Microbiology* 7. DOI: 10.3389/fmicb.2016.00459.

**Jung**, **A.** *et al.* (2005). "Structure of a bacterial BLUF photoreceptor: Insights into blue light-mediated signal transduction". *Proceedings of the National Academy of Sciences* 102, 35, pp. 12350–12355. DOI: 10.1073/pnas.0500722102.

**Jung**, **K.-H.** (2007). "The distinct signaling mechanisms of microbial sensory rhodopsins in archaea, eubacteria and eukarya". *Photochemistry and Photobiology* 83, 1, pp. 63–69. DOI: 10.1562/2006-03-20-ir-853.

**Jung**, **K.-H.**; **V. D. Trivedi**; **J. L. Spudich** (2003). "Demonstration of a sensory rhodopsin in eubacteria". *Molecular Microbiology* 47, 6, pp. 1513–1522. DOI: 10.1046/j.1365-2958.2003.03395.x.

**Kakitani**, **H.**; **T. Kakitani**; **H. Rodman**; **B. Honig** (1985). "On the mechanism of wavelength regulation in visual pigments". *Photochemistry and Photobiology* 41, 4, pp. 471–479. DOI: 10.1111/j.1751-1097.1985.tb03514.x.

**Kanada**, **S.**; **Y. Takeguchi**; **M. Murakami**; **K. Ihara**; **T. Kouyama** (2011). "Crystal structures of an O-like blue form and an anion-free yellow form of *pharaonis* Halorhodopsin". *Journal of Molecular Biology* 413, 1, pp. 162–176. DOI: 10.1016/j.jmb.2011.08.021.

**Karasuyama**, **M.**; **K. Inoue**; **R. Nakamura**; **H. Kandori**; **I. Takeuchi** (2018). "Understanding colour tuning rules and predicting absorption wavelengths of microbial rhodopsins by data-driven machine-learning approach". *Scientific Reports* 8, 1, p. 15580. DOI: 10.1038/s41598-018-33984-w.

**Karni**, **L.**; **M. Avron** (1988). "Ion content of the halotolerant alga *Dunaliella salina*". *Plant and Cell Physiology* 29, 8, pp. 1311–1314. DOI: 10.1093/oxfordjournals.pcp.a077640.

**Kato**, **H. E.** *et al.* (2012). "Crystal structure of the channelrhodopsin light-gated cation channel". *Nature* 482, 7385, pp. 369–374. DOI: 10.1038/nature10870.

**Kato**, **H. E.** *et al.* (2018). "Structural mechanisms of selectivity and gating in anion channelrhodopsins". *Nature* 561, 7723, pp. 349–354. DOI: 10.1038/s41586-018-0504-5.

**Kikuyama**, **M.** (1986). "Tonoplast action potential of characeae". *Plant and Cell Physiology* 27, 8, pp. 1461–1468. DOI: 10.1093/oxfordjournals.pcp.a077246.

— (1989). "Effect of $Ca^{2+}$ on tonoplast potential of permeabilized characeae cells". *Plant and Cell Physiology* 30, 2, pp. 253–258. DOI: 10.1093/oxfordjournals.pcp.a077737.

**Kim**, **Y. S.** *et al.* (2018). "Crystal structure of the natural anion-conducting channelrhodopsin *Gt*ACR1". *Nature* 561, 7723, pp. 343–348. DOI: 10.1038/s41586-018-0511-6.

**Kimura**, **Y.** *et al.* (1997). "Surface of Bacteriorhodopsin revealed by high-resolution electron crystallography". *Nature* 389, 6647, pp. 206–211. DOI: 10.1038/38323.

**Kinoshita**, **T.**; **M. Doi**; **N. Suetsugu**; **T. Kagawa**; **M. Wada**; **K.-i. Shimazaki** (2001). "Phot1 and Phot2 mediate blue light regulation of stomatal opening". *Nature* 414, 6864, pp. 656–660. DOI: 10.1038/414656a.

**Kiser**, **P. D.**; **M. Golczak**; **K. Palczewski** (2014). "Chemistry of the retinoid (visual) cycle". *Chemical Reviews* 114, 1, pp. 194–232. DOI: 10.1021/cr400107q.

**Klapoetke**, **N. C.** *et al.* (2014). "Independent optical excitation of distinct neural populations". *Nature Methods* 11, 3, pp. 338–346. DOI: 10.1038/nmeth.2836.

**Klar**, **T.**; **R. Pokorny**; **J. Moldt**; **A. Batschauer**; **L.-O. Essen** (2007). "Cryptochrome 3 from *Arabidopsis thaliana*: Structural and functional analysis of its complex with a folate light antenna". *Journal of Molecular Biology* 366, 3, pp. 954–964. DOI: 10.1016/j.jmb.2006.11.066.

**Kleinlogel**, **S.**; **K. Feldbauer**; **R. E. Dempski**; **H. Fotis**; **P. G. Wood**; **C. Bamann**; **E. Bamberg** (2011). "Ultra light-sensitive and fast neuronal activation with the $Ca^{2+}$-permeable channelrhodopsin CatCh". *Nature Neuroscience* 14, 4, pp. 513–518. DOI: 10.1038/nn.2776.

**Kleinlogel**, **S.**; **C. Vogl**; **M. Jeschke**; **J. Neef**; **T. Moser** (2020). "Emerging approaches for restoration of hearing and vision". *Physiological Reviews*. DOI: 10.1152/physrev.00035.2019.

**Kloppmann**, **E.**; **T. Becker**; **G. M. Ullmann** (2005). "Electrostatic potential at the retinal of three archaeal rhodopsins: Implications for their different absorption spectra". *Proteins: Structure, Function, and Bioinformatics* 61, 4, pp. 953–965. DOI: 10.1002/prot.20744.

**Kobayashi**, **T.**; **T. Saito**; **H. Ohtani** (2001). "Real-time spectroscopy of transition states in Bacteriorhodopsin during retinal isomerization". *Nature* 414, 6863, pp. 531–534. DOI: 10.1038/35107042.

**Kojima**, **K.**; **H. C. Watanabe**; **S. Doi**; **N. Miyoshi**; **M. Kato**; **H. Ishikita**; **Y. Sudo** (2018). "Mutational analysis of the conserved carboxylates of Anion Channelrhodopsin-2 (ACR2) expressed in *Escherichia coli* and their roles in anion transport". *Biophysics and Physicobiology* 15, pp. 179–188. DOI: 10.2142/biophysico.15.0_179.

**Kolbe**, **M.**; **H. Besir**; **L.-O. Essen**; **D. Oesterhelt** (2000). "Structure of the light-driven chloride pump Halorhodopsin at 1.8 Å resolution". *Science* 288, 5470, pp. 1390–1396. DOI: 10.1126/science.288.5470.1390.

**Kort**, **R.**; **X. Xu**; **W. D. Hoff**; **W. Crielaand**; **K. J. Hellingwerf** (1996a). "Evidence for *trans-cis* isomerization of the p-coumaric acid chromophore as the photochemical basis of the photocycle of photoactive yellow protein". *FEBS Letters* 382, 1-2, pp. 73–78. DOI: 10.1016/0014-5793(96)00149-4.

**Kort**, **R.** *et al.* (1996b). "The xanthopsins: A new family of eubacterial blue-light photoreceptors". *The EMBO journal* 15, 13, pp. 3209–18. DOI: 10.1002/j.1460-2075.1996.tb00685.x.

**Kottke**, **T.**; **J. Heberle**; **D. Hehn**; **B. Dick**; **P. Hegemann** (2003). "Phot-LOV1: Photocycle of a blue-light receptor domain from the green alga *Chlamydomonas reinhardtii*". *Biophysical Journal* 84, 2, pp. 1192–1201. DOI: 10.1016/S0006-3495(03)74933-9.

**Kottke**, **T.**; **A. Xie**; **D. S. Larsen**; **W. D. Hoff** (2018). "Photoreceptors take charge: Emerging principles for light sensing". *Annual Review of Biophysics* 47, 1. DOI: 10.1146/annurev-biophys-070317-033047.

**Kouyama**, **T.**; **S. Kanada**; **Y. Takeguchi**; **A. Narusawa**; **M. Murakami**; **K. Ihara** (2010). "Crystal structure of the light-driven chloride pump Halorhodopsin from *Natronomonas pharaonis*". *Journal of Molecular Biology* 396, 3, pp. 564–579. DOI: 10.1016/j.jmb.2009.11.061.

**Kovalev**, **K.** *et al.* (2020). "High-resolution structural insights into the Heliorhodopsin family". *Proceedings of the National Academy of Sciences* 117, 8, pp. 4131–4141. DOI: 10.1073/pnas.1915888117.

**Kovalev**, **K.** *et al.* (2019). "Structure and mechanisms of sodium-pumping KR2 rhodopsin". *Science Advances* 5, 4, eaav2671. DOI: 10.1126/sciadv.aav2671.

**Krause**, **B. S.** (2017). "Spektroskopische Charakterisierung der grün- absorbierenden Kanalrhodopsin-Chimäre ReaChR". Dissertation. Humboldt-Universität zu Berlin.

**Krause**, **B. S.**; **C. Grimm**; **J. C. D. Kaufmann**; **F. Schneider**; **T. P. Sakmar**; **F. J. Bartl**; **P. Hegemann** (2017). "Complex photochemistry within the green-absorbing channelrhodopsin ReaChR". *Biophysical Journal* 112, 6, pp. 1166–1175. DOI: 10.1016/j.bpj.2017.02.001.

**Krause**, **N.**; **C. Engelhard**; **J. Heberle**; **R. Schlesinger**; **R. Bittl** (2013). "Structural differences between the closed and open states of Channelrhodopsin-2 as observed by EPR spectroscopy". *FEBS Letters* 587, 20, pp. 3309–3313. DOI: 10.1016/j.febslet.2013.08.043.

**Kreimer**, **G.** (2009). "The Green Algal Eyespot Apparatus: A Primordial Visual System and More?" *Current Genetics* 55, 1, pp. 19–43. DOI: 10.1007/s00294-008-0224-8.

**Kremers**, **G.-J.**; **J. Goedhart**; **E. B. van Munster**; **T. W. J. Gadella** (2006). "Cyan and yellow super fluorescent proteins with improved brightness, protein folding, and FRET Förster radius". *Biochemistry* 45, 21, pp. 6570–6580. DOI: 10.1021/bi0516273.

**Krezel**, **A.**; **W. Bal** (2004). "A formula for correlating pKa values determined in $D_2O$ and $H_2O$". *Journal of Inorganic Biochemistry* 98, 1, pp. 161–166. DOI: 10.1016/j.jinorgbio.2003.10.001.

**Kropf**, **A.**; **B. P. Whittenberger**; **S. P. Goff**; **A. S. Waggoner** (1973). "The spectral properties of some visual pigment analogs". *Experimental Eye Research* 17, 6, pp. 591–606. DOI: 10.1016/0014-4835(73)90088-2.

**Kuhne**, **J.** *et al.* (2019). "Unifying photocycle model for light adaptation and temporal evolution of cation conductance in Channelrhodopsin-2". *Proceedings of the National Academy of Sciences*, pp. 1–10. DOI: 10.1073/pnas.1818707116.

**Lambert**, **T. J.** (2019). "FPbase: A community-editable fluorescent protein database". *Nature Methods* 16, 4, pp. 277–278. DOI: 10.1038/s41592-019-0352-8.

**Lanyi**, **J. K.** (1986). "Photochromism of Halorhodopsin. *Cis*/*trans* isomerization of the retinal around the 13-14 double bond". *Journal of Biological Chemistry* 261, 30, pp. 14025–14030.

— (2006). “Proton transfers in the Bacteriorhodopsin photocycle”. *Biochimica et Biophysica Acta* 1757, pp. 1012–1018. DOI: 10.1016/j.bbabio.2005.11.003.

**Larkin**, **M. A.** *et al.* (2007). “ClustalW and ClustalX version 2.0”. *Bioinformatics* 23, 21, pp. 2947–2948. DOI: 10.1093/bioinformatics/btm404.

**Lee**, **S.-S.**; **A. R. Choi**; **S. Y. Kim**; **H.-W. Kang**; **K.-H. Jung**; **J.-H. Lee** (2011). “*Acetabularia* Rhodopsin I is a light-stimulated proton pump”. *Journal of Nanoscience and Nanotechnology* 11, 5, pp. 4596–4600. DOI: 10.1166/jnn.2011.3650.

**Lemoine**, **F.**; **D. Correia**; **V. Lefort**; **O. Doppelt-Azeroual**; **F. Mareuil**; **S. Cohen-Boulakia**; **O. Gascuel** (2019). “NGPhylogeny.fr: New generation phylogenetic services for non-specialists”. *Nucleic Acids Research* 47, W1, W260–W265. DOI: 10.1093/nar/gkz303.

**Letunic**, **I.**; **P. Bork** (2019). “Interactive Tree of Life (iTOL) v4: Recent updates and new developments”. *Nucleic Acids Research* 47, W1, W256–W259. DOI: 10.1093/nar/gkz239.

**Levin**, **M.** (2014). “Molecular bioelectricity: How endogenous voltage potentials control cell behavior and instruct pattern regulation *in vivo*”. *Molecular Biology of the Cell* 25, 24, pp. 3835–3850. DOI: 10.1091/mbc.e13-12-0708.

**Lewis**, **A.**; **J. Spoonhower**; **R. A. Bogomolni**; **R. H. Lozier**; **W. Stoeckenius** (1974). “Tunable laser resonance Raman spectroscopy of Bacteriorhodopsin”. *Proceedings of the National Academy of Sciences* 71, 11, pp. 4462–4466. DOI: 10.1073/pnas.71.11.4462.

**Lewis**, **R. J.**; **J. A. Brannigan**; **K. Muchová**; **I. Barák**; **A. J. Wilkinson** (1999). “Phosphorylated aspartate in the structure of a response regulator protein”. *Journal of Molecular Biology* 294, 1, pp. 9–15. DOI: 10.1006/jmbi.1999.3261.

**Li**, **H.** *et al.* (2019). “Crystal structure of a natural light-gated anion channelrhodopsin”. *eLife* 8, pp. 1–17. DOI: 10.7554/eLife.41741.

**Li**, **X.** *et al.* (2005). “Fast noninvasive activation and inhibition of neural and network activity by vertebrate rhodopsin and green algae channelrhodopsin”. *Proceedings of the National Academy of Sciences* 102, 49, pp. 17816–17821. DOI: 10.1073/pnas.0509030102.

**Lindell**, **D.**; **M. B. Sullivan**; **Z. I. Johnson**; **A. C. Tolonen**; **F. Rohwer**; **S. W. Chisholm** (2004). “Transfer of photosynthesis genes to and from *Prochlorococcus* viruses”. *Proceedings of the National Academy of Sciences* 101, 30, pp. 11013–11018. DOI: 10.1073/pnas.0401526101.

**Logunov**, **S. L.**; **M. A. El-Sayed** (1997). “Redetermination of the quantum yield of photoisomerization and energy content in the K-intermediate of Bacteriorhodopsin photocycle and its mutants by the photoacoustic technique”. *The Journal of Physical Chemistry B* 101, 33, pp. 6629–6633. DOI: 10.1021/jp970955c.

**López**, **J. L.** *et al.* (2017). “Microbial and viral-like rhodopsins present in coastal marine sediments from four polar and subpolar regions”. *FEMS Microbiology Ecology* 93, 1. DOI: 10.1093/femsec/fiw216.

**Lórenz-Fonfría**, **V. A.** *et al.* (2013). “Transient protonation changes in Channelrhodopsin-2 and their relevance to channel gating”. *Proceedings of the National Academy of Sciences* 110, 14, E1273–E1281. DOI: 10.1073/pnas.1219502110.

**Lórenz-Fonfría**, **V. A.**; **J. Heberle** (2014). “Channelrhodopsin unchained: Structure and mechanism of a light-gated cation channel”. *Biochimica et Biophysica Acta (BBA) - Bioenergetics* 1837, 5, pp. 626–642. DOI: 10.1016/j.bbabio.2013.10.014.

**Lórenz-Fonfría**, **V. A.**; **B.-J. Schultz**; **T. Resler**; **R. Schlesinger**; **C. Bamann**; **E. Bamberg**; **J. Heberle** (2015). “Pre-gating conformational changes in the ChETA variant of Channelrhodopsin-2 monitored

by nanosecond IR spectroscopy". *Journal of the American Chemical Society* 137, 5, pp. 1850–1861. DOI: 10.1021/ja5108595.

**Losi**, **A.**; **K. H. Gardner**; **A. Möglich** (2018). "Blue-light receptors for optogenetics". *Chemical Reviews* 118, 21, pp. 10659–10709. DOI: 10.1021/acs.chemrev.8b00163.

**Lozier**, **R. H.**; **R. A. Bogomolni**; **W. Stoeckenius** (1975). "Bacteriorhodopsin: A light-driven proton pump in *Halobacterium halobium*". *Biophysical Journal* 15, 9, pp. 955–962. DOI: 10.1016/S0006-3495(75)85875-9.

**Lozier**, **R. H.**; **W. Niederberger** (1977). "The photochemical cycle of Bacteriorhodopsin". *Federation proceedings* 36, 6, pp. 1805–9.

**Luck**, **M.** *et al.* (2012). "A photochromic histidine kinase rhodopsin (HKR1) that is bimodally switched by ultraviolet and blue light". *Journal of Biological Chemistry* 287, 47, pp. 40083–40090. DOI: 10.1074/jbc.M112.401604.

**Luecke**, **H.**; **B. Schobert**; **J.-P. Cartailler**; **H.-T. Richter**; **A. Rosengarth**; **R. Needleman**; **J. K. Lanyi** (2000). "Coupling photoisomerization of retinal to directional transport in Bacteriorhodopsin". *Journal of Molecular Biology* 300, 5, pp. 1237–1255. DOI: 10.1006/jmbi.2000.3884.

**Luecke**, **H.**; **B. Schobert**; **J. K. Lanyi**; **E. N. Spudich**; **J. L. Spudich** (2001). "Crystal structure of Sensory Rhodopsin II at 2.4 Angstroms: Insights into color tuning and transducer interaction". *Science* 293, 5534, pp. 1499–1503. DOI: 10.1126/science.1062977.

**Luecke**, **H.**; **B. Schobert**; **H.-T. Richter**; **J.-P. Cartailler**; **J. K. Lanyi** (1999a). "Structural changes in Bacteriorhodopsin during ion transport at 2 Angstrom resolution". *Science* 286, 5438, pp. 255–260. DOI: 10.1126/science.286.5438.255.

— (1999b). "Structure of Bacteriorhodopsin at 1.55 Å resolution". *Journal of Molecular Biology* 291, 4, pp. 899–911. DOI: 10.1006/jmbi.1999.3027.

**Luis**, **J. M.**; **D. M. Bishop**; **B. Kirtman** (2003). "A different approach for calculating Franck-Condon factors including anharmonicity". *The Journal of Chemical Physics* 120, 2, pp. 813–822. DOI: 10.1063/1.1630566.

**Lunevsky**, **V. Z.**; **O. M. Zherelova**; **I. Y. Vostrikov**; **G. N. Berestovsky** (1983). "Excitation of *Characeae* cell membranes as a result of activation of calcium and chloride channels". *The Journal of Membrane Biology* 72, 1, pp. 43–58. DOI: 10.1007/BF01870313.

**MacKerell**, **A. D.** *et al.* (1998). "All-atom empirical potential for molecular modeling and dynamics studies of proteins". *The Journal of Physical Chemistry B* 102, 18, pp. 3586–3616. DOI: 10.1021/jp973084f.

**MacRobbie**, **E. a. C.** (1970). "The active transport of ions in plant cells". *Quarterly Reviews of Biophysics* 3, 3, pp. 251–294. DOI: 10.1017/S0033583500004741.

**MacRobbie**, **E. A. C.**; **J. Dainty** (1958). "Ion transport in *Nitellopsis obtusa*". *Journal of General Physiology* 42, 2, pp. 335–353. DOI: 10.1085/jgp.42.2.335.

**Maeda**, **A.**; **T. Iwasa**; **T. Yoshizawa** (1977). "Isomeric composition of retinal chromophore in dark-adapted Bacteriorhodopsin". *The Journal of Biochemistry* 82, 6, pp. 1599–1604. DOI: 10.1093/jbchem.a131855.

**Maeda**, **A.**; **T. Ogurusu**; **T. Yoshizawa**; **T. Kitagawa** (1985). "Resonance Raman study on binding of chloride to the chromophore of Halorhodopsin". *Biochemistry* 24, 10, pp. 2517–2521. DOI: 10.1021/bi00331a018.

**Mager**, **T.** *et al.* (2018). "High frequency neural spiking and auditory signaling by ultrafast red-shifted optogenetics". *Nature Communications* 9, 1, p. 1750. DOI: 10.1038/s41467-018-04146-3.

**Mahn**, **M.**; **M. Prigge**; **S. Ron**; **R. Levy**; **O. Yizhar** (2016). "Biophysical constraints of optogenetic inhibition at presynaptic terminals". *Nature Neuroscience* 19, 4, pp. 554–556. DOI: 10.1038/nn.4266.

**Mahn**, **M.** *et al.* (2018). "High-efficiency optogenetic silencing with soma-targeted anion-conducting channelrhodopsins". *Nature Communications* 9, 4125, pp. 1–15. DOI: 10.1038/s41467-018-06511-8.

**Mann**, **N. H.**; **A. Cook**; **A. Millard**; **S. Bailey**; **M. Clokie** (2003). "Bacterial photosynthesis genes in a virus". *Nature* 424, 6950, pp. 741–741. DOI: 10.1038/424741a.

**Manning**, **C. J.**; **R. A. Palmer**; **J. L. Chao** (1991). "Step-scan Fourier-transform infrared spectrometer". *Review of Scientific Instruments* 62, 5, pp. 1219–1229. DOI: 10.1063/1.1142003.

**Marti**, **T.**; **S. J. Rösselet**; **H. Otto**; **M. P. Heyn**; **H. G. Khorana** (1991). "The retinylidene Schiff base counterion in Bacteriorhodopsin". *Journal of Biological Chemistry* 266, 28, pp. 18674–18683.

**Massana**, **R.** *et al.* (2004). "Phylogenetic and ecological analysis of novel marine stramenopiles". *Applied and Environmental Microbiology* 70, 6, pp. 3528–3534. DOI: 10.1128/AEM.70.6.3528-3534.2004.

**Mast**, **S. O.** (1916). "The process of orientation in the colonial organism, *Gonium pectorale*, and a study of the structure and function of the eye-spot". *Journal of Experimental Zoology* 20, 1, pp. 1–17. DOI: 10.1002/jez.1400200102.

**Masuda**, **S.**; **C. E. Bauer** (2002). "AppA is a blue light photoreceptor that antirepresses photosynthesis gene expression in *Rhodobacter sphaeroides*". *Cell* 110, 5, pp. 613–623. DOI: 10.1016/S0092-8674(02)00876-0.

**Masuda**, **S.**; **K. Hasegawa**; **A. Ishii**; **T.-a. Ono** (2004). "Light-induced structural changes in a putative blue-light receptor with a novel FAD binding fold sensor of blue-light using FAD (BLUF); Slr1694 of *Synechocystis sp.* PCC6803". *Biochemistry* 43, 18, pp. 5304–5313. DOI: 10.1021/bi049836v.

**Mathies**, **R. A.**; **C. B. Cruz**; **W. T. Pollard**; **C. V. Shank** (1988). "Direct observation of the femtosecond excited-state *cis-trans* isomerization in Bacteriorhodopsin". *Science* 240, 4853, pp. 777–779. DOI: 10.1126/science.3363359.

**Matsuno-Yagi**, **A.**; **Y. Mukohata** (1977). "Two possible roles of Bacteriorhodopsin; a comparative study of strains of *Halobacterium halobium* differing in pigmentation". *Biochemical and Biophysical Research Communications* 78, 1, pp. 237–243. DOI: 10.1016/0006-291X(77)91245-1.

**Matsuoka**, **D.**; **T. Iwata**; **K. Zikihara**; **H. Kandori**; **S. Tokutomi** (2007). "Primary processes during the light-signal transduction of phototropin". *Photochemistry and Photobiology* 83, 1, pp. 122–130. DOI: 10.1562/2006-03-29-RA-861.

**Miranda**, **M. R. M.**; **A. R. Choi**; **L. Shi**; **A. G. Bezerra**; **K.-H. Jung**; **L. S. Brown** (2009). "The photocycle and proton translocation pathway in a cyanobacterial ion-pumping rhodopsin". *Biophysical Journal* 96, 4, pp. 1471–1481. DOI: 10.1016/j.bpj.2008.11.026.

**Möglich**, **A.**; **X. Yang**; **R. A. Ayers**; **K. Moffat** (2010). "Structure and function of plant photoreceptors". *Annual Review of Plant Biology* 61, 1, pp. 21–47. DOI: 10.1146/annurev-arplant-042809-112259.

**Mukherjee**, **S.**; **P. Hegemann**; **M. Broser** (2019). "Enzymerhodopsins: Novel photoregulated catalysts for optogenetics". *Current Opinion in Structural Biology* 57, pp. 118–126. DOI: 10.1016/j.sbi.2019.02.003.

**Mullen**, **K. M.**; **I. H. M. van Stokkum** (2007). "TIMP : An R package for modeling multi-way spectroscopic measurements". *Journal of Statistical Software* 18, 3. DOI: 10.18637/jss.v018.i03.

**Nack**, **M.**; **I. Radu**; **C. Bamann**; **E. Bamberg**; **J. Heberle** (2009). "The retinal structure of Channelrhodopsin-2 assessed by resonance Raman spectroscopy". *FEBS Letters* 583, 22, pp. 3676–3680. DOI: 10.1016/j.febslet.2009.10.052.

**Nack**, **M.**; **I. Radu**; **M. Gossing**; **C. Bamann**; **E. Bamberg**; **G. F. von Mollard**; **J. Heberle** (2010). "The DC gate in Channelrhodopsin-2: Crucial hydrogen bonding interaction between C128 and D156". *Photochemical & Photobiological Sciences* 9, 2, p. 194. DOI: 10.1039/b9pp00157c.

**Nagel**, **G.**; **M. Brauner**; **J. F. Liewald**; **N. Adeishvili**; **E. Bamberg**; **A. Gottschalk** (2005). "Light activation of Channelrhodopsin-2 in excitable cells of *Caenorhabditis elegans* triggers rapid behavioral responses". *Current Biology* 15, 24, pp. 2279–2284. DOI: 10.1016/j.cub.2005.11.032.

**Nagel**, **G.**; **D. Ollig**; **M. Fuhrmann**; **S. Kateriya**; **A. M. Musti**; **E. Bamberg**; **P. Hegemann** (2002). "Channelrhodopsin-1: A light-gated proton channel in green algae". *Science* 296, 5577, pp. 2395–2398. DOI: 10.1126/science.1072068.

**Nagel**, **G.** *et al.* (2003). "Channelrhodopsin-2, a directly light-gated cation-selective membrane channel". *Proceedings of the National Academy of Sciences* 100, 24, pp. 13940–13945. DOI: 10.1073/pnas.1936192100.

**Nakanishi**, **K.**; **V. Balogh-Nair**; **M. Arnaboldi**; **K. Tsujimoto**; **B. Honig** (1980). "An external point-charge model for Bacteriorhodopsin to account for its purple color". *Journal of the American Chemical Society* 102, 27, pp. 7945–7947. DOI: 10.1021/ja00547a028.

**Nakasako**, **M.**; **K. Zikihara**; **D. Matsuoka**; **H. Katsura**; **S. Tokutomi** (2008). "Structural basis of the LOV1 dimerization of *Arabidopsis* Phototropins 1 and 2". *Journal of Molecular Biology* 381, 3, pp. 718–733. DOI: 10.1016/j.jmb.2008.06.033.

**Nango**, **E.** *et al.* (2016). "A three-dimensional movie of structural changes in Bacteriorhodopsin". *Science* 354, 6319, pp. 1552–1557. DOI: 10.1126/science.aah3497.

**Needham**, **D. M.**; **C. Poirier**; **E. Hehenberger**; **V. Jiménez**; **J. E. Swalwell**; **A. E. Santoro**; **A. Z. Worden** (2019a). "Targeted metagenomic recovery of four divergent viruses reveals shared and distinctive characteristics of giant viruses of marine eukaryotes". *Philosophical Transactions of the Royal Society B*.

**Needham**, **D. M.** *et al.* (2019b). "A distinct lineage of giant viruses brings a rhodopsin photosystem to unicellular marine predators". *Proceedings of the National Academy of Sciences*. DOI: 10.1073/pnas.1907517116.

**Neher**, **E.** (1992). "Correction for liquid junction potentials in patch clamp experiments". *Methods in Enzymology* 207, pp. 123–131.

**Neher**, **E.**; **B. Sakmann** (1976). "Single-channel currents recorded from membrane of denervated frog muscle fibres". *Nature* 260, 5554, pp. 799–802. DOI: 10.1038/260170a0.

**Neher**, **E.**; **B. Sakmann**; **J. H. Steinbach** (1978). "The extracellular patch clamp: A method for resolving currents through individual open channels in biological membranes". *Pflügers Archiv - European Journal of Physiologygers Archiv European Journal of Physiology* 375, 2, pp. 219–228. DOI: 10.1007/BF00584247.

**Neumann-Verhoefen**, **M.-K.**; **K. Neumann**; **C. Bamann**; **I. Radu**; **J. Heberle**; **E. Bamberg**; **J. Wachtveitl** (2013). "Ultrafast infrared spectroscopy on Channelrhodopsin-2 reveals efficient energy transfer from the retinal chromophore to the protein". *Journal of the American Chemical Society* 135, 18, pp. 6968–6976. DOI: 10.1021/ja400554y.

**Nieva**, **J. L.**; **V. Madan**; **L. Carrasco** (2012). "Viroporins: Structure and biological functions". *Nature Reviews Microbiology* 10, 8, pp. 563–574. DOI: 10.1038/nrmicro2820.

**Nikolic**, **K.**; **N. Grossman**; **M. S. Grubb**; **J. Burrone**; **C. Toumazou**; **P. Degenaar** (2009). "Photocycles of Channelrhodopsin-2". *Photochemistry and Photobiology* 85, 1, pp. 400–411. DOI: 10.1111/j.1751-1097.2008.00460.x.

**Nogly**, **P.** *et al.* (2018). "Retinal isomerization in Bacteriorhodopsin captured by a femtosecond X-ray laser". *Science* 361, 6398, eaat0094. DOI: 10.1126/science.aat0094.

**Nonnengässer**, **C.**; **E.-M. Holland**; **H. Harz**; **P. Hegemann** (1996). "The nature of rhodopsin-triggered photocurrents in *Chlamydomonas*. II. Influence of monovalent ions". *Biophysical Journal* 70, 2, pp. 932–938. DOI: 10.1016/S0006-3495(96)79636-4.

**Nuss**, **M. C.**; **W. Zinth**; **W. Kaiser**; **E. Koelling**; **D. Oesterhelt** (1985). "Femtosecond spectroscopy of the first events of the photochemical cycle in Bacteriorhodopsin". *Chemical Physics Letters*, 117, pp. 1–7. DOI: 10.1016/0009-2614(85)80393-6.

**Nyns**, **E. C. A.** *et al.* (2019). "An automated hybrid bioelectronic system for autogenous restoration of sinus rhythm in atrial fibrillation". *Science Translational Medicine* 11, 481. DOI: 10.1126/scitranslmed.aau6447.

**Oda**, **K.** *et al.* (2018). "Crystal structure of the red light-activated channelrhodopsin Chrimson". *Nature Communications* 9, 1, p. 3949. DOI: 10.1038/s41467-018-06421-9.

**Oesterhelt**, **D.**; **P. Hegemann**; **J. Tittor** (1985). "The photocycle of the chloride pump Halorhodopsin. II: Quantum yields and a kinetic model". *The EMBO Journal* 4, 9, pp. 2351–2356. DOI: 10.1002/j.1460-2075.1985.tb03938.x.

**Oesterhelt**, **D.**; **W. Stoeckenius** (1971). "Rhodopsin-like protein from the purple membrane of *Halobacterium halobium*". *Nature New Biology* 233, 39, pp. 149–152. DOI: 10.1038/newbio233149a0.

— (1973). "Functions of a new photoreceptor membrane". *Proceedings of the National Academy of Sciences* 70, 10, pp. 2853–2857. DOI: 10.1073/pnas.70.10.2853.

**Ogden**, **D.**; **P. Stanfield** (1994). "Patch clamp techniques for single channel and whole-cell recording". *Microelectrode Techniques: The Plymouth Workshop Handbook*. Ed. by **D. Ogden**. Cambridge: Company of Biologists, pp. 53–78. ISBN: 0-948601-49-3.

**Ogurusu**, **T.**; **A. Maeda**; **N. Sasaki**; **T. Yoshizawa** (1981). "Light-induced reaction of Halorhodopsin prepared under low salt conditions". *The Journal of Biochemistry* 90, 5, pp. 1267–1274. DOI: 10.1093/oxfordjournals.jbchem.a133591.

**Ogurusu**, **T.**; **A. Maeda**; **N. Sasaki**; **T. Yoshizawa** (1982). "Effects of chloride on the absorption spectrum and photoreactions of Halorhodopsin". *Biochimica et Biophysica Acta (BBA) - Bioenergetics* 682, 3, pp. 446–451. DOI: 10.1016/0005-2728(82)90059-7.

**Oppermann**, **J.** *et al.* (2019). "MerMAIDs: A family of metagenomically discovered marine anion-conducting and intensely desensitizing channelrhodopsins". *Nature Communications* 10, 1, p. 3315. DOI: 10.1038/s41467-019-11322-6.

**Oren-Shamir**, **M.**; **U. Pick**; **M. Avron** (1990). "Plasma membrane potential of the alga *Dunaliella*, and its relation to osmoregulation". *Plant Physiology* 93, 2, pp. 403–408. DOI: 10.1104/pp.93.2.403.

**Ormö**, **M.**; **A. B. Cubitt**; **K. Kallio**; **L. A. Gross**; **R. Y. Tsien**; **S. J. Remington** (1996). "Crystal structure of the *Aequorea victoria* green fluorescent protein". *Science* 273, 5280, pp. 1392–1395. DOI: 10.1126/science.273.5280.1392.

**Otomo**, **A.**; **M. Mizuno**; **K. Inoue**; **H. Kandori**; **Y. Mizutani** (2019). "Allosteric communication to the retinal chromophore upon ion binding in a light-driven sodium ion pumping rhodopsin". *Biochemistry*. DOI: 10.1021/acs.biochem.9b01062.

**Otomo**, **A.** *et al.* (2018). "Resonance Raman investigation of the chromophore structure of Heliorhodopsins". *The Journal of Physical Chemistry Letters* 9, 22, pp. 6431–6436. DOI: 10.1021/acs.jpclett.8b02741.

**Pan**, **Z.-H.**; **T. H. Ganjawala**; **Q. Lu**; **E. Ivanova**; **Z. Zhang** (2014). "ChR2 mutants at L132 and T159 with improved operational light sensitivity for vision restoration". *PLOS ONE* 9, 6. DOI: 10.1371/journal.pone.0098924.

**Pankratov**, **Y. V.**; **O. A. Krishtal** (2003). "Distinct quantal features of AMPA and NMDA synaptic currents in hippocampal neurons: Implication of glutamate spillover and receptor saturation". *Biophysical Journal* 85, 5, pp. 3375–3387.

**Perálvarez-Marín**, **A.**; **M. Márquez**; **J.-L. Bourdelande**; **E. Querol**; **E. Padrós** (2004). "Thr-90 plays a vital role in the structure and function of Bacteriorhodopsin". *Journal of Biological Chemistry* 279, 16, pp. 16403–16409. DOI: 10.1074/jbc.M313988200.

**Perron-Savard**, **P.**; **G. De Crescenzo**; **H. L. Moual** (2005). "Dimerization and DNA binding of the *Salmonella enterica* PhoP response regulator are phosphorylation independent". *Microbiology* 151, 12, pp. 3979–3987. DOI: 10.1099/mic.0.28236-0.

**Peters**, **J.**; **R. Peters**; **W. Stoeckenius** (1976). "A photosensitive product of sodium borohydride reduction of Bacteriorhodopsin". *FEBS Letters* 61, 2, pp. 128–134. DOI: 10.1016/0014-5793(76)81019-8.

**Petroutsos**, **D.** *et al.* (2016). "A blue-light photoreceptor mediates the feedback regulation of photosynthesis". *Nature* 537, 7621, pp. 563–566. DOI: 10.1038/nature19358.

**Philosof**, **A.**; **O. Béjà** (2013). "Bacterial, archaeal and viral-like rhodopsins from the red sea". *Environmental Microbiology Reports* 5, 3, pp. 475–482. DOI: 10.1111/1758-2229.12037.

**Pilson**, **M. E. Q.** (2013). "Major constituents of seawater". *An Introduction to the Chemistry of the Sea*. Second. New York: Cambridge University Press, pp. 66–73. ISBN: 978-0-521-88707-6.

**Pinhassi**, **J.**; **E. F. DeLong**; **O. Béjà**; **J. M. González**; **C. Pedrós-Alió** (2016). "Marine bacterial and archaeal ion-pumping rhodopsins: Genetic diversity, physiology, and ecology". *Microbiology and Molecular Biology Reviews* 80, 4, pp. 929–954. DOI: 10.1128/MMBR.00003-16.

**Plazzo**, **A. P.**; **N. De Franceschi**; **F. Da Broi**; **F. Zonta**; **M. F. Sanasi**; **F. Filippini**; **M. Mongillo** (2012). "Bioinformatic and mutational analysis of Channelrhodopsin-2 protein cation-conducting pathway". *Journal of Biological Chemistry* 287, 7, pp. 4818–4825. DOI: 10.1074/jbc.M111.326207.

**Polland**, **H. .-J.**; **M. A. Franz**; **W. Zinth**; **W. Kaiser**; **E. Kölling**; **D. Oesterhelt** (1986). "Early picosecond events in the photocycle of Bacteriorhodopsin". *Biophysical Journal* 49, 3, pp. 651–662. DOI: 10.1016/S0006-3495(86)83692-X.

**Pravda**, **L.** *et al.* (2018). "MOLEonline: A web-based tool for analyzing channels, tunnels and pores (2018 Update)". *Nucleic Acids Research* 46, W1, W368–W373. DOI: 10.1093/nar/gky309.

**Prigge**, **M.**; **F. Schneider**; **S. P. Tsunoda**; **C. Shilyansky**; **J. Wietek**; **K. Deisseroth**; **P. Hegemann** (2012). "Color-tuned channelrhodopsins for multiwavelength optogenetics". *Journal of Biological Chemistry* 287, 38, pp. 31804–31812. DOI: 10.1074/jbc.M112.391185.

**Pushkarev**, **A.** *et al.* (2018). "A distinct abundant group of microbial rhodopsins discovered using functional metagenomics". *Nature* 558, 7711, pp. 595–599. DOI: 10.1038/s41586-018-0225-9.

**Radu**, **I.**; **C. Bamann**; **M. Nack**; **G. Nagel**; **E. Bamberg**; **J. Heberle** (2009). "Conformational changes of Channelrhodopsin-2". *Journal of the American Chemical Society* 131, 21, pp. 7313–7319. DOI: 10.1021/ja8084274.

**Rajasethupathy**, **P.** *et al.* (2015). "Projections from neocortex mediate top-down control of memory retrieval". *Nature* 526, 7575, pp. 653–659. DOI: 10.1038/nature15389.

**Rajput**, **J.** *et al.* (2010). "Probing and modeling the absorption of retinal protein chromophores *in vacuo*". *Angewandte Chemie* 122, 10, pp. 1834–1837. DOI: 10.1002/ange.200905061.

**Rappleye**, **M.**; **A. Berndt** (2019). "Structural basis for ion selectivity and engineering in channelrhodopsins". *Current Opinion in Structural Biology* 57, pp. 176–184. DOI: 10.1016/j.sbi.2019.04.008.

**Richter**, **H.-T.**; **R. Needleman**; **H. Kandori**; **A. Maeda**; **J. K. Lanyi** (1996). "Relationship of retinal configuration and internal proton transfer at the end of the Bacteriorhodopsin photocycle". *Biochemistry* 35, 48, pp. 15461–15466. DOI: 10.1021/bi9612430.

**Ritter**, **E.**; **K. Stehfest**; **A. Berndt**; **P. Hegemann**; **F. J. Bartl** (2008). "Monitoring light-induced structural changes of Channelrhodopsin-2 by UV-visible and Fourier transform infrared spectroscopy". *Journal of Biological Chemistry* 283, 50, pp. 35033–35041. DOI: 10.1074/jbc.M806353200.

**Rizzini**, **L.** *et al.* (2011). "Perception of UV-B by the *Arabidopsis* UVR8 protein". *Science* 332, 6025, pp. 103–106. DOI: 10.1126/science.1200660.

**Rockwell**, **N. C.**; **Y.-S. Su**; **J. C. Lagarias** (2006). "Phytochrome structure and signaling mechanisms". *Annual Review of Plant Biology* 57, 1, pp. 837–858. DOI: 10.1146/annurev.arplant.56.032604.144208.

**Rothschild**, **K. J.**; **O. Bousche**; **M. S. Braiman**; **C. A. Hasselbacher**; **J. L. Spudich** (1988). "Fourier transform infrared study of the Halorhodopsin chloride pump". *Biochemistry* 27, 7, pp. 2420–2424. DOI: 10.1021/bi00407a026.

**Roux**, **B.** (2017). "Ion channels and ion selectivity". *Essays in Biochemistry* 61, 2, pp. 201–209. DOI: 10.1042/EBC20160074.

**Rozenberg**, **A.** *et al.* (2020). "Lateral gene transfer of anion-conducting channelrhodopsins between green algae and giant viruses". *Current Biology* 30, pp. 1–11. DOI: 10.1016/j.cub.2020.09.056.

**Rueden**, **C. T.**; **J. Schindelin**; **M. C. Hiner**; **B. E. DeZonia**; **A. E. Walter**; **E. T. Arena**; **K. W. Eliceiri** (2017). "ImageJ2: ImageJ for the next generation of scientific image data". *BMC Bioinformatics* 18, 1, p. 529. DOI: 10.1186/s12859-017-1934-z.

**Ruffert**, **K.**; **B. Himmel**; **D. Lall**; **C. Bamann**; **E. Bamberg**; **H. Betz**; **V. Eulenburg** (2011). "Glutamate residue 90 in the predicted transmembrane domain 2 is crucial for cation flux through Channelrhodopsin 2". *Biochemical and Biophysical Research Communications* 410, 4, pp. 737–743. DOI: 10.1016/j.bbrc.2011.06.024.

**Ruiz**, **D.**; **P. Salinas**; **M. L. Lopez-Redondo**; **M. L. Cayuela**; **A. Marina**; **A. Contreras** (2008). "Phosphorylation-independent activation of the atypical response regulator NblR". *Microbiology* 154, 10, pp. 3002–3015. DOI: 10.1099/mic.0.2008/020677-0.

**Sachs**, **H. G.**; **P. J. Stambrook**; **J. D. Ebert** (1974). "Changes in membrane potential during the cell cycle". *Experimental Cell Research* 83, 2, pp. 362–366. DOI: 10.1016/0014-4827(74)90350-4.

**Sakai**, **T.** *et al.* (2001). "*Arabidopsis* Nph1 and Npl1: Blue light receptors that mediate both phototropism and chloroplast relocation". *Proceedings of the National Academy of Sciences* 98, 12, pp. 6969–6974. DOI: 10.1073/pnas.101137598.

**Sakamoto**, **K.**; **A. Nagatani** (1996). "Nuclear localization activity of Phytochrome B". *The Plant Journal* 10, 5, pp. 859–868. DOI: 10.1046/j.1365-313X.1996.10050859.x.

**Sakmann**, **B.**; **E. Neher** (1984). "Patch clamp techniques for studying ionic channels in excitable membranes". *Annual Review of Physiology* 46, pp. 455–472. DOI: 10.1146/annurev.physiol.46.1.455.

**Salem**, **L.**; **P. Bruckmann** (1975). “Conversion of a photon to an electrical signal by sudden polarisation in the N-retinylidene visual chromophore”. *Nature* 258, 5535, pp. 526–528. DOI: 10.1038/258526a0.

**Sass**, **H. J.** *et al.* (2000). “Structural alterations for proton translocation in the M state of wild-type Bacteriorhodopsin”. *Nature* 406, 6796, pp. 649–653. DOI: 10.1038/35020607.

**Sato**, **K.** *et al.* (2018). “Opn5L1 is a retinal receptor that behaves as a reverse and self-regenerating photoreceptor”. *Nature Communications* 9, 1, p. 1255. DOI: 10.1038/s41467-018-03603-3.

**Sattig**, **T.**; **C. Rickert**; **E. Bamberg**; **H.-J. Steinhoff**; **C. Bamann** (2013). “Light-induced movement of the transmembrane helix B in Channelrhodopsin-2”. *Angewandte Chemie* 125, 37, pp. 9887–9890. DOI: 10.1002/ange.201301698.

**Schapiro**, **I.**; **F. Melaccio**; **E. N. Laricheva**; **M. Olivucci** (2011). “Using the computer to understand the chemistry of conical intersections”. *Photochemical & Photobiological Sciences* 10, 6, pp. 867–886. DOI: 10.1039/C0PP00290A.

**Scheib**, **U.** *et al.* (2018). “Rhodopsin-cyclases for photocontrol of cGMP/cAMP and 2.3 Å structure of the adenylyl cyclase domain”. *Nature Communications* 9, 1, p. 2046. DOI: 10.1038/s41467-018-04428-w.

**Schenkl**, **S.**; **F. van Mourik**; **G. van der Zwan**; **S. Haacke**; **M. Chergui** (2005). “Probing the ultrafast charge translocation of photoexcited retinal in Bacteriorhodopsin”. *Science* 309, 5736, pp. 917–920. DOI: 10.1126/science.1111482.

**Schleicher**, **E.** *et al.* (2004). “On the reaction mechanism of adduct formation in LOV domains of the plant blue-light receptor phototropin”. *Journal of the American Chemical Society* 126, 35, pp. 11067–11076. DOI: 10.1021/ja049553q.

**Schneider**, **F.** (2013). “Design and electrophysiological characterization of rhodopsin-based optogenetic tools”. Dissertation. Humboldt-Universität zu Berlin.

**Schneider**, **F.**; **C. Grimm**; **P. Hegemann** (2015). “Biophysics of channelrhodopsin”. *Annual Review of Biophysics* 44, 1, pp. 167–186. DOI: 10.1146/annurev-biophys-060414-034014.

**Schobert**, **B.**; **L. S. Brown**; **J. K. Lanyi** (2003). “Crystallographic structures of the M and N intermediates of Bacteriorhodopsin: Assembly of a hydrogen-bonded chain of water molecules between Asp-96 and the retinal Schiff base”. *Journal of Molecular Biology* 330, 3, pp. 553–570. DOI: 10.1016/S0022-2836(03)00576-X.

**Schobert**, **B.**; **J. Cupp-Vickery**; **V. Hornak**; **S. O. Smith**; **J. K. Lanyi** (2002). “Crystallographic structure of the K intermediate of Bacteriorhodopsin: Conservation of free energy after photoisomerization of the retinal”. *Journal of Molecular Biology* 321, 4, pp. 715–726. DOI: 10.1016/S0022-2836(02)00681-2.

**Schobert**, **B.**; **J. K. Lanyi** (1982). “Halorhodopsin is a light-driven chloride pump”. *Journal of Biological Chemistry* 257, 17, pp. 10306–10313.

**Schreckenbach**, **T.**; **B. Walckhoff**; **D. Oesterhelt** (1977). “Studies on the retinal-protein interaction in Bacteriorhodopsin”. *European Journal of Biochemistry* 76, 2, pp. 499–511. DOI: 10.1111/j.1432-1033.1977.tb11620.x.

— (1978). “Specificity of the retinal binding site of Bacteriorhodopsin: Chemical and stereochemical requirements for the binding of retinol and retinal”. *Biochemistry* 17, 25, pp. 5353–5359. DOI: 10.1021/bi00618a005.

**Schulz**, **F.** *et al.* (2020). “Giant virus diversity and host interactions through global metagenomics”. *Nature* 578, pp. 432–436. DOI: 10.1038/s41586-020-1957-x.

**Seoh**, **S.-A.**; **D. Sigg**; **D. M. Papazian**; **F. Bezanilla** (1996). "Voltage-sensing residues in the S2 and S4 segments of the Shaker $K^+$ channel". *Neuron* 16, 6, pp. 1159–1167. DOI: 10.1016/S0896-6273(00)80142-7.

**Shalaeva**, **D. N.**; **M. Y. Galperin**; **A. Y. Mulkidjanian** (2015). "Eukaryotic G protein-coupled receptors as descendants of prokaryotic sodium-translocating rhodopsins". *Biology Direct* 10, 1, p. 63. DOI: 10.1186/s13062-015-0091-4.

**Shaner**, **N. C.**; **R. E. Campbell**; **P. A. Steinbach**; **B. N. G. Giepmans**; **A. E. Palmer**; **R. Y. Tsien** (2004). "Improved monomeric red, orange and yellow fluorescent proteins derived from *Discosoma sp.* red fluorescent protein". *Nature Biotechnology* 22, 12, pp. 1567–1572. DOI: 10.1038/nbt1037.

**Sharkov**, **A. V.**; **A. V. Pakulev**; **S. V. Chekalin**; **Y. A. Matveetz** (1985). "Primary events in Bacteriorhodopsin probed by subpicosecond spectroscopy". *Biochimica et Biophysica Acta (BBA) - Bioenergetics* 808, 1, pp. 94–102. DOI: 10.1016/0005-2728(85)90031-3.

**Sharon**, **I.** *et al.* (2009). "Photosystem I gene cassettes are present in marine virus genomes". *Nature* 461, 7261, pp. 258–262. DOI: 10.1038/nature08284.

**Sheves**, **M.**; **A. Albeck**; **N. Friedman**; **M. Ottolenghi** (1986). "Controlling the pKa of the Bacteriorhodopsin Schiff base by use of artificial retinal analogues". *Proceedings of the National Academy of Sciences* 83, 10, pp. 3262–3266. DOI: 10.1073/pnas.83.10.3262.

**Sheves**, **M.**; **N. Friedman**; **A. Albeck**; **M. Ottolenghi** (1985). "Primary photochemical event in Bacteriorhodopsin: Study with artificial pigments". *Biochemistry* 24, 5, pp. 1260–1265. DOI: 10.1021/bi00326a031.

**Shi**, **L.**; **S. R. Yoon**; **A. G. Bezerra**; **K.-H. Jung**; **L. S. Brown** (2006). "Cytoplasmic shuttling of protons in *Anabaena* Sensory Rhodopsin: Implications for signaling mechanism". *Journal of Molecular Biology* 358, 3, pp. 686–700. DOI: 10.1016/j.jmb.2006.02.036.

**Shibata**, **M.**; **H. Kandori** (2005). "FTIR studies of internal water molecules in the Schiff base region of Bacteriorhodopsin". *Biochemistry* 44, 20, pp. 7406–7413. DOI: 10.1021/bi050122+.

**Shichida**, **Y.**; **T. Matsuyama** (2009). "Evolution of opsins and phototransduction". *Philosophical Transactions of the Royal Society B: Biological Sciences* 364, 1531, pp. 2881–2895. DOI: 10.1098/rstb.2009.0051.

**Shihoya**, **W.** *et al.* (2019). "Crystal structure of Heliorhodopsin". *Nature* 574, pp. 132–136. DOI: 10.1038/s41586-019-1604-6.

**Shiina**, **T.**; **M. Tazawa** (1987). "$Ca^{2+}$-activated $Cl^-$ channel in the plasmalemma of *Nitellopsis obtusa*". *The Journal of Membrane Biology* 99, 2, pp. 137–146. DOI: 10.1007/BF01871233.

**Shiina**, **T.**; **M. Tazawa** (1988). "$Ca^{2+}$-dependent $Cl^-$ efflux in tonoplast-free cells of *Nitellopsis obtusa*". *The Journal of Membrane Biology* 106, 2, pp. 135–139. DOI: 10.1007/BF01871395.

**Shull**, **G. E.** (1990). "cDNA cloning of the beta-subunit of the rat gastric H,K-ATPase". *Journal of Biological Chemistry* 265, 21, pp. 12123–12126.

**Sineshchekov**, **O. A.**; **E. G. Govorunova**; **K.-H. Jung**; **S. Zauner**; **U.-G. Maier**; **J. L. Spudich** (2005). "Rhodopsin-mediated photoreception in cryptophyte flagellates". *Biophysical Journal* 89, 6, pp. 4310–4319. DOI: 10.1529/biophysj.105.070920.

**Sineshchekov**, **O. A.**; **E. G. Govorunova**; **H. Li**; **J. L. Spudich** (2015). "Gating mechanisms of a natural anion channelrhodopsin". *Proceedings of the National Academy of Sciences* 112, 46, pp. 14236–14241. DOI: 10.1073/pnas.1513602112.

**Sineshchekov**, **O. A.**; **E. G. Govorunova**; **J. L. Spudich** (2020a). "Probing channelrhodopsin electrical activity in algal cell populations". *Channelrhodopsin: Methods and Protocols*. Ed. by **R. E. Dempski**. Methods in Molecular Biology. New York, NY: Springer, pp. 85–96. ISBN: 978-1-07-160830-2. DOI: 10.1007/978-1-0716-0830-2_6.

**Sineshchekov**, **O. A.**; **K.-H. Jung**; **J. L. Spudich** (2002). "Two rhodopsins mediate phototaxis to low- and high-intensity light in *Chlamydomonas reinhardtii*". *Proceedings of the National Academy of Sciences* 99, 13, pp. 8689–8694. DOI: 10.1073/pnas.122243399.

**Sineshchekov**, **O. A.**; **H. Li**; **E. G. Govorunova**; **J. L. Spudich** (2016). "Photochemical reaction cycle transitions during anion channelrhodopsin gating". *Proceedings of the National Academy of Sciences* 113, 14, E1993–E2000. DOI: 10.1073/pnas.1525269113.

**Sineshchekov**, **O. A.** *et al.* (2020b). "Conductance mechanisms of rapidly desensitizing cation channelrhodopsins from cryptophyte algae". *mBio* 11, 2. DOI: 10.1128/mBio.00657-20.

**Singh**, **M.**; **K. Inoue**; **A. Pushkarev**; **O. Béjà**; **H. Kandori** (2018). "Mutation study of Heliorhodopsin 48C12". *Biochemistry* 57, 33, pp. 5041–5049. DOI: 10.1021/acs.biochem.8b00637.

**Skopintsev**, **P.** *et al.* (2020). "Femtosecond-to-millisecond structural changes in a light-driven sodium pump". *Nature* 583, pp. 314–318. DOI: 10.1038/s41586-020-2307-8.

**Smith**, **B. C.** (2011). *Fundamentals of Fourier transform infrared spectroscopy*. CRC Press. ISBN: 978-1-4200-6930-3.

**Smith**, **S. O.**; **J. Lugtenburg**; **R. A. Mathies** (1985a). "Determination of retinal chromophore structure in Bacteriorhodopsin with resonance Raman spectroscopy", pp. 95–109.

**Smith**, **S. O.**; **A. B. Myers**; **R. A. Mathies**; **J. A. Pardoen**; **C. Winkel**; **E. M. M. van den Berg**; **J. Lugtenburg** (1985b). "Vibrational analysis of the all-*trans* retinal protonated Schiff base". *Biophysical Journal* 47, 5, pp. 653–664. DOI: 10.1016/S0006-3495(85)83961-8.

**Smith**, **S. O.**; **A. B. Myers**; **J. A. Pardoen**; **C. Winkel**; **P. P. J. Mulder**; **J. Lugtenburg**; **R. Mathies** (1984). "Determination of retinal Schiff base configuration in Bacteriorhodopsin". *Proceedings of the National Academy of Sciences* 81, 7, pp. 2055–2059. DOI: 10.1073/pnas.81.7.2055.

**Smith**, **S. O.**; **J. A. Pardoen**; **J. Lugtenburg**; **R. A. Mathies** (1987a). "Vibrational analysis of the 13-*cis*-retinal chromophore in dark-adapted Bacteriorhodopsin". *The Journal of Physical Chemistry* 91, 4, pp. 804–819. DOI: 10.1021/j100288a011.

**Smith**, **S. O.**; **J. A. Pardoen**; **P. P. J. Mulder**; **B. Curry**; **J. Lugtenburg**; **R. Mathies** (1983). "Chromophore structure in Bacteriorhodopsin's O640 photointermediate". *Biochemistry* 22, 26, pp. 6141–6148. DOI: 10.1021/bi00295a016.

**Smith**, **S. O.** *et al.* (1987b). "Vibrational analysis of the all-*trans*-retinal chromophore in light-adapted Bacteriorhodopsin". *Journal of the American Chemical Society* 109, 10, pp. 3108–3125. DOI: 10.1021/ja00244a038.

**Smith**, **T.**; **M. Waterman** (1981). "Identification of common molecular subsequences". *Journal of Molecular Biology* 147, pp. 195–197. DOI: 10.1016/0022-2836(81)90087-5.

**Snellenburg**, **J. J.**; **S. P. Laptenok**; **R. Seger**; **K. M. Mullen**; **I. H. M. van Stokkum** (2012). "Glotaran: A Java-based graphical user interface for the R package TIMP". *Journal of Statistical Software* 49, 3, pp. 1–22. DOI: 10.18637/jss.v049.i03.

**Sonnhammer**, **E. L. L.**; **G. von Heijne**; **A. Krogh** (1998). "A hidden Markov model for predicting transmembrane helices in protein sequences". *Proceedings. International Conference on Intelligent Systems for Molecular Biology*, 6, pp. 175–182.

**Sprenger**, **W. W.**; **W. D. Hoff**; **J. P. Armitage**; **K. J. Hellingwerf** (1993). "The eubacterium *Ectothiorhodospira halophila* is negatively phototactic, with a wavelength dependence that fits the absorption spectrum of the photoactive yellow protein". *Journal of Bacteriology* 175, 10, pp. 3096–3104. DOI: 10.1128/jb.175.10.3096-3104.1993.

**Spudich**, **J. L.** (2006). "The multitalented microbial sensory rhodopsins". *Trends in Microbiology* 14, 11, pp. 480–487. DOI: 10.1016/j.tim.2006.09.005.

**Stanewsky**, **R.** *et al.* (1998). "The Cryb mutation identifies cryptochrome as a circadian photoreceptor in *Drosophila*". *Cell* 95, 5, pp. 681–692. DOI: 10.1016/S0092-8674(00)81638-4.

**Stavenga**, **D. G.**; **R. P. Smits**; **B. J. Hoenders** (1993). "Simple exponential functions describing the absorbance bands of visual pigment spectra". *Vision Research* 33, 8, pp. 1011–1017. DOI: 10.1016/0042-6989(93)90237-Q.

**Stierl**, **M.** *et al.* (2011). "Light modulation of cellular cAMP by a small bacterial photoactivated adenylyl cyclase, bPAC, of the soil bacterium *Beggiatoa*". *Journal of Biological Chemistry* 286, 2, pp. 1181–1188. DOI: 10.1074/jbc.M110.185496.

**Streit**, **W. R.**; **R. A. Schmitz** (2004). "Metagenomics - the key to the uncultured microbes". *Current Opinion in Microbiology* 7, 5, pp. 492–498. DOI: 10.1016/j.mib.2004.08.002.

**Sugiyama**, **Y.** *et al.* (2009). "Photocurrent attenuation by a single polar-to-nonpolar point mutation of Channelrhodopsin-2". *Photochemical & Photobiological Sciences* 8, 3, p. 328. DOI: 10.1039/b815762f.

**Sulis Sato**, **S.** *et al.* (2017). "Simultaneous two-photon imaging of intracellular chloride concentration and pH in mouse pyramidal neurons *in vivo*". *Proceedings of the National Academy of Sciences* 114, 41, E8770–E8779. DOI: 10.1073/pnas.1702861114.

**Sunagawa**, **S.** *et al.* (2015). "Structure and function of the global ocean microbiome". *Science* 348, 6237, pp. 1261359–1261359. DOI: 10.1126/science.1261359.

**Suttle**, **C. A.** (2007). "Marine viruses - Major players in the global ecosystem". *Nature Reviews Microbiology* 5, 10, pp. 801–812. DOI: 10.1038/nrmicro1750.

**Swartz**, **T. E.**; **S. B. Corchnoy**; **J. M. Christie**; **J. W. Lewis**; **I. Szundi**; **W. R. Briggs**; **R. A. Bogomolni** (2001). "The photocycle of a flavin-binding domain of the blue light photoreceptor phototropin". *Journal of Biological Chemistry* 276, 39, pp. 36493–36500. DOI: 10.1074/jbc.M103114200.

**Takahashi**, **T.**; **B. Yan**; **P. Mazur**; **F. Derguini**; **K. Nakanishi**; **J. L. Spudich** (1990). "Color regulation in the archaebacterial phototaxis receptor phoborhodopsin (Sensory Rhodopsin II)". *Biochemistry* 29, 36, pp. 8467–8474. DOI: 10.1021/bi00488a038.

**Tashiro**, **R.**; **K. Sushmita**; **S. Hososhima**; **S. Sharma**; **S. Kateriya**; **H. Kandori**; **S. Tsunoda** (2020). *Unique light-gated ion channel properties of a novel modular cation channelrhodopsin from an evolutionary important terrestrial green alga*. Preprint.

**Tavan**, **P.**; **K. Schulten**; **D. Oesterhelt** (1985). "The effect of protonation and electrical interactions on the stereochemistry of retinal Schiff bases". *Biophysical Journal* 47, 3, pp. 415–430. DOI: 10.1016/S0006-3495(85)83933-3.

**Taylor**, **A. R.** (2009). "A fast $Na^+/Ca^{2+}$-based action potential in a marine diatom". *PLOS ONE* 4, 3. DOI: 10.1371/journal.pone.0004966.

**Tazawa**, **M.**; **U. Kishimoto**; **M. Kikuyama** (1974). "Potassium, sodium and chloride in the protoplasm of Characeae". *Plant and Cell Physiology* 15, 1, pp. 103–110. DOI: 10.1093/oxfordjournals.pcp.a074969.

**Terakita**, **A.** (2005). “The opsins”. *Genome Biology* 6, 3, p. 213. DOI: 10.1186/gb-2005-6-3-213.

**Tester**, **M.** (1990). “Plant ion channels: Whole-cell and single-channel studies”. *The New Phytologist* 114, 3, pp. 305–340.

**Tian**, **Y.**; **S. Gao**; **E. L. Heyde**; **A. Hallmann**; **G. Nagel** (2018). “Two-component cyclase opsins of green algae are ATP-dependent and light-inhibited guanylyl cyclases”. *BMC Biology* 16, 1, pp. 1–18. DOI: 10.1186/s12915-018-0613-5.

**Tkatch**, **T.** *et al.* (2017). “Optogenetic control of mitochondrial metabolism and $Ca^{2+}$ signaling by mitochondria-targeted opsins”. *Proceedings of the National Academy of Sciences*. DOI: 10.1073/pnas.1703623114.

**Trapani**, **V.**; **G. Farruggia**; **C. Marraccini**; **S. Iotti**; **A. Cittadini**; **F. I. Wolf** (2010). “Intracellular magnesium detection: Imaging a brighter future”. *Analyst* 135, 8, pp. 1855–1866. DOI: 10.1039/C0AN00087F.

**Tsukamoto**, **T.**; **C. Kikuchi**; **H. Suzuki**; **T. Aizawa**; **T. Kikukawa**; **M. Demura** (2018). “Implications for the impairment of the rapid channel closing of *Proteomonas sulcata* Anion Channelrhodopsin 1 at high $Cl^-$ concentrations”. *Scientific Reports* 8, 1, p. 13445. DOI: 10.1038/s41598-018-31742-6.

**Tsunoda**, **S. P.**; **P. Hegemann** (2009). “Glu 87 of Channelrhodopsin-1 causes pH-dependent color tuning and fast photocurrent inactivation”. *Photochemistry and Photobiology* 85, 2, pp. 564–569. DOI: 10.1111/j.1751-1097.2008.00519.x.

**Tsunoda**, **S. P.** *et al.* (2017). “Functional characterization of sodium-pumping rhodopsins with different pumping properties”. *PLOS ONE* 12, 7. Ed. by **H. W. van Veen**. DOI: 10.1371/journal.pone.0179232.

**Tyerman**, **S. D.**; **G. P. Findlay**; **G. J. Paterson** (1986a). “Inward membrane current in *Chara inflata*: I. A voltage- and time-dependent $Cl^-$ component”. *The Journal of Membrane Biology* 89, 2, pp. 139–152. DOI: 10.1007/BF01869710.

— (1986b). “Inward membrane current in *Chara inflata*: II. Effects of pH, $Cl^-$-channel blockers and $NH_4{}^+$, and significance for the hyperpolarized state”. *The Journal of Membrane Biology* 89, 2, pp. 153–161. DOI: 10.1007/BF01869711.

**Uhl**, **R.**; **P. Hegemann** (1990). “Adaptation of *Chlamydomonas* phototaxis: I. A light-scattering apparatus for measuring the phototactic rate of microorganisms with high time resolution”. *Cell Motility* 15, 4, pp. 230–244. DOI: 10.1002/cm.970150406.

**van der Horst**, **G. T. J.** *et al.* (1999). “Mammalian Cry1 and Cry2 are essential for maintenance of circadian rhythms”. *Nature* 398, 6728, pp. 627–630. DOI: 10.1038/19323.

**Váró**, **G.**; **L. Zimányi**; **X. Fan**; **L. Sun**; **R. Needleman**; **J. Lanyi** (1995). “Photocycle of Halorhodopsin from *Halobacterium salinarium*”. *Biophysical Journal* 68, 5, pp. 2062–2072. DOI: 10.1016/S0006-3495(95)80385-1.

**Váró**, **G.** (2000). “Analogies between Halorhodopsin and Bacteriorhodopsin”. *Biochimica et Biophysica Acta (BBA) - Bioenergetics* 1460, 1, pp. 220–229. DOI: 10.1016/S0005-2728(00)00141-9.

**Váró**, **G.**; **J. K. Lanyi** (1991). “Effects of the crystalline structure of purple membrane on the kinetics and energetics of the Bacteriorhodopsin photocycle”. *Biochemistry* 30, 29, pp. 7165–7171. DOI: 10.1021/bi00243a018.

**Vierock**, **J.** (2019). “Molekularer Mechanismus protonenleitender Kanalrhodopsine und protonengekoppelte Zwei-Komponenten-Optogenetik”. Dissertation. Humboldt-Universität zu Berlin.

**Vogt**, **A.**; **Y. Guo**; **S. P. Tsunoda**; **S. Kateriya**; **M. Elstner**; **P. Hegemann** (2015). "Conversion of a light-driven proton pump into a light-gated ion channel". *Scientific Reports* 5, 16450, p. 16450. DOI: 10.1038/srep16450.

**Vogt**, **A.**; **A. Silapetere**; **C. Grimm**; **F. Heiser**; **M. Ancina Möller**; **P. Hegemann** (2019). "Engineered passive potassium conductance in the KR2 sodium pump". *Biophysical Journal* 116, 10, pp. 1941–1951. DOI: 10.1016/j.bpj.2019.04.001.

**Volkov**, **O.** *et al.* (2017). "Structural insights into ion conduction by Channelrhodopsin 2". *Science* 358, 6366. DOI: 10.1126/science.aan8862.

**Walter**, **T. J.**; **M. S. Braiman** (1994). "Anion-protein interactions during Halorhodopsin pumping: Halide binding at the protonated Schiff base". *Biochemistry* 33, 7, pp. 1724–1733. DOI: 10.1021/bi00173a015.

**Wang**, **T.**; **A. O. Sessions**; **C. S. Lunde**; **S. Rouhani**; **R. M. Glaeser**; **Y. Duan**; **M. T. Facciotti** (2013). "Deprotonation of D96 in Bacteriorhodopsin opens the proton uptake pathway". *Structure* 21, 2, pp. 290–297. DOI: 10.1016/j.str.2012.12.018.

**Wang**, **W.**; **J. H. Geiger**; **B. Borhan** (2014). "The photochemical determinants of color vision". *BioEssays* 36, 1, pp. 65–74. DOI: 10.1002/bies.201300094.

**Warshel**, **A.** (1978). "Charge stabilization mechanism in the visual and purple membrane pigments". *Proceedings of the National Academy of Sciences* 75, 6, pp. 2558–2562. DOI: 10.1073/pnas.75.6.2558.

**Watanabe**, **H. C.** *et al.* (2012). "Structural model of channelrhodopsin". *Journal of Biological Chemistry* 287, 10, pp. 7456–7466. DOI: 10.1074/jbc.M111.320309.

**Waterhouse**, **A.** *et al.* (2018). "SWISS-MODEL: Homology modelling of protein structures and complexes". *Nucleic Acids Research* 46, W1, W296–W303. DOI: 10.1093/nar/gky427.

**Weissleder**, **R.** (2001). "A clearer vision for *in vivo* imaging". *Nature Biotechnology* 19, 4, pp. 316–317. DOI: 10.1038/86684.

**Wendler**, **S.**; **U. Zimmermann**; **F.-W. Bentrup** (1983). "Relationship between cell turgor pressure, electrical membrane potential, and chloride efflux in *Acetabularia mediterranea*". *The Journal of Membrane Biology* 72, 1, pp. 75–84. DOI: 10.1007/BF01870315.

**Wietek**, **J.** (2018). "Anion-conducting channelrhodopsins". Dissertation. Humboldt-Universität zu Berlin.

**Wietek**, **J.**; **R. Beltramo**; **M. Scanziani**; **P. Hegemann**; **T. G. Oertner**; **J. S. Wiegert** (2015). "An improved chloride-conducting channelrhodopsin for light-induced inhibition of neuronal activity *in vivo*". *Scientific Reports* 5. DOI: 10.1038/srep14807.

**Wietek**, **J.**; **M. Broser**; **B. S. Krause**; **P. Hegemann** (2016). "Identification of a natural green light absorbing chloride conducting channelrhodopsin from *Proteomonas sulcata*". *Journal of Biological Chemistry* 291, 8, pp. 4121–4127. DOI: 10.1074/jbc.M115.699637.

**Wietek**, **J.** *et al.* (2014). "Conversion of channelrhodopsin into a light-gated chloride channel". *Science* 344, 6182, pp. 409–412. DOI: 10.1126/science.1249375.

**Wietek**, **J.** *et al.* (2017). "Anion-conducting channelrhodopsins with tuned spectra and modified kinetics engineered for optogenetic manipulation of behavior". *Scientific Reports* 7, 1, p. 14957. DOI: 10.1038/s41598-017-14330-y.

**Wigington**, **C. H.** *et al.* (2016). "Re-examination of the relationship between marine virus and microbial cell abundances". *Nature Microbiology* 1, 3. DOI: 10.1038/nmicrobiol.2015.24.

**Williams**, **D. L.** (2016). "Light and the evolution of vision". *Eye* 30, 2, pp. 173–178. DOI: 10.1038/eye.2015.220.

**Wooley**, **J. C.**; **A. Godzik**; **I. Friedberg** (2010). "A primer on metagenomics". *PLOS Computational Biology* 6, 2. DOI: 10.1371/journal.pcbi.1000667.

**Yee**, **D. C.**; **M. A. Shlykov**; **Å. Västermark**; **V. S. Reddy**; **S. Arora**; **E. I. Sun**; **M. H. Saier** (2013). "The transporter-opsin-G protein-coupled receptor (TOG) superfamily". *The FEBS Journal* 280, 22, pp. 5780–5800. DOI: 10.1111/febs.12499.

**Yeh**, **K.-C.**; **S.-H. Wu**; **J. T. Murphy**; **J. C. Lagarias** (1997). "A cyanobacterial phytochrome two-component light sensory system". *Science* 277, 5331, pp. 1505–1508. DOI: 10.1126/science.277.5331.1505.

**Yi**, **A.**; **N. Mamaeva**; **H. Li**; **J. L. Spudich**; **K. J. Rothschild** (2016). "Resonance Raman study of an anion channelrhodopsin: Effects of mutations near the retinylidene Schiff base". *Biochemistry* 55, 16, pp. 2371–2380. DOI: 10.1021/acs.biochem.6b00104.

**Yi**, **A. S.** *et al.* (2017). "Structural changes in an anion channelrhodopsin: Formation of the K and L intermediates at 80 K". *Biochemistry*. DOI: 10.1021/acs.biochem.7b00002.

**Yoshida**, **K.**; **S. P. Tsunoda**; **L. S. Brown**; **H. Kandori** (2017). "A unique choanoflagellate enzyme rhodopsin exhibits light-dependent cyclic nucleotide phosphodiesterase activity". *Journal of Biological Chemistry* 292, 18, pp. 7531–7541. DOI: 10.1074/jbc.M117.775569.

**Yoshizawa**, **S.** *et al.* (2014). "Functional characterization of Flavobacteria Rhodopsins reveals a unique class of light-driven chloride pump in bacteria". *Proceedings of the National Academy of Sciences* 111, 18, pp. 6732–6737. DOI: 10.1073/pnas.1403051111.

**Yutin**, **N.**; **E. V. Koonin** (2012). "Proteorhodopsin genes in giant viruses". *Biology Direct* 7, 1, p. 34. DOI: 10.1186/1745-6150-7-34.

**Zabelskii**, **D.** *et al.* (2020). *Viral channelrhodopsins: Calcium-dependent $Na^+/K^+$ selective light-gated channels*. Preprint.

**Zhang**, **F.** *et al.* (2007). "Multimodal fast optical interrogation of neural circuitry". *Nature* 446, 7136, pp. 633–639. DOI: 10.1038/nature05744.

**Zhu**, **J.**; **T. Mathes**; **Y. Hontani**; **M. T. Alexandre**; **K. Toh**; **P. Hegemann**; **J. T. M. Kennis** (2016). "Photoadduct formation from the FMN singlet excited state in the LOV2 domain of *Chlamydomonas reinhardtii* phototropin". *The Journal of Physical Chemistry Letters* 7, 21, pp. 4380–4384. DOI: 10.1021/acs.jpclett.6b02075.

**Zhu**, **L.**; **J. Kim**; **R. A. Mathies** (1999). "Picosecond time-resolved Raman system for studying photochemical reaction dynamics: Application to the primary events in vision". *Journal of Raman Spectroscopy* 30, 9, pp. 777–783.

**Zimanyi**, **L.**; **L. Keszthelyi**; **J. K. Lanyi** (1989). "Transient spectroscopy of bacterial rhodopsins with an optical multichannel analyzer. 1. Comparison of the photocycles of Bacteriorhodopsin and Halorhodopsin". *Biochemistry* 28, 12, pp. 5165–5172. DOI: 10.1021/bi00438a038.

**Zimanyi**, **L.**; **J. K. Lanyi** (1989). "Transient spectroscopy of bacterial rhodopsins with an optical multichannel analyzer. 2. Effects of anions on the Halorhodopsin photocycle". *Biochemistry* 28, 12, pp. 5172–5178. DOI: 10.1021/bi00438a039.

**Zimmerman**, **A. E.** *et al.* (2020). "Metabolic and biogeochemical consequences of viral infection in aquatic ecosystems". *Nature Reviews Microbiology* 18, 1, pp. 21–34. DOI: 10.1038/s41579-019-0270-x.

**Zscherp**, **C.**; **R. Schlesinger**; **J. Tittor**; **D. Oesterhelt**; **J. Heberle** (1999). "*In situ* determination of transient pKa changes of internal amino acids of Bacteriorhodopsin by using time-resolved attenuated total reflection Fourier-transform infrared spectroscopy". *Proceedings of the National Academy of Sciences* 96, 10, pp. 5498–5503. DOI: 10.1073/pnas.96.10.5498.

# B. Eigenständigkeitserklärung

Hiermit versichere ich, dass ich die vorliegende Dissertation mit dem Titel "Characterization of metagenomically identified channelrhodopsins" selbstständig verfasst und keine anderen als die angegebenen Quellen und Hilfsmittel benutzt habe und alle Ausführungen, die anderen Schriften wörtlich oder sinngemäß entnommen wurden, kenntlich gemacht sind.

Berlin, den 20. Oktober 2020

Johannes Oppermann